PAUL SCHERRER INSTITUT

PSI

LABOR FÜR RADIO- UND UMWELTCHEMIE
DER UNIVERSITÄT BERN UND
DES PAUL SCHERRER INSTITUTS

UNIVERSITÄT
BERN

Big Bang Nucleosynthesis

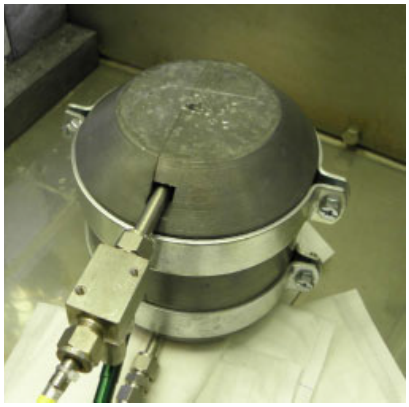

nTOF

1. $n \rightarrow p + e^- + \bar{\nu}_e$
2. $^1\mathrm{H} + n \rightarrow {}^2\mathrm{H} + \gamma$
3. $^2\mathrm{H} + p \rightarrow {}^3\mathrm{He} + \gamma$
4. $^2\mathrm{H} + d \rightarrow {}^3\mathrm{He} + n$
5. $^2\mathrm{H} + d \rightarrow {}^3\mathrm{H} + p$
6. $^3\mathrm{H} + d \rightarrow {}^4\mathrm{He} + n$
7. $^3\mathrm{H} + \alpha \rightarrow {}^7\mathrm{Li} + \gamma$
8. $^3\mathrm{He} + n \rightarrow {}^3\mathrm{H} + p$
9. $^3\mathrm{He} + d \rightarrow {}^4\mathrm{He} + p$
10. $^3\mathrm{He} + \alpha \rightarrow {}^7\mathrm{Be} + \gamma$
11. $^7\mathrm{Li} + p \rightarrow {}^4\mathrm{He} + \alpha$
12. $^7\mathrm{Be} + n \rightarrow {}^7\mathrm{Li} + p$

Annual Report 2015

Laboratory of Radiochemistry and Environmental Chemistry

Cover

The primordial Li problem

The disagreement of the predicted abundance of primordial ^{7}Li with the observed abundance is a longstanding problem in Big Bang Nucleosynthesis (BBN) theory. The depicted part of the nuclide chart shows possible reaction paths in this mass region. Scientists at n_TOF CERN could now study one of these key reactions, ^{7}Be(n, α), using a highly radioactive ^{7}Be target produced at PSI.

Photo left: ^{7}Be can be obtained by filtering the cooling water of the neutron spallation source SINQ at PSI. The photo shows the filter device.

Photo right: The manufacturing of the final target is performed using a remote-controlled dropping device and following evaporation.

PAUL SCHERRER INSTITUT

PSI

LABOR FÜR RADIO- UND UMWELTCHEMIE
DER UNIVERSITÄT BERN UND
DES PAUL SCHERRER INSTITUTS

UNIVERSITÄT
BERN

Annual Report 2015

Laboratory of Radiochemistry and Environmental Chemistry

Editors
A. Türler, M. Schwikowski, A. Blattmann

Paul Scherrer Institut
Labor für Radio- und Umweltchemie
5232 Villigen PSI
Switzerland
Durchwahl +41 56 310 24 04
Sekretariat +41 56 310 24 01
Fax +41 56 310 44 35

Universität Bern
Departement für Chemie und Biochemie
Labor für Radio- und Umweltchemie
Freiestrasse 3, 3012 Bern, Switzerland
Durchwahl +41 31 631 42 64
Sekretariat +41 31 631 42 42
Fax +41 31 631 42 20

Reports are available from
Angela Blattmann
angela.blattmann@psi.ch
Paul Scherrer Institut
5232 Villigen PSI
Switzerland

TABLE OF CONTENTS

Analytical Chemistry

Radwaste Analytics

Radionuclide Development

Radiopharmaceutical R&D Universität Bern

Environmental Radionuclides Universität Bern

EDITORIAL

It is with regret that I must announce that, after 29 consecutive years of producing the Laboratory of Radiochemistry and Environmental Chemistry (LCH) Annual Report, the tradition will come to an end.

The past year (2015) was a turbulent and decisive one for LCH. Intensive consultations with the PSI directorate came to the conclusion that the laboratory was not well positioned as part of the BIO division and that the excellent research performed by the laboratory as a whole, but especially in environmental chemistry, should be strengthened and have a better profile and visibility. Following a decision of the PSI directorate in November 2015, as of 1 January 2016 LCH was split into two: the Laboratory of Environmental Chemistry (LUC), encompassing the groups of Margit Schwikowski and Markus Amman and now located in the renamed Energy and Environment division (ENE) and the Laboratory of Radiochemistry (LRC), newly associated with the Nuclear Energy and Safety division (NES). While I will remain head of LRC, Margit Schwikowski was promoted to the position of laboratory head of LUC. It is not the first time in the history of LCH that a unit was split off. The Laboratory of Atmospheric Chemistry (LAC in the ENE division) was launched after the successful transfer of the Aerosol Chemistry group, headed by Urs Baltensperger, from LCH. The consensus, therefore, is that this reorganization is an encouraging sign of a developing healthy organism!

With this reorganization in place, it has not yet been decided if LRC or LUC will continue the tradition of presenting snapshots of ongoing research in the form of an annual report. Although the preparation of the report required an extra effort from all lab members, it was always very well received and significantly assisted in the presentation of our laboratory to visitors or with the preparation of audit reports.

In the last year of its existence, LCH had an outstanding publication record, listing 73 peer-reviewed articles. This excellent result confirmed that previous all-time record with more than 80 published articles was not a fluke. Michael Sigl, in the Analytical Chemistry group, deserves a special mention: he was first author in one of two Nature publications that followed from his stay as a post-doctoral fellow at Desert Research Institute, Reno, Nevada.

The year's social event took us to the Grimsel region, where we were able to visit one of several underground hydroelectric plants und understand the complicated network of water reservoirs. Due to a sophisticated control system, flexible electricity generation is possible, as well as pumping of water back into the reservoir at times of abundant electricity. This way, the Kraftwerke Oberhasli (KWO) can be regarded as a giant rechargeable battery with an excellent CO_2 balance. Due to the wonderful weather, we were happy not to spend all day underground and could enjoy the spectacular scenery formed by ancient glaciers, expertly explained to us by Margit. The end of the year was celebrated with a well-deserved Apero at Schloss Böttstein.

In closing, I would like to thank our faithful readers for their continued support and for the praise that we received over the years. This positive feedback was always an encouragement to employees that LCH was a laboratory to be proud of.

Andreas Türler

TOWARDS THE SELENIDES OF COPERNICIUM AND FLEROVIUM: COPERNICIUM - SELENIUM BOND FORMATION OBSERVED

N. M. Chiera, R. Eichler, P. Steinegger, A. Türler (Univ. Bern & PSI), R. Dressler, D. Piguet, A. Vögele (PSI), N. V. Aksenov, Y. V. Albin, G. A. Bozhikov, V. I. Chepigin, S. N. Dmitriev, V. Ya. Lebedev, S. Madumarov, O. N. Malyshev, O. V. Petrushkin, Y. A. Popov, A. V. Sabel'nikov, A. I. Svirikhin, G. K. Vostokin, A. V. Yeremin (FNLR, JINR, Russia)

Two different selenium allotropes – red amorphous selenium and trigonal selenium – were used as stationary surfaces in isothermal model experiments performed in preparation of a sensitive chemical separation and characterization of the superheavy elements Cn and Fl. The Monte-Carlo simulations of a diffusion controlled deposition of Hg – copernicium's lighter homologue – are in agreement with the obtained experimental data, assuming a ΔH_{ads}^{Hg}(red Se) < -85 kJ/mol, and a ΔH_{ads}^{Hg}(trigonal Se) > -60 kJ/mol interaction limits [1].

The different reactivity of Hg towards the two allotropic surfaces allowed for monitoring the Se surface crystallization grade, i.e. the spontaneous transformation of red amorphous Se to the trigonal allotrope, at a microscopic level. First on-line test experiments using the COLD detector array [2] with Se covered detector surfaces were performed. For this purpose, a mixed ^{242}Pu/^{nat}Nd oxide target (1 mg/cm^2 ^{242}Pu, 50 µg/cm^2 ^{nat}Nd) was prepared by molecular plating on a 2 µm Ti foil. A $^{48}Ca^{18+}$ beam with a primary energy of 272 MeV was delivered from the U-400 cyclotron at FLNR (Dubna). After passing through a 4 µm Ti window, a 0.5 cm cooling gas slit, and the Ti backing foil, the beam entered the target with an energy of about 244 MeV, producing ^{185}Hg and ^{287}Fl in the nuclear fusion reactions ^{142}Nd(^{48}Ca,5n) and ^{242}Pu(^{48}Ca,5n), respectively. The evaporation residues were thermalized in a recoil chamber internally covered with quartz, and flushed with a mixed gas flow (Ar/ He - 30:70, 1.8 L/min gas flow rate) through a 4 m long PFA® Teflon capillary to the thermochromatographic detection system COLD (Fig. 1).

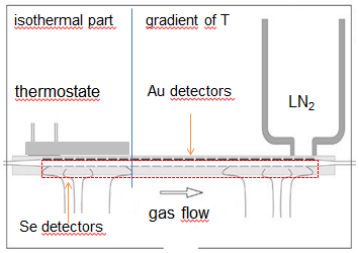

Fig. 1: Schematic disposition of the Au and Se covered PIN diodes detectors in the COLD channel array.

The Se surface crystallization was monitored by the ^{185}Hg deposition pattern. The deposition revealed an advanced crystallization (>80%) of the thin red amorphous Se surface forming presumably trigonal Se on the detectors after 5 weeks of storage.

Two events detected on Se-covered detectors were attributed to ^{283}Cn (Fig. 2). Monte Carlo simulations were performed, indicating that Cn reacted with trigonal Se with a probability > 95%, with a - ΔH_{ads}^{Cn}(t-Se) > 48 kJ/mol (Fig. 3). Despite the fact that CnSe formation is expected to be thermodynamically less favored [1], these first results surprisingly reveal an interaction with even a lower kinetic formation hindrance for Cn compared to the interaction of Hg with t-Se. Further on-line studies with Hg, Cn, and Fl on both trigonal and amorphous selenium surfaces are envisaged in 2016.

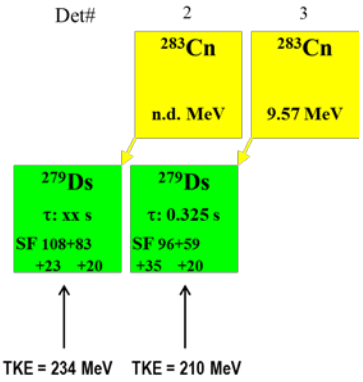

Fig. 2: ^{283}Cn events observed on the Se-covered detectors #2 and 3, after the target was irradiated with an overall beam dose of 6.30E+17 ^{48}Ca particles. No other spontaneous fissions signals were observed. Note the high total kinetic energy of the SF, considering the pulse height defect and gas stopping.

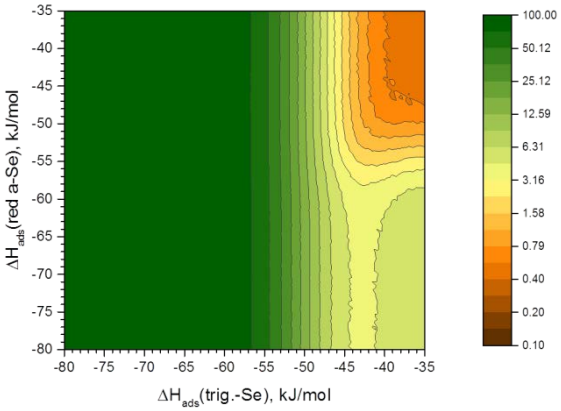

Fig. 3: A preliminary analysis of the probability to observe the two ^{283}Cn events on the Se-covered detectors, assuming a stationary surface composition on one side of the isothermal part of COLD as 4% red amorphous Se, 80% trigonal Se and 16% SiO_2; The other surfaces of the channel are assumed to consist of SiO_2.

ACKNOWLEDGEMENT

The work was supported by the Swiss National Science Foundation (SNF-200020_144511)

[1] N. Chiera et al., Ann Rep., Lab. of Radio & Environ. Chem., Univ. Bern & PSI, p. 5 (2015).

KINETIC STUDIES ON THE MERCURY – SELENIUM INTERACTION

N. M. Chiera, R. Eichler, A. Türler (Univ. Bern & PSI), A. B. Liechti (Univ. Bern), D. Piguet, A. Vögele (PSI), S. Madumarov (FNLR, Russia)

A kinetic effect in the adsorption behavior of elemental Hg on red amorphous Se and trigonal Se surfaces was observed in isothermal gas chromatography experiments. The formation of $HgSe_{(s)}$ was kinetically favored on red amorphous Se surfaces. Recently, first experimental evidence was obtained for copernicium - mercury's heavier homologue – revealing an interaction with trigonal Se at least as fast as with the red amorphous allotrope [1].

In order to understand the kinetic processes governing the Hg/Se interaction, inverse thermochromatographic (IT) studies with both the amorphous and the crystalline Se surfaces will be performed. For this purpose, an inverse thermochromatographic setup was developed (Fig. 1). A gradient of temperature from +40°C to +120°C will be applied in the Hg / trigonal Se IT experiments (Fig. 1a), while the Hg / red amorphous selenium interaction will be explored in the temperature range from -50°C to +50°C (Fig. 1b). These temperature intervals were selected based on the experimental observations [1] and on the phase transition points of Se. The aim of these IT experiments is to derive the lower limit temperature, at which the $HgSe_{(s)}$ formation is promoted on either of the allotropic Se surfaces. Together with the experimental setups shown in Figure 1, a model based on a multistep interaction process was developed, in which a reversible adsorption (1) is eventually followed by the formation of an activated complex (2) which leads to a covalent bond formation (3):

1) $Hg_{(g)} + Se_{(s)} \leftrightarrow Hg_{(ads)}{\sim}Se_{(s)}$

2) $Hg_{(ads)}{\sim}Se_{(s)} \leftrightarrow HgSe^{*}$ (slow step, rate-determining)

3) $HgSe^{*} \rightarrow HgSe_{(s)}$ (fast step)

The associated residence time in the adsorbed state (t_a) and the reaction time (t_r) (i.e. the time needed to reach the transition state) are calculated and randomized in Monte-Carlo simulations by a logarithmically distributed random variable between 0 and 0.999999:

$$ta = -Nm\frac{1}{vb}e^{-\frac{\Delta Hads}{RT}}\ln(1-random)$$

$$tr = -\frac{1}{k}\ln(1-random)$$

where N_m is the mean number of wall collisions between two jumps, υ_b is the Se phonon vibration frequency, ΔH_{ads} is the adsorption enthalpy of Hg on a specific Se allotropic surface, R the universal gas constant, T the temperature, and k is the kinetic constant. Based on Eyring's ansatz [2], the latter can be also written in the form:

$$k = -\frac{kbT}{h}\mathrm{A}e^{-\frac{\Delta H+}{RT}}$$

where k_b is the Boltzmann constant, h the Planck constant, A is a pre-exponential factor which takes into account experimental parameters and entropy changes, and ΔH^{+} is the activation enthalpy of the formation reaction of the activated complex $HgSe^{*}$.

If the given reaction time t_r is lower than the residence time t_a, then the activated complex is obtained, followed by the formation of a covalent bond between Hg and Se; otherwise a reversible physisorption process is assumed. Based on this kinetic model, Monte-Carlo simulations will be applied to the data evaluation of the inverse thermochromatographic experiments, allowing for choosing the physical meaningful set of A and ΔH^{+} that fits the experimental data best, and obtaining in this way kinetic information on the Hg / Se interaction.

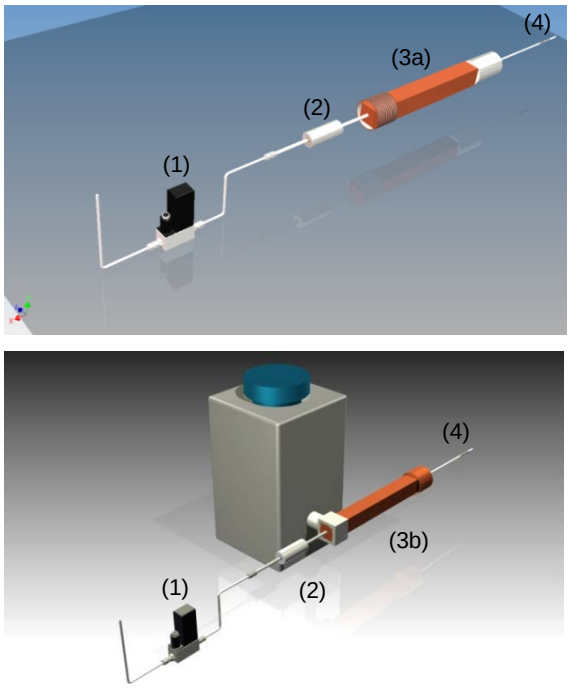

Fig. 1: Schematic of the developed setup. A 30 ml/min He gas flow (1) is passed through a ^{197}Hg carrier free source (2). The evaporated ^{197}Hg is transported to a 50 cm chromatographic column coated with trigonal Se (3a) or red amorphous Se (3b), inserted in a copper rod where a gradient of temperature is applied (see the text for the temperature ranges). The eventually not absorbed ^{197}Hg is captured in a charcoal trap (4).

ACKNOWLEDGEMENT

The work was supported by the Swiss National Science Foundation (SNF-200020_144511).

[1] N. Chiera et al., Ann Rep., Lab. of Radio & Environ. Chem., Univ. Bern & PSI, (2015).

[2] H. Eyring, J. Chem. Phys. **3**, 107-115 (1935).

QUALITATIVE ASSESSMENT OF THE THERMAL RELEASE OF THALLIUM FROM A HAFNIUM FOIL

P. Steinegger, R. Eichler, A. Türler (Univ. Bern & PSI), M. Asai, Y. Kaneya, A. Mitsukai, Y. Nagame, T. K. Sato, M. Schädel, S. Takeda, A. Toyoshima, K. Tsukada, A. Vascon (ASRC, JAEA, Japan), R. Dressler, D. Piguet (PSI)

The isothermal vacuum chromatography setup [1,2] was used for an on-line thermal release measurement of thallium from a 25 µm thin hafnium catcher foil (30 x 48 mm, *Goodfellow Cambridge Ltd.*). The radioactive thallium tracer was produced in the nuclear fusion reaction ^{152}Gd(^{35}Cl, 3n)^{184}Tl ($t_{1/2}$ = 10.1 *5* s) at the JAEA Tandem accelerator and provided to the experiment as described in [2]. The Tl^+ ion ISOL beam passed through a 3 mm entrance hole and was stopped in a resistively heated hafnium catcher foil. Due to the rather low kinetic energies of 30 keV ^{184}Tl featured a shallow implantation depth of about ≈ 7.2 nm (SRIM 2013) [3] only. After its segregation to the surface, thallium needs to desorb. It has been shown in [4] that desorption is not the rate determining step, whereas the segregation dominates the kinetics of the thermal release. The liberated ^{184}Tl was identified after having traversed through the isothermal chromatography section being operated at highest oven temperatures for minimum retention loss. For this purpose, the diamond-based escape detector [1,5] was employed for α-spectroscopic measurements. The release rate was determined in consecutive steps at four different foil temperatures (see indicated sequence in Fig. 1). These temperatures were measured beforehand with an accuracy of ±50 K using a portable radiation thermometer (IR-AH3SU, *CHINO*). As the continuously fed thallium inventory inside the catcher matrix is not easily accessible, only a qualitative assessment of the release seems possible. The measurement at the highest foil temperature (i.e., ≈ 1829 K) is taken as a 100% release yield, justified by the non-observation of the long-lived decay product ^{184}Ir in the Hf foil, held at these thermal conditions [2]. The released fraction F [%] within a time span t_r [s] from a foil with a thickness of d [m] amounts to

$$F[\%] = 100 - \frac{800}{\pi^2}\sum_{n=0}^{\infty}\frac{\exp\left\{-\frac{(2n+1)^2\pi^2 D t_r}{d^2}\right\}}{(2n+1)^2}$$

The temperature dependent diffusion coefficient D can be calculated using the Arrhenius equation

$$D = D_0 \exp\left(-\frac{E_a}{RT}\right)$$

Thus, knowing the diffusion constant D_0 and the diffusion activation energy E_a, one can determine the corresponding thermal release as a function of the temperature. As these parameters are not available for the examined system, the obtained data is compared to the theoretical release curves of thallium from zirconium using different release times t_r = 1s, 0.1 s, and 0.01 s (Fig. 1). D_0 and E_a are both extracted from [4] and apply to the case of radiation damage enhanced diffusion. One might argue a similar phenomenon for the current case with a shallow implantation depth leaving an exit path for the implanted ion in the Hf-lattice. This hypothesis is supported by comparing the release curves for two Zr foil thicknesses (Fig. 1), d = 25 µm and a thickness equal to the implantation depth of d = 7.2 nm.

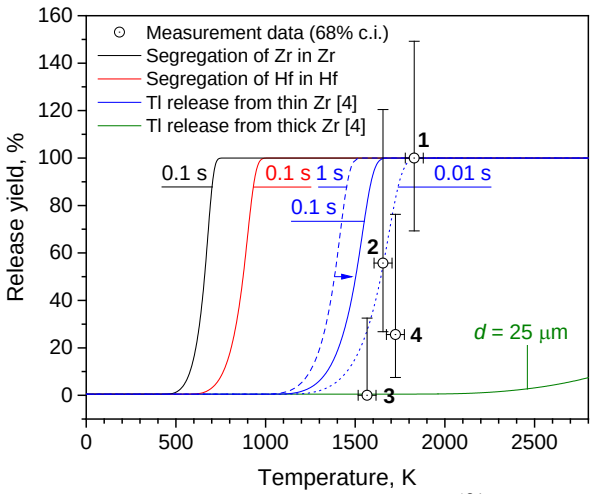

Fig. 1: The thermal release of implanted ^{184}Tl from a hafnium foil (68% c.i.) qualitatively compared to the one of Tl from a zirconium foil at various release times t_r (blue, d = 7.2 nm) and with the actual foil thickness (green, d = 25 µm). The self-diffusion driven segregation curves for zirconium (black, d = 7.2 nm) and hafnium (red, d = 7.2 nm) are shown for comparative reasons.

As mentioned above, the post-experimental γ-spectroscopic analysis revealed no losses of ^{184}Tl as a consequence of prolonged release above 1800 K [2]. In combination with the above presented findings, this indicates a complete thermal release of thallium from a few nanometers deep surface layer of a hafnium foil within an upper limit release time of $t_r \leq 2$ s.

ACKNOWLEDGEMENT

The work was supported by the Swiss National Science Foundation (SNF-200020_144511).

[1] P. Steinegger et al., Ann Rep., Lab. of Radio & Environ. Chem., Univ. Bern & PSI, 2014, p.7 (2015).
[2] P. Steinegger et al., J. Phys. Chem. C, (2015) submitted.
[3] J. F. Ziegler et al., Nucl. Instr. Meth. Phys. Res. B **268**, 1818-1823 (2010).
[4] D. Wittwer et al., Nucl. Instr. Meth. Phys. Res. B **297,** 86-93 (2013).
[5] P. Steinegger et al., Nucl. Instr. Meth. Phys. Res. A, in prep.

STOPPING OF EVAPORATION RESIDUES IN GASES HEATED BY INTENSE HEAVY ION BEAMS

R. Eichler, P. Steinegger, N. M. Chiera, A. Türler (Univ. Bern & PSI), R. Dressler, D. Piguet, A. Vögele (PSI), N. V. Aksenov, Y. V. Albin, G. A. Bozhikov, V. I. Chepigin, S. N. Dmitriev, V. Ya. Lebedev, S. Madumarov, O. N. Malyshev, O. V. Petrushkin, Y.A. Popov, A. V. Sabel'nikov, A. I. Svirikhin, G. K. Vostokin, A. V. Yeremin (FNLR, JINR, Russia)

Transactinide elements are produced artificially in heavy ion induced nuclear fusion reactions. All chemistry experiments related to transactinides rely on the thermalization of nuclear reaction products recoiling form production targets with the momentum of the incident beam particles [1]. The design of the experiments with required high overall sensitivity requires a reasonable understanding of heavy ion stopping in gases. With pre-separation using magnetic separators the gases for thermalization are held at ambient condition. Already there [2] we observed a drop in stopping power of Hg, Rn, and No in argon gas by a factor of about two compared to expectations derived using the SRIM code [3].

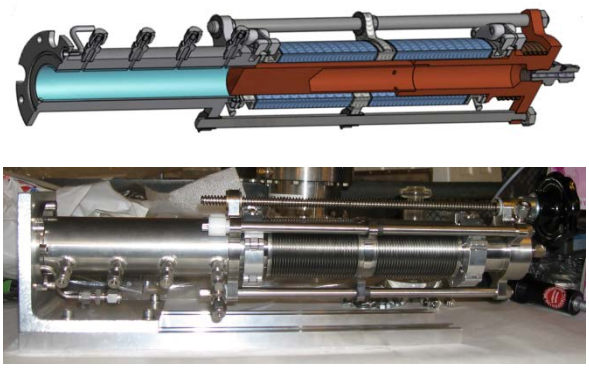

Fig. 1: Schematic and photographic images of the "variable length" recoil chamber as used for this work.

The chemistry experiments performed with transactinides seem to suffer from an unknown sensitivity loss that we attribute to the unknown stopping power of a gas in a recoil chamber heated by intense heavy ion beams passing through the gas volume. Here, an Nd_2O_3 target with natural isotopic composition (200 µg/cm^2 ^{nat}Nd) has been prepared by molecular plating on a 2 µm Ti backing foil. A $^{48}Ca^{18+}$ beam with a primary energy of 272 MeV was delivered from the U-400 cyclotron at FLNR (Dubna). After passing a 4 µm Ti window, a 0.5 cm gas slit, and the Ti backing foil, the beam energy at the entrance of the target was degraded to ~244 MeV. ^{185}Hg was produced in the nuclear fusion reaction ^{142}Nd(^{48}Ca,5n). The evaporation residues were thermalized in the variable recoil chamber as depicted in Fig. 1. and flushed with an inert carrier gas flow of (1.8 L/min) through a 4 m long PFA® Teflon capillary to the thermochromatographic detection system COLD (Fig. 1). The gold coverage in the detector allowed for an efficient trapping of the nuclear reaction products and thus, the determination of the transported amounts of the product. Pure argon and helium, as well as a mixture Ar/He~30/70 vol.-% were used as carrier gases. The recoil energy of ^{185}Hg is deduced from mometum conservation as 70 MeV. A preliminary analysis revealed a clear dependency of the relative yields of transported ^{185}Hg on the beam intensity (Fig.2) and on the range available in the recoil chamber (Fig. 3, recoil depth). In experiments with pure Ar as carrier gas an unexpected pattern was observed which is due to the inefficient flushing of the recoil volumes with large dimensions.

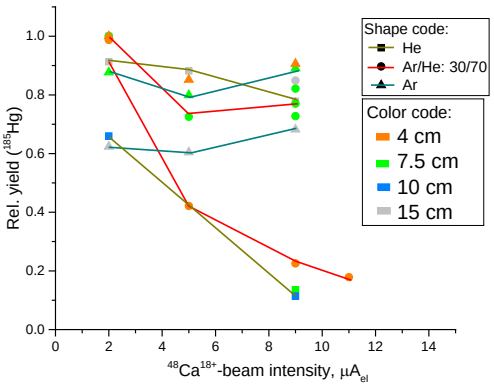

Fig. 2: The relative yields determined for ^{185}Hg dependent on the beam intensity. The varied gas mixtures are encoded by the symbol shape and line color. The chamber depth is encoded in colors.

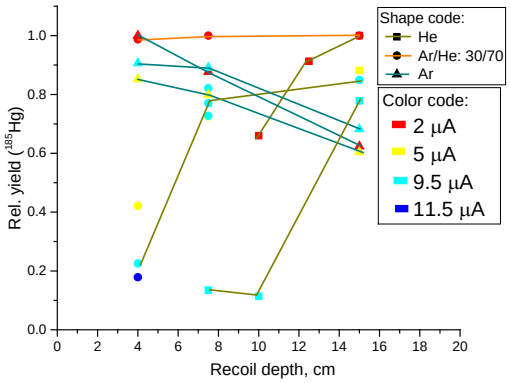

Fig. 3: Relative yields determined for ^{185}Hg dependening on the recoil chamber depth. The various gas mixtures are encoded by the symbol shape and line color. The beam intensity is encoded in colors.

A final analysis and comparison with expectations using SRIM [3] will reveal important data for the design of future transactinide experiments without preseparation.

ACKNOWLEDGEMENT

The work was supported by the Swiss National Science Foundation (SNF-200020_144511).

[1] A. Türler, V. Pershina Chem. Rev. 113, 2 (2013).
[2] D. Wittwer et al. Nucl. Instr. Meth. Phys. Res., Sect. B, **268**, 28 (2010).
[3] J.F. Ziegler et al. Nucl. Instr. Meth. Phys. Res., Sect B, **268**, 1818 (2010).

GAS CLEANING FOR THE SEABORGIUM CARBONYL STABILITY INVESTIGATIONS

N. Niggli (Univ. Bern), R. Eichler (PSI & Univ. Bern)

Recently, the production and adsorptive deposition of Sg carbonyl $Sg(CO)_6$ has been demonstrated [1]. In a subsequent work, experiments have been prepared to assess the thermal stability of the group 6 carbonyl compounds using a thermal decomposition on silver surfaces [2]. A kinetic decomposition model was developed to quantify the first bond dissociation enthalpy (FBDE) for the volatile and fragile hexacarbonyl compounds [3]. The success of these experiments depends on the efficient suppression of oxygen, water, and carbon dioxide contaminations in the carrier gases used for these experiments usually consisting of a mixture of He and CO. Such experiments last for several weeks, so long-term operation of the developed cleaning has to be demonstrated. Therefore, we built-up the COLD thermochromatography loop and modified the cleaning system by introducing a two-step chemical catcher. The first catcher consist of a steel cartridge containing MnO powder, with optional heating up to 900°C for faster reactions and for recovery purposes. This cartridge is intended to significantly reduce the oxygen contamination levels either directly by reacting with MnO to form Mn_2O_3 and MnO_2 or indirectly by catalyzing the oxidation of CO to CO_2. The second steel cartridge was filled with TEPAN-on-PMMA prepared after [4] that could be heated up to 100°C, for facilitating the reaction or for recovery purposes. The aim of both tested secondary getters is to remove the formed CO_2 by reversible chemical binding.

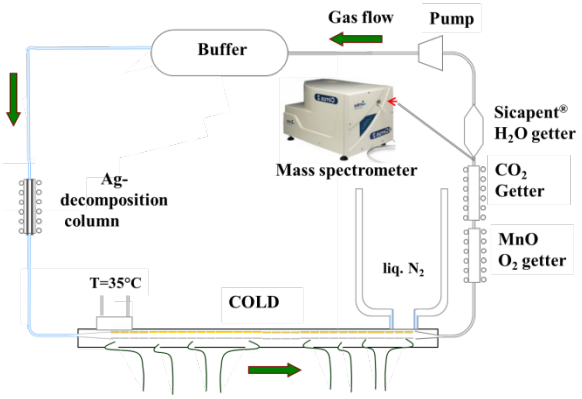

Fig. 1: Schematic of the modified COLD setup as used in this work. The temperature of the Ag decomposition column was set to 500°C.

The MKS Cirrus 2® atmospheric pressure mass spectrometer served for semi-quantitatively monitoring of the trace gases in the mixture, thus controlling on-line the quality of the purification. The combination of the MnO-based oxygen getter followed by a TEPAN cartridge and a Sicapent® cartridge yielded the most reliable and durable decontamination from the trace species O_2 and CO_2 from the used carrier gas mixture CO/He flow of 1.5 l/min.

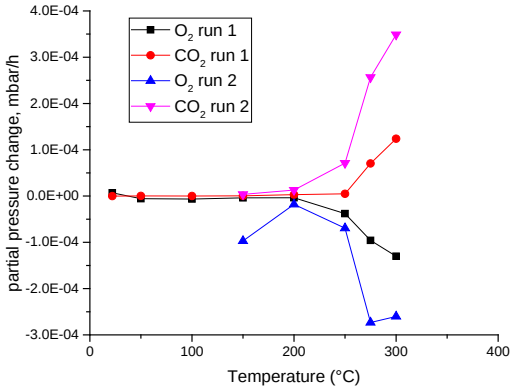

Fig. 2: The partial pressure of O_2 and CO_2 in the carrier gas as a function of a reactivated MnO cartridge. Note the onset of O_2 recovery at 200°C and also a CO_2 concentration increase due to the catalytic CO oxidation on MnO.

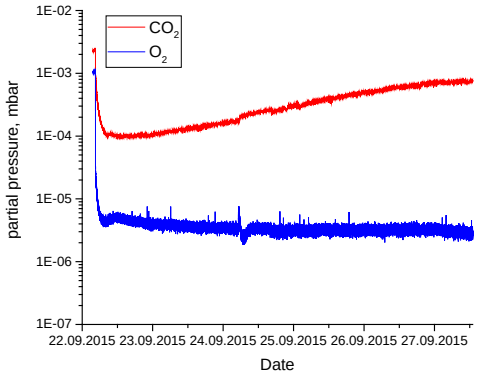

Fig. 3: The partial pressure of trace gas contaminations measured between the CO_2 getter and the Sicapent® within 5 days. Operation temperatures were as follows: MnO@275°C, TEPAN @ 30°C and Ag @ 550°C.

From the long-term test we conclude that the TEPAN cartridge can be safely operated for 2 days before recovery and the MnO cartridge can be operated for at least 5 days without recovery. However, we opt for a tandem system for both gas cleaning devices to be able to perform the recovery operation while running the experiment.

ACKNOWLEDGEMENT

The work was supported by the Swiss National Science Foundation (SNF-200020_144511).

[1] J. Even et al Science 113, 2 (2015).
[2] I. Usoltsev et al., Radiochim. Acta, accept. (2015).
[3] I. Usoltsev et al., Radiochim. Acta, subm. (2015).
[4] C. T. Campbell, Surf. Sci., **157** 43 (1985).

IUPAC TASKGROUP ON ATMOSPHERIC CHEMICAL KINETIC DATA EVALUATION

M. Ammann (PSI), R. A. Cox (UCam), J. N. Crowley (MPIC), H. Herrmann (TROPOS), M. E. Jenkin (AtChS), V. F. McNeill (Univ. Columbia), A. Mellouki (ICARE), M. J. Rossi (PSI), J. Troe (UGött), T. J. Wallington (Ford)

The IUPAC Task Group on Atmospheric Chemical Kinetic Data Evaluation consists of internationally recognized experts from universities, government labs, and industry and provides evaluated chemical data for atmospheric chemistry used in global, regional and urban climate and air quality atmospheric models. Over the past decade we have published our evaluations in the form of peer reviewed articles as part of a special issue in Atmospheric Chemistry and Physics [1]. Parallel to that we are continuously updating individual reactions on our website, which has recently moved to the ETHER site maintained by CNRS-Paris http://iupac.pole-ether.fr/.

It is essential that models of atmospheric chemistry contain up-to-date chemical mechanisms to provide the required accuracy and facilitate comparison of results from different models. It is also important that global chemical transport models, climate or Earth system models contain suitable mechanisms in simplified form that is suitably derived from the detailed mechanism. The results of laboratory experiments are not always unambiguous, especially if results using different methods obtained by different research groups are available. The use of laboratory data therefore requires a substantial effort of compilation, review, and assessment before preferred or recommended values can be made available for the atmospheric science community. The evaluation process itself starts with a consideration of to what degree the experimental data can be applied to atmospheric conditions of concentration, pressure and temperature. Next, an assessment of the experimental procedures is performed, followed by comparison of the results obtained by different experimental approaches and reported by different groups. The data set as a whole then provides the basis for preferred values of a given process and for estimates of the statistical errors and uncertainties [2].

The recognition of the importance of heterogeneous processes with aerosol particles for the gas phase chemistry, the aerosol composition, as well as their effects on climate and human health has led to efforts in establishing suitable descriptions and parameterizations for gas to particle transfer and reactions on the surface and within the bulk of the particles [2]. We therefore expanded our evaluation activity into heterogeneous processes for both solid and liquid particles [3,4].

In many processes covered by the two recent volumes on heterogeneous reactions, the experimental data base is in poor shape. Even for key processes, such as the reaction of N_2O_5 with aerosol particles, there are significant uncertainties in our understanding of the impact of this reaction on tropospheric budgets of nitrogen oxides and halogens. For important species, such as HO_2 radicals, the results from available studies are in conflict, so that no recommendation could be made. In other cases, inconsistencies among different experiments were resolved in retrospect by employing revised descriptions or updated thermodynamic information (e.g., water content) as a basis for reanalysis of older experimental data. This underlines the value of such evaluation work to provide the best possible state of knowledge to the atmospheric science community.

A new feature to facilitate the usage of the datasheets is provision of a single-line expression to parameterize pressure and temperature dependent gas-phase reactions that can be copied directly into spreadsheets or other software. Individual users may register to the website to subscribe to an RSS feed or a mailing list to be informed about updates to the database.

The website is an important method of keeping the data sheets current. Researchers can visit the website and find the latest IUPAC recommendations based upon the latest published data. The IUPAC group is working with CNRS colleagues to add functionality to the website to make it more interactive and to facilitate the direct extraction of data from the website using machine readable files.

In addition to updating the >1000 data sheets on the website as new data become available, the IUPAC Taskgroup is currently extending the gas-phase database to cover aspects of the degradation of large (> C4) biogenic and anthropogenic hydrocarbons (e.g. terpenes and aromatics). These species play important roles in tropospheric chemistry in global, rural and urban environments. The panel is also evaluating the available data for heterogeneous processes involving tropospheric organic aerosol and soot. Furthermore, the latest additional expansion will be to extend the evaluation towards bulk aqueous phase chemistry within aerosol particles and cloud droplets to finally encompass a comprehensive evaluation of atmospheric chemical kinetic data across all phases.

[1] http://www.atmos-chem-phys.net/special_issue8.html
[2] Cox, R. A., Chem. Soc. Rev., **41**, 6231-6246 (2012).
[3] Kolb, C. E. et al., Atmos. Chem. Phys., **10**, 10561-10605 (2010).
[4] Ammann, M. et al., Atmos. Chem. Phys., **13**, 8045-8228 (2013).
[5] Crowley, J. N. et al., Atmos. Chem. Phys., **10**, 9059-9223 (2010).

FORMATION KINETICS AND ABUNDANCE OF ORGANIC NITRATES IN ALPHA-PINENE OZONOLYSIS

T. Berkemeier, U. Pöschl, M. Shiraiwa (MPIC), G. Gržinić, M. Ammann (PSI)

Secondary organic aerosol (SOA) particles are formed by oxidation of volatile organic precursors by atmospheric oxidants such as ozone, NO_3 and OH radicals. Nitrogen oxides (NO, $NO_2 \equiv NO_x$) have been shown to affect the underlying chemistry by formation of organic nitrates [1,2] (cf. Fig. 1) and thus alter the total mass yield. However, the formation and partitioning of nitrogen containing compounds into SOA particles is still poorly understood since organic nitrate contents are difficult to quantify with standard analytical tools. Our collaboration unites a suitable experimental method available at PSI and new advances in the numerical description of growing particulates to unravel the kinetics of the process.

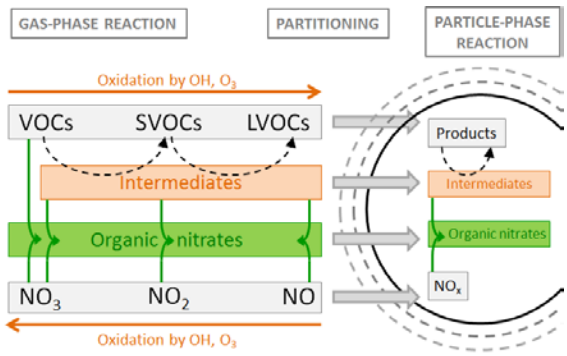

Fig. 1: Schematic representation of SOA formation, involving oxidation of volatile organic compounds (VOCs) to semi and low volatility organic compounds (SVOCs and LVOCs), which partition into the particle phase (grey arrows). Intermediates may react with nitrogen oxides to form organic nitrates in both, gas and particle phase (green arrows).

We use the short-lived radioactive tracer ^{13}N produced by PSI's PROTRAC facility [4] to quantify the amount of organic nitrates produced and retained in SOA particles. SOA particles nucleate homogeneously during either dark ozonolysis or OH photooxidation of α-pinene precursor gas by feeding varying mixtures of these trace gases into an aerosol flow tube system. The ^{13}N labelled molecules are introduced as ^{13}NO in the experiments. The length of the aerosol flow tube can be adjusted via movable inlets. A Scanning Mobility Particle Sizer (SMPS) system is placed behind the aerosol flow tube to determine the size distribution. The remaining gas flow is then directed into a detection system that separates gas and particle phase species and detects the trapped labelled nitrogen compounds via scintillation counters.

A comparison of the time dependence of particle mass, particle number and organic nitrate content provides valuable information on the kinetics of organic nitrate formation. The experiments show a tight correlation between organic nitrate content and particle count, implying that organic nitrates play an important role in the nucleation and growth of nanoparticles. Organic nitrate contents are found to be substantial throughout, but seem to play a major role in the initial formation phase (Fig. 2). The results show that a large fraction (> 15 %) of organic molecules in SOA may exist in a nitrated form, which is in line with previous measurements [5]. The organic nitrate content was found to be influenced weakly by relative humidity on the experimental time scale.

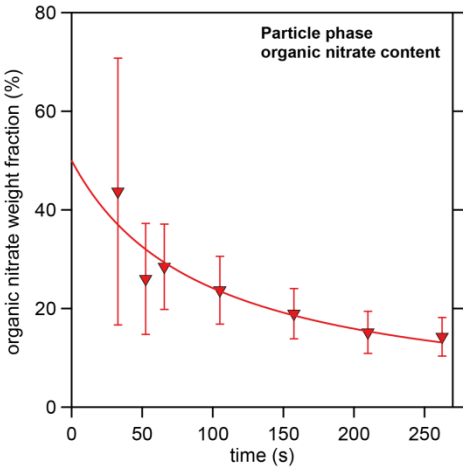

Fig. 2: Estimated organic nitrate content in the particle phase as function of residence time in the flow tube reactor during an α-pinene ozonolysis experiment.

Application of a kinetic box model, which uses simplified gas phase chemistry adopted from the Master Chemical Mechanism (MCM) [6] suggests that direct reaction between organic peroxy radicals (RO_2) and nitrogen monoxide (NO) are the predominant source of organic nitrates and reaction of nitrate radicals (NO_3) with α-pinene constitutes a minor formation path.

ACKNOWLEDGEMENT

We thank M. Birrer and A. Arangio for their help in experiments. This work is supported by Max Planck Society. M. A. appreciated support by the Swiss National Science foundation (grants 130175 and 149492).

[1] Ziemann, P.J., and Atkinson, R., Chem. Soc. Rev., **41,** 6582–6605 (2012).
[2] Renbaum, L. H., and Smith, G. D., Phys. Chem. Chem. Phys., **11**, 8040–8047 (2009).
[3] Shiraiwa *et al.*, Atmos. Chem. Phys., **12**, 2777–2794 (2012).
[4] Ammann, M., Radiochim. Acta, 89, 831 (2001).
[5] Rollins et al., Environ. Sci. Technol., **44**, 5540-5545, (2010).
[6] Saunders *et al.*, Atmos. Chem. Phys., **3**, 161–180 (2003).

OZONE PENETRATION AND REACTION IN ORGANIC AEROSOL

P. A. Alpert (IRCELYON), J.-D. Förster (MPIC), S. Steimer (ETHZ & PSI), S. Rossignol, M. Passananti, S. Perrier (IRCELYON), F. Ditas, C. Pöhlker (MPIC), B. Watts, J. Raabe (SLS), C. George (IRCELYON), M. Ammann (PSI)

Sea salt aerosol particles are associated with organic material biogenic in nature, such as algal and bacterial exudates, and influence budgets of reactive halogens and ozone [1]. Organic aerosols can be highly viscous at dry or cold conditions and thus it is important to quantify diffusion limitations of reactive gases through the organic matrix as a function of relative humidity (RH) [2]. We measured ozone diffusion and reaction through mixed Xanthan gum-iron particles as a function of RH using scanning transmission X-ray microscopy coupled with near edge X-ray absorption fine structure spectroscopy (STXM/NEXAFS).

Xanthan gum and $FeCl_2$ mixed with water was nebulized, dried, selected for size and impacted on a silicon nitride window placed in a custom built environmental micro-reactor (fabricated at the Max Planck Institute), under controlled RH and ozone exposure (~6.5×10^{-6} atm). Experiments were conducted at the PolLux beamline at the Swiss Light Source (SLS).

Figure 1a shows particles in a humidified atmosphere (RH=60%) before ozone exposure characterized as a homogeneous mix of Fe(II). After ozone exposure, particle Fe(II) fractions were reduced (Fig 1b), but are generally higher in particle cores relative to their surfaces indicating a oxidation reaction front. Figure 1c shows NEXAFS spectra of $FeCl_2$ reference material (Fe(II) oxidation state) and oxidized particles with previous literature [3]. A parameterization of the Fe(II) fraction is employed here first developed by Moffet et al. (2012) using iron standards, such as $FeCl_3$ (Fe(III) oxidation state) shown in Fig. 1c. Total Fe(II) fractions are derived from ratios of absorption peak heights at X-ray energies of 707.8 and 709.5 eV. Spectra of oxidized particles resemble a linear combination of $FeCl_2$ and $FeCl_3$ which implies the conversion only from Fe(II) to Fe(III) when exposed to ozone.

Figure 1d shows the Fe(II) fraction as a function of exposure time to water vapor and with and without the presence of ozone. At RH=0% and 20%, Fe(II) conversion is not observed. If iron oxidation did occur, it must have been on spatial scales not accessible by STXM/NEXAFS, i.e. <35 nm. This implies a small reacto-diffusion length. In other words, the distance ozone is able to diffuse and react may be so small that it affects only the surfaces of particles under these conditions. At RH=60%, Fe(II) fractions decreased with time indicating less reacto-diffusive limitation. We note that humidity exposure without the presence of ozone does not change particle oxidation state. Our results demonstrate that humidity induced diffusivity changes can suppress reactions with condensed phase organic compounds, thus increasing their lifetime.

The fate of organic marker compounds or lifetimes of toxic compounds residing in the atmosphere may be affected according to the record of relative humidity in an air mass.

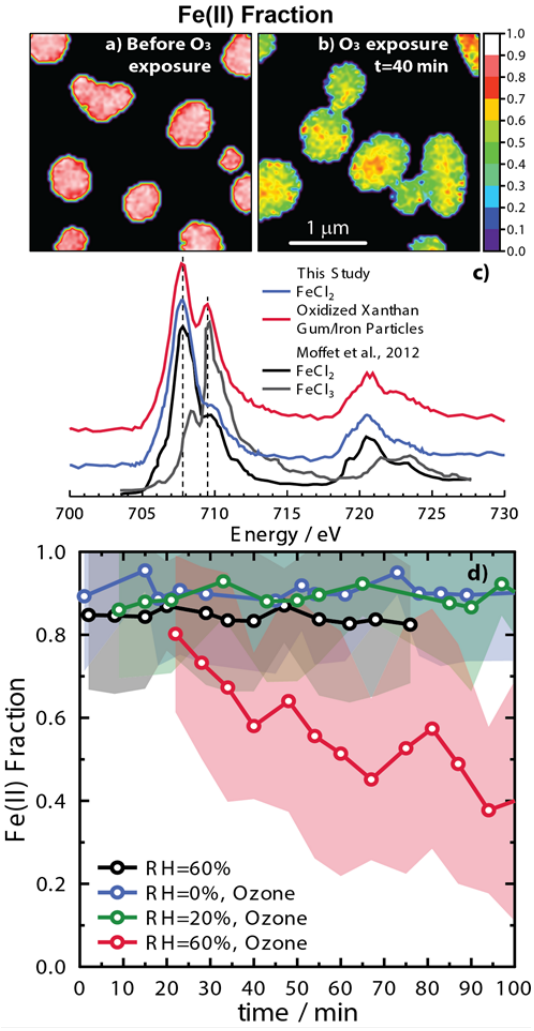

Fig. 1: (a) and (b): Chemical images of particle Fe(II) fractions. Scale bar is 1 µm. (c) Spectra of reference $FeCl_2$ and $FeCl_3$ and oxidized particles. Vertical lines indicate 707.8 and 709.5 eV. (d) Fe(II) fraction as a function of time and RH. Shaded areas indicate the standard deviation of calculated Fe(II) fraction over the 2-D projected area of particles.

ACKNOWLEDGEMENT

This work is supported the Swiss National Science Foundation (grant no 163074).

[1] Laskin et al., *J. Geophys. Res.*, **117**, D15302 (2012).

[2] Steimer et al., *Atmos. Chem. Phys.*, **14**, p. 10,761–10,772 (2014).

[3] Moffet et al., *J. Geophys. Res.*, **117**, D07204 (2012).

AN ENVIRONMENTAL MICROCHAMBER FOR X-RAY ABSORPTION MICROSCOPY INDICATIONS FOR LIQUID-LIQUID PHASE SEPARATION IN SECONDARY ORGANIC MATERIAL

J.-D. Förster, C. Pöhlker, D. Walter, F. Ditas, H. Tong, T. Berkemeier (MPIC), P. Alpert, M. Passananti, S. Rossignol, C. George (IRCELYON), B. Watts, J. Raabe (SLS), M. Ammann (PSI), M. Shiraiwa, M. O. Andreae (MPIC)

Natural sources emit various types of particles as well as volatile organic precursors, which can be converted subsequently to secondary organic aerosol (SOA) particles by photochemical processes. The impacts of atmospheric aerosol particles on climate depend on their physical and chemical properties, particularly on their phase and mixing state and on their hygroscopic response under variable relative humidity (RH) [1].

With our newly developed environmental microchamber (Fig. 1-3) for the scanning transmission x-ray microscope (STXM) at the PolLux beamline, whose design was inspired by existing models [2,3], we are able to study the microstructure of such particles down to the submicron size range and resolve their chemistry in the soft x-ray region with NEXAFS spectroscopy. Our instrument extends the microscope's capabilities to observations under controlled pressure (150 – 1000 mbar), temperature (RT to 250 K) and humidity levels (0 to >98% RH), making it a promising tool to mimic the atmospheric processing of aerosols [4].

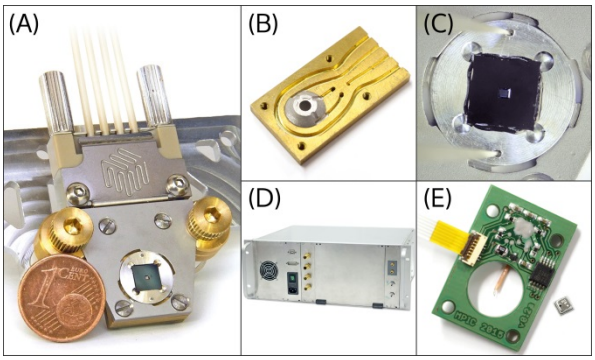

Fig. 1: (A) Microchamber assembly with microfluidic connector (Coin for size comparison); (B) Channel structures in the microchamber's base plate for coolant and sample gas flow. (28 x 15 mm²); (C) Si_3N_4 membrane window in sample holder; (D) Table top control unit for gas humidification, cooling and sensor monitoring; (E) Circuit board with thermocouple and environmental sensor for p, T and RH monitoring.[4]

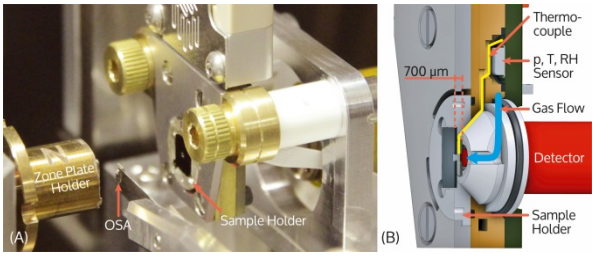

Fig. 2: (A) Chamber assembly inside the PolLux STXM and (B) sectional view through the main body.[4]

On our way towards more complex ambient aerosol samples, lab-generated SOA-particles served as test systems for water uptake in this first study. SOA particles were generated using a Potential Aerosol Mass (PAM) reactor [5] that provided an oxidizing environment for organic precursors, such as β-pinene. The particles formed were impacted on Si_3N_4-membranes, which were sealed against the STXM's high vacuum, and subsequently exposed to different RH levels inside the environmental microchamber.

Besides the expected water uptake at high RH levels, we surprisingly found independently from Renbaum-Wolff *et al.*[6] that at RH levels greater than 95±2 % liquid-liquid-phase separation (LLPS) occurred in the β-pinene SOA in the absence of inorganic salts, resulting in an aqueous and an organic-rich phase (Fig. 3).

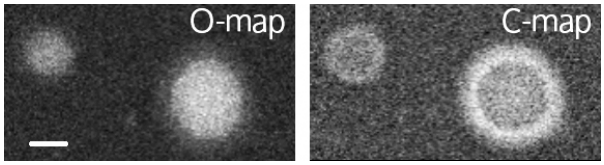

Fig. 3: Elemental maps for β-pinene-SOA particles at >97±2 % RH showing the spatial distribution of carbon and oxygen during LLPS. (Scalebar: 2 µm)

Our finding raises questions about the nature and occurrence of those effects in ambient aerosol particles as well as their representation in atmospheric models. STXM-NEXAFS is due to the high spatial and chemical resolution the ideal method to address these questions in subsequent studies.

ACKNOWLEDGEMENT

This work has been funded by the Max Planck Society. We thank the Paul Scherrer Institute for the allocation of beamtime at the SLS. M. Ammann appreciates support by the Swiss National Science foundation (grant no 163074). J.-D. Förster gratefully acknowledges support by Christian Gurk, Mark Lamneck, Berthold Kreuzburg and Frank Kunz.

[1] E. F. Mikhailov et al., Atmos. Chem. Phys. **15**, 15, 8847–8869, (2015).
[2] T. Huthwelker et al., Rev. Sci. Instrum. **81**, 113706 (2010).
[3] S. T. Kelly et al., Rev. Sci. Instrum. **84**, 073708 (2013).
[4] J.-D. Förster et al., Atmos. Meas. Tech. in preparation, (2016).
[5] E. Kang et al., Atmos. Chem. Phys., **7**, 5727-5744, (2007).
[6] L. Renbaum-Wolff et al., Atmos. Chem. Phys. Discuss., **15**, 33379-33405 (2015).

MODELLING THE KINETICS OF SHIKIMIC ACID OZONOLYSIS IN GLASSY, SEMI-SOLID AND LIQUID PHASE STATE

T. Berkemeier (MPIC), S. Steimer (PSI), U. Pöschl (MPIC), M. Shiraiwa (MPIC), M. Ammann (PSI)

Heterogeneous and multiphase reactions with ozone are important pathways of chemical ageing of organic aerosols, affecting their physicochemical properties. These reactions are studied extensively, but the effects of particle phase state are still not fully elucidated and cannot be described by classical models [1]. By applying the kinetic flux model KM-SUB [2] to systematic measurements of ozone uptake by shikimic acid [3], we investigate how moisture-induced phase transition affects gas uptake and chemical transformation of organic aerosols.

The experimental data shows a clear increase in ozone uptake coefficients with increasing relative humidity (RH, cf. Fig. 1), which can be attributed to humidity-dependence of ozone and shikimic acid diffusion [3]. The kinetic model captures this behavior over the entire time and humidity range.

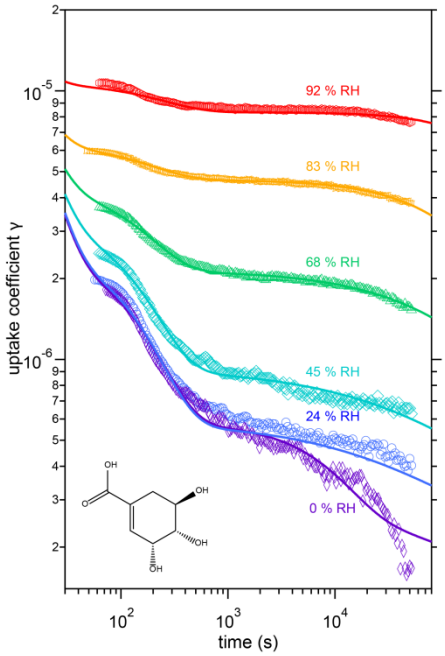

Fig. 1: Observed (markers) and modelled (lines) uptake coefficients of ozone, γ, onto a thin film of shikimic acid as a function of exposure time at relative humidities of 0, 24, 45, 68, 83, and 92 %. The structural formula of shikimic acid is displayed in the left bottom corner.

The kinetic modelling reveals that at high RH, ozone uptake is mainly controlled by reaction throughout the particle bulk, whereas at low RH, bulk diffusion is retarded severely and surface reaction becomes a dominant reaction pathway limited by replenishment of organic material at the surface. The kinetic model is used alongside a global optimization algorithm that constrains model input parameters according to the experimental data. The diffusion coefficients obtained this way can be compared to previous estimations in the literature and show good correlation, justifying the choice of shikimic acid as model compound for organic aerosol particles (Fig. 2).

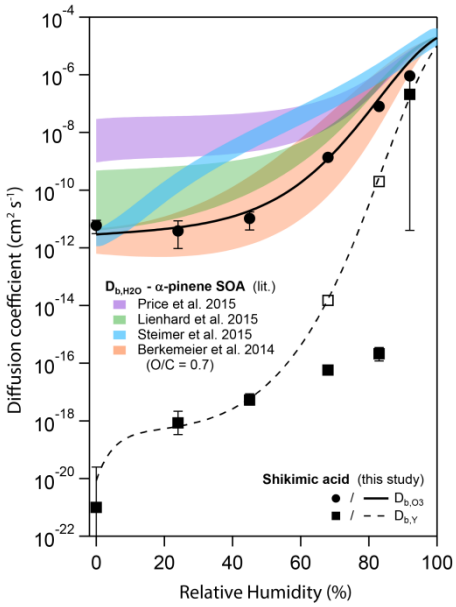

Fig. 2: Humidity dependence of the bulk diffusion coefficients of ozone (black circles) and shikimic acid (black squares) as determined by global optimization and comparison to literature values.

Both diffusion coefficients show strong humidity dependencies, emphasizing the importance of phase state on aerosol heterogeneous processing. The model returns diffusion coefficients of the organic compound shikimic acid (black squares), which could not yet be determined by experimental techniques.
Earlier studies showed that ozone uptake data to glassy or semi-solid organic aerosol cannot be described using traditional resistor style models [3], a shortcoming that has now been resolved using the kinetic flux model KM-SUB. Kinetic flux models however are computationally too expensive for usage in large-scale atmospheric models, but the obtained kinetic insight can be used as foundation for future studies, reproducing these results at much smaller computational expense.

ACKNOWLEDGEMENT
This work is supported by Max Planck Society. M. A. appreciated support by the Swiss National Science foundation (grants 130175) and the EU project PEGASOS.

[1] Berkemeier et al., Atmos. Chem. Phys., **13**, 6663–6686 (2013).
[2] Shiraiwa, M., Pfrang, C. and Pöschl, U., Atmos. Chem. Phys., **10**, 3673–3691 (2010).
[3] Steimer, S. S. et al., Phys. Chem. Chem. Phys., **17**, 31101–31109 (2015).

RADICAL PRODUCTION FROM THE PHOTOSENSITIZATION OF IMIDAZOLES WITH THE ADDITION OF HALIDES

P. Corral Arroyo (PSI & Univ. Bern), R. Aellig (ETHZ), T. Bartels-Rausch, A. Türler, M. Ammann (PSI)

Imidazole-2-carboxaldehyde (IC) is an emerging photosensitizer in atmospheric aerosols produced from the multiphase chemistry of glyoxal [1]. Previous experiments have shown that mixtures of IC and citric acid may produce HO_2 radicals via the role of citric acid (CA) as electron or H atom donor to react with the triplet excited state of IC, followed by reaction of the ensuing reduced IC ketyl radical with O_2 to form HO_2. CA is a proxy for oxidized secondary organic aerosol material. This work studies the HO_x radical production from the photochemistry of IC in the additional presence of bromide and iodide, which are orders of magnitude stronger H atom/electron donors than citric acid. Photosensitized halide oxidation may be an important halogen activation process in the marine boundary layer [2].

Irradiated coated wall flow tube experiments were carried out in N_2/O_2 (2:1) at atmospheric pressure. The total flow rate was 1.5 l min^{-1}. The relative humidity was 35% and the temperature was 20°C. The HO_2 produced was scavenged in the gas phase by NO (~400ppb), and the NO loss was evaluated to determine indirectly the HO_2 production.

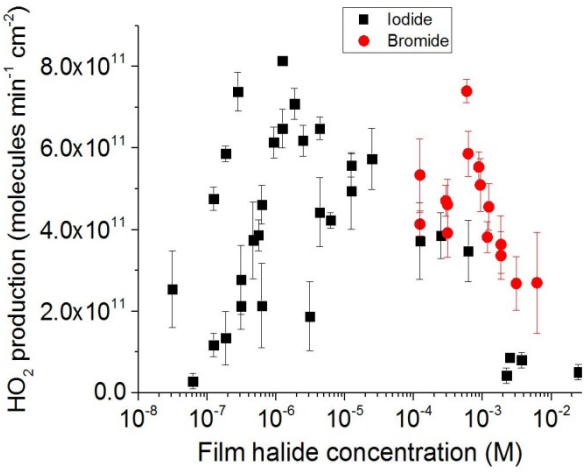

Fig. 1: HO_2 production from mixtures of IC and CA as a function of the bromide and iodide concentration in the organic film of the coated wall flow tube.

Fig.1 shows the HO_2 production from mixed IC/CA films as a function of the halide concentration for both bromide and iodide. Both halides seem to enhance HO_2 production in a certain concentration range, reach a maximum and then suppress the HO_2 production at larger concentration. In absence of halides, the HO_2 production is limited by the reaction of CA with IC triplets [3]. Halide ions can only compete with this if the product of their concentration with their rate coefficient with the IC triplet is exceeding that for citric acid. In the case of bromide, which is already an orders of magnitude stronger donor than CA, we observe the increase above 10^{-4} M, while for iodide the HO_2 production starts to increase above 10^{-7} M, which is consistent with the about a factor of 1000 larger rate constant of iodide with IC triplet than that of bromide [3]. At concentrations above 10^{-3} M for bromide and above 10^{-6} M for iodide the HO_2 production declines due to efficient scavenging of HO_2 by the X_2^- radicals produced from the oxidation of X^- (see Fig. 2 for the mechanism).

We note the substantial scatter in the data especially for iodide likely due to the scatter resulting from preparation of films with very low iodide concentrations.

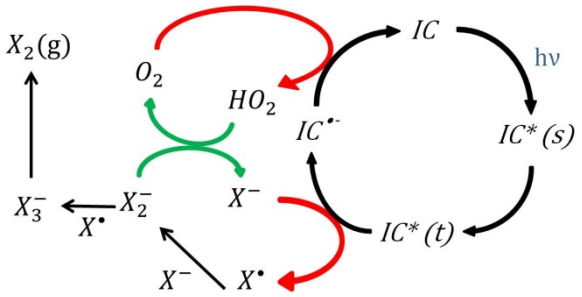

Fig. 2: Proposed mechanism to explain the enhanced HO_2 production at low halide (X^-) concentrations and the HO_2 scavenging at high concentrations.

As apparent from the mechanism, the further reaction of X_2^- with X lead to X_3^- which is in equilibrium with X_2, the molecular halogen compounds, which may be released to the gas phase. We indeed detected iodine (I_2) being released from the iodide containing films at high iodide concentrations by trapping it into a starch solution. A similar process is expected for Br_2 formation, thus indicating photosensitized halogen activation. Further experiments are needed to quantify I_2 and Br_2 production and overall quantum yields.

ACKNOWLEDGEMENT

This work was supported by the Swiss National Science Foundation (grant no 149492). We appreciate helpful discussions with R. Volkamer and C. George.

[1] Kampf et al., Atmos. Chem. Phys., **12**, 6323-6333 (2012).
[2] Reeser et al., J. Phys. Chem. A, **113**, 8591-8595 (2009).
[3] González Palacios et al., Atmos. Chem. Phys. Discuss., in review (2016).
[4] Tinel el al., C. R. Chimie **17**, 801–807 (2014).

RADICAL PRODUCTION FROM THE PHOTOSENSITIZATION OF IMIDAZOLES, BENZOPHENONE AND 4-BENZOYLBENZOIC ACID

P. Corral Arroyo (PSI & Univ. Bern) T. Bartels-Rausch (PSI), A. Türler (PSI & Univ. Bern), M. Ammann (PSI)

This work studies the HO_2 radical production from the photochemistry of benzophenone (BPh) [1], 4-Benzoylbenzoic acid (4-BBA) [2] and imidazole-2-carboxaldehyde (IC) [3] with citric acid (CA) as hydrogen atom donor. Those compounds exhibit absorbance coefficients of 21000 $M^{-1}cm^{-1}$, 435 $M^{-1}cm^{-1}$, and 2000 $M^{-1}cm^{-1}$ at 325 nm for BPh, 4-BBA and IC (up to about 350 nm), respectively, and may act as photosensitizers in the wavelength region where sun's spectrum on the Earth's surface increases. The excited triplet of the sensitizer reacts with the donor, CA, to produce a reduced ketyl radical, which reacts with O_2 to produce HO_2 [3].

Experiments were performed in a photochemical flow tube, where films composed of a mixture of either of the sensitizers with CA were exposed to nitrogen monoxide (NO) (~300ppb) in N_2/O_2 at atmospheric pressure and ratio and under irradiation in the UVA range above 300 nm at 20°C. The total flow rate of N_2 was 1.5 l min^{-1}. The HO_2 produced was scavenged in the gas phase by NO and the NO loss was evaluated to determine indirectly the HO_2 production. Fig. 1 shows a typical profile of the NO concentration dropping upon switching on UV light, measured at 35% relative humidity (RH).

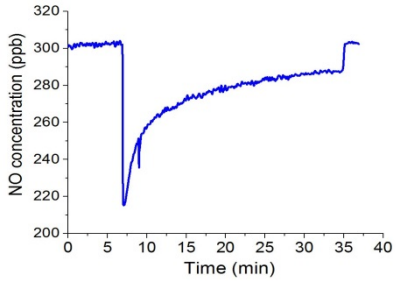

Fig. 1: Profile of NO loss for mixtures of benzophenone and citric acid in response to switching on UV light.

In contrast to experiments with IC, no steady state is reached for both BPh and 4-BBA. Some less soluble products may result from the radical chemistry of these systems. These products may accumulate on the surface to inhibit further release of HO_2 to the gas phase, leading to a reduction of the NO loss observed in the gas phase (Fig. 1). Another reason could be phase separation leading to the enrichment of the less polar BPh and 4-BBA at the surface followed by more rapid degradation of the sensitizer at locally high concentrations. We therefore evaluated the difference of the concentration of NO between the background (light off) and the first few tens of seconds of light on to quantify HO_2 production.

Fig. 2 shows a comparison of HO_2 production rates for the three different photosensitizers. On one hand, the differences are due to differences in absorbance coefficients (BPh highest), on the other hand the microphysical properties including potentially phase separation during film preparation could lead to partial enhancement of the 4-BBA case in comparison to the IC case. This becomes also apparent when comparing the RH dependence (Fig. 2) exhibiting highest reactivity at 0% RH for the two less polar ones, while at higher RH, where films may rather turn into homogeneous solutions, and the reactivities scale more closely with the absorbance coefficient of each sensitizer. At high RH the concentration of the donor CA is getting lower due to the increasing amount of water associated with the organic film.

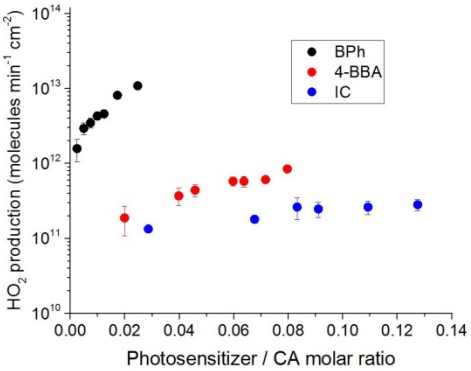

Fig. 2: HO_2 production as a function of the molar ratio of the photosensitizers (IC, 4-BBA and BPh) and CA in the film.

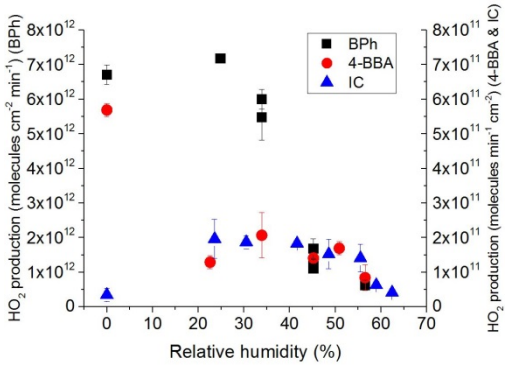

Fig. 3: HO_2 production as a function of relative humidity for mixtures of CA with the three photosensitizers (IC, BPh and 4-BBA) at 0.16 molar ratio.

In conclusion, mixtures of CA + H_2O with IC, benzophenone or 4-BBA are able to produce HO_2 being irradiated by near UV light by photosensitization and with significant yields to contribute to the aerosol aging and to the radical budgets in the atmosphere.

[1] Canonica, et al. J. Phys. Chem. A, **104 (6)**, (2000).
[2] George et al. Faraday Discussions, **130,** (2005).
[3] González Palacios et al., Atmos. Chem. Phys. Discuss., in review (2016).

PHOTOCHEMISTRY OF 4-NITROPHENOL IN BULK AQUEOUS SOLUTIONS AND IN AN ORGANIC AEROSOL

T. Bartels-Rausch (PSI), E. De Laurentii (Univ. Torino), S. Steimer (PSI), M. Ammann (PSI), D. Vione (Univ. Torino)

Nitrophenols are toxic aromatic compounds ubiquitously present in clouds, fog, and aerosol. They significantly participate in atmospheric photochemistry with nitrous acid (HONO) being one product. HONO is a source of hydroxyl radicals that contribute to the oxidative capacity and thus the ozone budget of the atmosphere and is thus of environmental concern. The specific reaction mechanism leading to HONO emission is open to debate, it is thought to be either formed by bond cleavage upon irradiation as initial step or in secondary steps from NO_2 (Fig. 1).

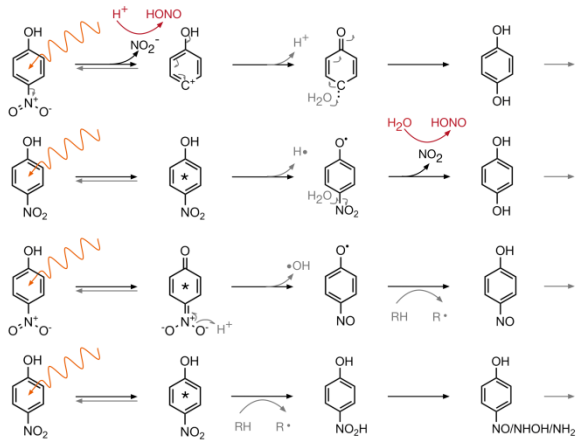

Fig. 1: Potential photochemical decomposition pathways of 4-nitrophenol in dilute aqueous solution as characteristic for fog and most clouds. Mechanisms were proposed based on product identification [1,2].

Organic material might provide high ionic strength, low viscosity, and high acidity in atmospheric aerosol. This complex environment impacts heterogeneous reaction rates [3] and photolysis yields of some nitrophenols [4] significantly. Such shifts in reaction mechanism are also discussed in frozen systems for complex reaction systems [5]. Taken the large number of possible reaction pathways for nitrophenol (Fig. 1), we investigated the yield of HONO upon irradiation of para-nitrophenol (4NP), in aqueous solutions of low ionic strength and in aqueous films resembling high solute strength atmospheric particles.

Figure 2 reports the formation quantum yields of HONO in both types of solution. The quantum yield gives the fraction of HONO production relative to the total of all loss processes of the photolytically excited nitrophenol combined. It is derived based on measured HONO formation rates and the calculated absorbed photon flux.

The results shown in Fig. 2 suggest that the irradiation of 4NP is quite effective in producing HONO over a wide pH range in both reaction media. Pathways that do not lead to HONO formation include thermal energy transfer, photolytic reduction by H-atom transfer to the nitro group, or photolytic cleavage of the NO bond in acidic environments (Fig. 1).

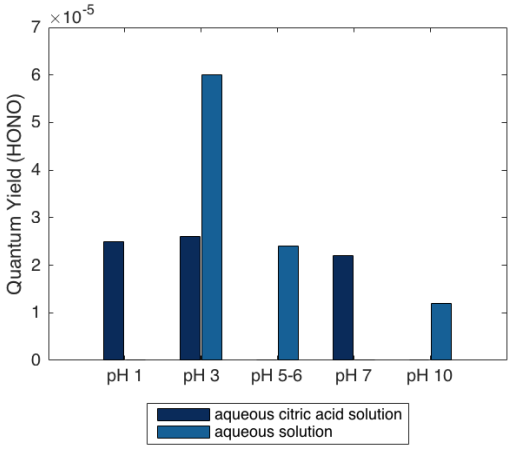

Fig. 2: Formation quantum yields of HONO from 0.1 mM initial 4-nitrophenol solutions in water and in 10 mol/kg aqueous citric acid solution.

The HONO yield in dilute aqueous solutions is twice of that in highly concentrated and very viscous citric acid solutions at pH 3. This finding is in qualitative agreement with reduced photo-reactivity of 24NP as viscosity increases [4]. In dilute solutions the HONO quantum yield increases at acidic conditions. In highly concentrated citric acid films the HONO yield is invariant to pH changes. A detailed analysis is work in progress.

---

[1] M. A. J. Harrison et al., Atmos. Environ., **39**, 231–248 (2005).
[2] A. Alif et al., Chemosphere, **16**, 2213–2223 (1987).
[3] S. Steimer et al., Atmos. Chem. Phys., **14**, 10761–10772 (2014).
[4] H. Lignell et al., PNAS, **111,** 13780–13785 (2014).
[5] T. Bartels-Rausch et al., Atmos. Chem. Phys., **14**, 1587–1633 (2014).

CONTRASTING THE EFFECT OF AN ALCOHOL AND A CARBOXYLIC ACID SURFACTANT ON THE ION DISTRIBUTION AT THE AQUEOUS SOLUTION - AIR INTERFACE

M.-T. Lee (Univ. Bern & PSI), F. Orlando (PSI), S. Kato (PSI & EMPA), M. Roeselová, M. Khabiri (CAS-UOCHB), M. A. Brown (ETHZ), A. Türler (Univ. Bern & PSI), M. Ammann (PSI)

We used in situ X-ray photoelectron spectroscopy with a liquid micro jet [1] to obtain insight into the effect of organic surfactants, butanoic acid (BuOOH) and 1-butanol (BuOH), on the density of bromide anions and sodium cations at the aqueous solution – air interface, in view of their relevance for halogen activation in the marine boundary layer. We compared our results with molecular dynamics (MD) simulations to develop a detailed understanding of the interfacial region of these ternary solutions.

Fig. 1 shows exemplary combined O 1s, Br 3d, Na 2s, and C 1s photoelectron spectra from 0.12 M NaBr aqueous solutions taken as a function of the BuOOH mole fraction, X, in the range 0 - 0.008 measured at a nominal photon energy of 229 eV and making use of the higher order light components to obtain C 1s and O 1s in the same kinetic energy (KE) window as described in our previous work [1]. Similar spectra were measured for BuOH. The peak assignments are given in the figure along with the relevant exciting photon energies.

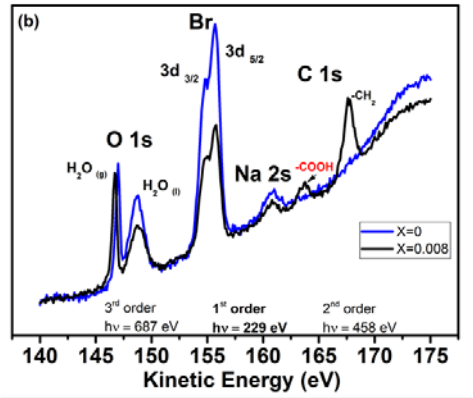

Fig. 1: Exemplary photoelectron spectra from aqueous solutions containing 0.12 M NaBr and 0 (blue) and 0.001 (black) mole fraction of 1-BuOOH excited by X-rays with a nominal photon energy of 229 eV.

Fig. 2 shows the relative departure of the bromide Br 3d photoemission signal from their value for the neat bromide solutions as a function of mole fraction of organic for the case of BuOOH. The Br 3d signal is proportional to the interfacial concentration within a characteristic depth of about 1.2 nm from the surface. In general, in the presence of 1-BuOH or BuOOH, we observed a distinct suppression of the PE signals for both Na, and Br, by about 15-25% and 15-45%, respectively, for 1-BuOH, and by about 20-50% and 30-40%, respectively, for BuOOH. It seems that BuOOH pushes the anion, Br^-, and the cation, Na^+ away from the interface more than 1-BuOH does. In addition, we did not see an apparent trend of the Br to Na integrated PE peak area ratio as a function of bulk organic concentration within the probe depth (data not shown).

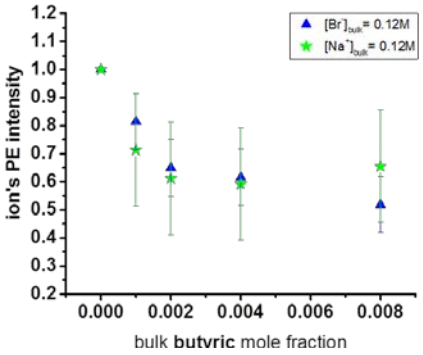

Fig. 2: Relative change of Br 3d and Na 2s PE signals as a function of BuOOH mole fraction for aqueous solutions of 0.12 M NaBr.

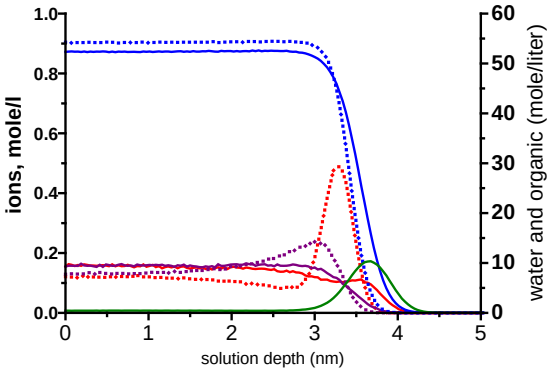

Fig. 3: Density profiles of bromide (red), sodium (purple), and water (blue) in presence (solid lines) and absence (dotted lines) of BuOOH (green) from MD simulations.

Complimentary MD simulations of the same solutions are qualitatively consistent with the experimental observation (Fig. 3), confirming the strong suppression of bromide and sodium ions in presence of the two surfactants. Subtle effects of organic surfactants control the changing structure at the interface. A more detailed analysis also including iodide ions for comparison is underway.

---

[1] Brown et al., Rev. Sci. Instrum., **84**, art. no. 073904 (2013).
[2] Lee et al., J. Phys. Chem. A., **119**, 4600−4608 (2015).
[3] Krisch et al., J. Phys. Chem. C., **111**, 13497-13509 (2007).

THE AFFINITY OF C1-C4 OXYGENATED VOLATILE ORGANIC COMPOUNDS FOR THE AIR-WATER INTERFACE USING LIQUID JET XPS

M.-T. Lee, A. Türler (Univ. Bern & PSI), M. A. Brown (ETHZ), M. Ammann (PSI)

The liquid-vapor interface is difficult to interrogate experimentally but is of interest from a theoretical and applied point of view, and has particular importance in atmospheric aerosol chemistry. Here we examine the liquid-vapor interface for mixtures of water and small alcohols or small carboxylic acids (C1-C4), abundant chemicals in the atmosphere. In our previous study, we have compared the results of X-ray photoelectron spectroscopy (XPS) measurements over all species at 0.5 M bulk concentration with the surface excesses derived from literature values for the surface tensions of surface tension measurements (Fig. 1). Based on a simple simulated model, linear correlation was found between the headgroup carbon 1s core-level signal intensity and the surface excess, with the offset being explained by the bulk contribution to the photoemission signal.

The recorded C 1s photoemission (PE) intensities of the head group carbon atoms reported in our previous study scale linearly with the mean surface excesses, Γ_{se} (Fig. 1, error bars in the x-axis represent the standard deviation of the Γ_{se}) due to the increasing propensity of these amphiphilic molecules for the interface. The correlation between XPS intensities with surface excess derived from the thermodynamic equilibrium quantity of surface tension provides further support to the growing consensus [1] that the liquid jet provides a measurement tool in vacuum for XPS that is representative of a static solution interface in ambient humidity because it is in local equilibrium [2,3].

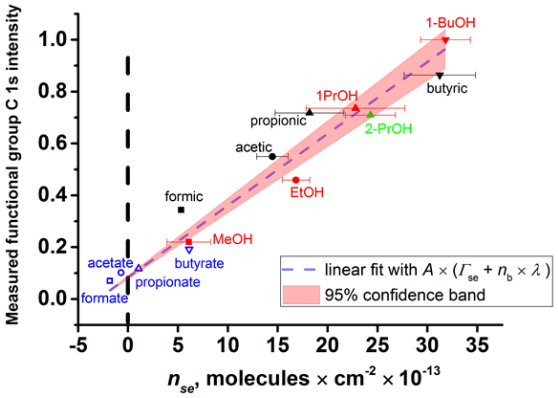

Fig. 1: Comparison of measured functional group C 1s PE intensity of organics and the corresponding surface excess values (n_{se}) as a function of organic species. The linear fit describes a one parameter fit with Γ_{se} the surface excess, n_b the bulk concentration (0.5 M) and λ, the inelastic mean free path of photoelectrons (1.2 nm), to provide estimates of the contribution of surface and bulk molecules, respectively, to the PE intensity.

The ratio of aliphatic to headgroup C 1s signal intensities indicated an increasing orientation towards the surface normal as a function of chain length, along with increasing importance of lateral hydrophobic interactions (Fig. 2).

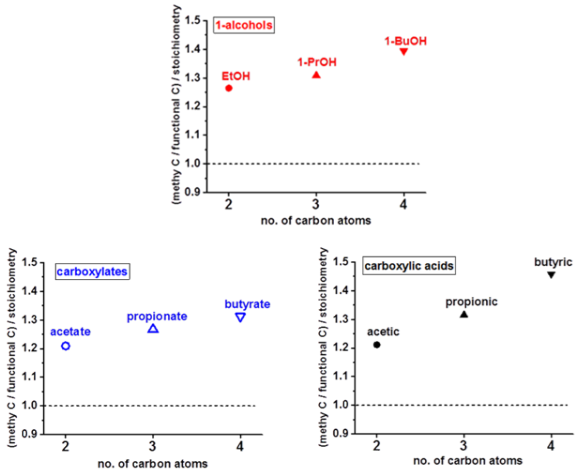

Fig. 2: Relative enhancement of the integrated -C-CH_2 PE intensity to -C-functional-group PE intensity ratio, normalized to the stoichiometry within the molecule, as a function of functional group, and chain length.

The C 1s photoemission intensity is reflecting the molecular structure, i.e., the ratio of the C 1s peak areas assigned to aliphatic carbon to that assigned to the functional group carbon should increase from one to three for C2 to C4 species, respectively. As shown in Fig. 2, where the aliphatic to functional group C 1s signal intensity ratio has been normalized to its stoichiometric value and plotted against the surface excess, this ratio exceeds stoichiometry for all species.

Overall, this enhanced ratio is in line with the intuitive expectation that the preferred orientation of the amphiphilic molecules is that the functional group carbons prefer the interfacial region, while the aliphatic chain points rather outward away from it into vacuum. Thus, aliphatic C 1s photoelectrons are less attenuated than functional group carbon C 1s photoelectrons. This effect increases with increasing chain length for each functional group family. This is notable especially for the carboxylates, which have very low surface excess.

[1] Brown et al., J. Phys. Chem. C., **119**, 4976-4982 (2015).
[2] Faubel et al., Z. Phys. D Atom Mol. Cl. **10**(2-3): 269-277 (1988).
[3] Winter and Faubel. Chem. Rev. **106**(4): 1176-1211 (2006).

AMBIENT PRESSURE X-RAY PHOTOELECTRON SPECTROSCOPY APPLIED TO THE STUDY OF LIQUID/GAS INTERFACES

L. Artiglia, F. Orlando (PSI), M. T. Lee (Univ. Bern & PSI), A. Kleibert (PSI/SLS), M. Ammann (PSI)

Atmospheric aerosols contain a substantial fraction of organic material [1] that participates in oxidative processing by gas phase oxidants, which affects their impacts on air quality and climate. In the present work, we focus on ozonolysis of shikimic acid, a component of biomass burning aerosol serving as a probe of oxidative degradation [2]. The ozonolysis of shikimic acid at the aqueous solution – air interface is initiated by the formation of reactive oxygen intermediates (ROIs), as suggested indirectly from kinetic behavior [3-5], although a direct identification is still lacking. We studied the interface of a 0.23 M shikimic acid aqueous solution exposed to ozone by X-ray photoelectron spectroscopy (XPS) using the near ambient pressure photoemission (NAPP) endstation equipped with a 20 µm liquid microjet [6] at the SIM beamline at SLS. We acquired core level C 1s spectra using a photon energy of 450 eV, leading to around 160 eV photoelectron kinetic energy. This leads to a probe depth of only very few nanometers, thus allowing directly probing *in-situ* the aqueous solution – gas interface. The first spectra were acquired on the "clean" solution (Figure 1, lowest spectrum), exhibiting 4 components assigned to the different carbon species found in shikimic acid, i.e., sp^2 (288.9 eV), sp^3 (290.1 eV), alcoholic (C-OH, 291.2 eV) and carboxylic (COOH, 294.0 eV), at relative intensity consistent with molecular structure, i.e. 2:1:3:1 (sp^2 : sp^3 : C-OH : COOH, inset at the top of Fig. 1).

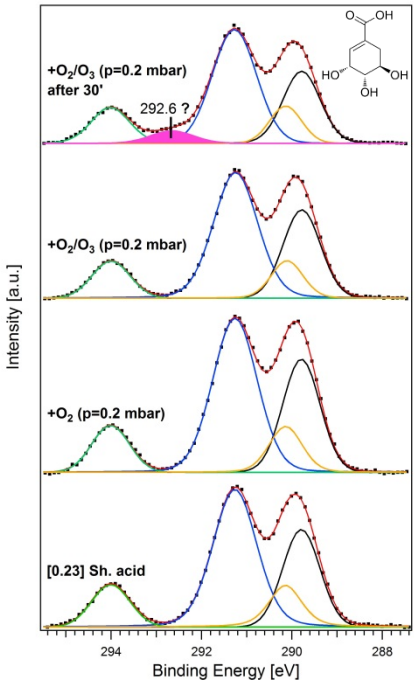

Fig. 1: C 1s spectra acquired before and during exposure to O_2 and O_3 (hν=450 eV). Inset (top, right): the shikimic acid structural formula.

Gases were dosed via a leak valve and a PTFE capillary placed close to the running jet. We first dosed clean oxygen (0.2 mbar constant pressure) and no changes were observed. Then an ozone generator was switched on in an external flow system upstream of the leak valve, so that an O_3 (approx. 10%)/O_2 mixture was dosed at the same constant pressure of 0.2 mbar. No changes were observed in the very first few minutes (Figure 1, 3rd spectrum from below), then the spectrum started to broaden in the binding energy region between the C-OH and COOH spectral components. The signal integrated after 30 minutes acquisition is displayed in Figure 1 (upper spectrum). A new component is present, centered at 292.6 eV, with an oxidation state neither of alcoholic nor of carboxylic carbon, but rather in the range of carbonyl functions. More detailed comparison (not shown) suggests that the appearance of the 292.6 eV component is balanced by a decrease of the 288.9 eV peak (sp^2 carbon atoms). This means that there is a correlation between the new carbon species formed at the interface and the disappearance of the double bond upon exposure to O_3 molecules. Previous studies of shikimic acid ozonolysis demonstrated that it follows a Langmuir-Hinshelwood type kinetic mechanism involving Criegee type chemistry [4,5,7]. In the first reaction minutes a surface reaction runs parallel to a bulk one. Although we were not expecting significant oxidation rates over the short time scale of liquid jet (ca. 0.1 ms liquid-gas interaction time between the nozzle aperture and the analysis spot), due to the low rate coefficient for this reaction in the bulk aqueous phase (10^3 $M^{-1}s^{-1}$, [4]), the 292.6 eV peak in the C 1s region might be due either to the formation of a surface stabilized ozone adduct or to a massive enhancement of the reaction rate at the surface that would lead to stable carbonyls. Further experiments are needed to confirm these preliminary findings. Moreover we plan to acquire the C K edge absorption spectrum and to make a depth profile analysis to confirm the surface accumulation of the new species.

[1] P. Saxena, L. J. Hildemann, Atmos. Chem. 1996, **24**, 57.
[2] P. M. Medeiros, B. R. T. Simoneit, Environ. Sci. Technol., **42**, 8310 (2008).
[3] M. Shiraiwa et al., Nature Chem., **3**, 291 (2011).
[4] S. S. Steimer et al., Atmos. Chem. Phys., **14**, 10761 (2014).
[5] S. S. Steimer, et al., Phys. Chem. Chem. Phys., **17**, 31101 (2015).
[6] M. A. Brown et al., Rev. Sci. Instr., **84**, 073904 (2013).
[7] R. Criegee, Angew. Chem. Int. Edit., **14**, 745 (1975).

ENVIRONMENTAL PHOTOCHEMISTRY OF OXIDE SURFACES: A NEW IN SITU XPS APPROACH

F. Orlando, A. Waldner, T. Bartels-Rausch, M. Birrer, M.-T. Lee (PSI), C. Proff (PSI/LBK), T. Huthwelker, A Kleibert (PSI/SLS) J. van Bokhoven (ETH & PSI), M. Ammann (PSI)

Titania (TiO_2) is a component of natural mineral dust that represents an important reactive aerosol in the atmosphere affecting the ozone budget and the climate [1, 2]. In this context, adsorption of water and hydroxylation of the surface, which are key aspects to understand TiO_2 photocatalysis in the environment, offer still major open questions. With the aim of improving the understanding of these issues, we have conducted first experiments using the new chamber for the near ambient pressure photoemission (NAPP) endstation [3] in a water adsorption experiment on a TiO_2 powder sample (Degussa P25) under UV-irradiation at relevant atmospheric conditions of humidity. The XPS and NEXAFS measurements were performed at the SIM and the PHOENIX beamlines at SLS.

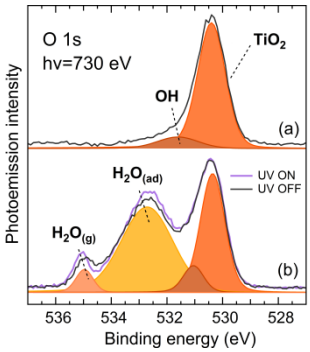

Fig. 1: TiO_2 powder. O 1s photoemission spectra of the sample measured (a) in vacuum and (b) at 0.06 mbar partial pressure of O_2 at 5% RH (0.36 mbar partial pressure of H_2O at 272 K) together with the fitting components. Overlapped in (b) is also the spectrum measured during UV exposure.

Fig. 1 shows the O 1s core level measured (a) in vacuum and (b) in humid conditions. Several components appear upon water vapor exposure besides the main peak at 530.4 eV, which corresponds to oxygen in the TiO_2 lattice. These components are associated to OH groups and molecular H_2O at about 531.1 and 533.8 eV, respectively [4]. The evolution of the spectral components as a function of RH is in line with previous experimental findings indicating a stepwise mechanism for H_2O adsorption on TiO_2: H_2O molecules first dissociate on the oxygen vacancies of TiO_2, leading to the formation of OH groups that act as nucleation centers for further adsorption of H_2O molecules [4]. The additional peak appearing at higher binding energy is associated with gas-phase H_2O. No increase of the C 1s intensity is observed during the experiment. Fig. 2 shows the comparison between O K-edge NEXAFS spectra measured in dark and under UV irradiation. The resonances A1 (531.3 eV) and A2 (534.0 eV) correspond to excitations to O 2p-Ti 3d mixed states [5]. The C1 (540.0 eV) and C2 (546.0 eV) peaks arise from electron transfer to mixed states derived from O 2p and Ti 4sp states [5].

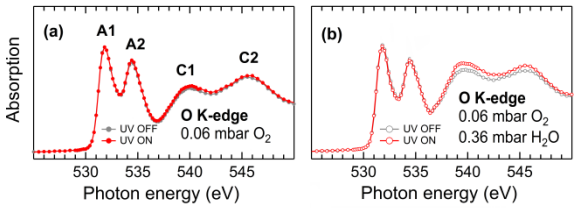

Fig. 2: TiO_2 powder. O K-edge NEXAFS spectra in presence of (a) 0.06 mbar O_2 and (b) with additional 0.36 mbar partial pressure of H_2O in dark conditions (grey) and under UV light irradiation (red).

The adsorption of H_2O on TiO_2 causes an increase in the region above 538 eV, coinciding with the C1 and C2 resonances, as shown by the comparison between the NEXAFS spectra measured under dry (a) and humid (b) conditions. The observed increase upon UV irradiation suggests that the concentration of H_2O molecules on the surface further increases under UV light, since O K-edge of liquid water features a broad main and postedge absorption feature in this photon energy region. This is in line with the previous experimental observation that UV light irradiation led to an enhanced concentration of hydroxyl groups [6]. The comparison between spectra in Fig. 2(a) and (b) indicates that this photo-induced effect is sizeable only if a sufficiently large amount of H_2O molecules is provided, i.e., the effect is almost negligible under dry conditions. It is worth noting that the contribution of the gas phase to the measured NEXAFS spectra is negligible because of the low water vapor partial pressure used. Moreover, C1 and C2 resonances do not overlap with those of the H_2O gas-phase [7]. The outlined scenario is supported by the O 1s photoemission spectra measured under humid conditions in dark (grey spectrum) and during UV irradiation (purple spectrum) reported in Fig. 1b, the latter showing an increase of the component associated to molecular water.

[1] H. Chen et al., Chem. Rev., **112**, 5919 (2012).
[2] M. E. Monge et al., J. Am. Chem. Soc., **132**, 8234 (2010).
[3] F. Orlando et al., Accepted in Topics in Catalysis, (2016).
[4] G. Ketteler et al., J. Phys. Chem. C, **111**, 8278 (2007).
[5] F. M. F. De Groot et al., Phys. Rev. B, **48**, 2074 (1993).
[6] M. Lampimäki et al., J. Phys. Chem. C, **119**, 7076 (2015).
[7] S. Myneni et al., J. Phys. Condens. Matter, **14**, L213 (2002).

WHO IS AFRAID OF KNUDSEN?

S. F. Schneider (Univ. Bern & PSI), A. Waldner (ETHZ & PSI), M. Birrer, M. Ammann, T. Bartels-Rausch (PSI)

Ice and snow play an integral role in transferring trace gases to and from the atmosphere, and the investigation of their surface processes is an on-going topic in environmental science [1]. Such experiments are routinely done at 0.01 – 5 mbar absolute pressure, for example in our Near Ambient Pressure Photoemission (NAPP) endstation [2]. This report summarizes the work carried out during an internship characterizing gas flows into the analysis cell of the NAPP endstation at PSI. To assess, for example, the impact of leaks in the system one needs to determine the flow rates. However, predicting gas flows in this pressure range is not straightforward, as the flow regime switches from a molecular to a viscous one with very different flow characteristics each.

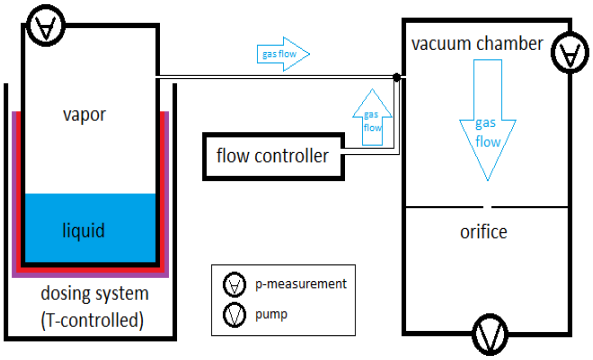

Fig. 1: Set-up consisting of two dosing lines to the analysis cell: (i) a gas reservoir (H_2O in the present work) at constant pressure connected via a capillary; (ii) a mass flow meter or a flow measurement based on pressure drop dosing N_2.

To establish a relation between the pressure in the analysis cell and the volumetric flow rate into the cell, the pressure in the cell was measured for different flows. Figure 2 shows excellent agreement between two independent methods and different data sets between 2 and 50 mbar. Since the flow in and out must be the same, the experimental results were compared to calculations of the flow exiting the analysis cell via the small orifice (Fig. 1). Flow calculations were done for the well-established molecular and viscous flow regimes. Figure 2 shows that the measured flows nicely approach the prediction for molecular flow at low pressure and for viscous flow at higher pressure. An exception is one data series in the low flow regime. Leaks in the system and inaccurate flow meter calibrations cannot be ruled out. An important result from this study is that flows into the analysis cell can be well predicted for typical experimental settings of NAPP experiments.

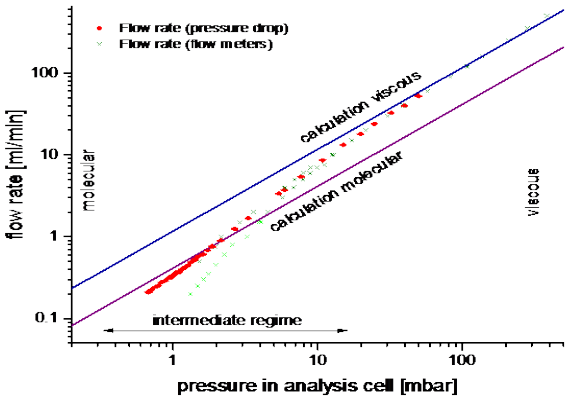

Fig. 2: Flow rate as a function of pressure in the analysis cell. Error bars were calculated on the basis of random errors. Data in light green are outliers.

The data in Fig. 2 enabled to establish a relationship between the flow through capillaries of varying diameter into the analysis cell and the driving pressure difference of the dosing system and the analysis cell. Considering common leakage rates, Fig. 3 indicates that flow rates between 0.3 and 7 ml/min can be achieved.

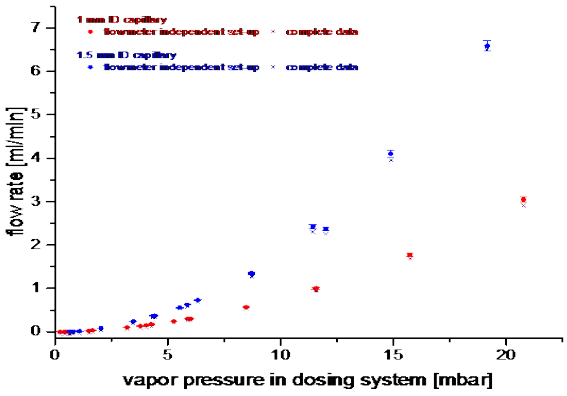

Fig. 3: Dependence of the flow rate on the vapor pressure in the dosing system. Error bars were calculated on the basis of random errors.

ACKNOWLEDGEMENT

We thank the Swiss National Science Foundation (grant 149 629) and Univ. Bern for funding.

[1] T. Bartels-Rausch et al., Atmos. Chem. Phys., **14**, 1587-1633 (2014).
[2] F. Orlando et al., Top. Catal., in press (2016).

HIGHLY REPRODUCIBLE X-RAY ABSORPTION SPECTROSCOPY ON CRYSTALLINE ICE SAMPLES AT SLS

X. Kong (PSI & Univ. Gothenburg), A. Waldner (ETHZ & PSI), F. Orlando, L. Artiglia, M. Birrer, M. Ammann, T. Bartels-Rausch (PSI)

Ice and snow play active roles in the water cycle, in the energy budget of the Earth, and in environmental chemistry of the atmosphere and cryosphere. With the state-of-art Near Ambient Pressure Photoelectron (NAPP) spectroscopy endstation, we employ combined X-ray photoelectron spectroscopy (XPS) and partial electron yield Near Edge X-ray Absorption Fine Structure (NEXAFS) spectroscopy to study the microphysical environment of ice surfaces at temperatures up to -22°C. Due to the short electron inelastic mean free path at the kinetic energies probed in this work, XPS and NEXAFS probe the upper few nanometers of ice crystals. Clear differences in the spectra of crystalline, well-ordered hydrogen bonding structures and of more disordered, liquid bonding structures have been used to quantify the increasing disorder of the hydrogen-bonding network at the surface of ice crystals as temperatures approach the melting point [1].

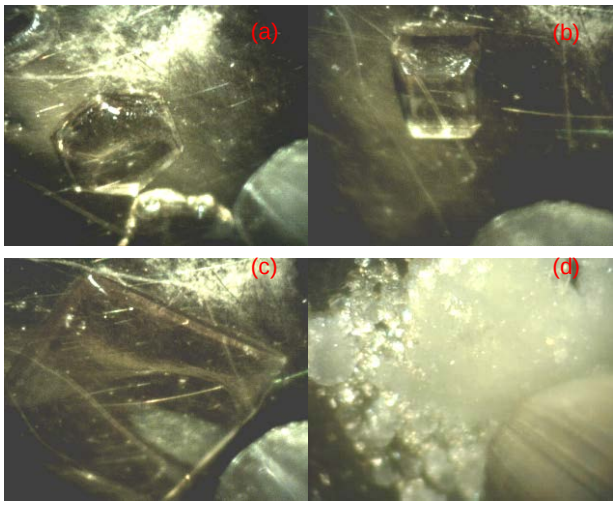

Fig. 1: Examples of ice samples.

Figure 1 shows examples of ice samples with different grain sizes formed at temperatures of -22°C (a, c) and -40°C (b, d) which are ready to be studied by NEXAFS spectroscopy. Pictures (a) and (b) show features of hexagonal, single crystalline ice in the stage of growing. The appearances are different, which might be due to the different orientations of ice crystals. Prior to XPS and NEXAFS measurements presented here, ice crystals were kept to grow slowly for a while in order to have a sufficient area, as shown in (c). As comparison, highly polycrystalline ice can also be formed with higher water supersaturation for experiments (d). A practical challenge is the stability of the ice sample, with its high vapor pressure, during the course of the experiments. The ice is kept stable by maintaining a constant partial pressure of water in the measurement cell that matches the vapor pressure of ice.

A series of NEXAFS results probing the oxygen of ice as shown in Fig. 1c, at two different temperatures, -22°C and -40°C, are shown in Fig. 2.

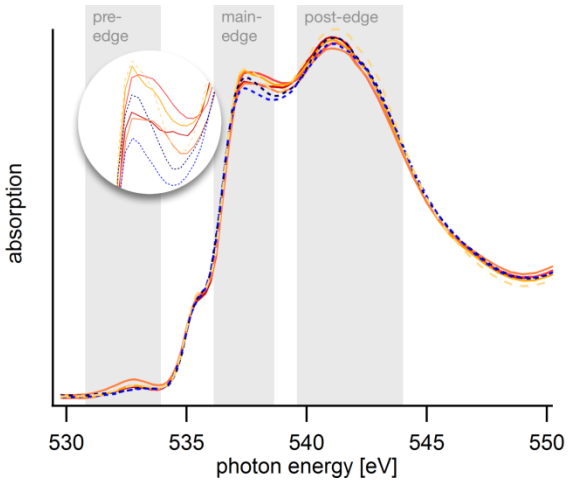

Fig. 2: Partial electron-yield oxygen K-edge NEXAFS spectra of pure ice at -22°C (red-yellow lines) and at -40°C (blue lines). Measurements have been done at the SIM beamline of PSI. Line styles denote individual ice samples. The insert enlarges the pre-edge region. All spectra were normalized to their integrated areas and to the X-ray beam flux over the total range of photon energies.

All spectra show a more intense post-edge as compared to the main-edge as is characteristic for ice [1]. Zooming the main-edge, insert in Fig 2, indicates that spectra at -22°C show a wider, less steep edge than those at -40°C. This might reflect an increased disorder in the uppermost hydrogen-bonding network as temperatures approach the melting point [2]. Last but not least, the spectra reveal an excellent reproducibility taken that Fig 2 combines results from different ice samples, taken over a period of up to 8 hours (solid, red-yellow lines), and using different measurement parameters. The good reproducibility clearly illustrates the excellent ice sample stability allowing long NEXAFS measurements to reach high resolution.

ACKNOWLEDGEMENT

This work was supported by the Swedish Research Council (#2014-6924) and the Swiss National Science Foundation (149629).

[1] H. Bluhm et al., J. Phys. - Condens. Mat., **14**, 227-233 (2002).

[2] T. Bartels-Rausch et al., Atmos. Chem. Phys., **14**, 1587-1633 (2014).

XPS DEPTH PROFILES OF FORMIC ACID IN ICE AT SLS

A. Waldner (ETHZ & PSI), F. Orlando, T. Huthwelker, M. Birrer, X. Kong, L. Artiglia, M. Ammann, T. Bartels-Rausch (PSI)

Uptake of atmospheric trace gases to the surfaces of cirrus clouds or to snow can modify the composition of the atmosphere and can play an integral role in transferring gases to and from the atmosphere [1]. Better knowledge of this process will help with the interpretation of concentration profiles in ice cores and with improving atmospheric chemistry models. The aim of this project is to examine the adsorption of acidic trace gases to ice surfaces on a molecular level with the near ambient pressure photoelectron end station (NAPP) at SLS. It was recently shown that strong acids can modify the surface structure of ice upon adsorption making it more disordered (liquid-like). It was further concluded that those acids literally dissolve in this layer [2]. Earlier photoelectron studies have detected adsorbed acetic acid at the ice surface and indicated that the acid is confined to the uppermost ice layers [3].

Each sample was formed in-situ by depositing water from the gas phase on a cooled sample holder. During the uptake measurements the ice sample is kept stable by maintaining a partial pressure of water in the gas phase that matches the vapour pressure of ice. After the ice has been equilibrated, it is exposed to formic acid (HCOOH) from the gas phase. Formic acid is one of the most abundant organic acids in the atmosphere and one of the strongest organic acids.

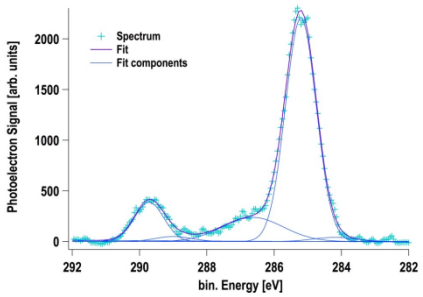

Fig. 1: Exemplary C1s photoelectron spectrum at a photon energy of 2200 eV of ice exposed to HCOOH.

Figure 1 shows a typical spectrum of the C1s spectral region on ice at 2200 eV photon energy taken at the Phoenix beam line of SLS. The C1s spectrum can be represented by a fit with 5 components, each representing a specific functional group. The carboxyl feature at 289.5 eV shows a strong response to changes in partial pressure of HCOOH. The other features are either caused by contamination that might be produced in-situ by radiation chemistry of HCOOH or by volatile organics displaced from the chamber walls.

The Phoenix beam line allows acquiring C1s spectra with photon energies of up to 6800 eV. By increasing the photon energy and therefore increasing the kinetic energy and inelastic mean free path of the photoelectrons, one can increase the probing depth. Using this one can derive depth profiles of adsorbed HCOOH in/on the ice.

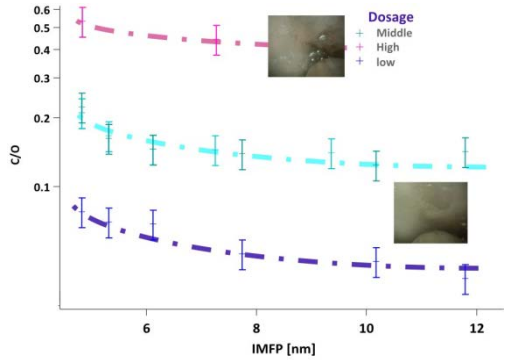

Fig. 2: Depth profile of HCOOH on ice: carboxyl C1s to O1s intensity ratio as function of the IMFP.

Figure 2 shows the ratios of the C1s carboxyl component to the O1s photoelectron signal as a function of increasing IMFP. Decreasing C/O ratios represent the case of a surface adsorbed species, as its C1s signal – stemming from the surface – is diluted by the O1s of clean ice as probing depth increases. A trace species that homogenously distributed over the probing range would lead to a constant C/O ratio.

Depending on the partial pressure of HCOOH the penetration depth of the formic acid in the ice varies. For dosing within the ice-stability regime (turquoise & blue), where previous studies have indicated Langmuir-type adsorption [4], a relatively strong decrease can be observed in the initial part of the profiles. Therefore, we can conclude that the HCOOH stays within the uppermost nanometres, meaning at the ice surface. Above the ice-stability regime (purple), where the formation of a solution is observed (upper picture), no obvious decrease could be seen indicating the presence of a homogenous formic acid – ice layer in the upper few nanometres.

ACKNOWLEDGEMENT
This project is supported by the Swiss National Science Foundation (grant #149629).

[1] T. Huthwelker et al., Chem. Rev., **106**, 1375-1444 (2006).
[2] V. F. McNeill et al., PNAS, **103**, 9422-9427 (2006).
[3] A. Křepelová et al., J. Phys. Chem. A, **117**, 401-409 (2013).
[4] P. von Hessberg et al., Phys. Chem. Chem. Phys. **10.17**, 2345-2355 (2008).

TEMPERATURE DEPENDENCE OF REACTIVE OZONE UPTAKE IN NaBr FILMS

J. Edebeli, A. Gilgen (PSI& ETHZ), T. Bartels-Rausch, M. Ammann (PSI)

The discovery of boundary layer ozone depletion events (ODEs) in polar environments has led to active field and laboratory studies to understand the trigger for such events [1-4]. Boundary layer ODEs have implications on the oxidative capacity of the lower atmosphere and the speciation of compounds such as mercury [1]. Boundary layer ODEs have also been observed in mid-latitudes, over salt lakes/salt pans [3]. It is clear that oxidation of halides (especially of bromide), for instance by ozone, is triggering ODEs. For the reaction of bromide with ozone, the temperature dependence is not clear. The aim of this study is to characterize the temperature dependence of ozone loss over sodium bromide (NaBr) solutions as a means for identifying the contributions of surface and bulk processes to the overall ozone uptake. A surface process might be crucial to provide sufficient bromide oxidation rates to trigger ODEs.

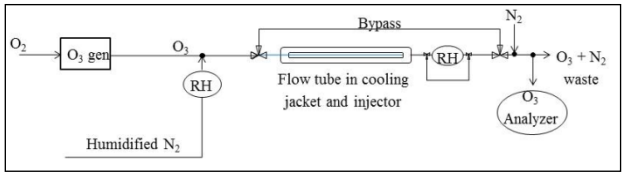

Fig. 1: Schematic of the flow tube experimental setup.

Experiments were conducted for temperatures between 16 °C and –15 °C using coated wall flow-tubes (Fig.1). The tubes were coated with NaBr solutions in citric acid (CA) as a well-characterized viscous matrix. We quantified ozone uptake by measuring the gas phase ozone concentration through the bypass and the flow-tube, respectively, and by using equation 1, where γ is the uptake coefficient, φ is the gas flow rate, SSA is the specific surface area of the tube, ω is the mean thermal velocity of the gas:

$$\gamma_{obs} = \log\left(\frac{[O_3]_{avg\_bypass}}{[O_3]_{flowtube}}\right) \times \frac{4\varphi}{SSA \times \omega_{O_3}} \qquad (1)$$

Fig. 2 presents a summary of the measured uptake (red dots) compared with modelled uptake. The measured uptake shows a relatively linear trend with inverse temperature for the temperature range studied, characteristic for a thermally activated homogeneous reaction. Modelled uptake coefficients are based on bulk rate coefficients (k^I_b) and their temperature dependence from Haag and Hoigné [5]. Bulk uptake is dependent on the diffusivity of O_3 (D_{O3}) within the film (equation 2):

$$\gamma_{bulk} = \frac{4HRT}{\omega_{O_3}} \sqrt{D_{O_3}.k_b^I} \qquad (2)$$

Where H is the Henry's constant, T is the temperature, and R is the gas constant. In turn, diffusivity decreases inversely with increasing viscosity (η) (Stokes-Einstein equation).

CA and NaBr both lead to increasing viscosity of the film compared to water with a stronger contribution from CA. The effect of viscosity on diffusivity and hence, bulk uptake were modelled (lines, Fig. 2). The measured data agree with the bulk uptake models (by order of magnitude) but the bulk models do not predict the experimentally observed temperature trend except when the effect of the diffusivity would not be accounted for (γ_novis, Fig 2).

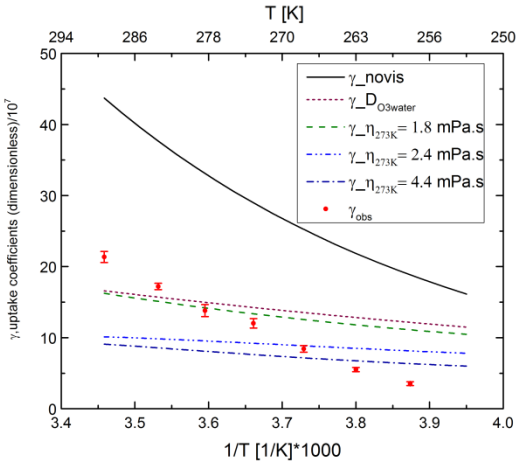

Fig. 2: Summary of experimental data (red dots) at 0.85M [Br^-] and 0.8M [CA] in the film, pH ≈ 2; modelled data (lines)

In summary, the experimental data seem to indicate that bulk reaction dominates bromide oxidation above –15 °C. However, the bulk reaction models do not predict the measured temperature dependence indicating some effects unaccounted for, which may include the influence of a surface process and/or salting effects to affect ozone solubility. Future work will include those and extend the temperature range down to –30 °C.

ACKNOWLEDGEMENT
The authors thank the Swiss National Science Foundation (SNF) for funding (grant 155 999).

[1] W.R. Simpson et al., Atmos. Chem. Phys., **7**, 4375-4418 (2007).
[2] J.P.D. Abbatt et al., Atmos. Chem. Phys., **12**, 6237-6271(2012).
[3] K. Hebestreit et al., Science, **283**, 55-57 (1999).
[4] L.A. Barrie et al., Nature, **334**, 138 - 141 (1988).
[5] R.W. Haag, J. Hoigné, Environ. Sci. Technol., **17**, 261-267 (1983).
[6] P.N. Johnson, R. A. Davis, J. Chem. Eng. data, **41**, 1485-1487 (1996).

DESIGNING DRILLED ICE FLOW TUBES TO INVESTIGATE THE UPTAKE OF TRACE ATMOSPHERIC GASES TO ICE

A.C. Hong (Univ. Toronto & PSI), J. Trachsel (ETHZ & SLF), M. Schneebeli (SLF), M. Ammann, T. Bartels-Rausch (PSI)

Air-ice chemical interactions occurring in the upper troposphere, where cirrus ice clouds are present, or in the boundary layer of snow-covered regions are important for describing the distribution and subsequent chemical fate of trace gases within ice and snow and determining the oxidative capacities of these environments. The nature of these interactions is governed by a compound's physicochemical properties as well as the ice microstructure. Some small, soluble trace gases such as hydrogen peroxide (H_2O_2), demonstrate complex uptake behavior to frozen aqueous media by reversible, fast adsorption to the interface, aggregation, and lateral interaction [1,2], as well as slow uptake, ostensibly through diffusion into the bulk [3]. However, the exact mechanism of this slow process is unknown. We hypothesize that the slow uptake of H_2O_2, a reservoir for HOx radicals and an important chromophore in snow and ice, occurs via accommodation into the grain boundaries of ice.

To provide mechanistic insight to the macroscopic phenomenon of atmospheric trace gas uptake to ice, and discern various uptake mechanisms, we designed, machined, and validated a novel flow reactor system (Fig. 1) featuring a Drilled Ice Flow Tube (DIFT). By controlling the degree of grain boundaries present in the DIFT, we can directly observe the effect of the ice microstructure on the slow uptake of H_2O_2, and can make mechanistic inferences.

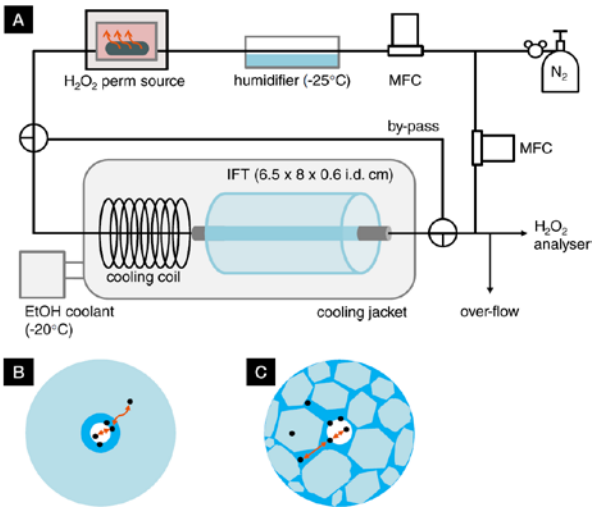

Fig. 1: Schematic of the flow reactor system (A) with a DIFT. H_2O_2(g) permeating at a known rate is diluted by a flow of humidified N_2, pre-cooled (-20 °C) before entering the DIFT, and is monitored with an instrument. The uptake of H_2O_2 can be analysed by using a monocrystalline (B) or polycrystalline (C) DIFT, respectively.

Using polarized microscopy, we visually verified that machining the DIFT did not introduce additional polycrystallinity at the interface of the drilled bore. Thin cross-sectional tiles of the bore were prepared and imaged under an optical microscope using a nadir, polarized light source. The degree of crystallinity was observed as individual crystals diffract light according to their spatial orientation. Fig. 2 compares a bore drilled into a polycrystalline DIFT using the new technique (a,c), to a bore drilled into a monocrystalline DIFT using an older technique (b,d) and shows that our current method is an improvement from the early iteration. We confirm that our flow reactor system is uniquely suited to distinguishing adsorptive and bulk uptake to grain boundaries.

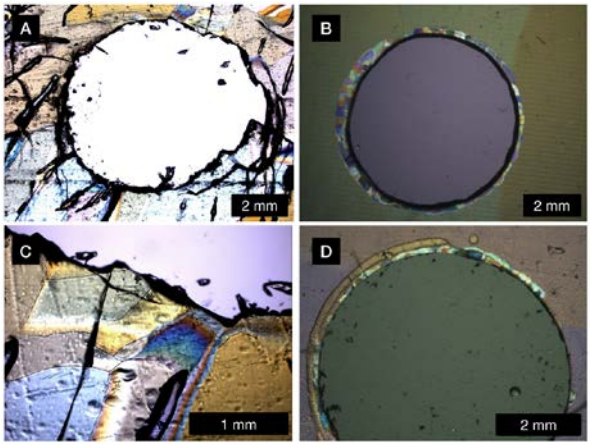

Fig. 2: Thin cross-sections of a polycrystalline (A) and monocrystalline (B) IFT are imaged. Detail of the polycrystalline IFT bore shows an absence of fracturing and additional polycrystallinity at the air-ice interface (C) and demonstrates that this is an improvement from our previous method (D).

ACKNOWLEDGEMENT

This project was supported by the Canadian National Science and Engineering Research Council (NSERC) CREATE IACPES program, the University of Toronto's Centre for Global Change Science Graduate Student Award, and the Department of Chemistry at the University of Toronto's Special Opportunities Travel Grant.

---

[1] S. M. Clegg and J. P. D. Abbatt, J. Phys. Chem. A, **105**, 27 (2001).
[2] N. Pouvesle et al., Phys. Chem. Chem. Phys, **12,** (2010).
[3] M. H. Conklin et al., J. Geophy. Res., **98,** D10 (1993).

END OF THE LITTLE ICE AGE IN THE ALPS WAS NOT FORCED BY INDUSTRIAL BLACK CARBON

M. Sigl, S. Brütsch (PSI), D. Osmont, P. Noti (Univ. Bern & PSI), P. Steffen (Univ. Bern), M. Schwikowski (PSI & Univ. Bern)

Light absorbing aerosols present in the atmosphere and cryosphere play an important role in the climate system. Their presence in ambient air and snow changes radiative properties of these media, thus contributing to increased atmospheric warming and snowmelt. High spatio-temporal variability of aerosol concentrations in these media and a shortage of long-term observations contribute to large uncertainties in properly assigning the climate effects of these aerosols through time.

Glaciers in the European Alps began to retreat abruptly from their mid-19th century maximum, marking what appeared to be the end of the Little Ice Age. Radiative forcing by increasing deposition of industrial black carbon to snow has been suggested as the main driver of the abrupt glacier retreats in the Alps [1]. Basis for this hypothesis were model simulations using ice-core measurements of elemental carbon (EC) at low temporal resolution from two ice cores in the Alps [2, 3] (Fig. 1).

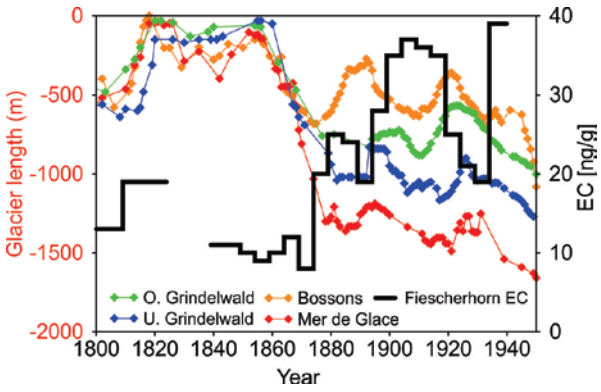

Fig. 1: Low-resolution Fiescherhorn elemental carbon (EC) ice core concentration record [2] superimposed on glacier length variations of the four Alpine glaciers Bosson, Mer de Glace and Oberer and Unterer Grindelwald between 1800 and 1950 AD [4].

We refute this interpretation by presenting sub-annually resolved, well replicated ice-core measurements of refractory black carbon (BC) using a SP2 soot photometer from an ice core in the Alps covering the past 250 years. For this we used the upper 57 m of a 81 m long ice core drilled at Colle Gnifetti (4450 m asl) in 2003. The chronology is constrained by historic Saharan dust fall events (1861, 1901, 1936, 1947, 1977 AD) and two well-known volcanic eruptions in 1783 (Laki) and 1815 (Tambora) for which distinctive tracers were identified in the ice-core trace element records.

These reconstructions allow precise comparison of the timing of observed acceleration of glacier melt in the mid-19th century with that of the increase of soot deposition on ice-sheets caused by the industrialization of Western Europe. While the new high-resolution BC reconstruction from Colle Gnifetti (Fig. 2) reproduces closely the main structure of the Fiescherhorn EC record (Fig. 1), our study suggests that at the time when European BC emission rates started to significantly increase (after 1870) the majority of Alpine glaciers have already experienced more than 70% of their total 19th century length reduction. Moreover, when industrial BC emissions reached their maximum values in the 1910-20s (indicated by ice-core BC concentrations exceeding 5x the pre-industrial background concentrations) Alpine glaciers showed no indications of increased melt. Industrial BC emissions can therefore not been considered as the primary forcing of the rapid deglaciation at the end of the Little Ice Age in the Alps.

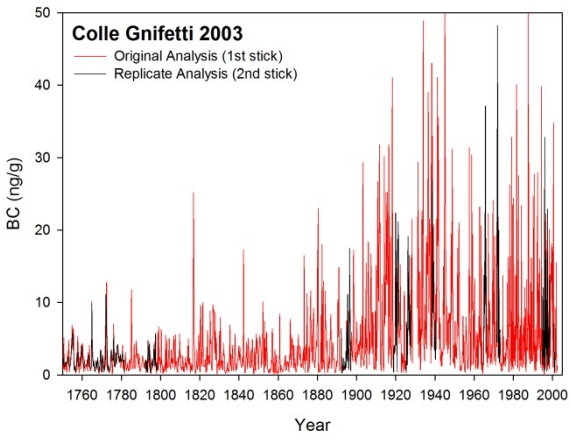

Fig. 2: A first well-replicated, sub-annually resolved reconstruction of BC from Colle Gnifetti ice core from 1750-2003 AD.

ACKNOWLEDGEMENT
This study is supported by the Swiss National Science Foundation (SNF) Sinergia Project n° 154450.

[1] T. H. Painter et al., PNAS, **110**, 15216–15221 (2013).
[2] T. M. Jenk et al., Atmos. Chem. Phys., **6**, 5381–5390 (2006).
[3] F. Thevenon et al., J. Geophys. Res., **114**, D17102 (2009).
[4] S. U. Nussbaumer, H. J. Zumbühl, Climatic Change. **111**, 301-334 (2012).
[5] I. A. Wendl et al., Atmos. Meas. Tech., **7**, 2667-2681 (2014).

350 YEARS OF BLACK CARBON EMISSIONS RECORDED IN THE LOMONOSOVFONNA ICE CORE, SVALBARD (NORWAY)

D. Osmont, L. Schmidely, I. Wendl (PSI & Univ. Bern), E. Isaksson (NPI), M. Sigl, T. M. Jenk (PSI), M. Schwikowski (PSI & Univ. Bern)

Ice cores retrieved from polar and high-mountain glaciers are a very powerful tool to reconstruct paleoclimatic and environmental conditions due to the fact that glaciers behave as natural archives by trapping chemical information from the atmosphere. Among the studied compounds, Black Carbon (BC), as other atmospheric aerosol constituents, has been of growing interest in recent years because of its impact on global warming and human health.

BC consists of aggregates of small carbon spherules produced by the incomplete combustion of fossil fuels and biofuels (including wildfires) from both anthropogenic and natural origin [1]. BC strongly absorbs visible light and therefore contributes directly to the warming of the atmosphere, and indirectly via the reduction of the snow albedo.

Our work is part of an inter-disciplinary project (SNF Sinergia "Paleo fires") aiming at reconstructing regional paleofire histories for the last 2000 years in order to understand the complex relationship between climate, fires and humans, by measuring BC and other fire tracers in ice cores from mountain glaciers. BC was analysed with a Single Particle Soot Photometer (SP2) according to the protocol given by Wendl et al. [2]. The analytical method has been previously optimized by including an autosampler and taking into account the BC loss with time. Here we present a 350-year BC record (1650-2004) from the Lomonosovfonna ice core, drilled in Svalbard in 2009, which covers 800 years of Arctic climate history.

The BC record (Fig.1) clearly shows an anthropogenic influence since the beginning of the industrial revolution. BC concentrations in the Lomonosovfonna ice core strongly correlate with nitrate and sulfate since 1850, which confirms the predominance of anthropogenic BC sources.

In detail, BC concentrations were slowly rising from a natural background after 1800 and increased sharply after 1860. Peak values were observed around 1880 and 1900 probably due to coal burning emissions in Western Europe and Northern America, in agreement with the D4 ice core from Greenland [3]. After a decline between the two World Wars possibly owing to the economic crisis and higher temperatures which probably led to snow melting and BC losses by runoff, BC emissions dramatically increased after the Second World War because of the economic growth and the extensive use of coal and oil. The highest values were found between the 1950s and the 1980s, followed by a clear decline due to the implementation of cleaner technologies and stricter environmental policies. Some sharp peaks with sub-annual resolution can be attributed to strong forest fires occurring in the Northern Hemisphere, such as the 1994 biomass burning event, also detected in Greenland [4]. Fire events are easier to identify during pre-industrial times, when the BC background signal was low. Such fire events were recorded in 1716, 1754, 1797, and correlate with peaks of other biomass burning proxies in the core like vanillic acid (private communication M. M. Grieman, Univ. of California, Irvine), ammonium or formate.

ACKNOWLEDGEMENT

This study is supported by the Swiss National Science Foundation (SNSF) Sinergia Project n° 154450.

[1] T. C. Bond et al., J. Geophys. Res. Atm., **118**, 5380 (2013).
[2] I. Wendl et al., Atmos. Meas. Tech., **7**, 2667 (2014).
[3] J. R. McConnell et al., Science, **317**, 1381 (2007).
[4] J. Dibb et al., Atmos. Environ., **30**, 553 (1996).

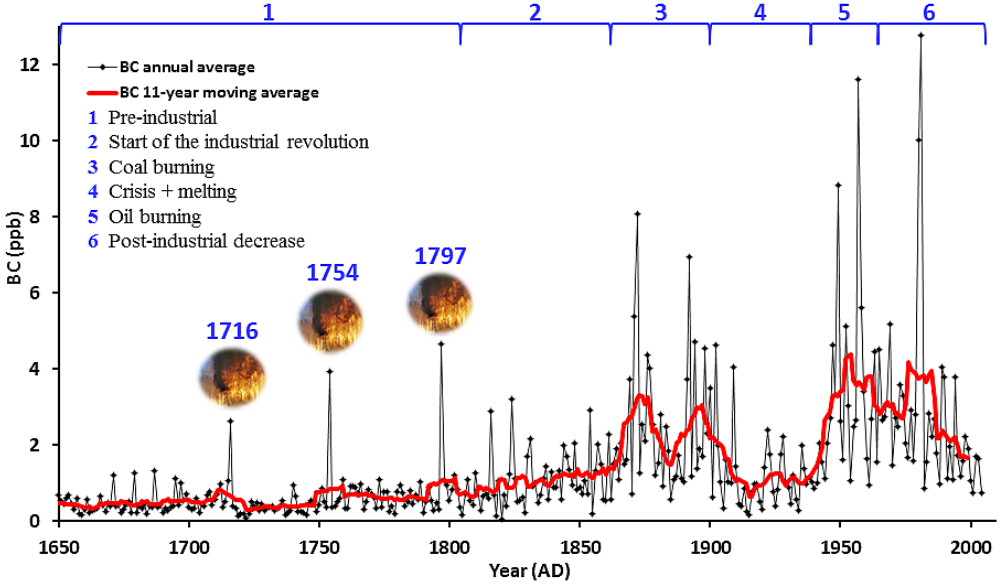

Fig. 1: BC concentration in the Lomonosovfonna ice core. The six different time periods are represented in blue and the clear paleo fire events are indicated with their respective year.

FROZENFIRE – FIRE AND VEGETATION DYNAMICS FROM THE COLLE GNIFETTI ICE CORE

S. O. Brügger (Univ. Bern), E. Gobet (Univ. Bern), M. Sigl, D. Osmont (PSI), M. Schwikowski (Univ. Bern & PSI), W. Tinner (Univ. Bern)

Wild fires are an ecological disturbance agent across ecosystems worldwide, driving vegetation dynamics and biomass availability [1]. Pollen and spores as proxies for vegetation composition and land-use activity, microscopic charcoal (>10 µm) as a proxy for regional fire activity, and soot as a proxy for fossil fuel combustion preserve in ice cores [2]. We analyzed the record from Colle Gnifetti glacier in Switzerland (4450 m a.s.l.) to assess vegetation and societal responses to climatic change and wildfire disturbance for the past millennium in the Mediterranean realm and temperate Europe - a period that experienced important climatic changes and an increasing globalization of economies.

The record contains a diverse pollen composition with sufficient pollen and charcoal (180 different pollen and spore morphotypes were identified). The large source area of the record ranges from cold subalpine (e.g. stone pine pollen), cool-temperate (e.g. beech and oak pollen), warm-temperate (e.g. sweet chestnut and oak pollen) to subtropical Mediterranean vegetation (e.g. olive tree pollen).

The record indicates an open landscape with cereal cultivation and pasture during the medieval climate optimum until 1300 AD (e.g. high herb pollen percentages) which is followed by an afforestation phase with reduced land use at 1350-1450 AD. The medieval optimum is also characterized by intense hemp cultivation, which was used for rope production. Further maxima of land use occurred at ca. 1500, 1600 and 1840 AD, before industrialization established at the European scale. The introduction of forest protection laws in Switzerland [3] and Italy [4] resulted in a recovery of forests, which is reflected in the tree pollen curve that increases rapidly between 1870 and 1900 AD.

The charcoal concentrations before 1750 AD are low with several pronounced peaks (e.g. 1540 AD, 1670 AD, 1720 AD) suggesting short periods of increasing wildfires. The peaks of 1540 and 1670 AD correlate with the driest (1540 AD) and the second driest (1669 AD) summer of the period 1500-2000 AD [6], which most likely resulted in an increase in dry biomass and therefore higher flammability. The charcoal peak in 1720 is possibly connected to the 1718/1719 AD dry period. [6] The charcoal concentrations increase to modern values after 1750 AD, preceding the introduction of maize cultivation by ca. 10-20 years.

Soot particles are regularly present after 1750 AD (when industrialization started in England) but expand only in the 20th century. The record shows a pronounced increase after 1950 AD to reach a maximum in the 1970s reflecting the intensified pollution of the atmosphere. The curve mirrors the globally observed increase of soot particles in lake sediments [7], which is related to the intensified fossil fuel burnings of the last decades.

The palaeoecological analyses of the high alpine ice archive point to complex linkages between climate, vegetation, fire, land use and pollution in Mediterranean and temperate Europe during the last millennium.

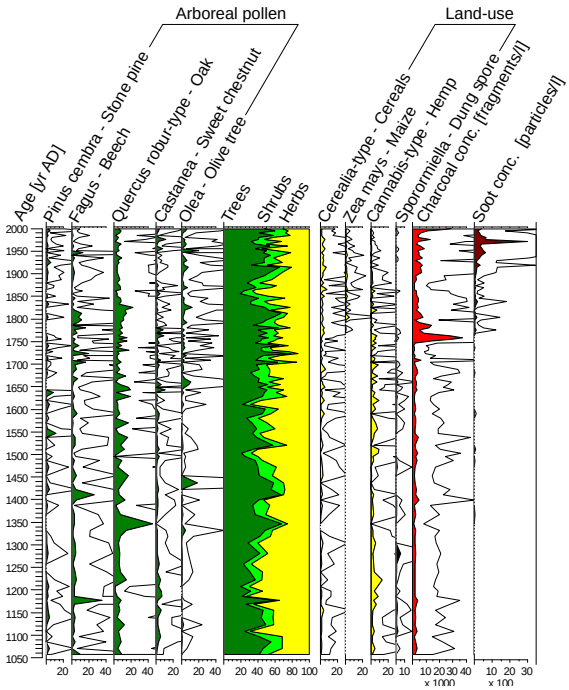

Fig. 1: Pollen percentage diagram of the Colle Gnifetti ice core record showing the most relevant pollen types, charcoal and soot particle concentrations spanning the last millennium (white curve = 10 x exaggeration).

ACKNOWLEDGEMENT

We are grateful to the SNF for the financial support of the Sinergia project "Paleo fires from high-alpine ice cores".

[1] M.A. Moritz et al., Nature, **515**, 58 (2014).
[2] A. Eichler et al., Quat. Sci. Rev. **30** (9), 1027 (2011).
[3] U. Amstutz, *Forum für Wissen*, 99-102 (2004).
[4] M.L. Freschi et al. in: Agnoletti M., Anderson S. (Eds.): Forest History: International Studies on Socioeconomic and Forest Ecosystem Change. CAB International, Wallingford, UK, 432 pp. (2000).
[5] G. Seiz et al., National Climate Observing System (GCOS Switzerland). Publication of the Federal Office of Meteorology and Climatology MeteoSwiss and ProClim, 92 p. (2007).
[6] C. Pfister and M. Rutishauser, Dürresommer im Schweizer Mittelland seit 1525. Trockenheit in der Schweiz. Report on the Workshop 'Droughts in Switzerland' held in Bern in spring 2000. 17 pp. (2000).
[7] N.L. Rose, Environ. Sci. & Tech., **49**(7), 4155 (2015).

INVESTIGATION OF METHODS FOR BLACK CARBON ANALYSIS IN SNOW AND ICE

T.M. Jenk (PSI), M. Liechti, G. Salazar, S. Szidat (Univ. Bern), C. Uglietti, M. Schwikowski (PSI & Univ. Bern)

Soot from incomplete combustion of fuels can be analyzed by means of different methods. When its light-absorbing properties are measured, soot is referred to as BC. When its concentration is measured by thermal-optical techniques, soot is known as elemental carbon (EC). BC (EC) is increasingly discussed in science and environmental policy areas as an example of an air pollutant that affects both human health and climate [1]. Due to its light absorbing properties, it also directly affects glacier melt [2]. Reconstructions of past BC (EC) emissions derived from ice cores are valuable to distinguish the natural from anthropogenic forcing. Due to the different methods applied to obtain such records, one should however be careful when combining datasets (e.g. records of BC and EC). Unfortunately, this is not always the case as datasets are also used by scientific communities (e.g. modelers) not directly involved in the analysis [3]. For BC and EC concentrations measured in snow, the method differences have been addressed and quantified with factors of up to 6 for EC/BC ratios [4, 5]. Another study evaluated inter-laboratory data for the Carbonaceous Particle Reference Material NIST SRM 1649a (Urban Dust, UD) which also revealed large discrepancies [6].

In our laboratory two different methods are applied. One is based on the thermal-optical technique using the Sunset OC/EC analyzer and can be coupled with accelerator mass spectrometry (AMS) for fossil and non-fossil source apportionment by ^{14}C, whereas the other is based on light absorption (single particle soot photometer, SP2). With these instruments, the difference for measurements of two standards – Aquadaq (AQD), used for SP2 calibration and UD (larger range in particle size with a major fraction of non-BC constituents) – as well as for a large snow sample from Jungfraujoch (JFJ, 2.5 kg) was investigated. The snow sample was split in aliquots for repeated measurements by each method after being homogenized in a mixer. Further, subsets of the aliquot were spiked with different concentrations of the two standards to investigate potential matrix effects (e.g. mineral dust in the snow). Whereas for SP2 measurements the samples were directly analyzed in the liquid phase, they had to be filtrated onto preheated quartz fiber filters prior to analysis with the Sunset system.

First, UD was analyzed with both methods to compare our results with known reference values [6] and AQD was used to determine the filtration efficiency (91 ± 7 %). Our results for BC (EC) concentrations in UD compared well as does the f_M determined by AMS (0.15 ± 0.05). We also confirmed the reported difference in the resulting concentrations for methods comparable to the ones applied here (Sunset-EC/SP2-BC = 3.5 ± 0.5).

In order to assure comparable results, the degree of homogenization in the snow sample was tested by repeated SP2 measurements of aliquots (Fig. 1).

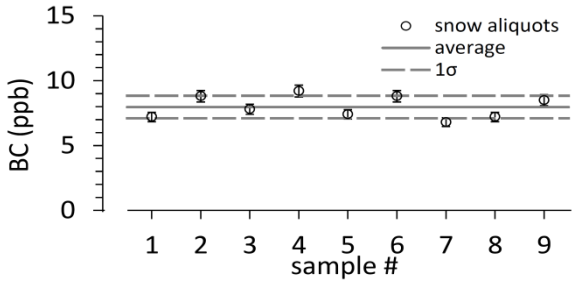

Fig. 1: Efficient homogenization of a large snow sample can be achieved (average 8.0 ± 0.9 ppb).

Both, AQD and UD were used for SP2 internal and external (standard procedure) calibration resulting in comparable results for the so determined snow sample concentration. Thus a potential matrix effect can be neglected for the SP2 method and samples with comparable loading of mineral dust. In Table 1, Sunset and SP2 results from measurements of different samples are compared.

Tab. 1: Method comparison for different samples.

Sample	Ballpark particle size estimates	Sunset-SP2 ratio
AQD	< 1µm	0.5 ± 0.4
UD	< 50 µm	3.5 ± 0.5
JFJ snow	< 5 µm	2.1 ± 0.5
JFJ snow + AQD	< 5 µm / < 1 µm	1.4 ± 0.1
JFJ snow + UD	< 5 µm / < 50 µm	5 ± 0.8
Grimsel snow	< 5 µm	1.7 ± 0.4
City snow	> 50 µm	~ 40
City snow - EC_{fossil}	< 50 µm	7 ± 3

In conclusion, a significant method dependent difference in the determined concentrations was observed, lying within the range of values reported elsewhere [4,5]. Our data suggests that this difference strongly depends on particle size (increases with size). This seems reasonable as the filtration process prior to Sunset analysis can be assumed to be less efficient for small particles, whereas large particles (> 1 µm) are not detected by the SP2 but are recorded (combusted) in the thermal method. This has implications for the investigation of longer time series as the particle size distribution can be assumed to change with time because of variations in fuel (wood to hard coal to gasoline) and combustion efficiencies. Our results emphasize that records obtained by different methods cannot be combined without a careful discussion.

[1] IPCC Fifth Assessment Report, AR5 (2015).
[2] J. Gabbi et al., The Cryosphere, **9** (2015).
[3] T. Painter et al., Geophys. Res. Lett., **34** (2007).
[4] S. Lim et al., AMT, **7** (2014).
[5] T.M. Jenk et al., Ann. Rep. LCH, Univ. Bern & PSI (2013) p. 33.
[6] L.A. Currie et al., J. Res. Natl. Inst. Stand. Technol., **107**, (2002).

EFFECT OF PARTICULATE MATTER ON THE ALBEDO OF ALPINE GLACIERS

A. Dal Farra, M. Schwikowski (PSI & Univ. Bern)

Glaciers worldwide are melting and several studies point to the decrease of surface albedo as a contributing factor in this alarming trend. Snow albedo can be reduced by the presence of particles, which accelerate melting by absorbing solar radiation and converting it into heat [1,2] and it has been shown that the same process is true for the albedo of bare ice [3]. The exposed bare ice results in the lowering of glacier albedo, partly because ice has a lower albedo then snow but also because the snow free surface often reveals an accumulation of a dark and well distributed particulate matter which is primarily composed of:

- Mineral dust (from local or distant sources)
- Soot (mostly of anthropogenic origin)
- Organic matter (humic substances)

Most studies however have focused on black carbon as the main driver of this effect neglecting the other two classes of light absorbing particles (mineral dust and organic matter).

In this research project we aim to define the interaction of each of these components with solar radiation in order to understand what their individual contribution is to the overall albedo lowering effect.

To study this phenomenon we focused on Plaine Morte glacier (a wide and flat glacier located between the cantons of Valais and Bern) already subject of many studies [4]. We selected this glacier because it presents a strong negative mass balance and has been snow free during the summer for the past seven years.

In August 2015 our fieldwork on this glacier took place and we were able to collect 110 samples of surface material (30x30 cm^2) following a grid method covering nearly all the glacier's surface. To quantify the relative presence of these components on each sample a thermal optical method [5] was employed. This method quantifies the fraction of organic carbon (OC) and of elemental carbon (soot); what is not detected is assumed as mineral fraction. The measurements show that for the analyzed samples the soot and the organic matter are around 0.91% and 4.0% revealing the preponderance in the glacier particulate matter of mineral dust (Fig. 1.b)

To determine the relative albedo lowering property of each component a hyperspectral imaging spectrometer was employed. This instrument allows the collection of images in which for every pixel a reflectance spectrum is captured. At 100 times magnification a pixel is about 130 nm and the spectra collected is in the range of 400 to 1000 nm. Numerous reflectance spectra were obtained for particles consisting of organic material, soot and several different minerals. An average spectrum was defined for the three components and its integral was calculated (Fig. 1a). The ratio between the three averages suggest that soot and organic matter reflected the least while minerals the most. Considering the link between absorption and reflection (1):

$$(1 = \alpha + \rho + \tau) \qquad (1)$$

with α being absorbance, ρ reflectance and τ transmittance, we assume that their ratio will be valid for each component's albedo lowering property (Fig. 1b) (with $\tau = 0$). Combining the two results we obtain a measure of which component contributes more to the lowering of surface albedo in the case of Plaine Morte glacier (Fig.1b). The results suggest that the primary cause of albedo reduction in Plaine Morte is the large presence of mineral dust. Although organic matter and soot are both stronger absorbents, they are present on the glacier in lower quantities.

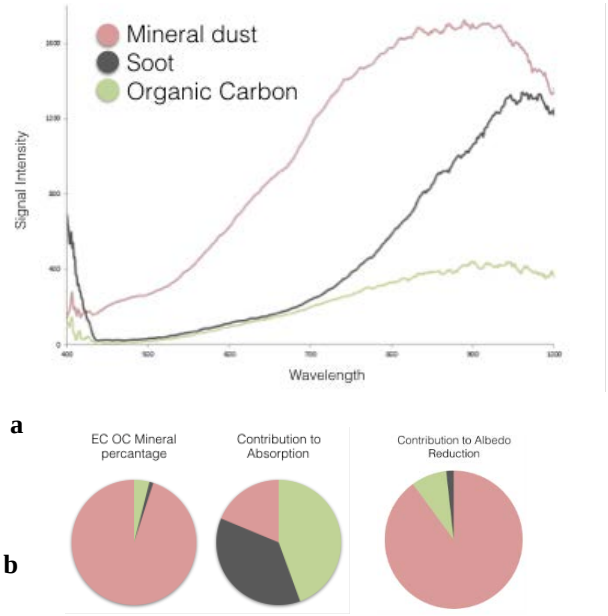

Fig. 1: a) Average reflectance spectra for the three components. b) Composition of particulate matter (left), contribution to absorption (middle) and percentage contribution of the different components to albedo reduction (right).

ACKNOWLEDGEMENTS

T. Bucheli from Agroscope, S. Szidat from University of Bern, S. Kaspari from Central Washington University, and the field team: J. Schindler, S. Avak, D. Osmond, L. Schmidely.

[1] M.Z. Jacobson et al., J. Geophys. Res. **109** (21), 1 (2004).
[2] S.G. Warren et al., Cold Reg. Sci. Technol. **5**, 2, 177 (1981).
[3] B. Qu et al., Atmos. Chem. Phys., **14**, 11117, (2014).
[4] M. Huss et al., Hydrol. Process., **22**, 19 (2008).
[5] Y. Zhang et al., Atmos. Chem. Phys., **12**, 10841. (2012).

ICE-CORE EVIDENCE OF EARLIEST EXTENSIVE AIR POLLUTION FROM COPPER METALLURGY IN THE ANDES 2700 YEARS AGO

A. Eichler, L. Tobler, G. Gramlich (PSI), T. Kellerhals (KUP), M. Schwikowski (PSI & Univ. Bern)

The exploitation of the extended polymetallic deposits of the Andes in South America led to significant emissions of toxic heavy metals into the atmosphere already in precolonial times. Copper (Cu) is one of the most essential resources of the Andean metallurgy. Although Cu was important for the wealth of precolonial cultures as the Incas, the beginning of earliest large-scale air pollution from Cu metallurgy is still debated. The oldest central Andean Cu metal artefacts from hammering native Cu date to ~1400 BC [1]. However, peat bog records from Tierra del Fuego in southern South America [2] suggest earliest anthropogenic Cu pollution and thus, the onset of precolumbian Cu metallurgy already around 1700-1300 BC, preceding that of any archaeological evidence (Fig. 1).

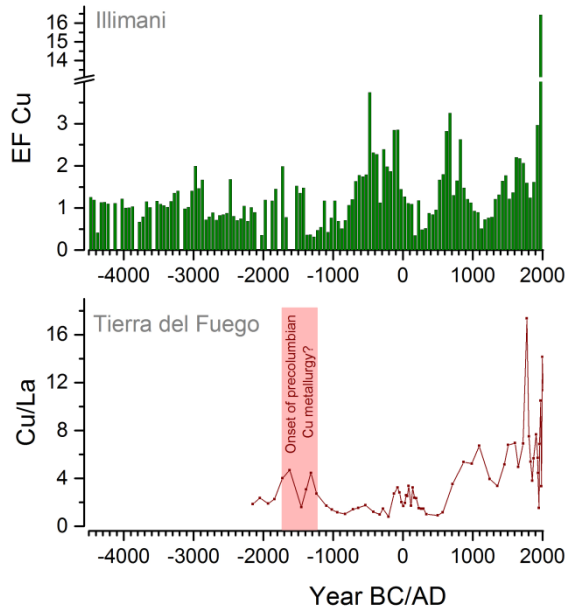

Fig. 1: Illimani ice core record of Cu EFs (50 year medians, green) together with the Cu/La ratio from the Tierra del Fuego peat bog (brown) [2].

Here we present a 6500-years Cu emission history for the Andean Altiplano in South America, based on ice core records from Illimani glacier in Bolivia (Fig. 1). To discriminate between the crustal and anthropogenic origin of Cu, enrichment factors (EFs) were calculated using Ce as the reference element, following the conventional equation:

(1) $EF\ Cu = ([Cu]/[Ce])_{sample}/([Cu]/[Ce])_{background}$

The [Cu]/[Ce] ratio for the natural background of the regional dust was determined from the ice core section BC 4500 – BC 2000, with only negligible anthropogenic influence. The same time period was also used to quantify variations in the background EF Cu (Fig. 2).

Although early maxima in the EF Cu are already visible during the Pre-ceramic period (e.g. around 3000 BC), earliest wide-spread Cu pollution exceeding the background range occurred during ~700-50 BC (Fig. 2). This first anthropogenic Cu maximum is consistent with a hypothesized onset of intensified Cu smelting during the Early Horizon from the central Andean Chiripa and Chavin cultures. Thus, our study does not confirm the early anthropogenic Cu maximum during the Initial Period [2], when cold working of native Cu as e.g. hammering dominated. It cannot be excluded that this early maximum in the peat bog record is within the background changes, which could not be quantified due to the limited period covered by that archive.

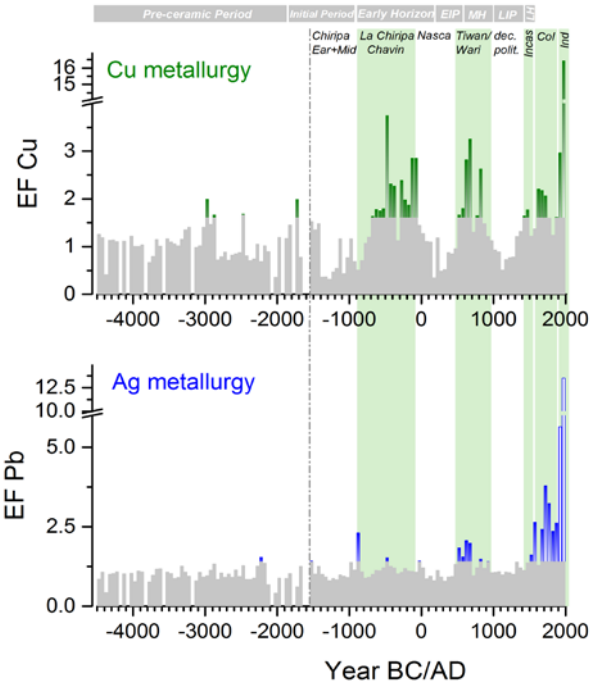

Fig. 2: Ice core records of EF Cu (green) and EF Pb (blue), reflecting the history of Andean Cu and Ag metallurgy. The natural background range (mean+2σ) deduced from the period 4500 - 2000 BC is shown in grey. The dominant civilizations in the Central Andes (green bars) are given for the different precolonial archaeological cultural periods (top grey bars).

Anthropogenic Cu emissions from the Early Horizon civilizations (700-50 BC) and the Middle Horizon Tiwanaku culture (500-850 AD) even exceeded those of the colonial period. This is explained by the fact that the colonist regarded Cu as “plebeian” metal because of its relative low value compared to silver and gold. Thus, mining activities during colonial time were more oriented towards precious metals. This is also reflected in the history of Andean Ag metallurgy deduced from the ice core Pb EF record [3], showing a strong intensification of Ag metallurgy during the colonial period (Fig. 2). The abrupt rise of the Cu production in South America during the 2nd half of the 20th century finally led to the highest anthropogenic Cu emissions within the past 6500 years.

[1] R.L. Burger et al., Science, **282**, 1108 (1998).
[2] F. de Vleeschouwer et al., PLOS, **9**, e111315 (2014).
[3] A. Eichler et al., Sci. Adv., **1**, e1400196 (2015).

RECENT ACCUMULATION AT THE QUELCCAYA ICE CAP RECONSTRUCTED FROM A SHALLOW FIRN CORE

S. Remke (ETHZ & PSI), T.M. Jenk (PSI), D. Hardy (Univ. Massachusetts), M. Vuille, J. Hurley (Univ. Albany), S. Brütsch, A. Eichler (PSI), Ch. Pandit (Univ. Bern), M. Schwikowski (PSI & Univ. Bern)

The Quelccaya Ice Cap is the largest glacier in the tropics. It is located in the eastern edge of the Andes, close to Illimani and Lake Titicaca. Ice cores from that region provide valuable information on past climate variability. Accumulation at the glaciers can be linked to the South American Summer Monsoon. So far two major ice core drilling projects have been conducted on the Quelccaya ice cap [1, 2]. The ice core drilled to bedrock in 2003 allowed to reconstruct the regional climate variability for the past 1800 years [2].

In 2003 an automated weather station (AWS) was installed at the top of the glacier [3, 4]. Aiming to extend the 2003 ice core record to the present for overlap with the AWS dataset, a drilling campaign was conducted in October 2014, recovering a 21 m firn core brought to PSI for analysis [3, 5]. A combined investigation of the AWS and ice core data is hoped to increase the understanding of depositional and post-depositional processes on the glacier and further allows direct comparison with the recorded AWS accumulation record.

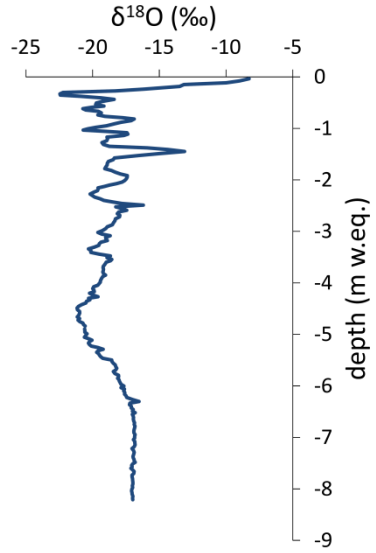

Fig. 1: Preliminary results of $\delta^{18}O$ for the first 10 m of the core vs depth (m w.eq.).

At present, the shallow core has been completely processed (cut for subsequent analysis), the density profile was assessed and around half of the samples were analyzed for major ions, Black Carbon (BC) and $\delta^{18}O$. Based on these results a preliminary first dating was established and accumulation rates were estimated for this upper part of the core.

The record of $\delta^{18}O$ indicates a significant influence of melt resulting in a heavily smoothed signal and the complete loss of seasonal variations below a depth of around 3 to 4 m w.eq. (Fig. 1). Therefore this signal could not be used for dating by annual layer counting.

On the contrary, BC concentrations revealed clear seasonal cycles throughout the analyzed section of the core (Fig. 2) which is explained by the low susceptibility of insoluble particles to be relocated with meltwater. In accordance with the annual cycle of wild fires peaking in August/September the core could be reliably dated and allowed reconstruction of the glacier accumulation back to 2008.

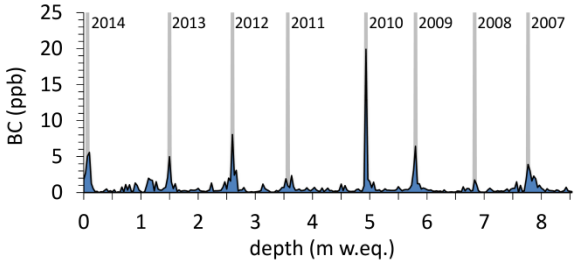

Fig. 3: Dating based on the black carbon concentration signal. Lines indicate Aug./Sept. of each year.

These results (Fig. 3) are comparable to previously reported values [2,4] and will be related to the AWS data in a next step.

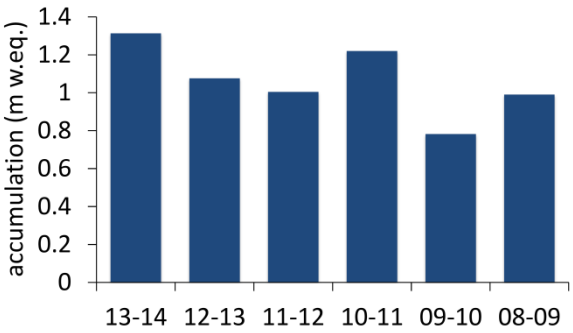

Fig. 3: Ice core reconstructed accumulation (dry to dry season) for the summit of the Quelccaya Ice Cap in m w.eq. (2008-2013).

Furthermore, concentrations of major ions, averaged for the analyzed part of the ice core, indicate a strong contribution from biogenic emissions to the total of chemical impurities measured. Tracers pointing to pacific moisture sources (e.g. MSA) were extremely low in concentration in agreement with Cl^-/Na^+ ratios being very different from the sea salt ratio. These findings suggest the dominant air mass trajectory to Quelccaya is over the Amazon basin.

[1] L.G. Thompson et al., Science, **229** (1985).
[2] L.G. Thompson et al., Science, **340** (2013).
[3] http://quelccaya.blogspot.ch/
[4] J.V. Hurley et al., JGR, **7467** (2015).
[5] T.M. Jenk et al., Ann. Rep. LCH, Univ. Bern & PSI (2014) p. 22.

DETERMINATION OF ACCUMULATION RATES FROM A SHALLOW FIRN CORE OF THE WEST ANTARCTIC ICE SHEET

C. Pandit (Univ. Bern), A. Eichler, S. Brütsch (PSI), S. Remke (ETHZ), A. Rivera, R. Zamora (CECS), M. Schwikowski (PSI & Univ. Bern)

There is a strong concern about the instability of the West Antarctic Ice Sheet (WAIS) and the retreat of its glaciers [1]. Pine Island Glacier (PIG) is one of the largest ice shelves in Antarctica, flowing together with the Thwaites Ice Stream into the Amundsen Bay. Those two contain enough ice to considerably raise the global sea level by ~ 0.5 m, if completely melted. Fastest changes in the ice flow velocity and ice thickness have been observed in the region of PIG [2]. However, little is known about changes in accumulation rates in this region, revealing the fastest loss of ice mass within Antarctica.

Fig. 1: The drilling site at the PIR divide. A firn core was collected in December 2014 by a team from the Centro de Estudios Cientificos (CECS), Chile.

The study site is the triple ice divide between Pine Island Glacier, Institute Ice Stream, and Rutford Ice Stream (PIR divide) in western Antarctica. This site is of particular interest, since a substantial volume of west Antarctic ice drains via these glaciers. Further a subglacial lake was recently discovered in this area [3]. A first reconnaissance study based on a 7 m firn core revealed a mean annual accumulation rate of ~25 cm water equivalent (w.eq.) per year [4]. However, strong melting of the firn core during transport from Antarctica to PSI disturbed the chemical records and complicated the assignment of annual layers.

This study focusses on the determination of accumulation rates of a new firn core, recovered in December, 2014. The 12.4 meter core was again drilled at the PIR divide by a team from CECS and sent to the PSI for chemical analysis. This time, no melting occurred during the transport. Sampling of the firn core was performed in the -20°C coldroom of the PSI. Outer core parts, potentially contaminated during the drilling and handling were removed using a band saw. Inner core parts were cut into 3-5 cm long pieces. 324 samples were obtained and analyzed for water stable isotope ratios $\delta^{18}O$ and δD using Wavelength Scanned Cavity Ringdown Spectroscopy and for major ions using Ion Chromatography. The sampling of the core is already finished, whereas chemical analysis is still ongoing.

Currently, we are working on the dating of the core, using annual layer counting. The first results show that some species reveal a pronounced seasonality (Fig. 2). $\delta^{18}O$ peaks in summer, whereas concentrations of major ions mainly derived from sea salt (sodium (Na^+), chloride (Cl^-), potassium (K^+)) show higher values in winter due to sea ice expansion and increased storminess. Methane sulfonate ($CH_3SO_3^-$) and sulphate (SO_4^{2-}) are high during the warm summer month, since they are mainly of marine biogenic origin. A preliminary dating for the upper 120 cm w.eq. of the firn core based on the seasonal variability of the different chemical species is shown in Fig. 2.

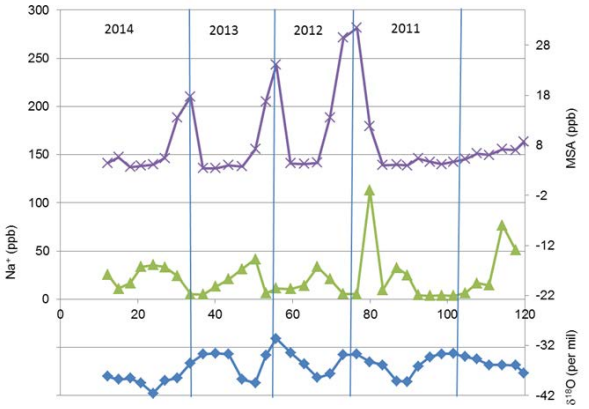

Fig. 2: The graph shows the records of $\delta^{18}O$ in per mil (blue) and MSA concentrations in ppb (purple) (right-hand Y axis) together with Na^+ concentrations in ppb (green, left-hand Y axis) and a preliminary dating for the upper 120 cm w.eq. of the PIR core. The x-axis is depth in cm water equivalent (w.eq.). The upper 15 cm w.eq. of snow were removed before drilling.

Seasonality is very well preserved for the investigated species and is not disturbed by melting. Thus, the new firn core from December 2014 is well suited for glaciochemical studies. The upper 100 cm w.eq. cover the period 2011-2014. Thus, the average annual accumulation rate for the upper 4 years is ~25 cm w.eq.. This value is in very good agreement with the accumulation rate deduced from the 7 m firn core of the reconnaissance study [4].

Future work includes the dating of the whole 12.4 m core together with the determination of annual accumulation rates and a comparison of the chemical records between the two cores of the PIR divide.

[1] E. Rignot et al., Geophys. Res. Letters, **41**, 3502 (2014).
[2] N. Wilkens et al., The Cryosphere **9**, 675 (2015).
[3] A. Rivera et al., Geophys. Res. Lett., 42, 3944 (2015).
[4] J. Fenwick, Master Thesis, University of Bern (2014).

VANISHING HIGH MOUNTAIN GLACIAL ARCHIVES: CHALLENGES AND PERSPECTIVES

Q.G. Zhang (ITPR CAS & PSI), S.C. Kang, (CAREERI CAS), P. Gabrielli (BPCRC OSU), M. Loewen (UManitoba), M. Schwikowski (PSI & Univ. Bern)

Glaciers in most mountain regions of the world have been retreating, thinning and disappearing at an accelerated rate in recent decades. Such trends are predicted to continue [1]. Glacial-archived information, one of the best libraries of the past climatic and environmental changes, is vanishing with rapid glacier reduction.

Mountain glaciers are considered one of the most sensitive indicators of climatic and environmental changes. The permanent freezing state of snow/ice permits well-preservation of atmospheric depositions. The relatively high snow accumulation in middle- and low-latitude mountain glaciers allows for the identification of decadal, inter-annual and seasonal variation of climatic and environmental parameters. In addition, being often adjacent to densely inhabited regions, mountain glaciers are more susceptible to the influence exerted by human activities and thus serve as excellent indicators of past anthropogenic activities.

Noticeably, under the context of accelerating mountain glacier decline worldwide, not only the glacier terminus but also the upper parts of the glaciers have now been subject to ablation. For example, plateau ice fields at the top of Kilimanjaro (5893 m asl) have been observed to thin remarkably during the recent two decades. An ice core drilled in 2003 on the Quelccaya ice cap (5670 m asl) in the Peruvian Andes showed the irreversible obliteration of various environmental proxies in its top due to unprecedented melt water percolation [2]. Similarly, ice cores drilled in 2011 on Mt. Ortles (3905 m asl, Eastern European Alps) can provide full environmental information only from the pre-1980 cold portion of this glacier [3]. In the Himalaya and the Tibetan Plateau, remarkable surface ablation of glaciers at extremely high elevations was discovered [4]. Ice cores drilled at Mt. Naimona'nyi (6050 m asl) in 2006, at Mt. Nyainqentanglha (5850 masl) in 2002 showed absence of some critical reference chemical peaks, suggestive of mass loss since the 1950s.

Overall the widespread glacier ablation at high altitudes is greatly reducing the possibility of obtaining past environmental records. The apparent thinning of cold glaciers' summits is actually eroding glacial records over the period of instrumental observation which is a fundamental prerequisite for calibrating subsequent ice core reconstructions. These vanishing records represent unique memories of the most recent and intensive human impact on the earth's system.

Facing the challenge of fast diminishing glacial archives, we should identify a set of still potentially valuable drilling sites, accelerate the rate at which ice cores are being recovered, adopt new advanced techniques for interpreting partially obliterated ice core records and store additional core sections. But, retrieving glacier archives may not be sufficient because ice fields are ablating faster than any possible extended salvage action. Ice samples are often destroyed when they are analyzed. Therefore we also propose a holistic assessment of nearby environmental compartments linked to glaciers to attain integrated environmental information. Glaciers can be considered transitional environments between the high troposphere and high altitude terrestrial ecosystems. Contaminants conserved for a long time within glaciers can be released in melt water and subsequently reintegrated in the global biogeochemical cycles. For instance, the recent increase of persistent organic pollutants recorded in glacial-fed lake sediments in the Swiss Alps was primarily attributed to the release of these substances from the melting glacier [5]. This indicated a possibly more general pattern that glaciers wane while glacier-fed lakes wax. The recent glacier decline implies the erosion of the most recent glacial records, representing "the missing link" for the reconstruction of environmental histories. The dynamic exchange of substances between melting glaciers and the related nearby ecosystems (Fig. 1) is ongoing and warrants a systemic study. In conclusion, rescued information from declining glaciers should be coupled with records extracted from the linked environmental compartments that can offer complementary information, to fully investigate regional and global environmental changes.

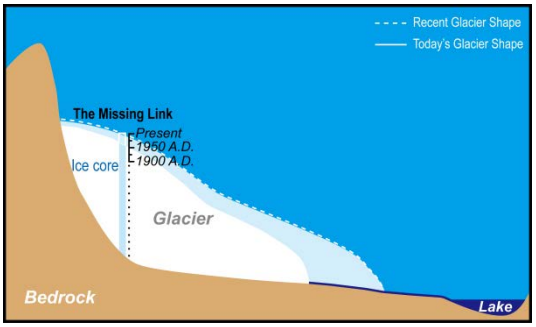

Fig. 1: Scheme of the interaction between glacial and lake sediment archives. Until recently mountain ice cores used to provide environmental time series till present; today glacier ablation is eroding the most recent ice core records while glacier-fed lakes may entrap contaminants released by glaciers.

[1] IPCC, Climate Change 2013 (2013).
[2] L.G. Thompson et al., Ann. Glaciol.**, 52,** 59 (2011).
[3] P. Gabrielli et al., Geogr. Fis. Din. Quat., **35,** 1 (2012).
[4] S. C. Kang et al., The Cryosphere, **9,** 3 (2015).
[5] C. Bogdal et al., ES&T. **44**, 11 (2010).

DATING OF THE ICE CORE FROM ORTLES GLACIER, EASTERN ALPS

C. Uglietti (PSI & OCCR Univ. Bern), T.M. Jenk (PSI), P. Gabrielli (Univ. Ohio), C. Barbante (Univ. Venice), K. Oeggl (Univ. Innsbruck), R. Dinale (Province of Bolzano), S. Szidat, G. Salazar (Univ. Bern), M. Schwikowski (PSI & Univ. Bern)

INTRODUCTION

The Ortles mountain (3905 m a.s.l.), South Tyrol, Italy, is the highest of the Eastern European Alps, located just ~30 km from where the famous 5200 years old "Tyrolean Ice Man" (Oetzi) emerged from an ablating ice field. The upper glacier, Alto dell'Ortles, may contain a unique paleo-environmental record for this area of the Alps [1]. Therefore, an international team lead by The Ohio State University drilled to bedrock a series of ice cores in September/October 2011 with the aim of better understanding the significance of the recent and future changes of climatic parameters, vegetation, land use and anthropogenic emissions in this region of the Alps located in the rapidly warming area of the Mediterranean.

Preliminary analyses of the ice cores showed a well preserved stratigraphy, with clearly distinguishable annual layers. A preliminary age of the bottom ice (652 ± 166 BC) was provided by conventional ^{14}C dating of a larch needle found at ~74 m of depth and the tritium peak corresponding to 1963 AD at ~41 m depth.

To establish a complete chronology of the ice cores, four sections of two of the four Ortles ice cores were shipped to PSI in order to perform ^{14}C dating using carbonaceous aerosols embedded in the ice matrix for the deeper parts of the ice cores. Further, liquid samples were shipped for ^{210}Pb analyses of the upper part.

^{14}C AND ^{210}Pb DATING

The analyses of ^{14}C were carried out on the four sections of the Ortles ice core using the same method as described in [2]. The ^{210}Pb activity was indirectly determined over the activity of its granddaughter nuclide ^{210}Po which was electrolytically deposited on Ag plates together with an internal standard of ^{209}Po. The ^{210}Po activity was determined by measuring its α-decay at an energy of 5.3 MeV [3]. The dating was then performed following the approach described in [3] and applied for the dating of various ice cores since. The record of the ^{210}Pb activities of the Ortles ice core does not show a strong influence from percolating meltwater, except maybe for the uppermost part which, however, does not significantly affect the dating. From a linear regression plot of the logarithmic ^{210}Pb activities against depth, the age depth relationship was obtained. The value of the axis intercept (109 ± 14 mBq kg^{-1}, Fig. 1, left panel (A)) corresponds to the ^{210}Pb activity at the surface and is typical for high-Alpine glaciers.

DEPTH-AGE MODEL

Combining the results from the above two independent dating methods, we applied two different approaches to derive a continuous depth-age relationship for the entire core (Fig. 1): the "Thompson 2-parameter model" (2-p model) and "brute force fitting" by Monte Carlo simulation (MC, 2000 simulation runs). The resulting fit for the 2-p model is poor. The data suggest very strong and rapid thinning at the bottom of the core for which the 2-p model cannot account for. Also, we cannot assume a constant accumulation based on the ^{14}C results. As expected for the method, the MC simulation results show a close fit to the data, accounting for the strong thinning between 45 and 55 m.w.eq. (the occurrence of a possible hiatus is under investigation) and indicating a change in accumulation (and/or strain rate) below a depth of 45 m.w.eq..

In summary, within the uncertainties the new dating results are in good agreement with the previously and independently determined dating horizons (conventionally ^{14}C dated larch needle and tritium peak related to the 1960s atomic bomb tests) indicating the bottom ice of the Ortles cores to be 7'000 to 8'000 years old.

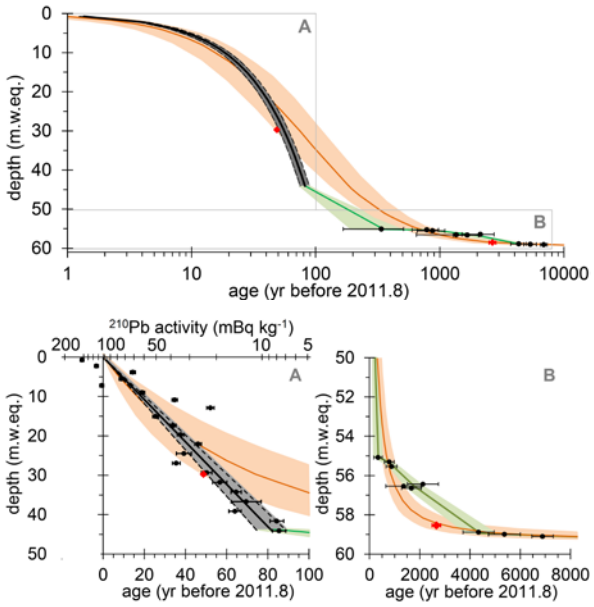

Fig. 1: Depth-age relationship of the Ortles ice core:

Top panel: Depth vs age (logarithmic scale). **A** ^{210}Pb age fit (black line) with 1σ uncertainty (grey shading). **B** ^{14}C ages with 1σ error bars (black dots). 2-p model (orange line) with 95% confidence band (orange shading). Monte Carlo simulation (green line) with 1σ probability band (green shading).

Bottom Panel: A Top 50 m.w.eq. of the core vs age (bottom axes, linear scale) and ^{210}Pb activity with 1σ error bars (black dots, top axes, logarithmic scale). **B** Bottom 10 m.w.eq. of the core vs age (linear scale). Red diamonds indicate the horizons for the 1963 tritium peak (48.8 yrs) and the conventionally ^{14}C dated larch needle (2602 ± 166 yrs cal BP).

[1] P. Gabrielli, et al., J. Glaciology, **56**, 843 (2010).
[2] C. Uglietti et al., this report, p. 35.
[3] H. Gäggeler et al., J. Glaciology, **29**(101), (1983).

^{14}C ANALYSES OF ICE SAMPLES FROM JUVFONNE ICE PATCH, JOTUNHEIMEN, NORWAY

C. Uglietti (PSI & OCCR Univ. Bern), A. Zapf (PSI, deceased), S. Szidat, G. Salazar (Univ. Bern), A. Nesje (Univ. Bergen), M. Schwikowski (PSI & Univ. Bern)

Ice patches (perennial snowfields) together with glaciers are undergoing a rapid melting in many parts of the world and numerous archaeological artefacts are potentially released from the ice. In the last decade approximately 2000 finds have emerged from the ice patches in the mountainous areas of southern Norway [1]. Studies reporting the geophysical characteristics of ice patches are few and, therefore, an urgent need of a better understanding of these features is required, before they melt completely away. Juvfonne (61.676˚N, 8.354˚E), in the Jotunheimen Mountains, Oppland County (Fig. 1) is a well-preserved Iron Age reindeer hunting area as documented by many of those artefacts retrieved around the melting ice patch. In May 2010 a ~30-m long tunnel was excavated for scientific and touristic purposes. Stratigraphic examination in the tunnel revealed several ~5 cm thick dark layers with fine-detritus organic residues, interpreted as previous ice-patch surfaces [1]. Few samples from the organic-rich layers were analyzed for ^{14}C, indicating an age of 3200 cal yrs BP [1].

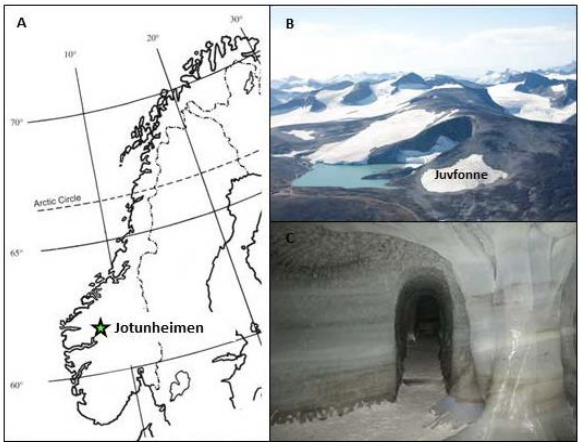

Fig 1: A. Juvfonne ice patch location: map of Norway with the Jotunheimen Mountains. B. Aerial view of Juvfonne ice patch. C. New tunnel with dark layers.

In order to validate the radiocarbon technique, which uses carbonaceous aerosols embedded in the ice matrix, two samples (JUV 1 and JUV 2) were collected adjacent to the dated organic-rich layers plus a surface sample (JUV 3). The results were published in [2] and were in agreement with the values obtained by the conventional Accelerator Mass Spectrometer (AMS) radiocarbon dating [1]. In 2012, a new tunnel (70 m long) was excavated because the first tunnel had almost melted away. A conventional AMS radiocarbon analysis was performed on fine-detritus plant fragments from the base of the new ice tunnel, revealing an age of ca 6700 cal. years BP. Therefore, another sampling was carried out in summer 2015 to collect sufficient clear ice adjacent to the plant fragment layer for the ^{14}C analyses on carbonaceous particles. Five ice blocks (~20×15×10 cm) were cut below this layer with a chainsaw and transported frozen to PSI.

All samples were decontaminated in the cold room by removing the outer layer (0.3 mm) and rinsed with ultra-pure water in a class 100 clean room [3]. The insoluble carbonaceous particles were filtered onto preheated quartz fiber filters and combusted by means of a thermo-optical organic carbon/elemental carbon (OC/EC) analyzer (Model4L, Sunset Laboratory Inc., USA), using a well-established protocol (Swiss_4S) for OC/EC separation [4]. Procedural blanks were estimated using artificial ice blocks of frozen ultra-pure water treated as real ice samples and were consistent with previous values [5, 6]. ^{14}C was determined with the compact radiocarbon AMS system 'MICADAS' at the University of Bern (LARA laboratory) equipped with a gas ion source, directly coupled to the OC/EC analyzer. Conventional ^{14}C ages were calibrated using OxCal v4.2.4 software [7] with the IntCal13 calibration curve [8]. Dates are given in years before present (cal yr BP). Overall (Fig. 2) the dating of the Juvfonne ice patch shows ages spanning from modern at the surface to ca. 7500 years BP at the bottom (clear ice below the rich organic layer), thus indicating that Juvfonne might have existed even before 7500 cal. yrs BP. So far, this is the oldest dated ice in Norway.

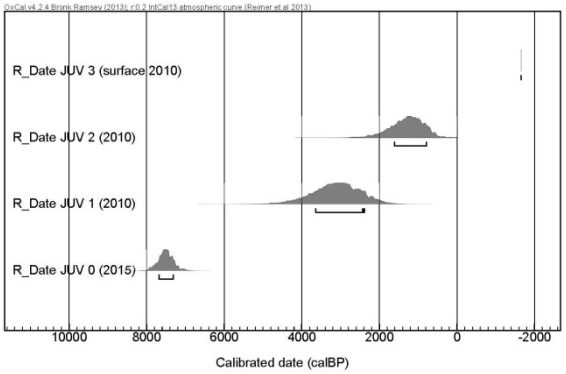

Fig 2: Sequence of the ^{14}C ice dating results for the Juvfonne ice patch. Brackets under the probability distributions show the 1 sigma probability age range.

ACKNOWLEDGEMENT

This work was supported by the Swiss National Science Foundation (200021_126515) and the Oeschger Center for Climate Research. Our Norwegian collaborators, in particular Dag Inge Bakke at Norsk Fjellmuseum, are acknowledged for excavating the ice tunnel and helping collecting the ice samples.

[1] A. Nesje et al., The Holocene **22**(4), 485, (2011).
[2] A. Zapf et al., Radiocarbon, **55** (2–3), (2013).
[3] T. M. Jenk et al., NIMB, **259**, 518, (2007).
[4] Y-L. Zhang et al., Atm. Chem. Phys., 12, (2012).
[5] T.M. Jenk et al., JGR, **114**, D14305, (2009).
[6] M. Sigl et al., J. Glaciology **55**, 985 (2009).
[7] C. Bronk Ramsey et al., Radiocarbon, **55**, (2013).
[8] P.J. Reimer, et al., Radiocarbon, **55**, (2013).

^{14}C DATING OF THE DEEPEST PART OF A MIAOERGOU ICE CORE, EASTERN TIEN SHAN, CHINA

C. Wang (PSI & Univ. Nanjing), T.M. Jenk (PSI), S. Hou (Univ. Nanjing), Y. Liu (CAREERI, CAS), S. Szidat (Univ. Bern), C. Uglietti, M. Schwikowski (PSI & Univ. Bern)

INTRODUCTION

In August 2005, two ice cores to bedrock (58.7 m and 57.6 m length for core 1 and 2, respectively) were recovered from a dome on the Miaoergou glacier in the eastern Tien Shan (43°03'19"N, 94°19'21"E, 4512 m a.s.l.) (Fig. 1). The low borehole temperature at the drilling site (-7.2 °C at 10 m depth and -8.2 °C at the bottom, respectively) is beneficial for the preservation of ice core records [1]. The age-depth relationship of the upper 42.4 m w.eq. of the core 2 was established by combination of the annual layer counting, ^{210}Pb dating and detection of the nuclear test time marker (beta activity, $^{239/240}$Pu) [1-4]. The different dating results correspond well with each other, suggesting an age of 228 years at the depth of 42.4 m w.eq. (Fig. 2). As consequence of the strong thinning effect the annual layer counting is impossible for the lower part of the ice core. There, ^{14}C analysis using the insoluble organic carbon in the ice was applied [5].

MATERIALS AND METHODS

One sample from the bottom-most part with a depth of 47.5-48.3 m w.eq. was collected for ^{14}C dating. The sample decontamination was performed at Paul Scherrer Institute by removing the ~3 mm outer layer with a bandsaw in a -20°C cold room and rinsing with ultrapure water in a class 100 laminar flow box. The insoluble carbonaceous particles of the sample were filtered onto freshly preheated quartz fiber filters (Pallflex Tissuquartz, 2500QAO-UP), then combusted stepwise (10 min at 340 °C; 12 min at 650 °C) using a thermal-optical carbon analyzer (Model4L, Sunset Laboratory Inc., USA) for separating organic carbon (OC) from elemental carbon (EC) and the resulting CO_2 was measured by the Mini Carbon Dating System (MICADAS) with a gas ion source for ^{14}C analysis at the University of Bern LARA laboratory. Details about sample preparation procedures and analytical methods can be found in [5-7].

An overall procedural blank was estimated using artificial ice blocks of frozen ultra-pure water which were treated the same way as real ice samples. Conventional ^{14}C ages were calibrated using OxCal v4.2.4 software with the IntCal13 calibration curve [8, 9].

RESULTS

The calibrated ^{14}C age close to bedrock at 47.9 m w.eq. is 5475±297 yrs before 2005 AD. The combination of the ^{14}C date and the others dates in the upper part is shown in the Fig. 2. In order to establish a continuous age-depth relation for the whole ice core, the "Thompson 2-parameter model" was applied [10]. The result shows that the 2-p model cannot fit the ages for the lower part, which suggests that the thinning at the lower part of the ice core is pronounced. This strong and rapid thinning effect has also been found in the other ice cores from the Ortles glacier, eastern Alps [7] and the Tsambagarav ice cap of the Mongolian Altai [11].

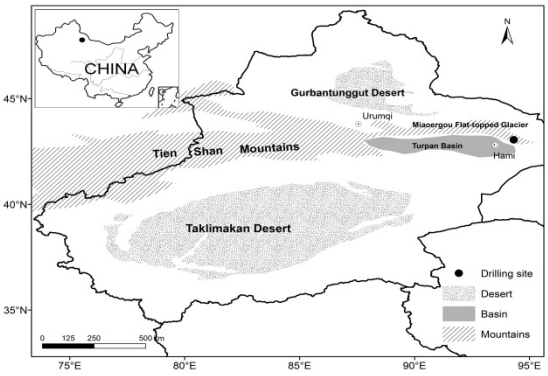

Fig. 1: Location of the Miaoergou ice core drilling site.

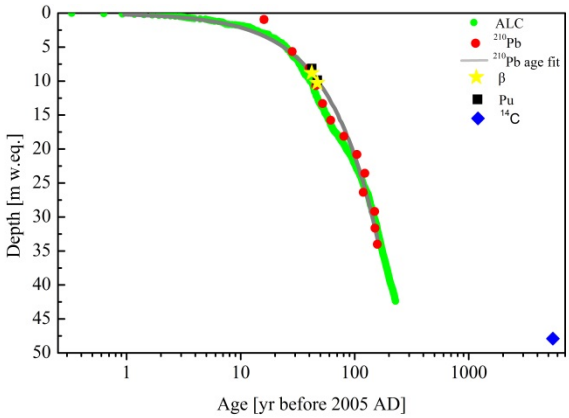

Fig. 2: Age-depth relation for the Miaoergou ice core. Annual layer counting (green dot), ^{210}Pb activity (red dots), ^{210}Pb age fit (gray line), beta activity peaks (yellow five-pointed star), plutonium peaks (black square) and ^{14}C value with 1σ-range (blue diamond).

This work is supported by the Swiss Government Excellence Scholarship granted to Wang, Chaomin, PhD student at Nanjing University.

[1] Y. Liu et al., J. Geophys. Res., **116**, D12307 (2011).
[2] C. Wang et al., Ann. Glaciol. **55**, 66 (2014).
[3] C. Wang et al., Ann. Glaciol. **57**, 71 (2016).
[4] H.W. Gäggeler et al., Ann. Rep. Lab of Radio- & Environ. Chemistry, Uni. Bern & PSI (2014).
[5] T.M. Jenk et al., J. Geophys. Res., **114**, D14305 (2009)
[6] M. Sigl et al., J. Glac.., **55**, 194 (2009).
[7] C. Uglietti et al., Ann. Rep. Lab. of Radio- & Environ. Chemistry, Uni. Bern & PSI, p. 33 (2015).
[8] B. Ramsey et al., Radiocarbon, **55**, 2-3 (2013).
[9] P. J. Reimer, et al., Radiocarbon, **55**, 4 (2013).
[10] L.G. Thompson et al., Ann. Glaciol., **14** (1990).
[11] P.A. Herren et al., Quarter. Sci., Rev., **69** (2013).

EXTRACTION OF DISSOLVED ORGANIC CARBON FOR RADIOCARBON ANALYSIS OF GLACIER ICE

J. Schindler (PSI & Univ. Bern), T.M. Jenk, S. Brütsch, A. Eichler (PSI), G. Salazar, S. Szidat (Univ. Bern), C. Uglietti, M. Schwikowski (PSI & Univ. Bern)

Glaciers in mid- and low latitudes are valuable archives for paleoclimatology, offering a continuous record of recent local climatic conditions in regions where the majority of mankind lived and lives. For meaningful interpretation of such archives, their accurate dating is essential. Among different complementing approaches, radiocarbon dating is a powerful method due to the continuous record and suitable age range of ^{14}C. Our group developed and ever since successfully applies radiocarbon dating of the particulate fraction of organic carbon (POC) found in glacier ice [1]. The dissolved organic carbon fraction (DOC) promises even better suitability for dating due to by factor 5 to 10 higher concentrations compared to POC [2] and a reduced reservoir effect. However, a straightforward analysis is hampered by the need of ultraclean sample processing with isotopic fidelity in the ppb concentration range considering the vulnerability of DOC samples to contamination [3].

To meet these requirements, we developed an extraction system for ultraclean analyses of DOC in glacier ice. For concentration and ^{14}C measurements, the DOC contained in the frozen ice samples needs to be extracted as CO_2. In brief, after cutting and cleaning an ice sample in the cold room, it is melted and further cleaned under helium inert gas conditions in a melting vessel. To separate POC and inorganic carbon (IC), the liquid sample is filtered, acidified and degassed with helium. The remaining DOC in the solution is oxidized by UV radiation in a quartz glass photo-reactor. Evolving CO_2 is degassed and led through cryogenic traps for cleaning and separation from the carrier gas. In a vacuum system, the CO_2 is further cleaned, quantified and sampled to glass vials for ^{14}C analyses via the gas inlet system of the MICADAS AMS [4].

After first tests, the trapping capacities of both cryogenic traps needed to be enhanced to ensure efficient and clean operation. Optimal parameters for the separation and handling of CO_2 samples were determined and allow reliable and reproducible processing of oxidized DOC samples.

For a characterization in terms of oxidation efficiency and isotopic signature, ultrapure standard solutions were prepared using different organic substances and ultrapure water cleaned from DOC and IC in our photo-reactor. Preliminary results suggest good absolute oxidation efficiencies, even for more volatile species: relative to potassium hydrogen phthalate (100 %), we find oxidation efficiencies of 106 %, 111 % and 95 % for oxalic acid, sodium formate and sodium acetate respectively. The time required for a complete oxidation of 100 µg carbon varies between 30 min and 120 min for the different substances.

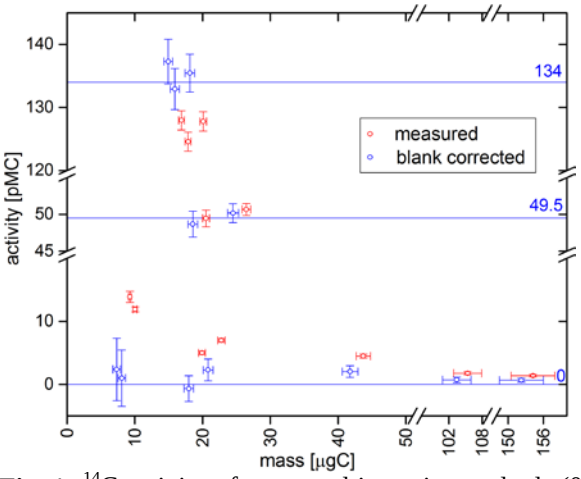

Fig. 1: ^{14}C activity of measured isotopic standards (0, 49.5 and 134 pMC) without (red) and with (blue) blank correction.

Gaseous fossil CO_2 did not show any detectable increase in ^{14}C activity due to sample processing, indicating leak-tight and clean operation. To determine the blank mass m_B and activity F_B of the oxidation step, oxalic acid standard solutions with different ^{14}C activity (0, 49.5 and 134 pMC) were injected into the photoreactor, oxidized and sampled for AMS analysis (8 samples, mass range 10 to 27 µgC). Based on these results, m_B and F_B were calculated by applying the isotopic mass balance equation in an iterative optimization approach. Starting from a randomly chosen range for F_B, the fossil and modern standard are first used to confine the possible range of m_B before the half-modern standard is then used to further restrict the initially chosen range of F_B. These steps are performed iteratively until the values stop converging. By including the uncertainties of the individual measurements in this process, the resulting values for the blank can be given with the associated uncertainties: $m_B = 2.0 \pm 0.5$ µgC and $F_B = 57 \pm 11$ pMC. Appling this for a blank correction of the measured oxalic acid standards results in good agreement with the expected activities within the uncertainties, as shown in Fig. 1. In principle, m_B and F_B still include the blank contribution from the production of the standard solutions. However, measurements of fossil standards over a range of sample masses (10 to 150 µgC) did not show significant influence of a mass dependent contribution to the blank, corroborating the direct use of m_B and F_B.
Next, we focus on determination of the overall blank including the cleaning and filtration of ice samples by using 'blank ice'. This will enable us to perform meaningful validation measurements with real ice samples.

[1] A. Zapf et al., Radiocarbon, **55** (2013).
[2] M. Legrand et al., Climate of the Past, **9** (2013).
[3] S. Preunkert et al., EST, **45** (2011).
[4] S. Szidat et al., Radiocarbon, **56** (2014).

DEVELOPMENT OF A CRYOCELL FOR HIGH SPATIAL RESOLUTION TRACE ELEMENT ANALYSIS OF ICE CORES USING LA-ICP-MS

S.E. Avak (Univ. Bern & PSI), M. Birrer (PSI), M. Wälle (ETHZ), T. Bartels-Rausch (PSI), M. Schwikowski (PSI & Univ. Bern), A. Eichler (PSI)

Past changes of atmospheric pollution can be reconstructed from ice core trace element records of cold mountain glaciers [1]. Due to climate warming cold glaciers are in danger to become polythermal. The preservation of trace element records with respect to postdepositional processes i.e., percolation of melt water depends on whether they are located at grain boundaries or embedded into the matrix.

Cryocell laser ablation inductively coupled plasma mass spectrometry (LA-ICP-MS) is the method of choice for the direct *in situ* chemical analysis of trace elements at high spatial resolution in glacier ice [2,3]. A recent study [4] investigated differences of certain element intensities between ice grain interior and grain boundaries. However, matrix matched external ice standards as well as an internal calibration necessary for an accurate quantification of signals is lacking.

During the beginning of this project a cryocell was successfully designed which is compatible to the laser ablation system of the Institute of Geochemistry and Petrology (IGP) at ETH Zurich (Fig. 1). The setup at IGP consists of a 193 nm ArF excimer laser coupled to a sector field ICP mass spectrometer (MS). Cooling of the cell at –15 °C is achieved through circulation of an ethylene glycol/water mixture in a helical channel system inside the cell.

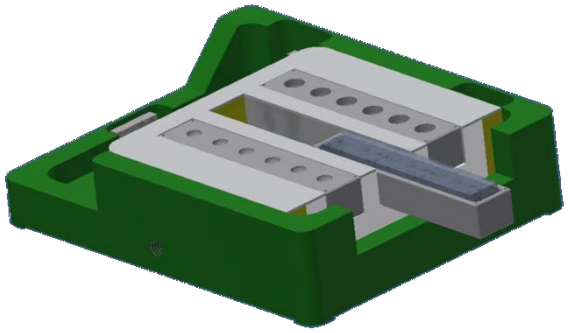

Fig. 1: The newly developed cryocell for LA-ICP-MS analysis of ice cores. It is able to simultaneously hold 8 cm long strips of ice and a series of frozen standard solutions.

Sample preparation involves both decontamination from metal residues after sawing and smoothing of the surface for laser ablation. For this purpose we use a custom-built height adjustable ice plane equipped with a ceramic ZrO_2 blade.

First tests involved the determination of the optimal laser parameters to obtain a neat ablation of frozen Milli-Q® water samples (Fig. 2). The development of matrix matched external calibration standards to quantify concentration differences between grain boundaries and ice grain interiors is currently ongoing. The basic idea for the preparation of calibration standards was reported in the literature. Small volumes (5 mL) of acidified (0.3 M HNO_3) standard solutions were shock frozen at –30°C [2]. During our investigations we used much smaller volumes (10 µL) which were shock frozen using dry ice. We observed two possibly related phenomena. A HNO_3 concentration larger than $2 \cdot 10^{-3}$ M leads to a very thin liquid film on top of the frozen droplets resulting in a completely different ablation behavior compared to frozen ice. Additionally, we only observed a signal in the ICP-MS for a few seconds when ablating low or non-acidified frozen standard solutions. Possible reasons explaining the latter observation could be a rapid decrease of ablated material as the laser penetrates deeper into the standard or an inhomogeneous freezing where the impurities cluster at the surface of the standards. The latter is supported by different ablation behaviors i.e., crater formation within the same frozen standard droplet. Further research is needed to determine the potential of ice serving as a homogenous calibration standard on a micrometer scale. Shock freezing using liquid nitrogen as well as the signal stability when ablating samples from a high-alpine glacier will be tested.

Once this analytical technique is established, this will smooth the way to investigate the potential of ice cores from polythermal glaciers as archives of past atmospheric pollution.

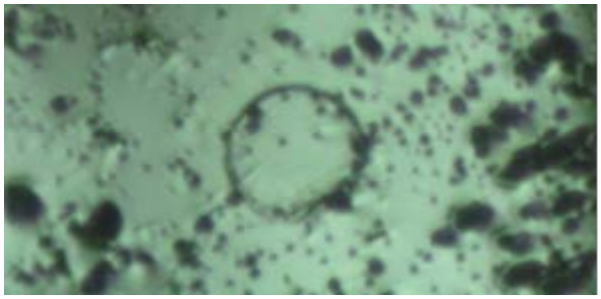

Fig. 2: Surface of a frozen Milli-Q® water sample after a single point ablation using a spot size of 163 µm, a repetition rate of 20 Hz and a laser energy density of 4 J cm^{-2}.

ACKNOWLEDGEMENT

This project is funded by the Swiss National Science Foundation Grant No. 155999.

[1] A. Eichler et al., Sci. Adv., **1**, 2 (2015).
[2] H. Reinhardt et al., Anal. Bioanal. Chem., **375** (2003)
[3] S. B. Sneed et al., J. Glaciol., **61**, 226 (2015).
[4] D. Della Lunga et al., J. Glaciol., **60**, 223 (2014).

Further information on this project can be found on: ***www.psi.ch/lch/miso***

IN THIN AIR – A NEW SHALLOW FIRN CORE FROM ILLIMANI, BOLIVIA

T.M. Jenk, R. Schild (PSI), D. Stampfli, F. Stampfli (PSI & icedrill.ch), J. Schindler, M. Schwikowski (PSI & Univ. Bern)

The glacier on Illimani, not far from La Paz in the eastern Bolivian Altiplano (Fig. 1), is one of the few in the mid- to low-latitudes giving access to ice covering the entire Holocene [1]. From two ice cores extracted in 1999 from the saddle between the summits of Pico Central and Pico Sur, a variety of scientific studies emerged such as the reconstruction of tropical South American temperature anomalies over the last ~1600 years [1] or a 2000 year history of Pb pollution including the time of South American high cultures [2]. In the framework of the SNSF Sinergia project Paleo Fires, we aimed to extend these earlier ice cores to the present, allowing overlap with the time of available fire monitoring remote sensing data from satellites. After calibration of the fire related chemical signal recorded in the ice with satellite data, a reconstruction of past natural fires, for which frequency and occurrence is still under debate, is pursued.

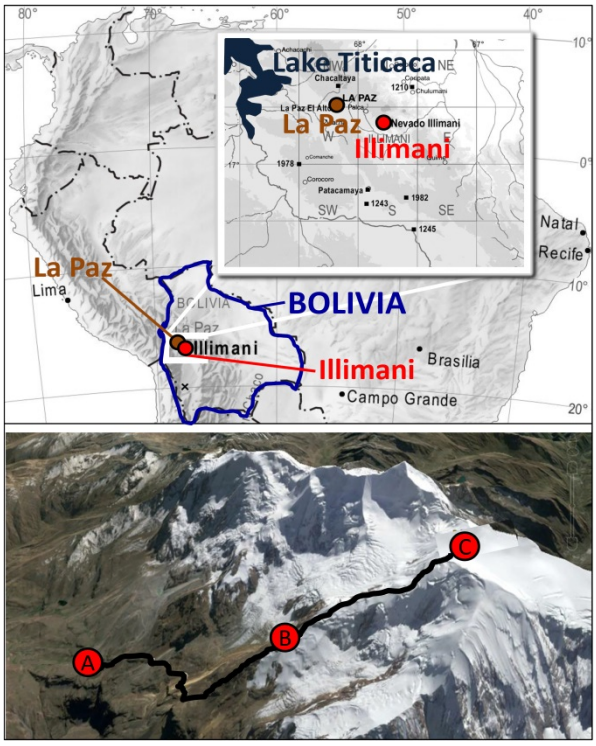

Fig. 1: Location of the Illimani. Bottom: Route from Base Camp (A) to High Camp (B) and drill site (C).

A time window from 1 to 19 June 2015 was selected for fieldwork with the ultimate goal to retrieve a shallow firn core covering at least the past 16 years for connection with the 1999 cores. While acclimatizing in La Paz (~3600 m asl.), field equipment was prepared and facilities and paperwork for later storage and shipment of the ice organized. On 6 June, we moved to Base Camp (4400 m asl.). The next day, a first trip to High Camp allowed inspection of the ascent route to the drill site, revealing optimal conditions. In the Base Camp, transport by local porters was organized and drilling equipment including all the mountain gear and food was moved higher. On 9 June we followed our material to High Camp (Fig. 2) for further acclimatization (5400 m asl.). For ice storage later, a snow cave was dug behind a small rock cliff lying in the shade most of the day (T_{max} -5° C).

On 12 June we left High Camp at 4:30 AM. After setting up tents for shelter and preparing the drilling equipment, the first core was taken at 10 AM (6300 m asl., 16°38'58.57" S, 67°47'03.57" W). Conditions were sunny and temperatures relatively cold (< -5°C), further lowered by the chill factor from wind speeds of 10-20 km/h. For drilling, these conditions were ideal and last year's depth record [3] for the drill employed [4] was improved to 25.7 m when extracting the last core around 2 PM (Fig. 2). After repacking and preparing the ice for transport we managed to finish drilling in one single day and were back in High Camp at ~5:30 PM. The ice was received from the snow cave in the morning of 14 June when cold ice bricks and isolation boxes arrived from La Paz. The same day, ice, equipment and the team safely arrived in La Paz.

By now, the ice is at PSI awaiting analysis. A thick ice lens (~10 cm) found at a depth of 23.1 m might be a tie point with the 1999 cores where a similar layer was found at 1.8 m depth (corresponding to 1998). With the additional two meters recovered, we are very optimistic that the cores do overlap.

Fig. 2: View of High Camp (top) and drilling at 6300 m asl. (bottom).

We thank J. Sandifort (Climbing South America) for logistic support and the Swiss National Science Foundation for funding (Sinergia Project n° 154450).

[1] T. Kellerhals et al., JGR, **115**, D16 (2010).
[2] A. Eichler et al., Sci. Adv., **1** (2015).
[3] T.M. Jenk et al., Ann. Rep. LCH, Univ. Bern & PSI (2014).
[4] P. Ginot et al., Mem. Natl. Inst. Polar Res., **56**, (2002).

A NEW DEEP ICE CORE FROM COLLE GNIFETTI (4454 m asl)

M. Sigl, T.M. Jenk, H. Weber (Univ. Bern), D. Stampli, J. Stampfli (PSI & icedrill.ch), J. Schindler, M. Schwikowski (PSI & Univ. Bern)

The Colle Gnifetti glacier saddle situated between Zumsteinspitze and Signalkuppe in the Monte Rosa range of the Southern Alps is among the very few places in the Alps to contain a continuous multi-millennial record of past atmospheric aerosol content and climate conditions [1-3]. The PSI has here previously drilled ice cores down to bedrock in 2003.

The past two decades have seen a wealth of new remote sensing products emerging that are able to track aerosol species in the Earth's atmosphere giving new insights into their specific sources, transport processes and atmospheric burden. These products, in combination with long-term observations, provide an opportunity for calibrating multi-millennial records of biomass burning, forest fires and mineral dust deposition obtained from Alpine ice cores with observational constraints.

Within the framework of the SNF-Sinergia project "*Paleo fires from high-alpine ice cores*" the Colle Gnifetti glacier saddle at 4450 m asl was selected for a drilling campaign in September 2015, in order to extend existing ice-core records from this site (i.e. the two bedrock cores CG03A and CG03B drilled in 2003 (45°55'45.7" N, 7°52'30.5" E) into the recent present.

From 23-29 September 2015 a team of six scientists from PSI and the University of Bern conducted fieldwork to retrieve two firn/ice cores (8 cm diameter). Drilling of a 76 m long ice core (CG15A), taken 18 m NW (45°55'46.1" N, 7°52'29.9" E; 4454 m asl.) of the CG03 ice cores reached bedrock; a second core (CG15B) drilled 2 m away reached a depth of 47 m when drilling was stopped.

The ice was shipped to PSI in insulated boxes and the upper 12 m of the CG15A core have at present been processed at the PSI. Discrete samples of 4 cm length (1.9 cm x 1.9 cm width) have been taken from the innermost part of the core section for subsequent analysis of black carbon (using a SP2 soot photometer) and soluble impurities (using ion chromatography). Large volume samples were also collected for subsequent charcoal and pollen analysis at the Institute of Plant Sciences, University of Bern. A series of visible Saharan dust layers in CG15A at 14.0, 14.6, 15.0, 17.1, 18.4 and 21.3 m depth will allow matching the new ice-core records to the established dust chronology from existing Colle Gnifetti ice cores CG03A and CG03B with strong dust events recorded in 1990, 1992, 1993, 1997, 1999, 2000 AD [2-5].

Fig. 1: The drilling camp on Colle Gnifetti (4450 m asl) as seen from Signalkuppe on 24 September 2015 in front of Zumsteinspitze and Duffourspitze (4633 m asl). Credit: Martina Barandun.

Fig. 2: The deepest ice-core section of the CG15A ice core (76.06 m depth) containing rock fragments from the underlying bedrock. Credit: Michael Sigl.

ACKNOWLEDGEMENT

This work was supported through the SNF-Sinergia project "Paleo fires from high-alpine ice cores".

[1] M. Schwikowski et al., Environ Sci Technol. **38** (4): 957 (2004).
[2] T. M. Jenk et al., J. Geophys. Res., **114**, 114, D14305 (2009).
[3] M. Sigl et al., J. Glaciology., **114**, D17102 (2009).
[4] J. Gabbi et al., The Cryosphere, **9**, 1385 (2015).
[5] H. Sodemann, Atmos. Chem. Phys., **6**, 667 (2006).

A VOLCANIC CLIMATE CRISIS IN THE LATE ANTIQUITY

M. Sigl (PSI), U. Büntgen (WSL), F. Ludlow (Yale University), J. R. McConnell (Desert Research Institute)

Cold climate periods are known to have played an important role in socioeconomic changes in human history. That they were caused or boosted by the eruptions of large volcanoes had been assumed, but never accurately quantified.

As earlier studies have determined, particularly cool periods triggered crop failures and famines in the past [1]. These events also may have contributed to pandemics and, social upheavals and migrations. Those atmospheric cool downs are widely known to be caused or strongly influenced by large volcanic eruptions as large amounts of volcanic sulfate particles injected into the upper atmosphere shield the Earth's surface from incoming solar radiation. However, until now there was no reliable method to accurately date them and thus measure their impact [2].

Analyzing ice cores from Greenland and Antarctica for volcanic sulfate provided a year-by-year history of atmospheric sulfate levels [3]. But only comparing the results with annually resolved and absolutely dated tree rings allowed to get a fairly accurate picture of the climatic development. According to these reconstructions, tropical volcanoes and large eruptions in the Northern Hemisphere high latitudes (such as in Iceland and North America) – in 536, 626, and 939 CE, for example – often caused severe and widespread summer cooling in the Northern Hemisphere by injecting sulfate and ash into the high atmosphere [3]. These particles also dimmed the atmosphere over Europe to such an extent that the effect was noted and recorded in independent archives by numerous historical eyewitnesses [3,4].

The findings resolve a long-standing debate regarding the causes of one of the most severe climate crises in recent human history during the Late Antiquity. Starting in March 536, a "mystery cloud" was observed in the Mediterranean region for 18 months [4]. It was caused by a large eruption in the high-latitudes of the Northern Hemisphere. The initial cooling was intensified when a second volcano located somewhere in the tropics erupted only four years later (Fig. 1). In the aftermath, exceptionally cold summers were observed throughout the Northern Hemisphere [5]. This thermal shock persisted for several years, with subsequent crop failures and famines – likely contributing to the outbreak of the Justinian plague that spread throughout the Eastern Roman Empire from 541 to 543 CE, and which ultimately decimated the human population across Eurasia [6].

The Future Earth program "Past Global Changes" (PAGES) has recently initiated the "Volcanic Impacts on Climate and Society" (VICS) working group (Fig. 2) with the project starting in 2016 and lasting for six years.

The principal aims of this group are to improve radiative forcing; understanding of volcanically induced climate variability; and understanding of societal impacts of volcanic eruptions.

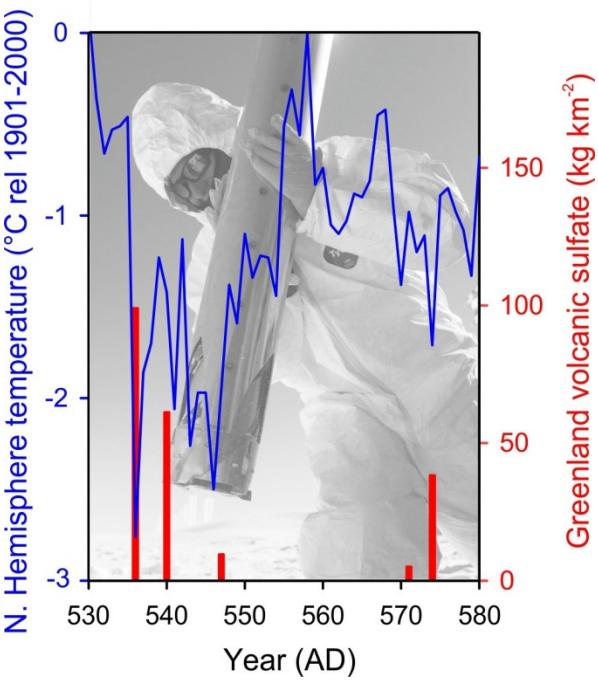

Fig. 1: Strong and widespread cooling occurred in the Northern Hemisphere in the immediate aftermath of large volcanic eruptions as indicated by ice cores from Greenland. Credit: M. Sigl

Fig. 2: Logo of the open community "Volcanic Impacts on Climate and Society" (VICS) working group http://www.pages-igbp.org/ini/wg/vics/intro, starting in 2016 endorsed by PAGES. Credit: PAGES

[1] U. Büntgen et al., Science, **331**, 578-582 (2011).
[2] M. G. L. Baillie, Geophys. Res. Lett., **35**, L15813 (2008).
[3] M. Sigl et al., Nature, **523**, 543-549 (2015).
[4] R. B. Stothers, Nature, **307**, 344-345 (1984).
[5] M. Stoffel et al., Nature Geosci., **8**, 784-788 (2015).
[6] U. Büntgen et al., Nature Geosci., **9**, 231 (2016).

CHANDA – WORKSHOP ON TARGET PREPARATION – THE NEEDS AND THE POSSIBILITIES

D. Schumann (PSI)

From 23.11.-25.11., the first CHANDA workshop on target preparation was performed at the Paul Scherrer Institute Villigen under the leadership of the RadWasteAnalytics group.

In the frame of the EC-funded integrated project CHANDA [1], the importance of nuclear target preparation for the accurateness and reliability of experimental nuclear data is addressed in a dedicated work package (WP3). The global goal of WP3 is the development of a network for nuclear target preparation and characterization, enabling to coordinate the target production corresponding to the experimental requirements.

The workshop was one of the deliverables within WP3 and was aimed to bring together isotope producers, target manufacturer and users for discussions about the needs and the possibilities of target preparation.

Although CHANDA is a program mainly focused on energy research, also synergies with other nuclear data applications have to be identified and integrated for establishing a competent and highly efficient network. Due to this special requirement, a special session on the interdisciplinary character of nuclear data was embedded into the workshop. For this session, we welcomed the internationally highly recognized specialists Prof. Syed Qaim (FZ Jülich), Prof. Rolf Michel (ZSR Hanover), Prof. Sylvie Leray (CEA Saclay), Prof. René Reifarth (Uni Frankfurt), Prof. Tibor Dunai (Uni Köln) and Prof. Andreas Türler (PSI and Uni Bern), who gave an overview on the progress and challenges in the field of nuclear data related to their own research area. In a panel discussion on Monday evening, the participants had the opportunity to discuss the needs and the possibilities for crosscutting activities in nuclear data research.

The sessions with contributions of the participants were dedicated to the following topics:

- Isotope production
- Target manufacturing and characterization
- Results of experiments
- Future plans

The details of the workshop program, the proceedings and further information can be found on the webpage [2].

---

[1] http://cordis.europa.eu/project/rcn/110083_en.html
[2] http://indico.psi.ch/conferenceDisplay.py?confId=3671

Fig. 1: Photo of the workshop participants

PREPARATION OF A ^{7}BE TARGET ON GRAPHITE AND POLYETHYLENE BACKINGS

E. A. Maugeri, S. Heinitz, D. Schumann (PSI)

The standard Big-Bang Nucleosynthesis (BBN) model predicts the abundance of the light nuclei produced when the temperature of the Universe was low enough to allow neutrons and protons to combine and form ^{2}H, ^{3}H, ^{3}He, ^{4}He and ^{7}Li [1]. The validity of this model has been proved by comparison to measurements of the abundances of ^{2}H, ^{3}He and ^{4}He, while it dramatically fails when predicting the ^{7}Li abundance. This represents one of the most controversial and still pending problems in nuclear astrophysics, known as the "Cosmological Lithium problem" [2]. In fact, the abundance of ^{7}Li observed in low-metallicity stars in the Galactic halo [3] is a factor of 2-3 lower than the value predicted by the BBN model. Since ^{7}Li is mainly produced by the electron capture decay of ^{7}Be, its abundance strongly depends on the production/destruction rate of ^{7}Be. ^{7}Be is mainly produced via the ^{3}He(α, γ)^{7}Be nuclear reaction and mainly destroyed via the ^{7}Be(n, p)^{7}Li one. The cross section of the last nuclear reaction was measured with a statistic error of the order of 0.7% [4]. Since this reaction was ruled out as a possible ^{7}Be sink, other secondary reactions leading to the destruction of ^{7}Be have to be considered.

The ^{7}Be(n,α)^{4}He reaction rate has been considered negligible compared to the main destruction reaction ^{7}Be(n, p)^{7}Li. However, the values reported in literature, see e.g. [5], were obtained via extrapolation from the first and only experimental value acquired in 1963 using thermal neutrons [6]. Those values are characterized by an uncertainty of a factor of ten. This uncertainty, indeed, does not allow considering this reaction to be negligible for the direct destruction of ^{7}Be, and, vice versa, "imposes" further research, in particular experimental investigations aiming towards more precise values on the cross section in the energy range of interest for the BBN, i.e. 20-100 keV. In the light of that, a dedicated experiment to measure the cross section of the ^{7}Be(n,α)^{4}He reaction at high energy has been launched in the framework of an international collaboration at the Neutron Time-of-Flight facility (n_TOF) at CERN. This investigation is, without doubt, very challenging, due to the high specific activity of ^{7}Be and the low cross section of the (n,α) reaction.

In the proposed experiment, the two high energetic α particles (about 9 MeV) of the ^{7}Be(n,α)^{4}He reaction are going to be measured in coincidence with two silicon detectors (200 µm thick with an active area of 3×3 cm^{2}) in a sandwich configuration, i.e. the target will be placed between two alpha detectors. For a good spectroscopic resolution, the alpha measurements require thin ^{7}Be targets. Two different ^{7}Be targets were prepared by our group for these purposes. The first target, Fig. 1, was obtained by electrodeposition of about 15 GBq of ^{7}Be onto a 5 µm Al foil, from a purified and ^{7}Li free, $^{7}Be(NO_3)_2$ solubilized in isopropanol solution. The electrodeposition lasted 60 min with a current constantly regulated at 1-1.5 mA.

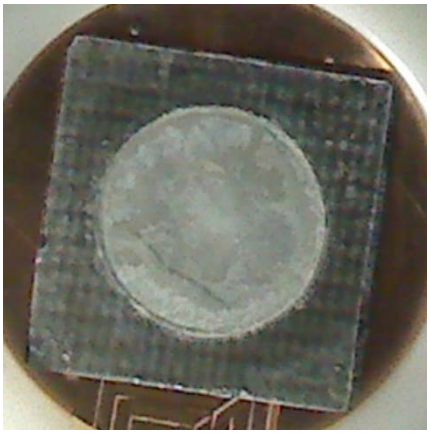

Fig. 1: ^{7}Be electro-deposited on 5 µm Al foil.

The second target, Fig. 2, was obtained by vaporization of about 15 GBq of ^{7}Be in form of 3.5 µL drops of a $^{7}Be(NO_3)_2$ solution on a thin polyethylene film. The drops were obtained using a dedicated remotely controlled device implemented for this specific experiment.

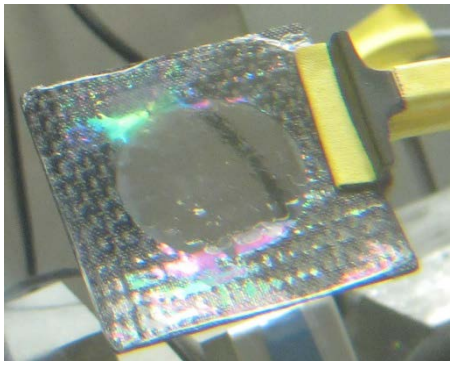

Fig. 2: ^{7}Be deposited on a thin polyethylene film.

The experiment has been performed in August 2015 in the Experimental Area II at n_TOF CERN with remarkable success. The first preliminary results show the feasibility of the experiment, thus the reliability of the prepared targets. A more detailed characterization of the targets will be performed in 2016 when the activity is low enough to allow for a γ-measurement with an envisaged low uncertainty.

ACKNOWLEDGEMENT

Thanks are due to the n_TOF group for the stimulating and fruitful collaboration.

[1] T.P. Walker et al., AJ, **376**, 51 (1991).
[2] R.H. Cyburt et al., Phys. Rev. D, **69**, 123519 (2004).
[3] F. Spite et al., A&A, **115,** 357 (1982).
[4] P. E. Koehler et al, Phys. Rev. C **37,** 917 (1988).
[5] P.D. Serpico et al., J. Cosmol. Astropart. Phys., **12**,10 (2004).
[6] P. Bassi et al., Nuovo Cimento, **28,** 1049 (1963).

BURNING GRAPHITE – AN ALTERNATIVE WAY FOR THE EXTRACTION OF ^{10}Be FROM PROTON IRRADIATED TARGET E

S. Heinitz (PSI), D. Kiselev (PSI/ABE), D. Schumann (PSI)

The long-lived isotope ^{10}Be ($T_{1/2}$ = 1.387 Ma) is a useful nuclide for geochemical processes relevant in soil and ice core dating as well as for studies on halo nuclei [1]. Large amounts of this isotope are produced at the PSI muon production facility by high energy proton spallation in polycrystalline graphite. Despite Be, also all other elements from H to B are formed within the graphite during proton irradiation as shown in Figure 1. Of special importance is the radioactive isotope of hydrogen, since substantial amounts of ^{3}H in the order of GBq/g of graphite remain in the target, that have to be confined during chemical processing.

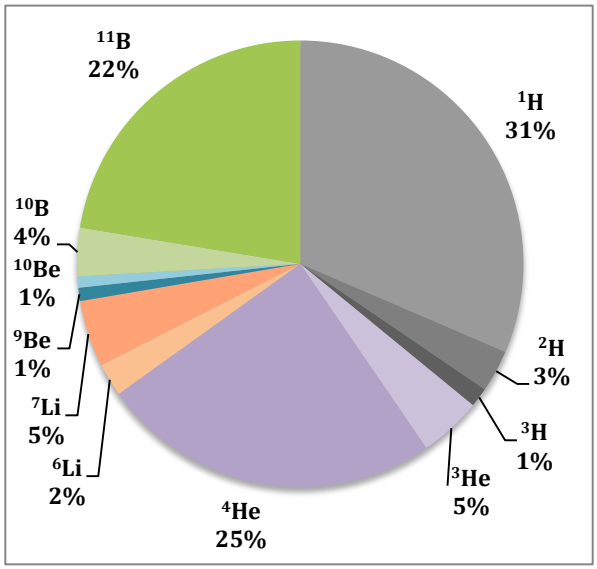

Fig. 1: Pie chart representing the calculated mass fractions of spallation products formed in proton irradiated graphite of target E92. Calculation performed with MCNPX.

To extract ^{10}Be from massive amounts of carbon, a chemical procedure based on wet oxidation has already been reported [2]. This process, however, generates large amounts of highly acidic waste contaminated with tritium, which complicates the disposal. In order to avoid the use of concentrated acids and to assure a reliable trapping of ^{3}H, burning of the graphite has been proposed [3].

Approx. 270 g of graphite from Target E92, which had received a total proton charge of 29 Ah between 2002 and 2005, have been burned at 1000°C in a stream of oxygen. Each piece of graphite was placed on a Pt foil in order to avoid diffusion of the oxidation products into the quartz boat. The volatile radioactive oxidation product $^{3}H_2O$ was trapped in 3 water bubblers connected in series and filled with 100 ml H_2O. As such, the water bubblers served as an effective trap to drastically reduce the amount of ^{3}H escaping the system [4] and to ease its disposal.

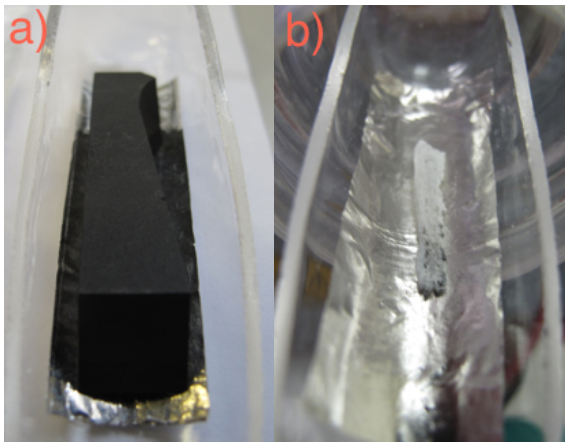

Fig. 2: Picture taken of a) a sample of Target E92 before and b) its residue after burning it in oxygen at 1000 °C.

The remainder, a white hygroscopic solid material mainly consisting of $^{6/7}Li_2O$, $^{9/10}$BeO and $^{10/11}B_2O_3$ depicted in Figure 1b), was dissolved in HF and was further purified by ion exchange chromatography. Radioactive contaminants such as ^{22}Na, ^{26}Al, ^{54}Mn, ^{60}Co, ^{101}Rh, ^{133}Ba, ^{172}Hf, and ^{207}Bi, which were formed by nuclear reactions on impurities in the graphite, have also been separated from the final product. The purified material represents a mixture of approx. 6 mg ^{9}Be and 4 mg or 3.8 MBq ^{10}Be.

Table 1 gives an overview on current and future graphite from Target E available for ^{10}Be recovery at PSI. While E79 and E92 have already been successfully processed, graphite from target E93 and E95 will be available mid of 2016.

Target Nr.	Applied proton charge [Ah]	Total graphite mass available [g]	^{10}Be mass [mg]
E79	6.64	24	0.1
E92	28.79	270	4.1
E93	39.34	≃ 600	12.4
E95	27.95	≃ 600	8.8

Tab. 1: Overview on available amounts of irradiated graphite from target station E with their corresponding total ^{10}Be inventory

[1] A. Krieger et al., Phys. Rev. Lett. **108** 142501 (2012).
[2] D. Schumann et al., RCA **96** 1–4 (2007).
[3] M. Argentini et al., Ann. Rep. of Radio- and Environ. Chemistry, Uni Bern & PSI, p. 41 (2000).
[4] R. V. Osborne, Sampling for tritiated water vapour, Proc. 3rd IRPA congress, Washington D.C., pp. 1428 – 1433 (1973).

SEPARATION AND PURIFICATION OF ^{53}Mn FROM IRRADIATED STEELS

B.-A. Dittmann, E. Strub, T. Dunai (Univ. Köln), N. Kivel (PSI/AHL), D. Schumann (PSI), R. Dressler (PSI)

INTRODUCTION

Terrestrial *in situ* cosmogenic nuclides (^{10}Be, $t_{1/2}$=1.6 Ma; ^{26}Al, $t_{1/2}$=0.7 Ma;) are essential tools in geoscientific applications, such as burial ages, erosion rates or exposure ages of terrestrial rocks or meteoroids. The long-lived nuclide ^{53}Mn with a half-life of 3.7 ± 0.4 Ma can extend the dating range to > 10 Ma. In combination with ^{10}Be it is a useful tool to study long-term landscape evolutions [1].

In order to measure ultra-trace amounts of ^{53}Mn by accelerator mass spectrometry (AMS), it is necessary to have reliable standards with typical ^{53}Mn/^{55}Mn ratios of about 10^{-9} – 10^{-10} for extra-terrestrial and 10^{-12} – 10^{-13} for terrestrial samples. A challenge in the production of these standards is the sufficient chemical removal of the stable isobaric nuclide ^{53}Cr, interfering the measurement.

The source material for the extraction and purification of ^{53}Mn is irradiated **martensitic steel,** originating from the SINQ target-irradiation program (STIP). The aim of this program was to study radiation damage effects induced by high-energy protons and spallation neutrons on martensitic steel samples [2].

EXPERIMENTAL

The chemical separations were carried out following the procedures described in [3]. The Mn fraction, which still contained traces of the interfering isobar ^{53}Cr and other radionuclides, such as ^{44}Ti/^{44}Sc, ^{60}Co and ^{133}Ba had to be purified. The purification was performed by precipitating Cr as $Cr(OH)_3$ with Urotropine (Hexamethylenetetramine) at pH 5.5 (Fig. 1).

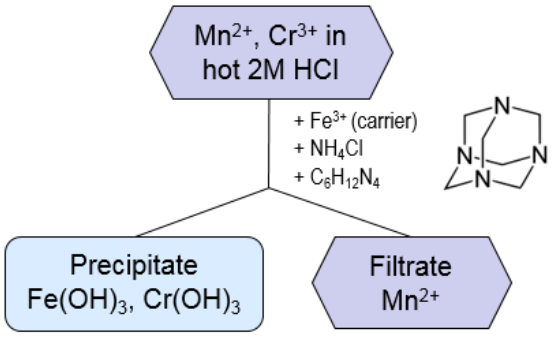

Fig. 1: Separation Cr from Mn using Urotropine.

The yield of the separation was determined by γ-spectrometry with ^{54}Mn and ^{51}Cr as tracers. Both Mn and Cr yields were near 100%.

From the Urotropine-containing solution, Mn was recovered by precipitation with H_2S and subsequent anion exchange chromatography to get rid of remaining Ti, Ca, Co, and Ba in 9M HCl solution (Fig. 2). The chemical yield for Mn was 80 – 90%.

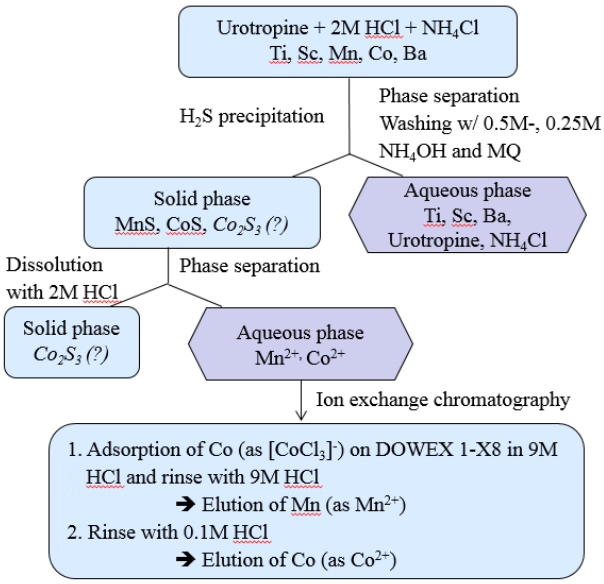

Fig. 2: Separation scheme.

RESULTS AND DISCUSSION

Up to now, 80% of the Mn fractions originating from the martensitic steel samples have already been processed. An aliquot of the purified material has been characterized by MC-ICP-MS measurement and the ^{53}Mn/^{55}Mn ratio was determined to $R_{(53/55)Stock}$ = 0.0137 ± 0.1%. This stock solution was used for the production of four different AMS standard materials with ^{53}Mn/^{55}Mn ratios in the order of 10^{-9}, 10^{-10}, 10^{-12} and 10^{-13}, respectively. The validation and AMS measurements of these standard materials are still ongoing. The method described here for the recovery of Mn from Fe and Cr rich materials could serve as an alternative for the currently applied procedure [4] used in geosciences. To prove the reliability of the method, terrestrial samples are currently processed at the University of Cologne.

In the future, the remaining purified Mn fraction will be used for the redetermination of the ^{53}Mn half-life. Therefore it is planned to conduct an isotope separation at ISOLDE@Cern in order to obtain a pure ^{53}Mn fraction free of ^{54}Mn.

[1] K. Dong et al., Nucl. Inst. Meth. B, **361**, (2015).
[2] Y. Dai et al., J. Nucl. Mater., **296**, (2001).
[3] R. Dressler et.al., JPG **39**, 105201 (2012).
[4] T. Fujioka et al., Nucl. Inst. Meth. B, **268**, (2010).

SEPARATION OF LANTHANIDES FROM PROTON-IRRADIATED LEAD TARGETS

Z. Talip (PSI), S. Pfister (Univ. Bern & PSI), D. Schumann (PSI), R. Michel (IRS)

INTRODUCTION

Heavy metals that are considered or in use as spallation target materials for accelerator driven systems (ADS) and spallation neutron sources (SNF) are Ta, W, Hg, Pb, and PbBi. The radionuclide inventory of these targets provides necessary information for the construction, licensing and disposal of ADS and SNF research facilities. Cross section data for the production of long lived radionuclides are especially crucial for the management of the long-term waste disposal of these facilities.

EXPERIMENTAL

In previous works [1, 2], radiochemical separations of several long-lived radionuclides from 11 proton irradiated lead targets (typical weight 125 mg/cm^2, 99.99% purity), which were irradiated in an energy range up to 2.6 GeV between 1993-97 at the SATURNE II synchrotron of the Laboratorie National Saturne (LNS) at Saclay and at TSL Uppsala, were reported. In the present study, the remaining LnF_3 fractions were used to separate long lived alpha emitting lanthanides such as ^{154}Dy, ^{146}Sm and ^{148}Gd/^{150}Gd. Initially, all the separations (until LaF_3 precipitation) were repeated three times with non-irradiated Pb samples by adding Ln tracers (Fig. 1) to determine the overall chemical yield of lanthanides.

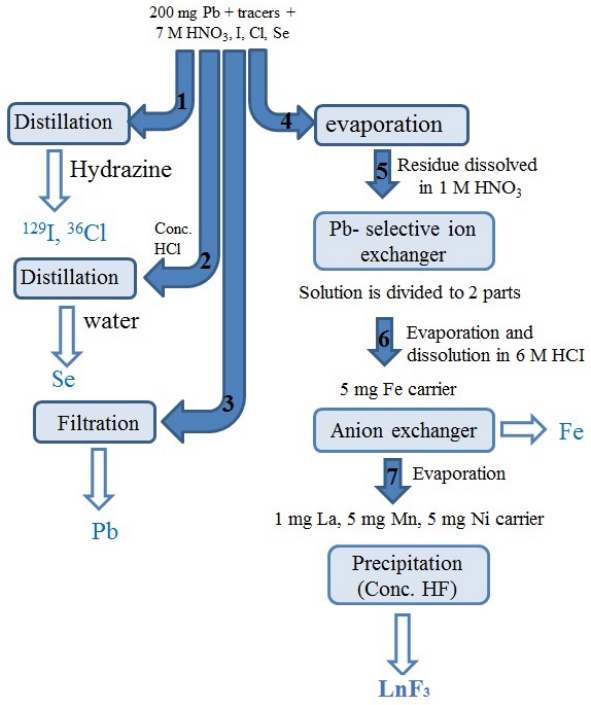

Fig. 1: Chemical separation scheme for the long-lived radionuclides from p-irradiated lead samples.

75% lanthanides yield was obtained until LaF_3 precipitation.

The LaF_3 fractions were dissolved in 0.5 M H_3BO_3 and conc. HNO_3. Lanthanide separation was performed applying gradient elution technique at pH 4.6 thanks to the different distribution coefficients of lanthanides in the DOWEX 50X8 cation exchanger – α-hydroxy-isobutyric acid (α-HIB) separation system. In order to remove the complexing agent from the Ln fractions, commercially available Ln-specific ion exchange resin (TRISKEM) was used with 6 M HNO_3 as eluent in a following purification step.

RESULTS AND DISCUSSION

Lanthanide fractions from 11 p-irradiated Pb samples were processed. An example of the separation profile is presented in Fig. 2.

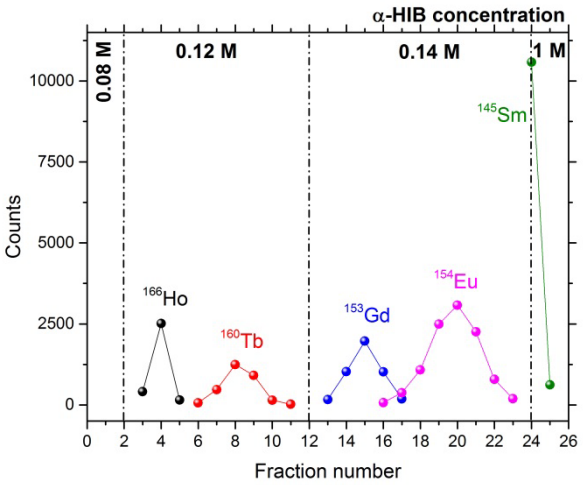

Fig. 2: Separation profile of lanthanides in the DOWEX50x8 cation exchanger – α-HIB separation system with gradient elution technique.

In a next step, molecular plating will be used to prepare thin layers of the Ln fractions for alpha-counting to determine the cross sections for the production of ^{154}Dy, ^{146}Sm and ^{148}Gd/^{150}Gd in Pb.

[1] D. Schumann, R. Michel, G. Korschinek, K. Knie, J.-C. David, Nucl. Instruments Methods Phys. Res. Sect. A, **562**, 1057 (2006).
[2] D. Schumann and J.-Ch. David, Nucl. Data Sheets, **119**, 288-291, (2014).

γ- AND α-SPECTROMETRY OF PROTON-IRRADIATED W AND Ta TARGETS

Z. Talip, R. Dressler, A. Vögele, D. Schumann (PSI), E. Strub (Univ. Köln), R. Michel (IRS)

INTRODUCTION

Solid tungsten, cladded by a tantalum hull, is considered as possible target design in the future European Spallation Source (ESS). The knowledge of the residue nuclide production during high-power proton irradiation of these materials is of vital importance for the safe operation of the facility as well as for a state-of-the-art waste and disposal management.

EXPERIMENTAL

Proton irradiations of Ta and W targets, 11 each, were performed with a special stacked foil technique between 1993-96 at the Laboratoire National Saturne (LNS), Saclay, (for details see [1]). Proton fluences between 10^{14} and 10^{16} were applied. Extended γ-spectroscopic examinations of the short-lived components have been reported in [2].

Our present γ-spectrometric measurements of long-lived nuclides were performed using high-purity germanium (HPGe) detectors and data acquisition times between 1 and 10 days. The efficiency calibration of the system was performed using a ^{152}Eu point source in 10 cm distance. GENIE2000 (Canberra) was used to evaluate the γ-spectra obtained. Each spectrum was analyzed interactively, making sure to get maximum information out of each sample. Background subtraction was performed only for the determination of ^{60}Co. First, non-destructive α-spectrometry measurements have been performed using the α-analyst and GENIE software from Canberra.

RESULTS AND DISCUSSION

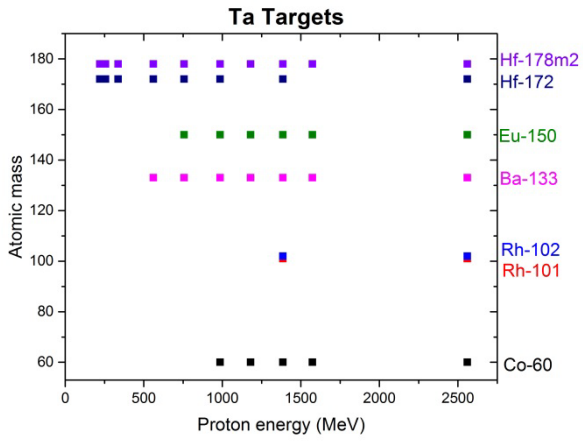

Fig. 1: Residual γ-ray emitting radionuclides in Ta targets as a function of proton energy.

Fig. 1 shows an overview on the identified radionuclides in dependence on the proton energy in the Ta targets. Similar results were obtained for the W targets. The cross sections for the production of these radionuclides were calculated. Data for ^{133}Ba and ^{150}Eu in W and Ta targets irradiated by 560-1386 MeV protons are presented in Table 1 as examples.

Tab. 1: Cross sections for the production of ^{133}Ba and ^{150}Eu in Ta and W targets.

Proton energy, MeV	Cross section (mbarn)			
	Ta		W	
	^{133}Ba	^{150}Eu	^{133}Ba	^{150}Eu
1386	55.1 ± 2.0	6.7 ± 0.4	75.2 ± 2.8	12.6 ± 0.7
117	32.2 ± 1.3	5.2 ± 0.5	33.9 ± 1.4	4.2 ± 0.5
986	22.5 ± 0.9	4.4 ± 0.3	23.1 ± 0.9	4.8 ± 0.4
755	5.7 ± 0.3	2.6 ± 0.3	6.3 ± 0.3	2.2 ± 0.3
560	0.8 ± 0.1		0.9 ± 0.1	

α-spectrometric measurements (without prior chemical separation) of a Ta sample irradiated with proton energies higher than 500 MeV clearly shows the presence of ^{148}Gd (Fig. 2). This result is in good agreement with the findings of *Kelley* and *Titarenko* [3,4]. However, for accurate cross section measurements with low uncertainties, prior chemical isolation of the lanthanide group, followed by fractionation of single elements, will be mandatory.

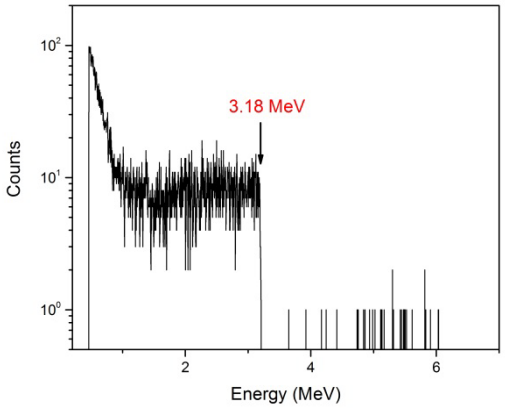

Fig. 2: α spectrum of 2560 MeV p-irradiated Ta (counting time 22 h).

ACKNOWLEDGEMENT

This project is funded by the Swiss National Science Foundation (SNF grant no 5201.24003.808).

[1] M. Gloris et al., NIM A **463**, 593 (2001).
[2] M. Gloris, PhD thesis, Hannover (1998).
[3] K. C. Kelley et al., Nucl. Phys. A **760**, 225 (2005).
[4] Y. E. Titarenko et al., Physics of Atomic Nuclei, **74**, 551 (2011).

RADIOCHEMICAL SEPARATION OF Nb FROM Mo – TOWARDS THE PRODUCTION OF A ^{91}Nb-TARGET

D. Schumann, R. Dressler (PSI), B. Thomas, K. Sonnabend, R. Reifarth (Goethe University), U. Giesen (PTB)

MOTIVATION

The cross section of the reaction ^{91}Nb(p,γ)^{92}Mo at 2 MeV proton energy - the astrophysical relevant energy region for *p*-process nucleosynthesis - is of special interest to answer questions about the production of the most abundant *p* nucleus ^{92}Mo. The high proton current delivered by the HF-linear-accelerator FRANZ, which is currently being built at Goethe University Frankfurt, Germany, enables the execution of such measurements in standard kinematics.

ISOTOPE PRODUCTION

To produce a sufficient number of ^{91}Nb atoms, an enriched ^{92}Mo target has been activated with protons of $E_p \approx 19$ MeV at PTB using the ^{92}Mo(p,2p)^{91}Nb reaction.

Fig. 1: ^{92}Mo powder was melted, rolled, and afterwards pressed onto an Al backing. Photo of the target before (left) and after (right) irradiation.

RADIOCHEMICAL SEPARATION

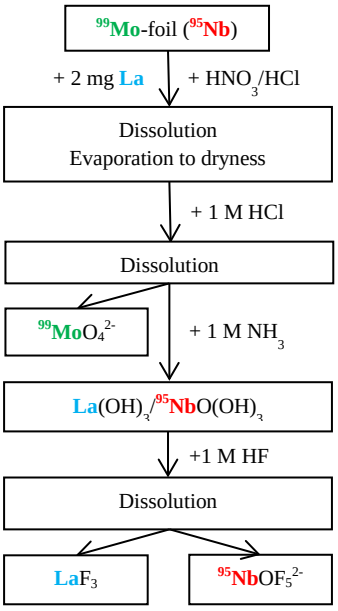

Fig. 2: radiochemical separation procedure

For the development of the chemical separation system, model studies with the easy-to-measure γ-emitters ^{95}Nb and ^{99}Mo – produced by neutron activation of ^{nat}Zr (as ZrO_2) and metallic ^{nat}Mo, respectively - were performed. ^{95}Zr ($T_{1/2}$=64d) decays into ^{95}Nb ($T_{1/2}$=35d), which can be obtained in carrier-free form after dissolving the Zr in HNO_3/HCl, evaporation to dryness and following liquid-liquid extraction from 5M HCl/4M HF solution into methyl isobutyl ketone according to [1]. As a non-isotopic carrier, 2 mg of La (in form of $La(NO_3)_3$) were added. The irradiated Mo (641 mg) has been dissolved in HNO_3/HCl, the solution was spiked with ^{95}Nb, evaporated to dryness and the residue re-dissolved in 1M HCl. Concentrated NH_3 was added to precipitate ^{95}Nb together with lanthanum as hydroxides, whereas ^{99}Mo stayed in the solution. ^{95}Nb can then be dissolved in 1 M HF, keeping the La carrier as LaF_3 in the precipitate. A flow scheme of the chemical separation procedure is shown in Figure 2.

RESULTS

In Figure 3, the results of the model separation procedure are shown. A depletion factor of $>10^3$ could be achieved for Mo, the recovery of Nb was 92%.

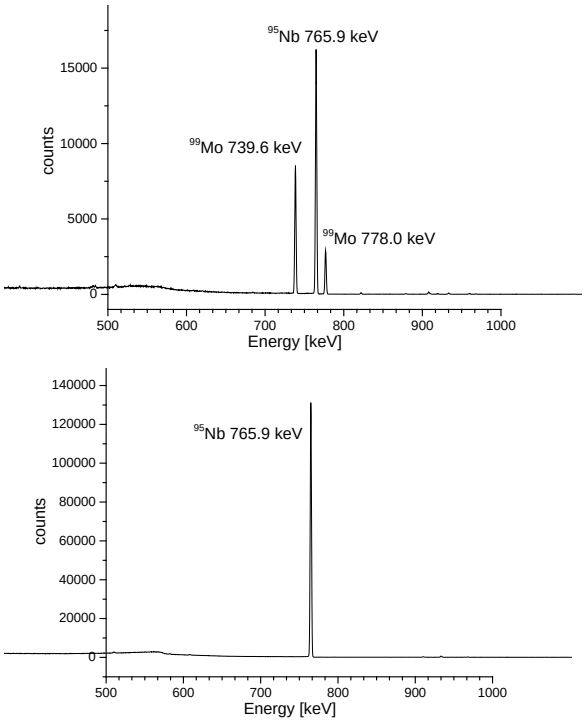

Fig. 3: top: the dissolved Mo containing ^{99}Mo and ^{95}Nb; bottom: the Nb fraction after separation.

ACKNOWLEDGEMENT

This work is supported by Deutsche Forschungsgemeinschaft (DFG, contract number SO907/2-1).

[1] D. Schumann, R. Dressler, RCA 2015, DOI 10.1515/ract-2015-2398.

RADIOCHEMICAL DETERMINATION OF ^{129}I AND ^{36}Cl IN THE MEGAPIE TARGET

B. Hammer-Rotzler (PSI & Uni Bern), J. Neuhausen (PSI), C. Vockenhuber (ETHZ), V. Boutellier (PSI/AHL), M. Wohlmuther (PSI/ABK), A. Türler (PSI & Uni Bern), D. Schumann (PSI)

After the successful operation of the liquid lead bismuth (LBE) spallation target MEGAPIE in 2006 at PSI, an extended Post Irradiation Examination (PIE) program was launched. In this context, we reported earlier on the determination of Po isotopes [1] as well as of γ-emitters [2] and rare earth elements [3] in the irradiated target material. From a safety perspective, special attention has to be paid to the behavior of radioactive isotopes of volatile elements in such systems. Therefore, we extended our studies to the halogen nuclides ^{129}I and ^{36}Cl.

To assess the distribution of these nuclides within the target system, four kinds of samples from different locations within the MEGAPIE target were analyzed: i) samples from bulk LBE, ii) samples from the LBE-steel interface, iii) samples from the contact surface between LBE and the cover gas and iv) samples from Pd and Ag absorber foils installed in the cover gas to trap volatile elements released from the LBE. For a detailed description of the sampling procedure see [3, 4]. The LBE and Pd samples were dissolved in HNO_3 together with iodine and chlorine carrier. The solutions were then heated to 100°C under N_2 atmosphere to distil the halogens into an aqueous hydrazine solution. After acidification, the halogens were precipitated by adding $AgNO_3$. Cl was separated from the precipitate by re-dissolving in 25% NH_3 and subsequent re-precipitation. Both precipitates were washed and dried carefully. The steel samples were treated in a similar way to leach the adherent halogens. For the Ag samples, the distillation was omitted, and the Ag-halogenides were directly precipitated with the Ag from the absorber foil. Blank samples were prepared employing identical procedures as described above, using similar amounts of inactive LBE from the same batch of LBE used for the MEGAPIE experiment.

^{129}I/I and ^{36}Cl/Cl ratios were determined at the Laboratory of Ion Beam Physics at ETH Zurich, using the 0.6MV TANDY AMS and the 6MV EN TANDEM accelerator, respectively. For details of the measurement techniques and the facilities see [4, 5].

The individual contributions of the four different sample types to the total radioactivity were estimated based on the sample dimensions. More details on this rather complex evaluation can be found in [4]. The results of this estimation are summarized for ^{129}I in Tab. 1 and compared to predictions on the radionuclide production during the MEGAPIE irradiation [6]. We observe a reasonably good agreement of the analytically determined total amount with the predictions (within a factor of ≈ 2). The major part of ^{129}I is found to be deposited on the steel walls of the liquid metal container. Bulk samples contain only a minor fraction of the total ^{129}I detected in the target. A similar trend is also observed for ^{36}Cl, with the situation being less clear because of the large scatter of the data. On the free surface of the LBE that was in contact with the cover gas during operation of the target, a strong enrichment of the two halogen nuclides compared to the bulk is observed. However, the contribution of this fraction to the total radioactivity is small because the area of this LBE cover gas interface is much smaller than the target inner surface and therefore negligible. A small fraction of ^{129}I and ^{36}Cl was found on the noble metal absorber foils in the expansion tank. This finding does not point to a substantial release of the halogens to the cover gas. However, the fraction of the total ^{129}I amount on the absorber (0.01%) is much higher than the fraction estimated to be present in the expansion tank under equilibrium conditions (5×10^{-14}%) [7], indicating a certain affinity of the noble metal absorber foils to halogens. The tendency of the halogens to separate from the LBE and accumulate on surfaces is probably related to their incorporation into surface layers e.g. in form of oxy-halides.

Tab. 1: Summary of ^{129}I activity distribution over the different types of samples

	estimated total activity [Bq]	predicted activity [Bq]	% of predicted amount	% of estimated total activity
bulk	295±18	8560	3.4±0.2	7
LBE/cover gas interface	1.2 ± 0.1		$(14\pm1)\times10^{-3}$	0.03
LBE/steel interface	$(3.7\pm2)\times10^{3}$		43±23	93
absorber	$(38\pm2)\times10^{-2}$		$(44\pm2)\times10^{-4}$	0.01
Sum	3997±2018		47±24	

ACKNOWLEDGEMENT

Funded by the projects ANDES, SEARCH and GETMAT in the frame of EURATOM FP7

[1] B. Hammer et al., Nuclear Data Sheets, **119**, 280 (2014).
[2] B. Hammer et al., J. Nucl. Mater., **450**, 78 (2013).
[3] B. Hammer et al., Anal. Chem. **87**, 5656 (2015).
[4] B. Hammer-Rotzler et al., Radiochim. Acta **103**, 745 (2015).
[5] M. Christl et al., Nucl. Instrum. Methods Phys. Res. Sect. B, **294**, 29 (2013).
[6] L. Zanini et al., PSI-Report Nr. 08-04, Paul Scherrer Inst., Villigen, Switzlerland (2008).
[7] J. Neuhausen, PSI - TM-18-05-02 (2005).

EVAPORATION OF IODINE FROM LIQUID LEAD BISMUTH EUTECTIC

E. A. Maugeri, J. Neuhausen, A. Vögele, D. Schumann (PSI)

Liquid lead bismuth eutectic (LBE) is proposed as coolant and spallation target material in novel nuclear reactors such as Accelerator Driven Systems (ADS). In such reactors, fission iodine may be transferred to the coolant in case of fuel pin failures. The subsequent possible evaporation of iodine from the LBE is a safety issue. Therefore, the study of this phenomenon is mandatory for the licensing of such facilities. So far, only one study exists on this topic [1]. As a consequence, within the EU-FP7 project SEARCH this research was continued.

Iodine doped-LBE samples were prepared by melting LBE together with about 1 mass-% of PbTe in a fused silica tube under He atmosphere at 830 °C for 1h. After mechanical removal of solid scales remaining on the top surface, the samples were irradiated with neutrons in the NAA facility at SINQ to produce iodine. The iodine isotope used for γ-spectrometric analysis was ^{131}I, produced via ^{130}Te (n,γ) ^{131}Te (β^-) ^{131}I. Samples were analyzed using a standard γ-spectrometry setup employing an HPGe-detector controlled by Canberra's Genie2K® software package. Homogeneous distribution of the iodine in the LBE was confirmed by cutting slices (thickness 60μm) from an irradiated sample with a rotary microtome (Leica, RM2235) after irradiation and determining their ^{131}I activity.

The evaporation of iodine was studied by the transpiration method, using a setup similar to that described in [2], but modified to achieve higher purity of the carrier gas by employing a closed loop gas cycle equipped with SICAPENT drying column and Ta-getter. For an evaporation experiment, the activity of the iodine doped LBE sample was measured before the experiment. Then, the sample was inserted in a fused silica tube and heated to the desired temperature for 1h. To determine the released amount of iodine, initially it was tried to determine the activity remaining in the sample simply by measuring it after the experiment in a similar geometry used for determining the initial activity of the LBE. This should allow assessing the released amount from the difference of the two measurements. However, it turned out that the ^{131}I remaining in the sample tends to accumulate on its top surface, altering the attenuation of the emitted γ-radiation. It was also tried to directly determine the total activity released from the sample. For this purpose, the ^{131}I deposited in the fused silica tube was collected by rinsing with acidic (HNO_3) and alkaline (NaOH) aqueous solutions and determined by γ-spectrometry. Additionally, the activity deposited in a charcoal filter located at the exhaust of the transpiration tube to capture volatile iodine species was measured. It turned out that the sum of the activities found remaining in the LBE as well as in the tube and the charcoal was almost always less than the amount of iodine present in the sample before the experiment, indicating a loss of iodine in the analysis procedure. Most probably, very volatile iodine species are formed during the rinsing, whose partial loss could not be avoided. As a consequence, for later experiments, a fraction of the initial sample was dissolved in 7M HNO_3 before the experiment, and the complete sample was dissolved after the experiment. The total activity of ^{131}I in the initial sample and that remaining in the LBE after the experiment was then determined from aliquots of the HNO_3 solutions. Fig. 1 shows a comparison of the temperature dependence of the fractional iodine release - determined from the initial and final ^{131}I content in the present experiments- to results of the literature study [1], where in contrast to the present study the iodine isotopes were generated by dissolving small amounts of U-metal in the LBE and subsequent n-irradiation. In the present study, the onset of iodine release occurs at significantly lower temperature, and the release of iodine is practically complete at high temperature, while in [1] a fraction of about 15% iodine remains in the LBE even at the highest temperatures. Both differences might be explained by the presence of a U-oxide surface layer that was detected on the samples in [1]: The iodine remaining at high temperature in [1] is probably due to a fraction of iodine strongly bound in the oxide layer, while also the generally lower release observed in [1] could be caused by a retardation of iodine transport through this layer. These phenomena remain to be studied in more detail in order to obtain a reliable physico-chemical description of the LBE-I system with thermodynamic and kinetic data sufficient for licensing of ADS and similar facilities.

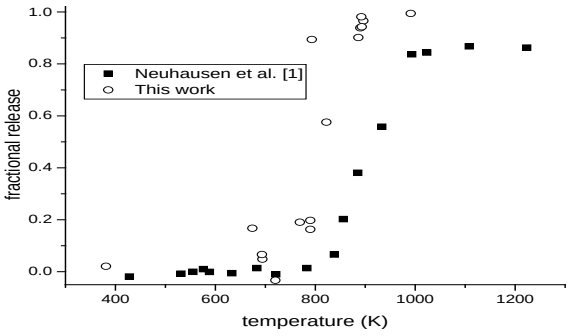

Fig. 1: Fractional release of iodine from liquid LBE as a function of temperature.

ACKNOWLEDGEMENT

This work was funded by the project SEARCH (Contract No. 295736, EURATOM FP7).

[1] J. Neuhausen et al., Radiochim. Acta, **94**, 239 (2006).

[2] M. Rizzi et al., J. Nucl. Mater. **450**, 304 (2014).

ADSORPTION OF POLONIUM SPECIES ON STAINLESS STEEL IN VARIOUS GASEOUS ATMOSPHERES

B. Gonzalez Prieto (SCK CEN), J. Neuhausen, R. Eichler, A. Vögele, D. Piguet, D. Schumann (PSI)

Polonium is amongst the most hazardous radionuclides formed as a result of neutron capture/activation and spallation reactions in lead-bismuth eutectic (LBE)-based accelerator driven systems (ADS). Aside from fundamental understanding of the evaporation of Po from LBE in conditions relevant to these nuclear installations, research on effective filter materials to capture evaporating Po species is required. The adsorption of Po on different surfaces has been studied [1, 2]. However, there is a lack of knowledge on the interaction between Po or Po-containing species and ADS construction materials, such as stainless steel (SS). In this work these interactions were investigated under various gaseous atmospheres using thermochromatography. ^{206}Po-doped Bi and LBE foils were obtained by irradiation of inactive foils of these materials with intense proton beams of up to 3µA. The proton energy was 36 MeV facilitating the nuclear reaction ^{209}Bi(p,4n)^{206}Po. ^{206}Po was separated from the less volatile metal matrices by evaporation at 900-1100 °C under a He or H_2 flow and deposited on an Au foil placed at lower temperature (≈ 330-420 °C). Thus, more than 97 % of the Po originally present on the foils was collected together with small quantities of Bi (less than 1 % of the initial amount), monitored using γ-spectroscopy of ^{206}Bi. The obtained Au foil was then used as Po source in the thermochromatography experiments. The thermochromatography setup consisted of a SS316L column loaded into an Inconel tube placed inside a tubular furnace with a negative temperature gradient ranging from 950 °C to room temperature. The Au foils with the ^{206}Po were loaded into the SS316L column and heated to 950 °C under dry and moist He, H_2, and O_2 gas flows of 25ml/min for two hours. Three experiments were performed in 'dry' (with < 150 ppm of H_2O) He, H_2, and O_2 respectively. The shape of the thermochromatograms (red bars in Fig. 1) indicate the deposition of a single Po species in the three investigated gases. However, the difference in the adsorption enthalpies (ΔH_{ads}), calculated by a Monte Carlo code developed for gas thermochromatography [4], suggest the deposition of different Po species. Despite the good separation of Po from the metal matrices, BiPo, and/or PbPo when using Po-doped LBE foils, might still be formed when Po evaporates from the Au foil. Under inert gases (He) these species are likely to deposit on the SS316L column (ΔH_{ads} = -154 kJ/mol). On the other hand, under H_2, these molecules might react with the carrier gas leading to their disintegration and final deposition as elemental Po with ΔH_{ads} = -177 kJ/mol. In O_2 the formation of Po oxides, most probably PoO_2, is likely as a result of the reaction between Po and the carrier gas. The ΔH_{ads} of this species is -239 kJ/mol.

In moist atmospheres, similarly to previous thermochromatography and transpiration studies in fused silica tubes [1, 3], the experiments revealed the formation of more volatile Po species (blue bars in Fig. 1). Po hydroxides are the most plausible candidates formed in moist He and H_2, while Po-oxyhydroxides might be formed under moist O_2. While in fused silica tubes the volatile species were transported down to room temperature [1], in SS316L they are deposited at higher temperature. This is important for LBE-based nuclear installations, since it proves the effectiveness of SS316L as filter material for various Po species, including the most volatile Po molecules formed at more humid conditions.

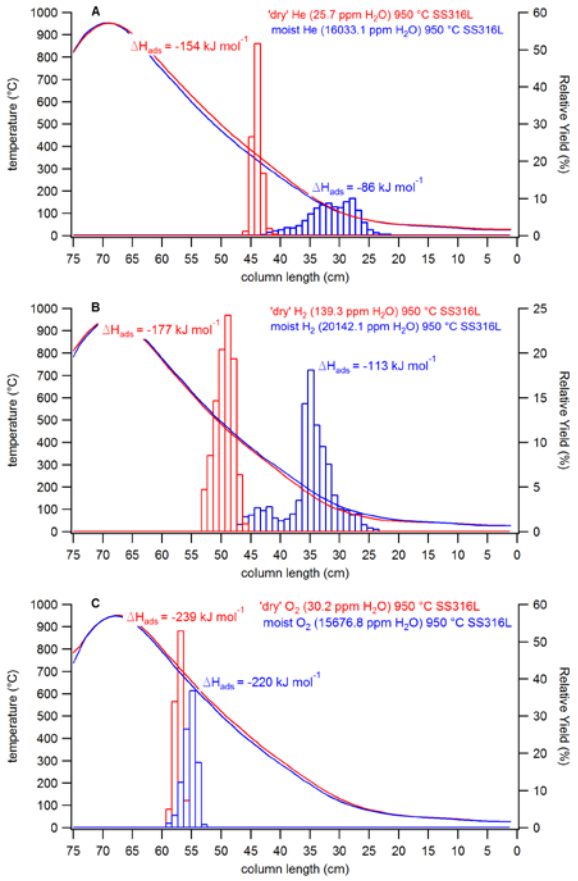

Fig. 1: Thermochromatograms of ^{206}Po in a SS316L column under 'dry' (*red bars*) and moist (*blue bars*) (A) He, (B) H_2 and (C) O_2. The corresponding temperature gradients are shown as color-coded curves. The used carrier gas and its moisture content in each experiment are indicated.

ACKNOWLEDGEMENT

This work was funded by MYRTE (HORIZON2020).

[1] E.A. Maugeri, et al., J. Nucl. Mater., **450**, 292 (2014).

[2] E.A. Maugeri, et al., Ann Rep., Lab. of Radio & Environ. Chem., Univ. Bern & PSI, p. 37 (2014).

[3] B. Gonzalez Prieto, PhD thesis, KU Leuven, Belgium (2015).

[4] I. Zvara, Radiochim. Acta, **38**, 95 (1985).

INTERACTION OF POLONIUM RELEASED FROM LEAD-BISMUTH EUTECTIC WITH STAINLESS STEEL AND FUSED SILICA IN DRY GASEOUS ATMOSPHERES

B. Gonzalez Prieto (SCK CEN), J. Neuhausen, R. Eichler, A. Vögele, D. Piguet, D. Schumann (PSI)

The high radiotoxicity of polonium and its propensity to evaporate makes it one of the most hazardous radionuclides generated in accelerator driven systems (ADS) where lead-bismuth eutectic (LBE) is used as coolant and/or spallation target. Consequently, in the ADS project MYRRHA several research groups have studied the evaporation and adsorption behavior of Po [1-5]. In this framework the adsorption of Po has been investigated on various noble metals and fused silica with Po sources other than doped LBE samples by thermochromatography. In this work we investigated the interaction of Po containing species, evaporating from Po-doped LBE samples, and fused silica under 'dry' carrier gases. Additionally, the interaction of Po species released under the same conditions with the construction material of MYRRHA, *i.e.* stainless steel (SS316L), was also studied.

^{206}Po-doped LBE samples were prepared by melting together pieces of ^{206}Po-doped Bi disks, obtained by irradiation with a 36 MeV proton beam and inactive Pb at 600 °C under a H_2 flow. The resulting ^{206}Po-doped LBE samples were used as Po source in thermochromatography experiments. The thermochromatography setup consists of either a SS316L or a fused silica column loaded in an Inconel tube placed inside tubular furnace with a negative temperature gradient ranging from 700 °C to room temperature. The ^{206}Po-doped LBE samples were loaded in the columns and heated to 700 °C under a 25 mL/min flow of 'dry' (<110 ppm of moisture measured by a dew-point transmitter (Michell Easidew)) He, H_2, and O_2 for various experimental durations. The adsorption enthalpies (ΔH_{ads}) of the deposited Po species were calculated using a Monte Carlo code developed for gas thermochromatography [6].

Three experiments were conducted for both column materials (SS316L and fused silica), one for each investigated carrier gas. The more negative values of ΔH_{ads} observed in SS316L experiments (red bars in Fig. 1) revealed a stronger interaction of Po with SS316L than with fused silica (blue bars in Fig. 1). Generally, sharper deposition patterns were obtained for SS316L when compared to those in fused silica, indicating different deposition mechanisms. In fused silica under 'dry' He, even more than one peak and a transport to low temperatures was observed (Fig. 1A), indicating the additional formation of more volatile species. The microscopic interpretation of these phenomena is not clear so far, but - importantly for LBE-based ADS - in SS316L interaction of the Po species with the surface was considerably stronger in all three gases with no formation of very volatile Po species. Regarding the influence of the nature of the carrier gases, it was clearly demonstrated that different Po species were formed in the various atmospheres He, H_2 and O_2. Owing to the use of LBE as Po source, Po, PbPo and BiPo are the most likely species released from the LBE sample. PbPo and/or BiPo are likely to be stable and transported in He. However, in H_2 these molecules might react with the carrier gas forming transient hydrides which later disintegrate and finally deposit as elemental Po. In O_2, Po directly reacts with the carrier gas forming oxides which deposit at higher temperatures.

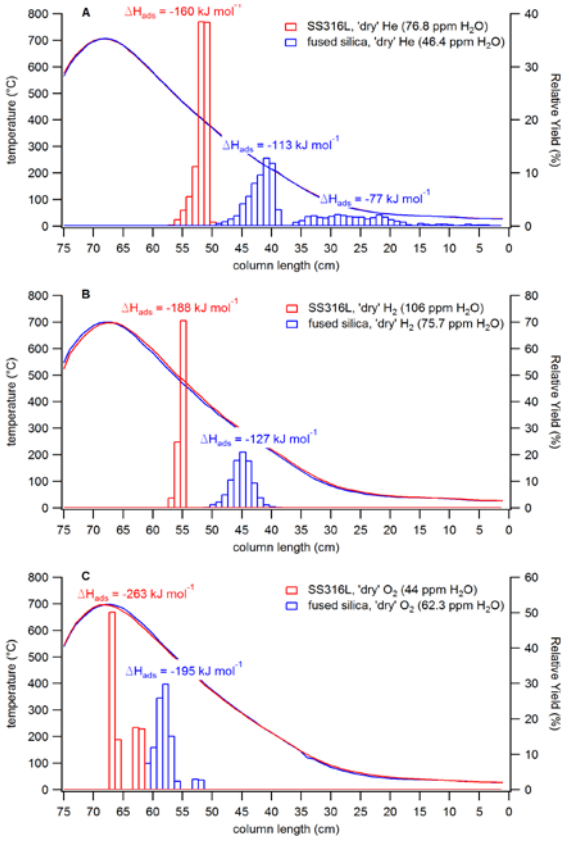

Fig. 1: Thermochromatograms of ^{206}Po evaporated from LBE heated to 700 °C in SS316L (*red bars)* and fused silica (*blue bars)* columns under 'dry' (A) He, (B) H_2 and (C) O_2. The corresponding temperature gradients are shown as color-coded curves. The column material, the carrier gases, and their moisture content in each experiment are indicated.

ACKNOWLEDGEMENT
This work was funded by MYRTE (HORIZON2020).

[1] B. Gonzalez Prieto, et al., J. Nucl. Mater., **450**, 299 (2014).
[2] M. Rizzi, et al., J. Nucl. Mater., **450**, 304 (2014).
[3] B. Gonzalez Prieto, et al., Radiochim. Acta., **102(12)**, 1083 (2015).
[4] B. Gonzalez Prieto, et al., J. Radioanal. Nucl. Chem., **302**, 195 (2015).
[5] E.A. Maugeri, et al., J. Nucl. Mater., **450**, 292 (2014).
[6] I. Zvara, Radiochim. Acta, **38**, 95 (1985).

INTERACTION OF POLONIUM RELEASED FROM LEAD-BISMUTH EUTECTIC WITH STAINLESS STEEL AND FUSED SILICA IN MOIST GASEOUS ATMOSPHERES

B. Gonzalez Prieto (SCK CEN), J. Neuhausen, R. Eichler, A. Vögele, D. Piguet, D. Schumann (PSI)

A major safety concern arises from the generation of the highly radiotoxic and relatively volatile polonium in lead-bismuth eutectic (LBE)-based accelerator driven systems (ADS). Recently, it was found in research for the ADS project MYRRHA that the release and volatility of Po were largely enhanced in humid atmospheres [1, 2]. Since humid conditions prevail in some ADS accident scenarios, e.g. steam generator tube rupture, the understanding of Po behavior under these conditions becomes one of the most relevant requirements for the licensing of such nuclear installations. To gain insight into the adsorption behavior of the more volatile Po species released from LBE in humid atmospheres on different surfaces, we investigated their interaction with fused silica and the construction material of MYRRHA, stainless steel (SS316L), in thermochromatography experiments.

^{206}Po-doped LBE samples were obtained either by direct irradiation of LBE foils with a 36 MeV proton beam or by melting Po-doped Bi disks obtained in similar proton irradiations together with inactive Pb pieces. The same thermochromatography setup and experimental conditions as in the preceding report were used, except for the use of moist instead of 'dry' gases, obtained by bubbling the carrier gases through a water reservoir at room temperature. The moisture content was determined using a dew-point transmitter (Michell Easidew). Monte Carlo simulations were performed to determine the adsorption enthalpies (ΔH_{ads}) of the deposited Po species.

Three experiments were conducted for both column materials (SS316L and fused silica), one for each investigated moist carrier gas. Compared to the observations found under 'dry' conditions (see Fig. 1 of preceding report) significantly weaker adsorption interaction was observed in both column materials, indicating an increased volatility of Po in humid atmospheres (Fig. 1), indicating the formation of more volatile Po species. In the moist experiments, the peaks were also broader compared to 'dry' conditions. This effect is most pronounced in moist He (red bars in Fig. 1A). Comparing the interaction between Po and the two column materials under humid conditions, similarly to the 'dry' experiments for the main deposition peaks generally more negative ΔH_{ads} were found in SS316L (red bars in Fig. 1). Moreover, even if more volatile Po species are formed, as indicated by the complex deposition pattern especially in moist He, the transport of Po down to room temperature was completely suppressed in SS316L columns. This is an important result for LBE-based ADS, since it indicates that in presence of SS316L either the formation of the most volatile Po species is inhibited or they interact more strongly with steel compared to fused silica [1]. In fused silica, in moist He (blue bars Fig. 1A) part of the released Po was transported even down to a Ag foil placed at the exit of the column acting as a room temperature catcher for Po species.

The fact that the very volatile Po species depositing at room temperature in fused silica columns occurs in moist He but not in moist H_2 indicates that this species contains Po in an oxidized rather than a reduced state. In H_2-containing gas these volatile molecules are reduced to less volatile species which deposit at higher temperatures. The most plausible candidates for such species are Po hydroxides. In moist O_2, Po oxides were converted into a slightly more volatile species, most likely oxyhydroxides.

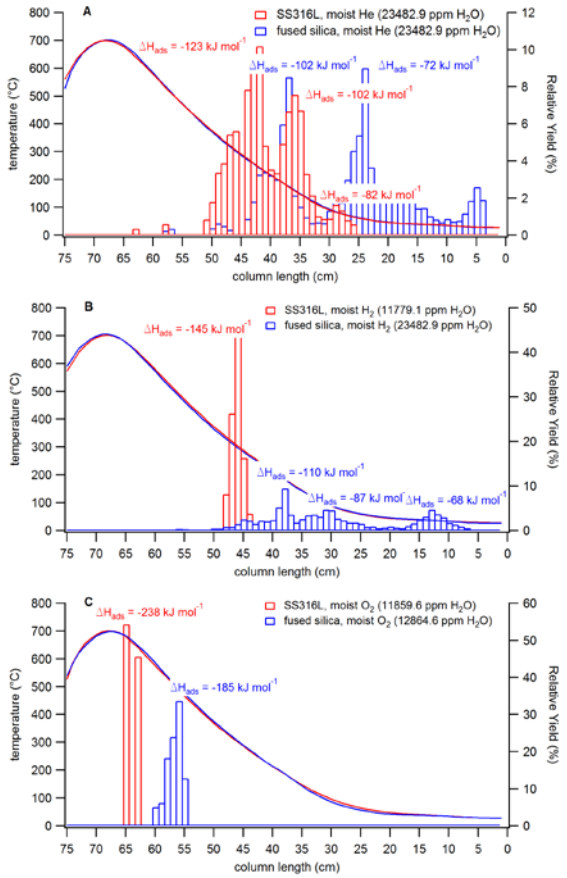

Fig. 1: Thermochromatograms of ^{206}Po evaporated from LBE heated to 700 °C in SS316L (*red bars)* and fused silica (*blue bars)* columns under moist (A) He, (B) H_2, and (C) O_2. The corresponding temperature gradients are shown as color-coded curves. The column material, the carrier gases, and their moisture content are indicated for each experiment.

ACKNOWLEDGEMENT
This work was funded by MYRTE (HORIZON2020).

[1] E.A. Maugeri, et al., J. Nucl. Mater., **450**, 292 (2014).
[2] B. Gonzalez Prieto, PhD thesis, KU Leuven, Belgium (2015).

^{43}Sc PRODUCTION DEVELOPMENT BY CYCLOTRON IRRADIATION OF ^{46}Ti

K. Domnanich (Univ. Bern & PSI), C. Müller, A. Sommerhalder (PSI/CRS),
A. Türler (Univ. Bern & PSI), N. van der Meulen (PSI)

INTRODUCTION

The positron-emitter ^{43}Sc is considered to be an attractive PET radionuclidic alternative to ^{44}Sc. While its half-life and positron energy ($t_{1/2}$ = 3.89 h, $E_{\beta+}$= 476 keV, I= 88%, E_{γ}= 372 keV, I= 23%) are similar to ^{44}Sc ($t_{1/2}$ = 3.97 h, $E_{\beta+}$ 1475.4 keV, I= 94.34%, E_{γ}= 1157 keV, I= 100%) the absence of accompanying high-energy γ-rays, is thought to be advantageous regarding the dose burden to patients. To date, several different production routes for ^{43}Sc have been described in the literature: ^{42}Ca(d,n)^{43}Sc, ^{43}Ca(p,n)^{43}Sc and ^{46}Ti(p,α)^{43}Sc. However, production of ^{43}Sc in sufficient quantities and radionuclidic purity encompasses several challenges, a low cross section for proton induced reactions, co-production of ^{44}Sc and scarce availability of deuteron providing cyclotrons [1-3]. This work, however, focused on the investigation of the ^{46}Ti(p,α)^{43}Sc production pathway.

EXPERIMENTAL

Target Preparation and Irradiation: ^{46}Ti targets were prepared by placing 10-30 mg reduced ^{46}Ti on top of ~150 mg graphite, pressed and encapsulated in aluminum. The irradiation was performed with 15 ±1.9 MeV protons at varying beam currents (30-50 μA) for 1-4 hours. Since enriched Ti is only available in insoluble oxide form, the reduction of 97% $^{46}TiO_2$ to ^{46}Ti was performed at GSI, Darmstadt [4].

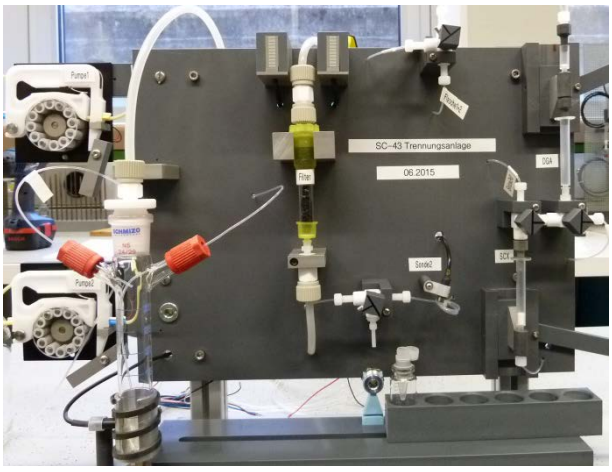

Fig. 1: ^{43}Sc/^{46}Ti separation setup designed for bench experiments

Chemical Separation: The separation was performed using the ^{43}Sc/^{46}Ti bench separation setup shown in Figure 1. The irradiated ^{46}Ti targets were dissolved in ~5mL boiling 6 M HCl within 15-20 min. The molarity of the HCl was diluted to 4 M and then passed through a preconditioned DGA extraction chromatographic resin column. Under these conditions ^{43}Sc(III) was sorbed, meanwhile Ti(III) was not retained. Additional 4M HCl were applied to ensure a complete removal of Ti(III). ^{43}Sc(III) was eluted with 0.1M HCl and then sorbed on a second column, consisting of SCX cation exchange resin. The elution of ^{43}Sc was performed with 700 μL 4.8M NaCl/ 0.13M HCl eluent.

RESULTS AND DISCUSSION

Using the abovementioned irradiation conditions, yields of 95-180 MBq ^{43}Sc at end of bombardment were produced per target. The radionuclidic purity of the obtained ^{43}Sc-eluate was 98.3 ±0.2 %, with 1.5 % ^{44g}Sc as the main impurity. The longer-lived impurities, namely, ^{44m}Sc, ^{46}Sc, ^{47}Sc, and ^{48}Sc were less than 0.04 %. However, the co-produced Y- isotopes ^{86}Y, ^{87g}Y, ^{87m}Y and ^{88}Y could not be separated because of their close similarity to Sc, and were present at 0.28 % in the final eluate. The isotopic Y-distribution suggests a Sr-impurity as possible source, originating from the preceding reduction of the target material. The optimization of the TiO_2 reduction process to obtain enriched ^{46}Ti target material of higher purity is currently the topic of investigation. The chemical separation is based on an easy and robust method, enabling the elution of ~90% of the overall ^{43}Sc-activity in a small volume of 700 μL NaCl/ HCl solution.

The ^{43}Sc-activity produced by proton irradiation of two different target materials, $^{43}CaCO_3$ and ^{46}Ti, was used to perform a PET phantom study at the ETH Zürich. The obtained PET-phantom images, shown in Figure 2, corroborate the increased resolution imaging with ^{43}Sc in comparison to ^{44}Sc.

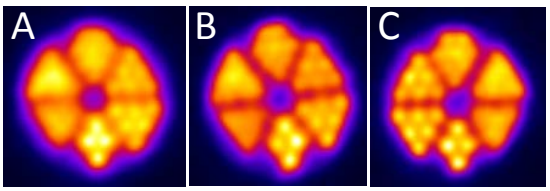

Fig. 2: PET phantom images of ^{44}Sc (A), ^{43}Sc produced from ^{43}Ca and containing 76% ^{43}Sc and 24% ^{44}Sc (B) and ^{43}Sc produced from ^{46}Ti, containing 98% ^{43}Sc and 1.5% ^{44}Sc.

ACKNOWLEDGEMENT

This project is funded by the Swiss National Science Foundation (SNF grant no CR23I2_156852).

[1] R. Walczak et al., EJNMMI Physics, 2:33 (2015).
[2] P. Kopecky et al., Appl. Radiat. Isotope, **44** (1993).
[3] EXFOR- database, version from 06.01.2016.
[4] B. Lommel et al., J Radioanal Nucl Chem, **299** (2013).

^{44}Sc LABELLING OF DOTA- AND NODAGA- FUNCTIONALISED PEPTIDES: PRECLINICAL IN VITRO AND IN VIVO INVESTIGATIONS

K. Domnanich (Univ. Bern & PSI), C. Müller, R. Farkas, R. Schmid,
A. Sommerhalder (PSI/CRS), R. Schibli (ETHZ & PSI), A. Türler (Univ. Bern & PSI), N. van der Meulen (PSI)

INTRODUCTION

Recently, the application of the novel radionuclide ^{44}Sc for PET imaging attracted much attention. The combination of low-energy positron emission, along with a high branching ratio and a suitable half-life ($t_{1/2}$ = 3.97 h, $E_{\beta+}$ 1475.4 keV, 94.34%), encouraged a number of preclinical studies with a large variety of biomolecules. The DOTA-chelator was considered as best choice for the stable complexation of ^{44}Sc, due to the possibility to provide eight coordination sites, which are all coordinated by Sc(III) [1-3]. The suitability of a NOTA or NODAGA chelator has not been investigated thus far, however, which would be interesting for NOTA/NODAGA-derivatized peptides currently employed in clinical trials with ^{68}Ga [4]. The aim of this study was to compare the *in vitro* and *in vivo* behavior of a pair of peptides with a DOTA- and NODAGA-chelator (DOTA/NODAGA-RGD and DOTA/NODAGA-NOC), after radiolabelling with ^{44}Sc and ^{68}Ga.

EXPERIMENTAL

Production and Separation of ^{44}Sc

^{44}Ca targets were irradiated at PSI with 11 MeV protons and a beam current of 50 µA for 90 min. The target was dissolved in 3 M HCl and loaded onto a column containing DGA resin. ^{44}Sc was eluted with 0.1 M HCl and subsequently acidified to yield a 3 M HCl solution, which was then passed through a second, smaller DGA column. The elution from the second column was performed with 700 µL 0.05M HCl and directly used for labelling reactions.

Radiolabelling and *in vitro* stability

Radiolabelling of ^{44}Sc and ^{68}Ga with DOTA/NODAGA-RGD and DOTA/NODAGA-NOC was performed at a specific activity of 10 MBq/nmol. The *in vitro* stability of the radiolabelled ^{44}Sc- and ^{68}Ga-peptides was investigated in 0.9% NaCl and in metal challenge experiments with Cu^{2+} and Fe^{3+}. Aliquots were retrieved after one and four half-lives, respectively, and analyzed by TLC.

RESULTS AND DISCUSSION

Production and Separation of ^{44}Sc

The high osmolarity of the ^{44}Sc eluate when using SCX resin as second column [1] was not suitable for direct *in vivo* application. The currently-implemented DGA resin allows concentrating > 80% of the ^{44}Sc radioactivity into a small volume of 700 µL 0.05M HCl.

Radiolabelling and *in vitro* stability

Radiolabelling with ^{44}Sc was readily achieved with DOTA-compounds, but was more challenging for NODAGA-compounds. Both DOTA- and NODAGA-functionalized peptides could be reproducibly labelled with ^{68}Ga. The presence of different metal cations can cause displacement of the radionuclide from the chelator. None of the applied conditions affected the integrity of ^{44}Sc-labelled DOTA-compounds. The ^{44}Sc labelled NODAGA-peptides were significantly less stable, however, indicating an onset of disintegration already one half-life post-labelling. In contrast, the ^{68}Ga-NODAGA-peptides were completely stable, whereby the amount of intact ^{68}Ga-DOTA-RGD and ^{68}Ga-DOTA-NOC was only decreased in the presence of Cu^{2+}.

Preclinical PET imaging studies with ^{44}Sc and ^{68}Ga-labelled peptides

PET/CT experiments were performed 3 h after injection of ^{44}Sc- and ^{68}Ga-labelled DOTA/NODAGA-RGD (Figure 1) and DOTA/NODAGA-NOC (results not presented). Clearly, less ^{44}Sc-DOTA-RGD than ^{68}Ga-DOTA-RGD accumulated in the liver, whereas the distribution of ^{44}Sc-NODAGA-RGD was comparable to ^{68}Ga-NODAGA-RGD. The differences of the tissue distribution between DOTA- and NODAGA-derivatized peptides were due to their properties and not an indication of *in vivo* instability of ^{44}Sc-NODAGA-compounds. It could be shown that stable complexation of ^{44}Sc with the NODAGA chelator can be achieved up to one half-life post labelling. However, to fully exploit the excellent PET-imaging properties of ^{44}Sc, labelling with DOTA-derivatized biomolecules is thought to be the more favorable option.

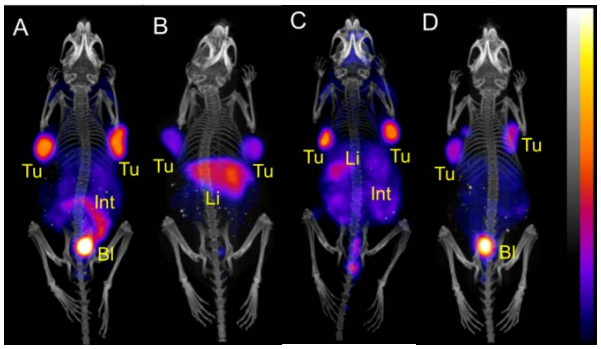

Fig. 1: PET/CT scans of U87MG tumour-bearing mice 3 h after injection of ^{44}Sc-DOTA-RGD (A), ^{68}Ga-DOTA-RGD (B), ^{44}Sc-NODAGA-RGD (C) and ^{68}Ga-NODAGA-RGD (D). (Tu= U87MG tumour xenografts Int= intestines, Li= liver, Bl= urinary bladder).

[1] N. P. van der Meulen et al., Nucl. Med. & Bio. **42** (2015).
[2] C. Müller et al, J. Nucl. Med. **54** (2013).
[3] A. Majkowska-Philip et al., J. Inorg. Biochem. **105** (2011).
[4] J. H. Kim et al, Cancer Biother. & Radiopharm. **27** (2012).

^{64}Cu PRODUCTION DEVELOPMENT BY CYCLOTRON IRRADIATION OF ^{64}Ni

N. van der Meulen (PSI), A. Blanc, R. Farkas (PSI/CRS) R. Schibli (ETH & PSI), A. Türler (Univ. Bern & PSI), C. Müller (PSI/CRS)

INTRODUCTION

^{64}Cu ($T_{1/2}$ = 12.7 h) is used as a radiotracer for positron emission tomography (PET) and is a promising radiotherapy agent for the treatment of cancer. It decays by β^+-emission (17.9%) or electron capture transition to ^{64}Ni, and by β^-emission (37.1%) to ^{64}Zn [1]. While its positron emission is effective for PET, it has been reported that its electron capture decay, associated with Auger emission, provides its radiotherapy element by more efficient cell killing when the radionuclide is deposited in the cell [2]. ^{64}Cu is also commonly used as a dosimeter to determine the neutron flux in a nuclear reactor [3].

The radionuclide is commonly produced via the ^{64}Ni(p,n)^{64}Cu nuclear reaction. The ^{64}Ni target is generally electroplated on a gold disc at a thickness of 50 to 100 µm. and irradiated with protons. After bombardment, ^{64}Cu has been separated from its ^{64}Ni target and contaminants using anion exchange, where the ^{64}Ni was strategically removed such that it could be recycled [4].

EXPERIMENTAL

Target Preparation and Irradiation: ^{64}Ni electroplated targets (~50 mg) were prepared and irradiated, using H^+ from PSI's Injector 2 cyclotron, at ~11 ±1.9 MeV protons at a beam current of 50 µA for up to 4 hours.

Fig. 1: ^{64}Cu chemical separation apparatus for hot cell production.

Chemical Separation: The Ni target material was dissolved in 5.0 M HCl, after which it was diluted to 0.2 M HCl/60% acetone and passed through a column containing AG MP-50 cation exchange resin. ^{64}Cu was eluted from the resin using 0.1 M HCl/95% acetone solution, while the ^{57,60}Co impurities were eluted with 0.1 M HCl/95% acetone. ^{64}Ni was eluted with 2.0 M HCl and put aside for recycling. The product eluent was evaporated to dryness and collected in 0.05 M HCl.

Radiolabeling of NODAGA-RGD

$^{64}CuCl_2$ was mixed with sodium acetate solution (0.5 M, pH 8) at a ratio of 1: 0.5 to obtain a solution of pH 5-5.5. The NODAGA-RGD was added to obtain a specific activity of up to 50 MBq/nmol and the reaction mixture was incubated at 95 °C for 10 minutes. HPLC, utilizing a C-18 reverse-phase column, was used for quality control.

Tumour mice preparation and PET imaging

U87MG tumor-bearing mice were injected intravenously with ^{64}Cu-labelled NODAGA-RGD (~10 MBq, ~1 nmol, 100-200 µL) and imaged using a Genisys^8 bench-top preclinical PET scanner. During the scan, the mice were anesthetized by inhalation of a mixture of isoflurane and oxygen.

RESULTS AND DISCUSSION

Irradiations and chemical separations yielded up to 3.4 GBq radionuclidically pure ^{64}Cu, which proved to be >99 % chemically pure, as the product labelled to NODAGA-RGD up to 100 MBq/nmol and 50 MBq/nmol 24 hours after chemical separation. Subsequent injection into tumor-bearing mice has produced high quality images, where the tumor has excellent activity uptake (Figure 2).

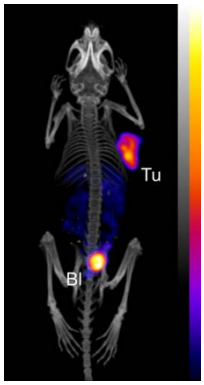

Fig. 2: U87MG tumour-bearing mouse, injected with 9,5 MBq ^{64}Cu-NODAGA-RGD. Scan took place 24 hours post injection and lasted for 10 min.

[1] Weber et al., The Society of Nuclear Medicine, New York, NY (1989).
[2] Blower et al., Nucl. Med. Biol. **23** (1996).
[3] Bé et al., Appl. Rad. Isot. **70** (2012).
[4] McCarthy et al., Nucl. Med. Biol. **24** (1997).

THE ISOTOPES ^{149}Tb AND ^{152}Tb IN PRECLINICAL INVESTIGATIONS: THE 2015 MEDICAL ISOTOPE CAMPAIGN FOR EXPERIMENT IS528 AT ISOLDE

C. Vermeulen (PSI/CRS), C. Müller (PSI/CRS), U. Koester (ILL), K. Johnston (CERN-ISOLDE), van der Meulen (PSI)

During the 2015 Ta target run, PSI concentrated on the collection and purification of ^{149}Tb and ^{152}Tb. Both isotopes could be harvested in sufficient quantities to allow transport to PSI, purification and significant imaging and therapy investigations.

As in our previous ISOLDE campaigns, the cumulative Tb yields were significantly boosted by use of resonant laser ionization of the respective Dy precursors. The new Dy laser ionization scheme using Ti-sapphire lasers instead of dye lasers provided excellent Dy yields and very stable laser ionization. The ion beam composition was measured on-line with the ISOLTRAP MR-TOF mass spectrometer [Fig 1] to validate the laser tuning and to quantify the contribution of Dy, Tb, Gd, Eu and the dominant oxide sidebands PrO, CeO, LaO. This enabled optimized collections, in particular for ^{149}Tb. With 1.5 hours of collection and 2 hours decay before shipping, up to 200 MBq could be shipped to PSI.

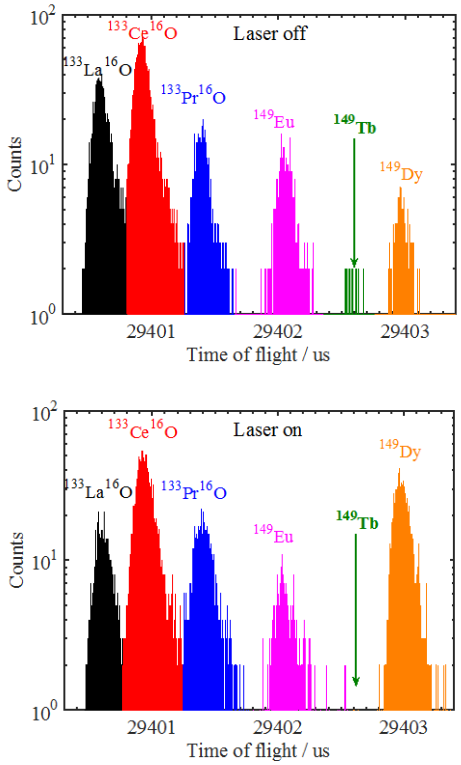

Fig. 1: The effect of selective laser ionization on the oxide sideband / product ratio.

Complementing our previous therapy studies with ^{149}Tb-cm09 and ^{161}Tb-cm09 that demonstrated therapeutic efficacy of these radiopharmaceuticals [1,2], we were now focusing on possible side effects of such a treatment. For this purpose, healthy mice without tumors were injected at increasing activity levels for the purpose of investigating kidney damage after alpha therapy with ^{149}Tb-folate and compared with the damage caused by ^{161}Tb-folate based beta therapy. These mice are monitored regarding body weight and potential changes of blood plasma parameters. Raising levels of blood urea nitrogen and creatinine would be an indication for loss of kidney function.

In 2014 we could inject 3 mice with 2 MBq/mouse and study their evolution; in 2015 we continued this ^{149}Tb-cm09 dose escalation study with 6 mice injected with 5 MBq/mouse. For the ^{149}Tb pilot study with peptides we managed to label DOTANOC and DOTA-RGD at high specific activity of up to 10 MBq/nmol. This will allow the performance of a relevant therapy study in the next production run. We also managed to label both peptides with the imaging isotope ^{152}Tb. They have been injected into AR42J and U87MG tumor-bearing mice, which were imaged using a benchtop small animal PET/CT scanner (Genisys8, Sofie Biosciences). Tumor visualization was readily achieved with both targeting agents and, due to the high sensitivity of this scanner; it was possible to image tumors also at late time points after injection of the mice.

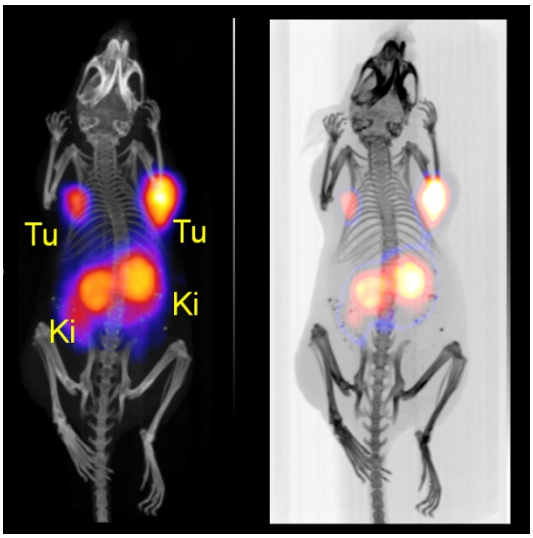

Fig. 2: PET/CT of a mouse 5 h after injection of ^{152}Tb-DOTANOC.

In order to facilitate an experiment at CHUV, we separated ^{152}Tb and sent 150 MBq to Lausanne where it was possible to label a neurotensin derivative (NT-20.3-Ile) and inject 4 tumor-bearing mice with 8 MBq each, for scanning 1.5-2 h after injection using a small-animal PET scanner.

[1] Müller et al., J. Nucl. Med., **53** (2012).
[2] Müller et al., Pharmaceuticals, **7** (2014).

THE DCB-UNIBE RADIOPHARMACEUTICAL LABORATORY AT SWAN HOUSE

J. Moreno, O. Leib, M. Bunka, N. Meneses (Univ. Bern), T. Basaco, A. Türler (Univ. Bern & PSI), G. Pla (ETHZ & Univ. Bern)

During 2015 the team at the DCB-UNIBE radiopharmaceutical laboratory (Fig. 1) continued with the production of [^{68}Ga]DOTA-TATE, which is used as radiotracer for the diagnosis of neuroendocrine tumors (NETs) by Positron Emission Tomography coupled with Computer Tomography (PET/CT). The radiotracer was produced to support the clinical study called "GAIN", which is coordinated by the Department of Nuclear Medicine at the Inselspital and SWAN Isotopen AG. The number of patients treated with the [^{68}Ga]DOTA-TATE for clinical studies was of approximately 20 as during 2014.

Fig. 1: Team at the DCB-UNIBE Laboratory in SWAN Haus, Bern

The [^{68}Ga]DOTA-TATE was also used in patients who received a special authorization from Swissmedic. In this period the number of batches released for these patients significantly increased from 10 in 2014 to 26 batches in 2015. Indeed the [^{68}Ga]DOTA-TATE from the DCB-UNIBE radiopharmaceutical laboratory was distributed not only to the local hospital facilities in Bern but also to the university hospital in Lausanne (CHUV). A picture of the Pb pot and box used for transportation of [^{68}Ga]DOTA-TATE is shown in Fig. 2.

Fig. 2: Transportation of DCB-UNIBE [^{68}Ga]-DOTATATE in the lead container and type A box.

For the release, several QC tests are performed to prove the quality and specifications of the product. As example the radionuclide purity (RNP) of [^{68}Ga]DOTA-TATE in different batches is shown in Fig. 3. The RNP purity is defined essentially by the relative content of ^{68}Ge measured by high resolution gamma-ray spectrometry to the total activity of [^{68}Ga]DOTA-TATE. Indeed, the manufacture of [^{68}Ga]DOTA-TATE has been validated with two types of commercially available generators.

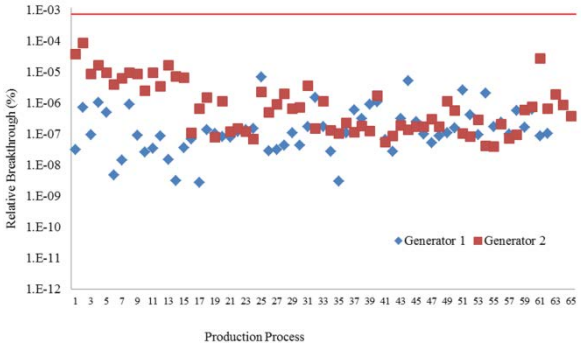

Fig. 3: Radionuclide purity: content of ^{68}Ge measured by high resolution gamma spectrometry relative to the total activity of [^{68}Ga]DOTA-TATE in released samples for two types of generators

Remark: the vertical red line indicates the acceptance limit

In addition to the production of [^{68}Ga]DOTA-TATE, in this period the validation work for the manufacture of the therapeutic radiopharmaceutical [^{177}Lu]DOTA-TOC has been completed. Within this work the following aspects were included: i) risk assessment on associated concerns to guarantee the quality and robustness of processes, ii) monitoring of environmental conditions, iii) microbiological monitoring of hot cells and production rooms, iv) periodical calibration and requalification of analytical and production instrumentation, v) validation of the aseptic conditions of the dispensation process, vi) validation of the analytical methods, vii) study of the stability of the product over the shelf life, etc.

[^{177}Lu]DOTA-TOC will be used for peptide receptor radionuclide therapy (PRRNT) of neuroendocrine tumors in patients, who receive special authorization for PRRNT treatment from the regulatory authorities.

CHARACTERIZATION OF DOTA-GIRENTUXIMAB CONJUGATES FOR LABELLING WITH THERAPEUTIC RADIONUCLIDES

T. Basaco, A. Türler (Univ. Bern & PSI), J. Moreno, N. Meneses, S. Lagache, M. Heller (Univ. Bern), S. Pektor, M. Miederer (Univ. Mainz)

Girentuximab (cG250) is a chimeric monoclonal antibody (mAb) reactive to the carbonic anhydrase IX protein (CAIX antigen), which is overexpressed on the cell surface of renal cell carcinomas (RCCs). [1] Therefore radioconstructs of G250 based on therapeutics radionuclides are potential candidates for radioimmunotherapy of RCCs. [2] The goals of this study are: i) to conjugate G250 native antibody with the bifunctional chelating agent DOTA (1,4,7,10-tetraazacyclododecane-N,N',N'',N'''-tetraacetic acid) via a benzyl-thiocyano group as a linker (p-SCN-βn-DOTA), ii) to characterize the conjugates by High Performance Size Exclusion Chromatography (SE-HPLC/UV), PolyAcrylamide Gel Electrophoresis (SDS-PAGE) and Mass Spectrometry (LC/MS-MS); iii) to evaluate the immunoreactivity of radioconstructs of ^{177}Lu and ^{225}Ac.

Fig. 1: SE-HPLC/UV Chromatograms of DOTA-G250 conjugates. The position of conjugate peak is

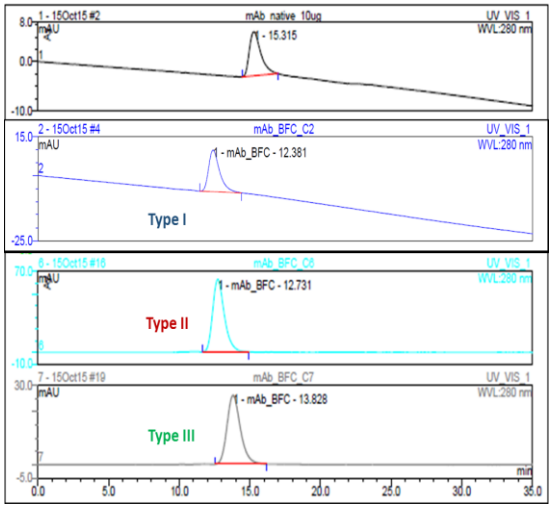

shifted to the left compared to the position of the peak for native G250. Remarks DOTA/mAb ratio: Type I >Type II > Type III.

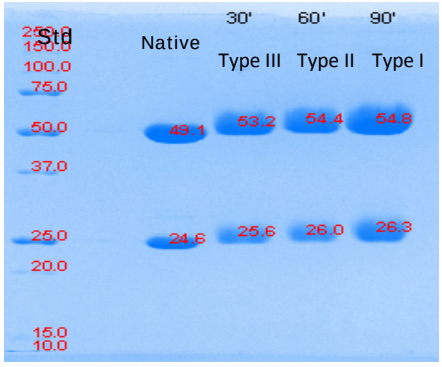

Fig. 2: SDS-PAGE Chromatogram of the DOTA-G250 conjugates. The conjugate zones were broader and shifted to higher molecular weight compared to the native zones.

Characterization by LC-MS/MS. The peptide sequence coverage in the conjugates was 98% and 92% for the light (LC) and heavy chains (HC), respectively. Potential DOTA modification sites were identified mostly through lysine residues.

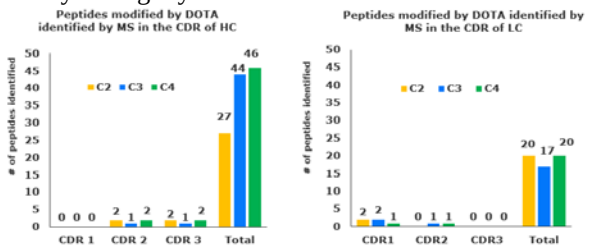

Fig. 3: Number of peptides modified by DOTA in each complementarity determining region (CDRs) of the HC (left) and LC (right) compared to the total of peptide modifications for different conjugates.

The ratio of DOTA molecules per molecule of mAb ranged from 1 to 6 in the LH and from 5 to 21 in HC.

The DOTA-G250 conjugates were labelled with ^{177}Lu- and the radioconstructs were purified with a radiochemical yield of > 90 %.

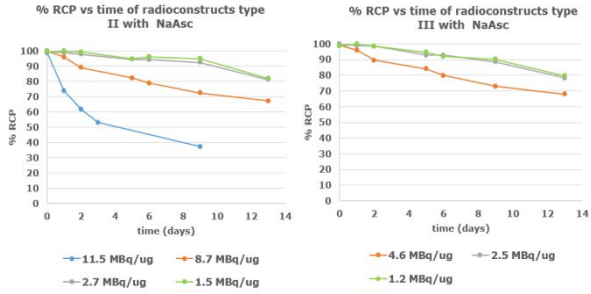

Fig. 4: Radiochemical purity (RCP) vs time of [^{177}Lu]DOTA-G250 conjugates at 37°C in HSA 1% by ITLC.

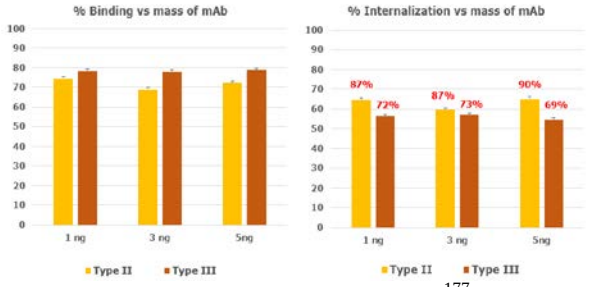

Fig. 5: Binding and internalization of [^{177}Lu]DOTA-G250 at similar specific activity 3 MBq/µg after 48 h of labeling in HSA 1% at 37°C.

In an additional step it is intended to label the conjugated DOTA-G250 with the alpha emitter ^{225}Ac and study the biological properties of the radioconstructs.

[1] Zatovicova, M., et al., Monoclonal antibody G250 targeting CA: Binding specificity, internalization and therapeutic effects in a non-renal cancer model. Int J Oncol, **45**(6), 2455-67 (2014).

[2] A.H. Brouwers et al., J Nucl Med, **45**, 327, (2004).

THE CYCLOTRON LABORATORY AT THE SWAN HOUSE IN BERN

S. Braccini, M. Auger, T.S. Carzaniga, A. Ereditato, K.P. Nesterukv (AEC-LHEP, Univ. Bern),
P. Scampoli (Univ. Bern & Univ. Napoli Federico), M. Bunka (DCB, Univ. Bern), A. Türler (Univ. Bern & PSI)

The Laboratory for High Energy Physics (LHEP) is engaged in research on medical applications of particle physics since the beginning of the SWAN project in 2008. This activity is nowadays one of the pillars of the Albert Einstein Center for Fundamental Physics (AEC), established at the University of Bern in 2011. Research is centred on the Bern cyclotron laboratory, a facility conceived for both medical radioisotope production and multi-disciplinary scientific activities [1].

Fig. 1: The Bern cyclotron with its characteristic beam transport line.

The heart of the laboratory is the IBA Cyclone 18 MeV high current cyclotron shown in Fig. 1. This accelerator is able to produce proton beams with a maximum current of 150 μA in single or dual beam mode. By simultaneous bombardment of two liquid targets, 500 GBq of ^{18}F can be produced in about 80 minutes. This yields to about 250 GBq of FDG, the most common PET radiotracer. Routine production for medical purposes runs during the night, leaving the possibility to use the proton beams for research during the day. To fully exploit the scientific potential of the accelerator, access to the beam area is needed. This is not possible in the cyclotron bunker due to the large radiation dose rate (50-100 μSv/h). To overcome this problem, one of the 8 out ports is connected to a 6-m long external beam transfer line (BTL), which leads the beam to a second bunker with independent access. This solution, although more expensive, represents the main feature of the Bern facility. Since the end of the commissioning in 2013, the BTL allowed for a rich research program encompassing nuclear, accelerator and detector physics, radiation protection and other multi-disciplinary developments. In particular, a novel wide intensity range (1 pA-20 μA) high-accuracy (250 μm) beam monitor detector was developed. This apparatus – named UniBEaM – is based on the collection of scintillating light produced by a silica-doped fibre passed through the beam.

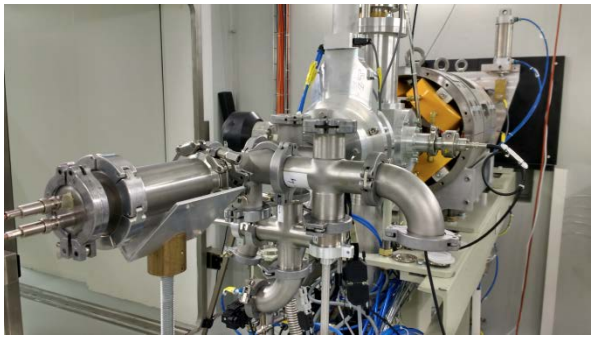

Fig. 2: The BTL equipped with two UniBEaM detectors for x-y beam monitoring followed by the target for the measurements of nuclear excitation functions.

The synergy with the radiochemistry and radio pharmacy team from DCB of the University of Bern is very fruitful. Together with the Laboratory of Radiochemistry of the Paul Scherrer Institute (PSI), the DCB and AEC-LHEP teams promoted a multi-disciplinary project funded in 2015 by the Swiss National Science Foundation (SNSF). Scandium-43 is proposed as novel PET radioisotope, having nearly ideal nuclear decay properties for PET. During the first year, the AEC-LHEP team developed an apparatus to measure nuclear excitation functions (Fig. 2). The goal is to improve existing data for the reactions ^{43}Ca(p, n)^{43}Sc and ^{46}Ti(p, α)^{43}Sc, aiming at an optimum production.

Fig. 3: The solid target station for the production of radionuclides.

Along this line, a solid target station has been installed in the cyclotron (Fig. 3). These activities represent two cornerstones towards the ultimate goal of the project: produce clinically relevant amounts of this radioisotope with a quality appropriate for clinical trials.

[1] S. Braccini, The new Bern PET cyclotron, its research beam line, and the development of an innovative beam monitor detector, AIP Conf. Proc. 1525 (2013) 144-150; http://arxiv.org/abs/1601.06820

A CONTINUOUS-FLOW GAS INTERFACE OF A THERMAL-OPTICAL ANALYZER WITH ^{14}C AMS FOR SOURCE APPORTIONMENT OF ATMOSPHERIC AEROSOLS

K. Agrios (Univ. Bern & PSI), G. Salazar, S. Szidat (Univ. Bern)

Radiocarbon (^{14}C) measurements with accelerator mass spectrometry (AMS) can apportion emissions of carbonaceous aerosols into fossil and non-fossil sources [1]. This speciation relies on the principle that ^{14}C is extinct in fossil substances, whereas it is on the contemporary level modern materials. The technique constitutes an unambiguous tool, since the intrinsic $^{14}C/^{12}C$ of the aerosol will not be affected by complex chemical transformations in atmosphere, such as it occurs for the formation of secondary organic aerosol (SOA). Our laboratory developed a separation method for the direct determination of ^{14}C in organic carbon (OC) and elemental carbon (EC), two sub-fractions of total carbon (TC) of atmospheric air particulate matter [1]. The radiocarbon analysis should take place in both fractions separately, since it has been proved that they often have different emission origins and affect differently human health and earth climate.

Currently, we routinely analyze carbonaceous aerosols samples by ^{14}C-AMS by using various analytical combustion instrumentation coupled to a MICADAS (MIni radioCArbon System) AMS through a gas inlet system (GIS) that involves trapping and releasing of the CO_2 [2,3]. This coupling allows for high-throughput ^{14}C analysis of aerosols in the small mass range down to < 10µg C.

The study of the thermal sub-fractions within the OC or EC may give even further information about the chemical composition of the OC/EC fractions and at the same time, information about the sources of the sub-fractions. However, sub-fractions peaks separated with a modified thermal ramp appear too close to each other, which required an interface that injects the CO_2 in real-time mode into the AMS. Since the GIS does not allow such analysis, an interface was developed of a thermal-optical Sunset OC/EC analyzer hyphenated to the MICADAS in continuous-flow mode [3]; see Fig. 1.

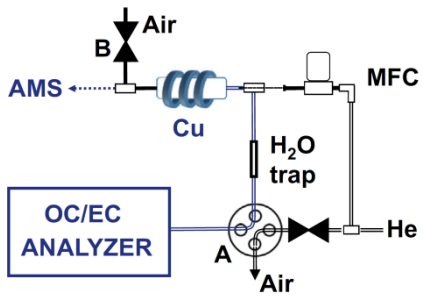

Fig. 1: The technical scheme for continuous-flow ^{14}C measurements [3].

Figure 2 presents the real-time radiocarbon analysis of TC and OC for two different exemplary atmospheric aerosol filters to demonstrate the potential of the performance of the interface. In the top figure, TC is separated into OC and EC with an intermediate mixed phase and the intrinsic ^{14}C signature is traced, which indicates the transition from more non-fossil OC to more fossil EC. In the bottom figure, OC is further split thermally into two fractions. The semi-volatility OC fraction (evolving at 200 °C) is characterized by lower $^{14}C/^{12}C$ ratios with an increasing trend towards the lower volatility OC fraction (375 °C).

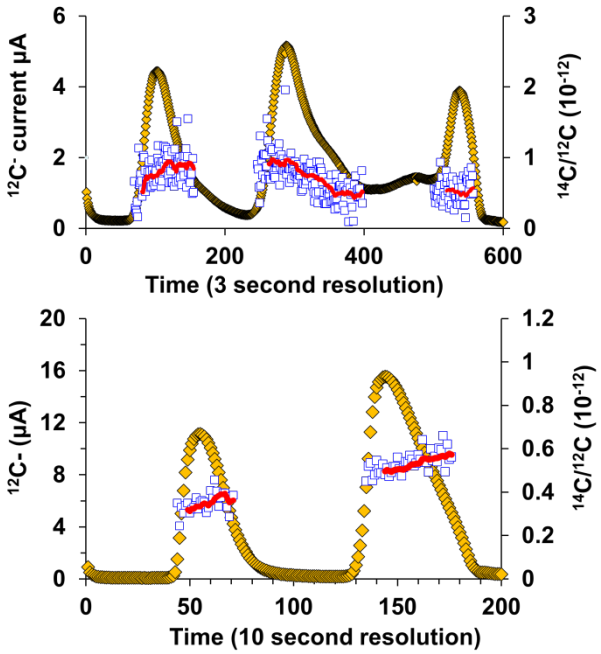

Fig. 2: Continuous-flow ^{14}C analysis of two different exemplary aerosols samples. **Top:** TC fractions evolving at 375 °C (pure OC), 475 °C (OC-EC mixture) and 650 °C (pure EC). **Bottom:** OC sub-fractions evolving at 200 °C (semi-volatility OC) and 375 °C (low-volatility OC). The red lines represent smoothed $^{14}C/^{12}C$ ratios for the individual temperature steps.

[1] Y.L. Zhang et al., Atmos. Chem. Phys., **12**, 10841 (2012).
[2] G. Salazar et al., Nucl. Instr. Meth. Phys. Res. B, **361**, 163 (2015).
[3] K. Agrios et al., Nucl. Instr. Meth. Phys. Res. B., **361,** 288 (2015).

A MILLENNIAL-LONG RECORD OF FLOOD FREQUENCY FOR THE NORTH-WESTERN ALPS INFERRED FROM VARVED LAKE SEDIMENTS

B. Amann, M. Grosjean (GIUB), S. Szidat (Univ. Bern)

In a warming climate, changes in the water cycle are of general interest as well as their impacts on water resources as well as the frequency and intensity of storms and floods in the near future. In Europe, regional climate models do not show consistent and robust results for such changes and how extreme events will evolve in response to future climate change [1]. Natural archives may provide paleo-hydroclimatic data in order to assess such changes in the longer context.

Sediment cores with overlapping segments were retrieved in August 2011 from the deepest point of Lake Oeschinen, a proglacial lake situated at 1580 m a.s.l. in the North-western Alps. The chronology of the sediment record back to AD 884 is shown in Fig. 1. It is based on multiple varve counts and validated with ^{210}Pb analyses (for the 20th century) and historical floods chronicled in written documents (back to the 14th century). To verify the varve counting in the rest of the sequence, six terrestrial plant macrofossils were dated with ^{14}C using accelerator mass spectrometry [2] and calibrated using the IntCal13 calibration curve [3].

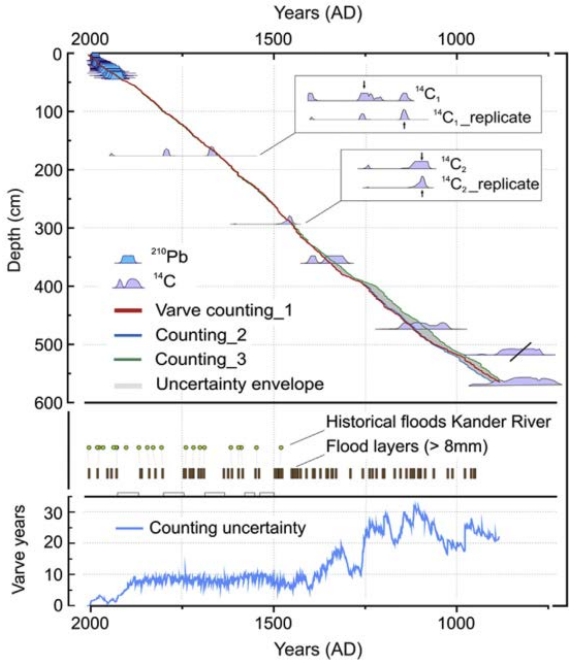

Fig. 1: Sediment chronology derived from varve counting, ^{210}Pb and ^{14}C dates [1]. **Middle panel:** comparison between the occurrence of prominent turbidite layers and the presence of historical disasters in the Kander area. **Lower panel:** time series of the varve counting uncertainty.

Figure 2 compares warm season precipitation reconstruction from Lake Oeschinen with Greater Alpine summer temperature (31-year filtered data). Over the entire last millennium, there is no relationship between the two time-series.

On the other hand, the frequency of flood layers (>5 mm) in the sediments of Lake Oeschinen coincides well with the flood frequency in the Northern Alpine area and with wetter and cooler summer conditions in the Alps [1]. In previous studies, the relation between flood frequency and moist climate has remained speculative or information was inferred from low-resolution lake level changes due to the lack of robust regional precipitation reconstructions. For the first time, our precipitation reconstruction allows for a direct comparison.

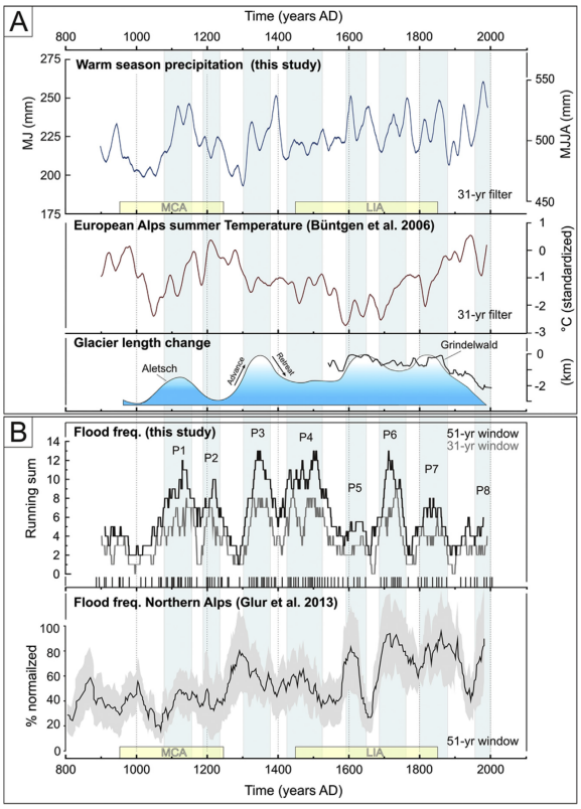

Fig. 2: Comparison of A) local warm season precipitation [1] and temperature of the Greater Alpine Region [4], as well as fluctuations of local glaciers, and B) frequency of flood layers from Lake Oeschinen [1] and flood frequency from the Northern Alps [5].

ACKNOWLEDGEMENT

This research was carried out within the Swiss National Science Foundation grant 200020-134945/1.

[1] B. Amann et al., Quat. Sci. Rev., **115**, 89 (2015).
[2] S. Szidat et al., Radiocarbon, **56**, 561 (2014).
[3] P. Reimer et al., Radiocarbon, **55**, 1869 (2013).
[4] U. Büntgen et al., J. Clim., **19**, 5606 (2006).
[5] L. Glur et al., Sci. Rep., **3**, 2770 (2013).

CHARACTERIZATION OF THE AXIAL JET SEPARATOR WITH A CO_2/HELIUM MIXTURE: TOWARDS GC-AMS HYPHENATION

G. Salazar, Szidat (Univ. Bern), K. Agrios, R. Eichler (PSI)

Accelerator Mass Spectrometry (AMS) is highly sensitive to radionuclides, thus the combination with gas chromatography (GC) is a powerful tool to study ^{14}C-labelled molecules [1]. However, the conventional AMS offline method takes days to analyze the eluates of a single chromatogram. For high-throughput detection with AMS, gas-accepting ion sources have been developed. Injection interfaces for AMS should be developed to efficiently transfer the CO_2 and separate the carrier gas to keep the pressure of the ion source lower than $1x10^{-3}$ Pa. The "axial jet separator" (aJs) is a new momentum interface developed in our laboratory [2,3]. The rationale is that the axial speeds of the components of a gas mixture jet are approximately equal to the carrier gas (w_n) when exiting a nozzle; however, the components have different densities (ρ_n) (see Eq. 1). Therefore, the components can be separated due to their different axial momentum flows (J_n).

$$J_n = A_n \rho_n w_n^2 \quad \text{[Eq. 1]}$$

Fig. 1 describes the system used to deliver a mixture of CO_2/helium into the axial jet separator. Inside of the aJS, a jet is formed in the confinement tubing. At the same time, the confinement tubing is being pumped, creating a backward flow. Only gas components with high momentum flow will be transmitted into the introduction line while components with low momentum flow will be pumped away.

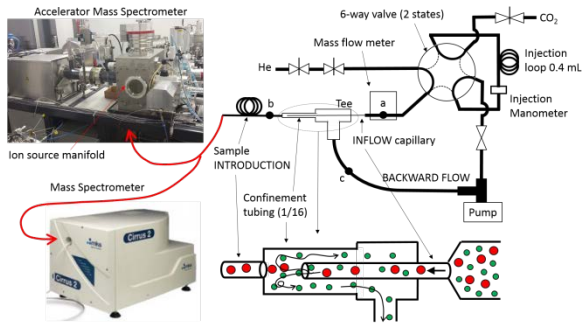

Fig. 1: Injection system for the aJS [3]. The separation and transmission efficiency were studied with conventional mass spectrometry and AMS instruments.

Many geometrical parameters can affect the aJS. Fig. 2a shows how the nozzle size affects the inflow for optimum CO_2 transmission. In contrast, the helium transmission is very low at the same inflow (Fig. 2b), allowing the introduction of a flow of 0.6 mL/min from an initial of 8 mL/min, giving a separation factor of 2.2.

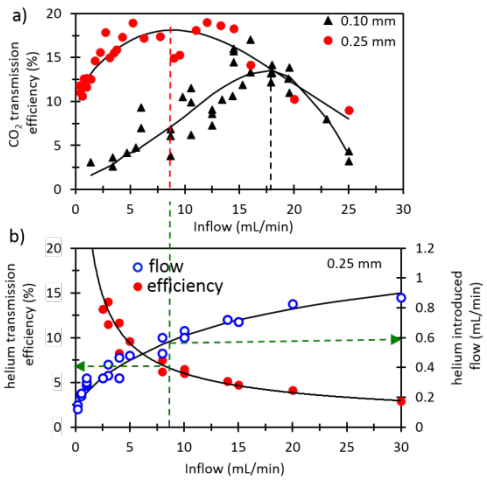

Fig. 2: Gas transmission across the aJS into a MS. a) Optimization of the inflow at varied nozzle sizes to maximize CO_2 transmission. b) Helium transmission at the optimum inflow for CO_2

At these conditions, the aJS was tested with our MICADAS AMS [3]. Fig. 3 shows that it is possible to detect the ^{14}C from a small amount of injected CO_2 gas at a high inflow with an ionization efficiency of 3%. The aJS separator shows a transmission efficiency from inlet to outlet of 17%. This is about half compared to a conventional jet separator, but performance of the aJs is less sensitive to misalignments.

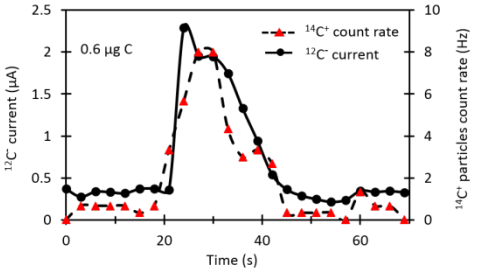

Fig. 3: ^{14}C and ^{12}C signals for an injection of CO_2 with 0.6 µg C and $^{14}C/^{12}C$ mol ratio of $1.6x10^{-12}$. For this measurement, a 0.10 mm nozzle at an inflow of 12 mL/min was used.

[1] A. L. Burlingame, *Biological mass spectrometry*; Methods in Enzymology; Elsevier Academic Press: Amsterdam, Boston, 423 (2005).

[2] G. Salazar et al., Nucl. Instr. Meth. Phys. Res. B, **361**, 163 (2015).

[3] G. Salazar et al., Anal. Chem., accepted, doi:10.1021/acs.analchem.5b03586 (2015).

FOSSIL AND NON-FOSSIL SOURCES OF CARBONACEOUS AEROSOLS DURING A HIGH LOADED EPISODE IN PREILA, LITHUANIA

A. Vlachou, C. Bozzetti, U. Baltensperger, I. El Haddad, A. S. H. Prévôt (PSI/LAC),
V. Ulevicious, S. Byčenkienė (SRI Center), K. Agrios (Univ. Bern & PSI), G. Salazar, S. Szidat (Univ. Bern)

Lithuania suffers from high concentrations of carbonaceous aerosols especially during the grassland clearing season in early spring. These episodes are related to transportation of polluted air masses stemming from biomass burning in the general Baltic region. Preila, which is located in a protected national park, is a pristine and coastal background representative site. During early March 2014, extremely high concentrations of particulate matter were captured by the Aerodyne Aerosol Chemical Speciation Monitor (ACSM) which was deployed in Preila measurement station (Figure 1(a)).

To gain insight into the chemical composition of the carbonaceous aerosols produced during this high loaded event, the ACSM mass spectra were analyzed with the positive matrix factorization (PMF) methodology. Due to the lack of local emissions in Preila, the PMF analysis could only recognize two main sources that contributed to the event: primary and secondary. For further investigation of the sources, we performed radiocarbon measurements in order to separate them into fossil and non-fossil. Therefore, the radiocarbon content of organic (OC) and elemental carbon (EC) from 5 filter samples representative of the high loaded event were analyzed with a thermo-optical OC/EC Sunset analyzer coupled with the Accelerator Mass Spectrometer MICADAS [1].

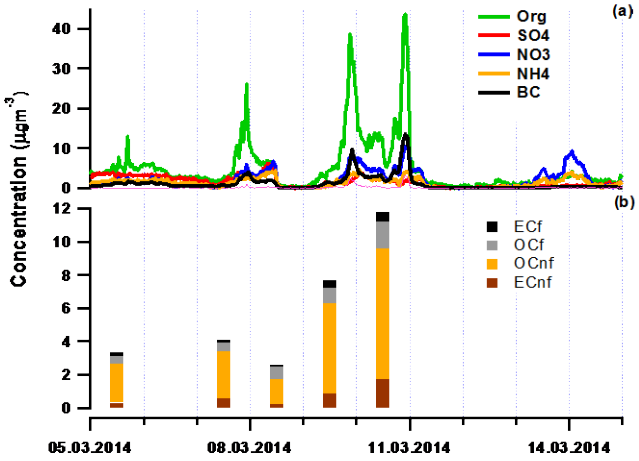

Fig. 1: Time series of the concentrations of organic and inorganic components coming from the ACSM measurements (a) and concentrations of the fossil and non-fossil fraction of OC and EC (b).

The non-fossil fraction was dominating throughout the event with non-fossil OC (OCnf) reaching up to 7.8 µgm^{-3}, followed by non-fossil EC (ECnf) with a maximum of 1.7 µgm^{-3} on the 10th of March.

Fossil EC (ECf) reached a maximum of 0.6 µgm^{-3} and the non-fossil part (ECnf) 1.7 µgm^{-3} (Figure 1(b). The ECnf/EC ratio was 0.67 on average, a value observed in Alpine sites which are substantially affected by wood burning [2].

A further investigation of the primary (POC) and secondary (SOC) origins of the organic aerosols was achieved by coupling the ACSM-PMF results with the radiocarbon analysis and organic marker measurements following a chemical mass balance-like approach. To obtain the uncertainty of the fossil and non-fossil POC and SOC fractions, a sensitivity analysis was performed [3].

Figure 2 shows the relative contributions of the non-fossil and fossil fractions to the total carbon (TC), the TC absolute concentrations, the SOCnf and the SOCf relative contributions to OC along with their uncertainties. The results show that the OCnf part contributes up to 70% to the TC, indicating that the main source is biomass burning. The SOCnf was estimated to contribute up to 37% to the OC, making the POCnf the main contributor which was on average 65%. The POCf was estimated to contribute around 95% on average.

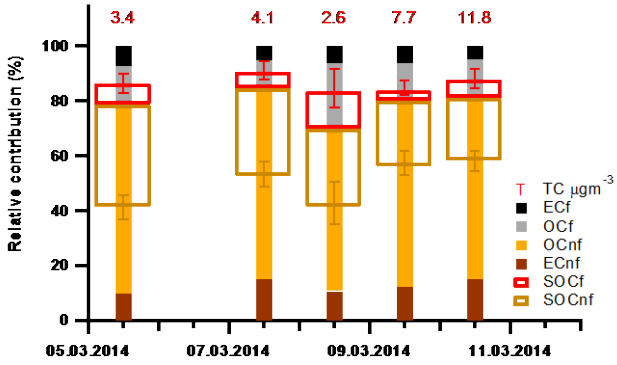

Fig. 2: Relative contributions of OCnf, OCf, ECnf and ECf to TC as well as SOCnf and SOCf relative contributions to the OC fraction. The uncertainties of SOCnf and SOCf indicate the 1st and 3rd quartiles stemming from the sensitivity analysis.

[1] K. Agrios et al., Nucl. Instrum. Meth. Phys. Res. B., **361**, 288 (2015).
[2] P. Zotter et al., Atmos. Chem. Phys., **14**, 13551 (2014).
[3] V. Ulevicious et al., Atmos. Chem. Phys. Discuss., **15**, 26315 (2015).

ISOLATION AND ^{14}C ANALYSIS OF ATMOSPHERIC HUMIC-LIKE SUBSTANCES

M. Vonwiller (Univ. Bern & PSI), G. Salazar, S. Szidat (Univ. Bern)

Humic-like substances (HULIS) are an unresolved complex mixture of organic compounds, which accounts for 12-60% of the total organic carbon (OC) in ambient aerosols [1]. They are comparable in structure to humic acids in soils, but with molecular sizes rather similar to fulvic acids. The characterization of HULIS is still incomplete and a meaningful comparison of different studies about this class of compounds is difficult, because their composition and amount is strictly method dependent. More detailed information on atmospheric HULIS and thus a significant effort towards standardized characterization and isolation methods is required. The information on the radiocarbon (^{14}C) content allows the source discrimination of biogenic and biomass-burning emissions from fossil-fuel combustion [2], thus contributing a share to a better understanding on the sources and formation of these carbonaceous aerosol constituents.

The evaluation of different isolation approaches (e.g., [3]) resulted in a straightforward HULIS extraction procedure for subsequent ^{14}C analysis by accelerator mass spectrometry (^{14}C-AMS). In brief, aerosol samples on quartz fiber filters are water extracted, filtered through a 0.2 µm PTFE filter and concentrated by lyophilisation. The sample is re-dissolved in ultrapure H_2O and acidified to pH 2 before loading the sample on a preconditioned HLB Oasis solid phase extraction (SPE) cartridge. During a washing step with 0.1 M HCl, inorganic salts and acids of small molecular weight are removed. The HULIS fraction is afterwards eluted with methanol (MeOH), filtered again and concentrated under a gentle stream of N_2. The eluate is redissolved in ultrapure water, frozen at -18°C and then lyophilized to remove remaining MeOH. The dried SPE eluates are combusted and the CO_2 is transferred to the ^{14}C-AMS system via a gas inlet system [4].

The procedure blank was quantified in terms of its mass (1.0±0.5 µg C) and its $^{14}C/^{12}C$ ratio by isotopic dilution analysis using a fossil and a modern standard (Fluka humic acid and IHSS Suwannee river humic acid, respectively). Consequently, the sample mass for the AMS measurement should be ≥20 µg C for a reasonable precision of the ^{14}C data after correction of the procedure blank.

The non-fossil contribution (f_{NF}) to the HULIS fraction in winter is shown in Fig. 1 for two samples from a large campaign in Switzerland [5]. The Moleno sampling site is located in southern Switzerland near a highway in an Alpine valley. The area is dominated by human activities such as wood burning and traffic emissions which tend to concentrate on the valley floor. The Bern sampling site is located in an urban street canyon with high traffic frequency.

Considering the high non-fossil contribution to OC in an Alpine valley from biomass burning [4], the higher non-fossil contribution for HULIS indicates a very dominant impact from this source. Even in a highly traffic-influenced street canyon, results for f_{NF}(HULIS) were ~100%, substantially higher than f_{NF}(OC) of the same samples. These results are in agreement with the outcome of an earlier study about HULIS source apportionment performed in our laboratory using a different extraction technique. Drawbacks of both methods are the need for large sample amounts and the problem to discriminate between modern sources and biomass burning. To gain more insight into the origin of HULIS, more samples need to be analyzed and further method development towards compound class specific radiocarbon analysis is necessary.

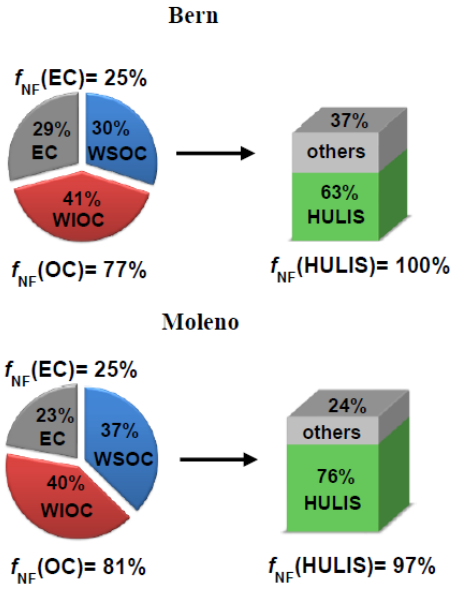

Fig. 1: Source apportionment of HULIS in Bern and Moleno in winter. The carbonaceous aerosol is separated into elemental carbon (EC) and organic carbon (OC), whereof the latter is sub-divided into water-insoluble and water-soluble OC (WIOC and WSOC, respectively). HULIS is part of WSOC.

[1] E. R. Graber et al., Atmos. Chem. Phys, **6**, 729, 2006.
[2] S. Szidat, Chimia, **63**, 157, 2009.
[3] B. Varga et al., Talanta, **55**, 561, 2001.
[4] S. Szidat et al., Radiocarbon, **56**, 561 (2014).
[5] P. Zotter et al., Atmos. Chem. Phys., **14**, 13551 (2014).

LIST OF PUBLICATIONS

HEAVY ELEMENTS

L. Baudis, G. Benato, P. Carconi, C. Cattadori, P. D. Felice, K. Eberhardt, R. Eichler, A. Petrucci, M. Tarka, M. Walter
Production and characterization of ^{228}Th calibration sources with low neutron emission for GERDA
J. Instrum. **10** (12): P12005, doi: 10.1088/1748-0221/10/12/P12005 (2015).

L. Baudis, G. Benato, R. Dressler, F. Piastra, I. Usoltsev, M. Walter
Enhancement of light yield and stability of radio-pure tetraphenyl-butadiene based coatings for VUV light detection in cryogenic environments
J. Instrum. **10** (09): P09009, doi: 10.1088/1748-0221/10/09/P09009 (2015).

N. M. Chiera, R. Eichler, A. Vögele, A. Türler
Vapor deposition coating of fused silica tubes with amorphous selenium
Thin Solid Films, doi: 10.1016/j.tsf.2015.08.043 (2015).

S. Eliseev, K. Blaum, M. Block, S. Chenmarev, H. Dorrer, C. E. Düllmann, C. Enss, P. E. Filianin, L. Gastaldo, M. Goncharov, U. Köster, F. Lautenschläger, Y. N. Novikov, A. Rischka, R. X. Schüssler, L. Schweikhard, A. Türler
Direct measurement of the mass difference of ^{163}Ho and ^{163}Dy solves the Q-value puzzle for the neutrino mass determination
Phys. Rev. Lett. **115** (6): 062501, doi: 10.1103/PhysRevLett.115.062501 (2015).

J. Even, D. Ackermann, M. Asai, M. Block, H. Brand, A. D. Nitto, C. E. Düllmann, R. Eichler, F. Fan, H. Haba, W. Hartmann, A. Hübner, F. P. Heßberger, M. Huang, E. Jäger, D. Kaji, J. Kanaya, Y. Kaneya, J. Khuyagbaatar, B. Kindler, J. V. Kratz, J. Krier, Y. Kudou, N. Kurz, M. Laatiaoui, B. Lommel, J. Maurer, S. Miyashita, K. Morimoto, K. Morita, M. Murakami, Y. Nagame, H. Nitsche, K. Ooe, Z. Qin, T. K. Sato, M. Schaädel, J. Steiner, T. Sumita, M. Takeyama, K. Tanaka, A. Toyoshima, K. Tsukada, A. Türler, I. Usoltsev, Y. Wakabayashi, Y. Wang, N. Wiehl, A. Yakushev, S. Yamaki
In situ synthesis of volatile carbonyl complexes with short-lived nuclides
J. Radioanal. Nucl. Chem. **303** (3): 2457-2466, doi: 10.1007/s10967-014-3793-7 (2015).

D. Rudolph, U. Forsberg, P. Golubev, L. G. Sarmiento, A. Yakushev, L. L. Andersson, A. Di Nitto, C. E. Düllmann, J. M. Gates, K. E. Gregorich, C. J. Gross, R. D. Herzberg, F. P. Heßberger, J. Khuyagbaatar, J. V. Kratz, K. Rykaczewski, M. Schädel, S. Åberg, D. Ackermann, M. Block, H. Brand, B. G. Carlsson, D. Cox, X. Derkx, K. Eberhardt, J. Even, C. Fahlander, J. Gerl, E. Jäger, B. Kindler, J. Krier, I. Kojouharov, N. Kurz, B. Lommel, A. Mistry, C. Mokry, H. Nitsche, J. P. Omtvedt, P. Papadakis, I. Ragnarsson, J. Runke, H. Schaffner, B. Schausten, P. Thörle-Pospiech, T. Torres, T. Traut, N. Trautmann, A. Türler, A. Ward, D. E. Ward, N. Wiehl
Selected spectroscopic results on element 115 decay chains
J. Radioanal. Nucl. Chem. **303** (2): 1185-1190, doi: 10.1007/s10967-014-3445-y (2015).

F. Schneider, T. Beyer, K. Blaum, M. Block, S. Chenmarev, H. Dorrer, Ch. E. Düllmann, K. Eberhardt, M. Eibach, S. Eliseev, J. Grund, U. Köster, Sz. Nagy, Yu. N. Novikov, D. Renisch, A. Türler, K. Wendt
Preparatory studies for a high-precision Penning-trap measurement of the Ho-163 electron capture Q-value
Eur. Phys. J. **A51**: 89-97, doi: 10.1140/epja/i2015-15089-8 (2015).

S. Söllradl, M. Greiwe, V. J. Bukas, M. R. Buchner, M. Widenmeyer, T. Kandemir, T. Zweifel, A. Senyshyn, S. Günther, T. Nilges, A. Türler, R. Niewa
Nitrogen-Doping in ZnO via Combustion Synthesis?
Chem. Mater. **27** (12): 4188–4195, doi: 10.1021/cm504200q (2015).

S. Söllradl, M. J. Mühlbauer, P. Kudejova, A. Türler
Development and Test of a Neutron Imaging Setup at the PGAA Instrument at FRM II
Physics Procedia **69**: 130–137, doi: 10.1016/j.phpro.2015.07.019 (2015).

A. Türler, R. Eichler, A. Yakushev
Chemical studies of elements with Z≥104 in gas phase
Nucl. Phys. A**944**, 640–689, doi:10.1016/j.nuclphysa.2015.09.012, (2015).

A. Türler
Lawrencium bridges a knowledge gap
Nature, **520**: 166-167, doi:10.1038/520166a (2015).

I. Usoltsev, R. Eichler, Y. Wang, J. Even, A. Yakushev, H. Haba, M. Asai, H. Brand, A. Di Nitto, Ch.E. Düllmann, F. Fangli, W. Hartmann, M. Huang, E. Jäger, D. Kaji, J. Kanaya, Y. Kaneya, J. Khuyagbaatar, B. Kindler, J.V. Kratz, J. Krier, Y. Kudou, N. Kurz, B. Lommel, S. Miyashita, K. Morimoto, K. Morita, M. Murakami, Y. Nagame, H. Nitsche, K. Ooe, T.K. Sato, M. Schädel, J. Steiner, P. Steinegger, T. Sumita, M. Takeyama, K. Tanaka, A. Toyoshima, K. Tsukada, A. Türler, Y. Wakabayashi, N. Wiehl, S. Yamaki, Z. Qin
Decomposition Studies of the Group VI Hexacarbonyl Complexes. Part 1: Production and decomposition of $Mo(CO)_6$ and $W(CO)_6$
Radiochimica Acta, online, DOI:10.1515/ract-2015-2445 (2015).

SURFACE CHEMISTRY

M. A. Brown, M.-T. Lee, A. Kleibert, M. Ammann, J. B. Giorgi
Ion spatial distributions at the air– and vacuum – aqueous K_2CO_3 interfaces
J. Phys. Chem. C **119** (9): 4976-4982, doi: 10.1021/acs.jpcc.5b00257 (2015).

C. George, M. Ammann, B. D'Anna, D. J. Donaldson, S. A. Nizkorodov
Heterogeneous photochemistry in the atmosphere
Chem. Rev. **115** (10): 4218-4258, doi: 10.1021/cr500648z (2015).

G. Gržinić, T. Bartels-Rausch, T. Berkemeier, A. Türler, M. Ammann
Viscosity controls humidity dependence of N_2O_5 uptake to citric acid aerosol
Atmos. Chem. Phys. **15** (23): 13615-13625, doi: 10.5194/acp-15-13615-2015 (2015).

S. Kato, M. Ammann, T. Huthwelker, C. Paun, M. Lampimaki, M.-T. Lee, M. Rothensteiner, J. A. van Bokhoven
Quantitative depth profiling of Ce^{3+} in Pt/CeO_2 by in situ high-energy XPS in a hydrogen atmosphere
Phys. Chem. Chem. Phys. **17** (7): 5078-5083, doi: 10.1039/C4CP05643D (2015).

M. Lampimäki, S. Schreiber, V. Zelenay, A. Křepelová, M. Birrer, S. Axnanda, B. Mao, Z. Liu, H. Bluhm, M. Ammann
Exploring the environmental photochemistry on the $TiO_2(110)$ surface in situ by Near Ambient Pressure X-ray Photoelectron Spectroscopy
J. Phys. Chem. C **119** (13): 7076-7085, doi: 10.1021/jp511340n (2015).

M.-T. Lee, M. A. Brown, S. Kato, A. Kleibert, A. Türler, M. Ammann
The competition between organics and bromide at the aqueous solution – air interface as seen from ozone uptake kinetics and X-ray photoelectron spectroscopy
J. Phys. Chem. A, doi: 10.1021/jp510707s (2015).

S. S. Steimer, T. Berkemeier, A. Gilgen, U. K. Krieger, T. Peter, M. Shiraiwa, M. Ammann
Shikimic acid ozonolysis kinetics of the transition from liquid aqueous solution to highly viscous glass
Phys. Chem. Chem. Phys. **17** (46): 31101-31109, doi: 10.1039/c5cp04544d (2015).

S. S. Steimer, U. K. Krieger, Y. F. Te, D. M. Lienhard, A. J. Huisman, B. P. Luo, M. Ammann, T. Peter
Electrodynamic balance measurements of thermodynamic, kinetic, and optical aerosol properties inaccessible to bulk methods
Atmos. Meas. Tech. **8** (6): 2397-2408, doi: 10.5194/amt-8-2397-2015 (2015).

ANALYTICAL CHEMISTRY

C. Buizert, B. Adrian, J. Ahn, M. Albert, R. B. Alley, D. Baggenstos, T. K. Bauska, R. C. Bay, B. B. Bencivengo, C. R. Bentley, E. J. Brook, N. J. Chellman, G. D. Clow, J. Cole-Dai, H. Conway, E. Cravens, K. M. Cuffey, N. W. Dunbar, J. S. Edwards, J. M. Fegyveresi, D. G. Ferris, J. J. Fitzpatrick, T. J. Fudge, C. J. Gibson, V. Gkinis, J. J. Goetz, S. Gregory, G. M. Hargreaves, N. Iverson, J. A. Johnson, T. R. Jones, M. L. Kalk, M. J. Kippenhan, B. G. Koffman, K. Kreutz, T. W. Kuhl, D. A. Lebar, J. E. Lee, S. A. Marcott, B. R. Markle, O. J. Maselli, J. R. McConnell, K. C. McGwire, L. E. Mitchell, N. B. Mortensen, P. D. Neff, K. Nishiizumi, R. M. Nunn, A. J. Orsi, D. R. Pasteris, J. B. Pedro, E. C. Pettit, P. B. Price, J. C. Priscu, R. H. Rhodes, J. L. Rosen, A. J. Schauer, S. W. Schoenemann, P. J. Sendelbach, J. P. Severinghaus, A. J. Shturmakov, M. Sigl, K. R. Slawny, J. M. Souney, T. A. Sowers, M. K. Spencer, E. J. Steig, K. C. Taylor,

M. S. Twickler, B. H. Vaughn, D. E. Voigt, E. D. Waddington, K. C. Welten, A. W. Wendricks, J. W. C. White, M. Winstrup, G. J. Wong, T. E. Woodruff (WAIS Divide Project Members)
Precise interpolar phasing of abrupt climate change during the last ice age
Nature **520** (7549): 661-665, doi: 10.1038/nature14401 (2015).

C. Buizert, K. M. Cuffey, J. P. Severinghaus, D. Baggenstos, T. J. Fudge, E. J. Steig, B. R. Markle, M. Winstrup, R. H. Rhodes, E. J. Brook, T. A. Sowers, G. D. Clow, H. Cheng, R. L. Edwards, M. Sigl, J. R. McConnel, K. C. Taylor
The WAIS Divide deep ice core WD2014 chronology - Part 1: Methane synchronization (68-31 kaBP) and the gas age-ice age difference
Clim. Past **11**(2): 153-173, doi: 10.5194/cp-11-153-2015 (2015).

R. Dadic, M. Schneebeli, N. Bertler, M. Schwikowski, M. Matzl
Extreme snow metamorphism in the Allan Hills, Antarctica, as an analogue for glacial conditions with implications for stable isotope composition
J. Glaciology 61(230), 1171-1182 doi: 10.3189/2015JoG15J027 (2015).

A. Eichler, G. Gramlich, T. Kellerhals, L. Tobler, M. Schwikowski
Pb pollution from leaded gasoline in South America in the context of a 2000-year metallurgical history
Sci. Adv. **1** (2), doi: 10.1126/sciadv.1400196 (2015).

J. Gabbi, M. Huss, A. Bauder, F. Cao, M. Schwikowski
The impact of Saharan dust and black carbon on albedo and long-term mass balance of an Alpine glacier
Cryosphere **9** (4): 1385-1400, doi: 10.5194/tc-9-1385-2015 (2015).

B. Grigholm, P. A. Mayewski, S. Kang, Y. Zhang, U. Morgenstern, M. Schwikowski, S. Kaspari, V. Aizen, E. Aizen, Takeuchi, K. A. Maasch, S. Birkel, M. Handley, S. Sneed
Twentieth century dust lows and the weakening of the westerly winds over the Tibetan Plateau
Geophys. Res. Lett., doi: 10.1002/2015GL063217 (2015).

S. Kang, F. Wang, U. Morgenstern, Y. Zhang, B. Grigholm, S. Kaspari, M. Schwikowski, J. Ren, T. Yao, D. Qin, P. A. Mayewski
Dramatic loss of glacier accumulation area on the Tibetan Plateau revealed by ice core tritium and mercury records
Cryosphere **9** (3): 1213-1222, doi: 10.5194/tc-9-1213-2015 (2015).

F. Mekhaldi, R. Muscheler, F. Adolphi, A. Aldahan, J. Beer, J. R. McConnell, G. Possnert, M. Sigl, A. Svensson, H. A. Synal, K. C. Welten and T. E. Woodruff
Multiradionuclide evidence for the solar origin of the cosmic-ray events of AD 774/5 and 993/4
Nat Commun **6**: 9611, doi: 10.1038/ncomms9611 (2015).

S. H. Mernild, E. Hanna, J. R. McConnell, M. Sigl, A. P. Beckerman, J. C. Yde, J. Cappelen, J. K. Malmros and K. Steffen
Greenland precipitation trends in a long-term instrumental climate context (1890-2012): evaluation of coastal and ice core records
Int J Climatol **35** (2): 303-320, doi: 10.1002/joc.3986 (2015).

L. E. Mitchell, C. Buizert, E. J. Brook, D. J. Breton, J. Fegyveresi, D. Baggenstos, A. Orsi, J. Severinghaus, R. B. Alley, M. Albert, R. H. Rhodes, J. R. McConnell, M. Sigl, O. Maselli, S. Gregory, J. Ahn
Observing and modeling the influence of layering on bubble trapping in polar firn
J Geophys Res-Atmos **120** (6): 2558-2574, doi: 10.1002/2014JD022766 (2015).

P. A. Pavlova, T. M. Jenk, P. Schmid, C. Bogdal, C. Steinlin, M. Schwikowski
Polychlorinated biphenyls in a temperate Alpine glacier: 1. Effect of percolating meltwater on their distribution in glacier ice
Environ. Sci. Technol. **49** (24): 14085-14091, doi: 10.1021/acs.est.5b03303 (2015).

P.A. Pavlova, M. Zennegg, F.S. Anselmetti, P. Schmid, C. Bogdal, C. Steinlin, M. Jäggi, M. Schwikowski
Release of PCBs from Silvretta glacier (Switzerland) investigated in lake sediments and meltwater
Environ Sci Pollut Res. DOI 10.1007/s11356-015-5854-z.

M. Sigl, M. Winstrup, J. R. McConnell, K. C. Welten, G. Plunkett, F. Ludlow, U. Büntgen, M. Caffee, N. Chellman, D. Dahl-Jensen, H. Fischer, S. Kipfstuhl, C. Kostick, O. J. Maselli, F. Mekhaldi, R. Mulvaney, R. Muscheler, D. R. Pasteris, J. R. Pilcher, M. Salzer, S. Schüpbach, J. P. Steffensen, B. M. Vinther, T. E. Woodruff
Timing and climate forcing of volcanic eruptions for the past 2,500 years
Nature **523** (7562): 543-549, doi: 10.1038/nature14565 (2015).

L. Sold, M. Huss, A. Eichler, M. Schwikowski, M. Hoelzle
Unlocking annual firn layer water equivalents from ground-penetrating radar data on an Alpine glacier
Cryosphere **9** (3): 1075-1087, doi: 10.5194/tc-9-1075-2015 (2015).

C. Steinlin, C. Bogdal, P. A. Pavlova, M. Schwikowski, M. P. Lüthi, M. Scheringer, P. Schmid, K. Hungerbühler
Polychlorinated biphenyls in a temperate Alpine glacier: 2. Model results of chemical fate processes
Environ. Sci. Technol. **49** (24): 14092-14100, doi: 10.1021/acs.est.5b03304 (2015).

C. Uglietti, P. Gabrielli, C. A. Cookec, P. Vallelonga, L. G. Thompson
Widespread pollution of the South American atmosphere predates the industrial revolution by 240 y
PNAS **112** (8), 2349–2354, doi: 10.1073/pnas.1421119112 (2015).

I. A. Wendl, A. Eichler, E. Isaksson, T. Martma, M. Schwikowski
800-year ice-core record of nitrogen deposition in Svalbard linked to ocean productivity and biogenic emissions
Atmos. Chem. Phys. **15** (13): 7287-7300, doi: 10.5194/acp-15-7287-2015 (2015).

Y. L. Zhang, S. C. Kang, Q. G. Zhang, B. Grigholm, S. Kaspari, Q. L. You, D. H. Qin, P. A. Mayewski, Z. Y. Cong, J. Huang, M. Sillanpaa, F. Chen
A 500 year atmospheric dust deposition retrieved from a Mt. Geladaindong ice core in the central Tibetan Plateau
Atmos. Res. **166**: 1-9, doi: 10.1016/j.atmosres.2015.06.007 (2015).

Q. Zhang, S. Kang, P. Gabrielli, M. Loewen, M. Schwikowski
Vanishing high mountain glacial archives: Challenges and perspectives
Environ. Sci. Technol. **49** (16): 9499-9500, doi: 10.1021/acs.est.5b03066 (2015).

RADWASTE ANALYTICS

B. Alpert, M. Balata, D. Bennett, M. Biasotti, C. Boragno, C. Brofferio, V. Ceriale, D. Corsini, P. K. Day, M. De Gerone, R. Dressler, M. Faverzani, E. Ferri, J. Fowler, F. Gatti, A. Giachero, J. Hays-Wehle, S. Heinitz, G. Hilton, U. Köster, M. Lusignoli, M. Maino, J. Mates, S. Nisi, R. Nizzolo, A. Nucciotti, G. Pessina, G. Pizzigoni, A. Puiu, S. Ragazzi, C. Reintsema, M. R. Gomes, D. Schmidt, D. Schumann, M. Sisti, D. Swetz, F. Terranova, J. Ullom
HOLMES
Eur. Phys. J. C **75** (3): 1-11, doi: 10.1140/epjc/s10052-015-3329-5 (2015).

C.-Y. Chuang, P. H. Santschi, L.-S. Wen, L. Guo, C. Xu, S. Zhang, Y. Jiang, Y.-F. Ho, K. A. Schwehr, A. Quigg, C.-C. Hung, M. Ayranov, D. Schumann
Binding of Th, Pa, Pb, Po and Be radionuclides to marine colloidal macromolecular organic matter
Mar. Chem. **173**: 320-329, doi: 10.1016/j.marchem.2014.10.014 (2015).

C. Y. Chuang, P. H. Santschi, C. Xu, Y. L. Jiang, Y. F. Ho, A. Quigg, L. D. Guo, P. G. Hatcher, M. Ayranov, D. Schumann
Molecular level characterization of diatom-associated biopolymers that bind Th-234, Pa-233, Pb-210, and Be-7 in seawater: A case study with Phaeodactylum tricornutum
J. Geophys. Res.-Biogeo. **120** (9): 1858-1869, doi: 10.1002/2015jg002970 (2015).

C. Guerrero, D. Cano-Ott, E. Mendoza, T. Wright, n_TOF Collaboration
Correction of dead-time and pile-up in a detector array for constant and rapidly varying counting rates
Nucl. Instrum. Methods Phys. Res., Sect. A **777**: 63-69, doi: 10.1016/j.nima.2014.12.008 (2015).

B. Hammer-Rotzler, J. Neuhausen, V. Boutellier, M. Wohlmuther, A. Türler, D. Schumann
Radiochemical determination of rare earth elements in proton-irradiated lead–bismuth eutectic
Anal. Chem. **87** (11): 5656-5663, doi: 10.1021/acs.analchem.5b00955 (2015).

B. Hammer-Rotzler, J. Neuhausen, C. Vockenhuber, V. Boutellier, M. Wohlmuther, A. Türler, D. Schumann
Radiochemical determination of ^{129}I and ^{36}Cl in MEGAPIE, a proton irradiated lead-bismuth eutectic spallation target
Radiochim. Acta, doi: 10.1515/ract-2015-2420 (2015).

T. Heftrich, M. Bichler, R. Dressler, K. Eberhardt, A. Endres, J. Glorius, K. Göbel, G. Hampel, M. Heftrich, F. Käppeler, C. Lederer, M. Mikorski, R. Plag, R. Reifarth, C. Stieghorst, S. Schmidt, D. Schumann, Z. Slavkovská, K. Sonnabend, A. Wallner, M. Weigand, N. Wiehl, S. Zauner
Thermal neutron capture cross section of the radioactive isotope ^{60}Fe
Phys. Rev. C **92** (1): 015806, doi: 10.1103/PhysRevC.92.015806 (2015).

C. Lederer, C. Massimi, E. Berthoumieux, N. Colonna, R. Dressler, C. Guerrero, F. Gunsing, F. Käppeler, N. Kivel, M. Pignatari, R. Reifarth, D. Schumann, A. Wallner, S. Altstadt, S. Andriamonje, J. Andrzejewski, L. Audouin, M. Barbagallo, V. Bécares, F. Bečvář, F. Belloni, B. Berthier, J. Billowes, V. Boccone, D. Bosnar, M. Brugger, M. Calviani, F. Calviño, D. Cano-Ott, C. Carrapiço, F. Cerutti, E. Chiaveri, M. Chin, G. Cortés, M. A. Cortés-Giraldo, I. Dillmann, C. Domingo-Pardo, I. Duran, N. Dzysiuk, C. Eleftheriadis, M. Fernández-Ordóñez, A. Ferrari, K. Fraval, S. Ganesan, A. R. García, G. Giubrone, M. B. Gómez-Hornillos, I. F. Gonçalves, E. González-Romero, F. Gramegna, E. Griesmayer, P. Gurusamy, S. Harrisopulos, M. Heil, K. Ioannides, D. G. Jenkins, E. Jericha, Y. Kadi, D. Karadimos, G. Korschinek, M. Krtička, J. Kroll, C. Langer, E. Lebbos, H. Leeb, L. S. Leong, R. Losito, M. Lozano, A. Manousos, J. Marganiec, S. Marrone, T. Martinez, P. F. Mastinu, M. Mastromarco, M. Meaze, E. Mendoza, A. Mengoni, P. M. Milazzo, F. Mingrone, M. Mirea, W. Mondalaers, C. Paradela, A. Pavlik, J. Perkowski, R. Plag, A. Plompen, J. Praena, J. M. Quesada, T. Rauscher, A. Riego, F. Roman, C. Rubbia, R. Sarmento, P. Schillebeeckx, S. Schmidt, G. Tagliente, J. L. Tain, D. Tarrío, L. Tassan-Got, A. Tsinganis, L. Tlustos, S. Valenta, G. Vannini, V. Variale, P. Vaz, A. Ventura, M. J. Vermeulen, R. Versaci, V. V*lac*houdis, R. Vlastou, T. Ware, M. Weigand, C. Weiß, T. J. Wright, P. Žugec n_TOF. Collaboration,
Erratum: ^{62}Ni(n,γ) and ^{63}Ni(n,γ) cross sections measured at the n_TOF facility at CERN
[Phys. Rev. C 89, 025810 (2014)], Phys. Rev. C 92, 019903(E) (2015), DOI: 10.1103/PhysRevC.92.019903.

A. S. Murphy, D. Schumann, T. Stora
Exploitation of accelerator waste for radioactive ion beams: A nuclear astrophysics application
Nuclear Physics News **25** (1): 23-29, doi: 10.1080/10619127.2014.910431 (2015).

J. Neuhausen, A. Aerts, H. Glasbrenner, S. Heinitz, M. Jolkkonen, Y. Kurata, T. Obara, J.-C. David, N. Thiollière, L. Zanini
Handbook on Lead-bismuth Eutectic Alloy and Lead Properties, Materials Compatibility,
Thermalhydraulics and Technologies, 2015 Edition, OECD Nuclear Energy Agency, NEA. No. 7268, 2015,
https://www.oecd-nea.org/sacience/pubs/2015/7268-lead-bismuth-2015.pdf

K. Ostdiek, T. Anderson, W. Bauder, M. Bowers, P. Collon, R. Dressler, J. Greene, W. Kutschera, W. Lu, M. Paul, D. Robertson, D. Schumann, M. Skulski, A. Wallner
Towards a measurement of the half-life of Fe-^{60} for stellar and early Solar System models
Nucl. Instrum. Methods B **361**: 638-642, doi: 10.1016/j.nimb.2015.05.033 (2015).

C. Paradela, M. Calviani, D. Tarrío, E. Leal-Cidoncha, L. S. Leong, L. Tassan-Got, C. Le Naour, I. Duran, N. Colonna, L. Audouin, M. Mastromarco, S. Lo Meo, A. Ventura, G. Aerts, S. Altstadt, H. Álvarez, F. Álvarez-Velarde, S. Andriamonje, J. Andrzejewski, G. Badurek, M. Barbagallo, P. Baumann, V. Bécares, F. Bečvář, F. Belloni, B. Berthier, E. Berthoumieux, J. Billowes, V. Boccone, D. Bosnar, M. Brugger, F. Calviño, D. Cano-Ott, R. Capote, C. Carrapiço, P. Cennini, F. Cerutti, E. Chiaveri, M. Chin, G. Cortés, M. A. Cortés-Giraldo, L. Cosentino, A. Couture, J. Cox, S. David, M. Diakaki, I. Dillmann, C. Domingo-Pardo, R. Dressler, W. Dridi, C. Eleftheriadis, M. Embid-Segura, L. Ferrant, A. Ferrari, P. Finocchiaro, K. Fraval, K. Fujii, W. Furman, S. Ganesan, A. R. García, G. Giubrone, M. B. Gómez-Hornillos, I. F. Gonçalves, E. González-Romero, A. Goverdovski, F. Gramegna, E. Griesmayer, C. Guerrero, F. Gunsing, P. Gurusamy, R. Haight, M. Heil, S. Heinitz, M. Igashira, S. Isaev, D. G. Jenkins, E. Jericha, Y. Kadi, F. Käppeler, D. Karadimos, D. Karamanis, M. Kerveno, V. Ketlerov, N. Kivel, M. Kokkoris, V. Konovalov, M. Krtička, J. Kroll, C. Lampoudis, C. Langer, C. Lederer, H. Leeb, R. Losito, M. Lozano, A. Manousos, J. Marganiec, T. Martínez, S. Marrone, C. Massimi, P. Mastinu, E. Mendoza, A. Mengoni, P. M. Milazzo, F. Mingrone, M. Mirea, W. Mondelaers, C. Moreau, M. Mosconi, A. Musumarra, S. O'Brien, J. Pancin, N. Patronis, A. Pavlik, P. Pavlopoulos, J. Perkowski, L. Perrot, M. T. Pigni, R. Plag, A. Plompen, L. Plukis, A. Poch, C. Pretel, J. Praena, J. Quesada, T. Rauscher, R. Reifarth, A. Riego, F. Roman, G. Rudolf, C. Rubbia, P. Rullhusen, J. Salgado, C. Santos, L. Sarchiapone, R. Sarmento, A. Saxena, P. Schillebeeckx, S. Schmidt, D. Schumann, C. Stephan, G. Tagliente, J. L. Tain, L. Tavora, R. Terlizzi, A. Tsinganis, S. Valenta, G. Vannini, V. Variale, P. Vaz, R. Versaci, M. J. Vermeulen, D. Villamarin, M. C. Vincente, V. Vlachoudis, R. Vlastou, F. Voss, A. Wallner, S. Walter, T. Ware, M. Weigand, C. Weiß, M. Wiesher, K. Wisshak, T. Wright, P. Žugec
High-accuracy determination of the ^{238}U/^{235}U fission cross section ratio up to ≈ 1 GeV at n_TOF at CERN
Phys. Rev. C **91** (2): 024602, doi: 10.1103/PhysRevC.91.024602 (2015).

D. Schumann, R. Dressler
Development of an extraction system for the separation of Dubnium from Rutherfordium using MIBK and HCl/HF solutions
Radiochimica Acta, 2015, DOI 10.1515/ract-2015-2398.

A. Tsinganis, M. Barbagallo, E. Berthoumieux, M. Calviani, E. Chiaveri, N. Colonna, M. Diakaki, I. Duran, C. Guerrero, F. Gunsing, E. Leal-Cidoncha, L. S. Leong, C. Paradela, D. Tarrio, L. Tassan-Got, R. Vlastou and the n_TOF Community
The fission programme at the CERN n_TOF facility
Physics Procedia **64**: 130-139, doi: 10.1016/j.phpro.2015.04.017 (2015).

A. Wallner, M. Bichler, K. Buczak, R. Dressler, L. K. Fifield, D. Schumann, J. H. Sterba, S. G. Tims, G. Wallner, W. Kutschera
Settling the half-life of ^{60}Fe: Fundamental for a versatile astrophysical chronometer
Phys. Rev. Lett. **114** (4): 041101, doi: 10.1103/PhysRevLett.114.041101 (2015).

M. Weigand, T. A. Bredeweg, A. Couture, K. Göbel, T. Heftrich, M. Jandel, F. Käppeler, C. Lederer, N. Kivel, G. Korschinek, M. Krtička, J. M. O'Donnell, J. Ostermöller, R. Plag, R. Reifarth, D. Schumann, J. L. Ullmann, A. Wallner
The 63Ni(n, γ) cross section measured with DANCE
Phys. Rev. C **92** (4): 045810, doi: 10.1103/PhysRevC.92.045810 (2015).

C. Weiß, E. Chiaveri, S. Girod, V. Vlachoudis, O. Aberle, S. Barros, I. Bergström, E. Berthoumieux, M. Calviani, C. Guerrero, M. Sabaté-Gilarte, A. Tsinganis, J. Andrzejewski, L. Audouin, M. Bacak, J. Balibrea-Correa, M. Barbagallo, V. Bécares, C. Beinrucker, F. Belloni, F. Bečvář, J. Billowes, D. Bosnar, M. Brugger, M. Caamaño, F. Calviño, D. Cano-Ott, F. Cerutti, N. Colonna, G. Cortés, M. A. Cortés-Giraldo, L. Cosentino, L. Damone, K. Deo, M. Diakaki, C. Domingo-Pardo, E. Dupont, I. Durán, R. Dressler, B. Fernández-Domínguez, A. Ferrari, P. Ferreira, P. Finocchiaro, R. Frost, V. Furman, S. Ganesan, A. Gheorghe, T. Glodariu, K. Göbel, I. F. Gonçalves, E. González-Romero, A. Goverdovski, E. Griesmayer, F. Gunsing, H. Harada, T. Heftrich, S. Heinitz, A. Hernández-Prieto, J. Heyse, D. G. Jenkins, E. Jericha, Y. Kadi, F. Käppeler, T. Katabuchi, P. Kavrigin, V. Ketlerov, V. Khryachkov, A. Kimura, N. Kivel, M. Kokkoris, M. Krtička, E. Leal-Cidoncha, C. Lederer, H. Leeb, J. Lerendegui, M. Licata, S. Lo Meo, D. López, R. Losito, D. Macina, J. Marganiec, T. Martínez, C. Massimi, P. F. Mastinu, M. Mastromarco, F. Matteucci, E. Mendoza, A. Mengoni, P. M. Milazzo, F. Mingrone, M. Mirea, S. Montesano, A. Musumarra, R. Nolte, R. Palomo Pinto, C. Paradela, N. Patronis, A. Pavlik, J. Perkowski, I. Porras, J. Praena, J. M. Quesada, T. Rauscher, R. Reifarth, A. Riego-Perez, M. S. Robles, C. Rubbia, J. Ryan, A. Saxena, P. Schillebeeckx, S. Schmidt, D. Schumann, P. Sedyshev, G. Smith, A. Stamatopoulos, P. Steinegger, S. V. Suryanarayana, G. Tagliente, J. L. Tain, A. Tarifeño-Saldivia, L. Tassan-Got, S. Valenta, G. Vannini, V. Variale, P. Vaz, A. Ventura, R. Vlastou, A. Wallner, S. Warren, M. Weigand, T. Wright, P. Žugec
The new vertical neutron beam line at the CERN n_TOF facility design and outlook on the performance
Nucl. Instrum. Methods A **799**: 90-98, doi: 10.1016/j.nima.2015.07.027 (2015).

W. F. Yang, L. D. Guo, C. Y. Chuang, P. H. Santschi, D. Schumann, M. Ayranov
Influence of organic matter on the adsorption of Pb-210, Po-210, Be-7 and their fractionation on nanoparticles in seawater
Earth. Planet. Sci. Lett. **423**: 193-201, doi: 10.1016/j.epsl.2015.05.007 (2015).

P. Žugec, M. Barbagallo, N. Colonna, D. Bosnar, S. Altstadt, J. Andrzejewski, L. Audouin, V. Bécares, F. Bečvář, F. Belloni, E. Berthoumieux, J. Billowes, V. Boccone, M. Brugger, M. Calviani, F. Calviño, D. Cano-Ott, C. Carrapiço, F. Cerutti, E. Chiaveri, M. Chin, G. Cortés, M. A. Cortés-Giraldo, M. Diakaki, C. Domingo-Pardo, R. Dressler, I. Duran, N. Dzysiuk, C. Eleftheriadis, A. Ferrari, K. Fraval, S. Ganesan, A. R. García, G. Giubrone, M. B. Gómez-Hornillos, I. F. Gonçalves, E. González-Romero, E. Griesmayer, C. Guerrero, F. Gunsing, P. Gurusamy, S. Heinitz, D. G. Jenkins, E. Jericha, Y. Kadi, F. Käppeler, D. Karadimos, N. Kivel, P. Koehler, M. Kokkoris, M. Krtička, J. Kroll, C. Langer, C. Lederer, H. Leeb, L. S. Leong, S. Lo Meo, R. Losito, A. Manousos, J. Marganiec, T. Martínez, C. Massimi, P. F. Mastinu, M. Mastromarco, M. Meaze, E. Mendoza, A. Mengoni, P. M. Milazzo, F. Mingrone, M. Mirea, W. Mondalaers, C. Paradela, A. Pavlik, J. Perkowski, M. Pignatari, A. Plompen, J. Praena, J. M. Quesada, T. Rauscher, R. Reifarth, A. Riegov, F. Roman, C. Rubbia, R. Sarmento, A. Saxena, P. Schillebeeckx, S. Schmidt, D. Schumann, G. Tagliente, J. L. Tain, D. Tarrío, L. Tassan-Got, A. Tsinganis, S. Valenta, G. Vannini, V. Variale, P. Vaz, A. Ventura, R. Versaci, M. J. Vermeulen, V. Vlachoudis, R. Vlastou, A. Wallner, T. Ware, M. Weigand, C. Weiß, T. Wright
Experimental neutron capture data of ^{58}Ni from the CERN n_TOF facility
EPJ Web of Conferences **93**, doi: 10.1051/epjconf/20159302009 (2015).

P. Žugec, M. Barbagallo, N. Colonna, D. Bosnar, S. Altstadt, J. Andrzejewski, L. Audouin, V. Bečares,F. Bečvăr, F. Belloni, E. Berthoumieux, J. Billowes, V. Boccone, M. Brugger, M. Calviani, F. Calvino,D. Cano-Ott, C. Carrapico, F. Cerutti, E. Chiaveri, M. Chin, G. Cortes, M.A. Cortes-Giraldo, M. Diakaki,C. Domingo-Pardo, R. Dressler, I. Duran, N. Dzysiuk, C. Eleftheriadis, A. Ferrari, K. Fraval, S. Ganesan, A.R. Garcia, G. Giubrone, M.B. Gomez Hornillos, I.F. Goncalves, E. Gonzalez-Romero, E. Griesmayer, C. Guerrero, F. Gunsing, P. Gurusamy, S. Heinitz, D.G. Jenkins, E. Jericha, Y. Kadi, F. Käppeler, D. Karadimos, N. Kivel, P. Koehler,M. Kokkoris, M. Krtička, J. Kroll, C. Langer, C. Lederer, H. Leeb, L.S. Leong, S. Lo Meo, R. Losito, A. Manousos, J. Marganiec, T. Martinez, C. Massimi, P.F. Mastinu, M. Mastromarco, M. Meaze, E. Mendoza, A. Mengoni, P.M. Milazzo, F. Mingrone, M. Mirea, W. Mondalaers, C. Paradela, A. Pavlik, J. Perkowski, M. Pignatari, A. Plompen, J. Praena, J.M. Quesada, T. Rauscher, R. Reifarth, A. Riegov, F. Roman, C. Rubbia, R. Sarmento, A. Saxena, P. Schillebeeckx, S. Schmidt, D. Schumann, G. Tagliente, J.L. Tain, D. Tarrio, L. Tassan-Got, A. Tsinganis, S. Valenta, G. Vannini, V. Variale, P. Vaz, A. Ventura, R. Versaci, M.J. Vermeulen, V. Vlachoudis, R. Vlastou, A. Wallner, T. Ware, M. Weigand, C.Weiss, T. Wright
Experimental neutron capture data of ^{58}Ni from the CERN n_TOF facility
EPJ Web of Conferences 93, 02009 (2015) http://dx.doi.org/10.1051/epjconf/20159302009.

RADIONUCLIDE DEVELOPMENT - CHEMISTRY

N. P. van der Meulen, M. Bunka, K.A. Domnanich, C. Müller, S. Haller, C. Vermeulen, A. Türler, R. Schibli
Cyclotron production of 44Sc: from bench to bedside
Nucl. Med. Biol. **42** (9) 745, (2015).

F. Szelecsenyi, G.F. Steyn, Z. Kovacs, C. Vermeulen, K. Nagatsu, M.-R. Zhang, K. Suzuki
Excitation functions of natZr + p nuclear processes up to 70 MeV: New measurements and compilation.
Nucl. Instr. Meth. Res. B **343**173, (2015).

ENVIRONMENTAL RADIONUCLIDES UNIVERSITÄT BERN

K. Agrios, G. Salazar, Y. L. Zhang, C. Uglietti, M. Battaglia, M. Luginbuhl, V. G. Ciobanu, M. Vonwiller, S. Szidat
Online coupling of pure O-2 thermo-optical methods-C-14 AMS for source apportionment of carbonaceous aerosols
Nucl. Instrum. Method B **361**: 288-293, doi: 10.1016/j.nimb.2015.06.008 (2015).

B. Amann, S. Szidat, M. Grosjean
A millennial-long record of warm season precipitation and flood frequency for the North-western Alps inferred from varved lake sediments: implications for the future
Quat. Sci. Rev. **115**: 89-100, doi: 10.1016/j.quascirev.2015.03.002 (2015).

M. Beekmann, A. S. H. Prévôt, F. Drewnick, J. Sciare, S. N. Pandis, H. A. C. Denier van der Gon, M. Crippa, F. Freutel, L. Poulain, V. Ghersi, E. Rodriguez, S. Beirle, P. Zotter, S. L. von der Weiden-Reinmüller, M. Bressi, C. Fountoukis, H. Petetin, S. Szidat, J. Schneider, A. Rosso, I. El Haddad, A. Megaritis, Q. J. Zhang, V. Michoud, J. G. Slowik, S. Moukhtar, P. Kolmonen, A. Stohl, S. Eckhardt, A. Borbon, V. Gros, N. Marchand, J. L. Jaffrezo, A. Schwarzenboeck, A. Colomb, A. Wiedensohler, S. Borrmann, M. Lawrence, A. Baklanov, U. Baltensperger
In situ, satellite measurement and model evidence on the dominant regional contribution to fine particulate matter levels in the Paris megacity
Atmos. Chem. Phys. **15** (16): 9577-9591, doi: 10.5194/acp-15-9577-2015 (2015).

L. R. Crilley, W. J. Bloss, J. Yin, D. C. S. Beddows, R. M. Harrison, J. D. Allan, D. E. Young, M. Flynn, P. Williams, P. Zotter, A. S. H. Prevot, M. R. Heal, J. F. Barlow, C. H. Halios, J. D. Lee, S. Szidat, C. Mohr
Sources and contributions of wood smoke during winter in London: assessing local and regional influences
Atmos. Chem. Phys. **15** (6): 3149-3171, doi: 10.5194/acp-15-3149-2015 (2015).

P. L. Hayes, A. G. Carlton, K. R. Baker, R. Ahmadov, R. A. Washenfelder, S. Alvarez, B. Rappenglück, J. B. Gilman, W. C. Kuster, J. A. de Gouw, P. Zotter, A. S. H. Prévôt, S. Szidat, T. E. Kleindienst, J. H. Offenberg, P. K. Ma, J. L. Jimenez
Modeling the formation and aging of secondary organic aerosols in Los Angeles during CalNex 2010
Atmos. Chem. Phys. **15** (10): 5773-5801, doi: 10.5194/acp-15-5773-2015 (2015).

A. Kotrschal, A. Corral-Lopez, S. Szidat, N. Kolm
The effect of brain size evolution on feeding propensity, digestive efficiency and juvenile growth
Evolution, 69, 3013-3020, doi:10.1111/evo.12784 (2015).

J. P. Krüger, J. Leifeld, S. Glatzel, S. Szidat, C. Alewell
Biogeochemical indicators of peatland degradation – a case study of a temperate bog in northern Germany
Biogeosciences **12** (10): 2861-2871, doi: 10.5194/bg-12-2861-2015 (2015).

S. Liu, A. C. Aiken, K. Gorkowski, M. K. Dubey, C. D. Cappa, L. R. Williams, S. C. Herndon, P. Massoli, E. C. Fortner, P. S. Chhabra, W. A. Brooks, T. B. Onasch, J. T. Jayne, D. R. Worsnop, S. China, N. Sharma, C. Mazzoleni, L. Xu, N. L. Ng, D. Liu, J. D. Allan, J. D. Lee, Z. L. Fleming, C. Mohr, P. Zotter, S. Szidat, A. S. H. Prevot
Enhanced light absorption by mixed source black and brown carbon particles in UK winter
Nat. Commun. **6**, doi: ARTN 8435 10.1038/ncomms9435 (2015).

G. O. Mouteva, S. M. Fahrni, G. M. Santos, J. T. Randerson, Y. L. Zhang, S. Szidat, C. I. Czimczik
Accuracy and precision of C-14-based source apportionment of organic and elemental carbon in aerosols using the Swiss_4S protocol
Atmos. Meas. Tech. **8** (9): 3729-3743, doi: 10.5194/amt-8-3729-2015 (2015).

B. Nozière, M. Kalberer, M. Claeys, J. Allan, B. D'Anna, S. Decesari, E. Finessi, M. Glasius, I. Grgić, J. Hamilton, T. Hoffmann, Y. Iinuma, M. Jaoui, A. Kahnt, C.J. Kampf, I. Kourtchev, W. Maenhaut, N. Marsden, S. Saarikoski, J. Schnelle-Kreis, J.D. Surratt, S. Szidat, R. Szmigielski, A. Wisthaler
The molecular identification of organic compounds in the atmosphere: State of the art and challenges
Chem. Rev., 115, 3919-3983, doi:10.1021/cr5003485 (2015).

G. Salazar, Y.L. Zhang, K. Agrios, S. Szidat
Development of a method for fast and automatic radiocarbon measurement of aerosol samples by online coupling of an elemental analyzer with a MICADAS AMS
Nucl. Instr. Meth. B, 361, 163-167, doi:10.1016/j.nimb.2015.03.051 (2015).

C. Solís, E. Chávez, M.E. Ortiz, E. Andrade, E. Ortíz, S. Szidat, L. Wacker
AMS-C14 analysis of graphite obtained with an Automated Graphitization Equipment (AGE III) from aerosol collected on quartz filters
Nucl. Instr. Meth. B, 361, 419-422, doi:10.1016/j.nimb.2015.05.027 (2015).

Y.-L. Zhang, R.-J. Huang, I. El Haddad, K.-F. Ho, J.-J. Cao, Y. Han, P. Zotter, C. Bozzetti, K.R. Daellenbach, F. Canonaco, J.G. Slowik, G. Salazar, M. Schwikowski, J. Schnelle-Kreis, G. Abbaszade, R. Zimmermann, U. Baltensperger, A.S.H. Prévôt, S. Szidat
Fossil vs. non-fossil sources of fine carbonaceous aerosols in four Chinese cities during the extreme winter haze episode of 2013
Atmos. Chem. Phys. 15, 1299-1312, doi:10.5194/acp-15-1299-2015 (2015).

Y.L. Zhang, M. Cerqueira, G. Salazar, P. Zotter, Ch. Hueglin, C. Zellweger, C. Pio, A.S.H. Prévôt, S. Szidat
Wet deposition of fossil and non-fossil derived particulate carbon: insights from radiocarbon measurement
Atmos. Environ., 115, 257-262, doi:10.1016/j.atmosenv.2015.06.005 (2015).

Y.L. Zhang, J. Schnelle-Kreis, G. Abbaszade, R. Zimmermann, P. Zotter, R.-R. Shen, K. Schaefer, L. Shao, A. Prevot, S. Szidat
Source apportionment of elemental carbon in Beijing, China: insights from radiocarbon and organic marker measurements
Environ. Sci. Technol., 49, 8408-8415, doi:10.1021/acs.est.5b01944 (2015).

REPORTS AND TECHNICAL NOTES

T. Stocker, P. Dürring, R. Fischer, R. Purtschert, T. Wagner, S. Szidat, C. Schlosser, M. Konrad, S. Schmid, J. Eikenberg, R. Siegwolf
Kohlenstoff-14, Krypton-85, Argon-37
Bundesamt für Gesundheit (BAG), Report „Umweltradioaktivität und Strahlendosen in der Schweiz 2014“, S. 98-108, Juli 2015.

M. Sigl, J.R. McConnell, M. Toohey, G. Plunkett, F. Ludlow, M. Winstrup, S. Kipfstuhl, Y. Motizuki
The history of volcanic eruptions since Roman times
Past Global Changes Magazine Vol. 23 (2), 48-49 (2015).

CONTRIBUTIONS TO CONFERENCES, WORKSHOPS AND SEMINARS

HEAVY ELEMENTS

N.M. Chiera, N. V. Aksenov, Y. V. Albin, G. A. Bozhikov, V. I. Chepigin, S. N. Dmitriev, R. Dressler, R. Eichler, V. Ya. Lebedev, O. N. Malyshev, O. V. Petrushkin, D. Piguet, Y.A. Popov, A. V. Sabel'nikov, P. Steinegger, A. I. Svirikhin, A. Türler, G. K. Vostokin, A. Vögele, A. V. Yeremin
Towards selenides of the SHE copernicium and flerovium - unexpected Cn-Se bond observation
5th International Conference on the Chemistry and Physics of the Transactinide Elements TAN 2015, Urabandai, Fukushima, Japan, 25-29 May, 2015.

N.M. Chiera, N. V. Aksenov, Y. V. Albin, G. A. Bozhikov, V. I. Chepigin, S. N. Dmitriev, R. Dressler, R. Eichler, V. Ya. Lebedev, O. N. Malyshev, O. V. Petrushkin, D. Piguet, Y.A. Popov, A. V. Sabel'nikov, P. Steinegger, A. I. Svirikhin, A. Türler, G. K. Vostokin, A. Vögele, A. V. Yeremin
Towards Cn and Fl selenides: unexpected Cn-Se bond formation
TASCA15 – 14th Workshop on Recoil Separator for Superheavy Element Chemistry, GSI, Darmstadt, Germany, 23 October, 2015.

R. Eichler
Gas phase chemistry with SHE – Experiments
SHE Symposium College Station, Texas, 30 March - 1 April, 2015.

R. Eichler
Chemical Investigation of SHE at PSI and University of Bern
FLNR Dubna Seminar series, Dubna, Russian Federation, 23 April, 2015.

R. Eichler
Superheavy Element Chemistry: New Experimental Results Challenge Theoretical Understanding
Symposium New Horizons 2015, Makutsi farm, South Africa, 22-29 November, 2015.

R. Eichler
Gas phase chemical investigation of element 113 and beyond
The International Chemical Congress of Pacific Basin Societies (Pacifichem), Honolulu, Hawaii, USA, 15-20 December, 2015.

H.W. Gäggeler, P. Schwerdtfeger, A. Hermann, N. Gaston
Correlation between single-atom adsorption enthalpies and solid-state properties
Convergence of Theory & Experiment in Heavy Element Chemistry, ACS National Meeting, Denver CO, USA, 25 March, 2015.

H.W. Gäggeler, I. Usoltsev, R. Eichler
Can NO replace CO for formation of volatile compounds with d-elements?
5th International Conference on the Chemistry and Physics of the Transactinide Elements TAN 2015, Urabandai, Fukushima, Japan, 25-29 May, 2015.

H.W. Gäggeler
Memories from my post-doctoral stay in Gurgen's group from 1975-76
FLNR Dubna, Dubna, Russian Federation, 12 October, 2015.

P. Steinegger, M. Asai, R. Dressler, R. Eichler, Y. Kaneya, A. Mitsukai, Y. Nagame, D. Piguet, T. K. Sato, M. Schädel, S. Takeda, A. Toyoshima, K. Tsukada, A. Türler, A. Vascon
On-line Isothermal Vacuum Chromatography of Tl on Quartz
5th International Conference on the Chemistry and Physics of the Transactinide Elements TAN 2015, Urabandai, Fukushima, Japan, 25-29 May, 2015.

P. Steinegger
Diamond detectors, Tl adsorption on quartz (and E113)
TASCA15 – 14th Workshop on Recoil Separator for Superheavy Element Chemistry, GSI, Darmstadt, Germany, 23 October, 2015.

P. Steinegger
Adsorption interaction of Tl on quartz: the role of diamond
4th ADAMAS Workshop, GSI, Darmstadt, Germany, 2-4 December, 2015.

A. Türler
Chemistry Experiments for Transactinide Elements (plenary talk)
5th International Conference on the Chemistry and Physics of the Transactinide Elements TAN 2015, Urabandai, Fukushima, Japan, 25-29 May, 2015.

A. Türler on behalf of the Carbonyl collaboration
Carbonyl chemistry developments for SHE studies
TASCA15 – 14th Workshop on Recoil Separator for Superheavy Element Chemistry, GSI, Darmstadt, Germany, 23 October, 2015.

A. Türler
Present status and future plans of chemical experiments with superheavy elements at PSI/UNIBE
The International Chemical Congress of Pacific Basin Societies (Pacifichem), Honolulu, Hawaii, USA, 15-20 December, 2015.

I. Usoltsev, R. Eichler on behalf of the Carbonyl collaboration
Probing the thermal stability of group VI metal hexacarbonyl complexes
5th International Conference on the Chemistry and Physics of the Transactinide Elements TAN 2015, Urabandai, Fukushima, Japan, 25-29 May, 2015.

SURFACE CHEMISTRY

M. Ammann
In situ X-ray photoelectron spectroscopy on ice, mineral oxides and aqueous solutions of atmospheric relevance
Seminar in Solid State Physics, University of Zürich, Switzerland, 18 November, 2015.

M. Ammann
Hockey, Waboba or snorkeling at the halide solution air interface
Gordon Research Conference, Waterville, New Hampshire, USA, 2-8 August, 2015.

L. Artiglia, F. Orlando, M.-T. Lee, M. Ammann
Reaction of gas phase ozone with shikimic acid aqueous solution investigated by in situ –XPS
2nd Ambient Pressure X-Ray Photoelectron Spectroscopy Workshop, Berkeley, USA, 7-9 December, 2015.

T. Bartels-Rausch
Can laboratory data explain field observations: The fluxes of HNO_3 and HNO_4 from snow in the lab and in Antarctica
European Geoscience Union General Assembly, Vienna, Austria, 12-17 April, 2015.

T. Bartels-Rausch, M. Ammann, F. Orlando, L. Artiglia, X. Kong, A. Waldner, Th. Huthwelker
The nature of frozen salt solutions: A new in-situ XPS approach
Swiss Geoscience Meeting, Basel, Switzerland, 20-21 November, 2015.

X. Kong, A. Waldner, F. Orlando, M. Ammann, T. Bartels-Rausch
Adsorption and dissociation of acidic trace gases on ice surfaces
Seminar of Laboratoire PhLAM - UFR de Physique, Lille, France, 27 October, 2015.

M.-T. Lee
Composition of the Sea-Salt Solution-Air Interface as Affected by Organics
Seminar of the Laboratory of Radiochemistry and Environmental Chemistry, Paul Scherrer Institut and University of Berne, Villigen, Switzerland, 8 May, 2015.

M.-T. Lee, M. A. Brown, F. Orlando, S. Kato, A. Kleibert, A. Türler, M. Ammann
The Competition between organics and bromide at the aqueous solution–air interface as seen from X-ray photoelectron spectroscopy
SAOG - Swiss Working Group for Surface and Interface Science, Fribourg, Switzerland, 23 January, 2015.

F. Orlando, A. Waldner, M.T.-Lee, M. Birrer, T. Bartels-Rausch, C. Proff, J. v. Bokhoven, M. Ammann
A novel analysis chamber for near ambient pressure XPS of solid surfaces for environmental and catalysis research
SAOG - Swiss Working Group for Surface and Interface Science, Fribourg, Switzerland, 23 January, 2015.

F. Orlando, A. Waldner, M.T.-Lee, M. Birrer, T. Bartels-Rausch, C. Proff, Th. Huthwelker, A. Kleibert, J. v. Bokhoven, M. Ammann
Near Ambient Pressure XPS at the SLS – In Situ Cell Design for Solid/Vapor Interfaces and First Results in Environmental TiO_2 Photocatalysis
American Chemical Society 62nd International Symposium & Exhibition, San Jose, California, USA, 18-23 October, 2015.

A. Waldner
The new NAPP chamber at SLS and its implications for ice research
Seminar of the Laboratory of Radiochemistry and Environmental Chemistry, Paul Scherrer Institut and University of Berne, Villigen, Switzerland, 16 October, 2015.

A. Waldner, F. Orlando, M. Ammann, A. Kleibert, Th. Huthwelker, T. Peter, T. Bartels-Rausch
Adsorption and dissociation of acidic trace gases on ice surfaces - Caught in the act with core level spectroscopy
European Geoscience Union General Assembly, Vienna, Austria, 12-17 April, 2015.

A. Waldner, F. Orlando, M. Birrer, M. Ammann, Th. Huthwelker, T. Bartels-Rausch
Acidic trace gas adsorption on ice: XPS and NEXAFS analysis with the new NAPP solid chamber at SLS
Swiss Geoscience Meeting, Basel, Switzerland, 20-21 November, 2015.

A. Waldner, F. Orlando, M. Birrer, M. Ammann, Th. Huthwelker, T. Bartels-Rausch
Acidic tarce gas interaction with ice: XPS analysis with the new NAPP chamber for solid interfaces at SLS
2nd Ambient Pressure X-Ray Photoelectron Spectroscopy Workshop, Berkeley, USA, 7-9 December, 2015.

A. Waldner, F. Orlando, M. Birrer, M. Ammann, Th. Huthwelker, A. Kleibert, T. Peter, T. Bartels-Rausch
Interaction of acidic trace gases with ice
Swiss Global Change Day, Bern, Switzerland, 1 April, 2015.

ANALYTICAL CHEMISTRY

S.E. Avak, M. Birrer, M. Wälle, T. Bartels-Rausch, M. Schwikowski, A. Eichler
Development of a cryocell for high-resolution trace element analysis of ice cores using LA-ICP-MS, 13th Swiss Geoscience Meeting, University of Basel, Switzerland, 20-21 November, 2015.

S.O. Brügger, E. Gobet, M. Sigl, D. Osmont, D. Colombaroli, M. Schwikowski, W. Tinner
FROZENFIRE – a contribution to Paleo Fires from high-alpine ice cores over the last two millennia
14th International Swiss Climate Summer School 2015 "Extreme events and climate, Ascona, Switzerland, 23-28 August 2015.

A. Eichler, G. Gramlich, T. Kellerhals, L. Tobler, M. Schwikowski
Ice core based Pb pollution from gasoline in South America in the context of a 2000 year metallurgical history, European Geosciences Union General Assembly 2015, Vienna, Austria, 12-17 April, 2015.

R. Dadic, M. Schneebeli, N. Bertler, M. Schwikowski, N. Matzl
Extreme metamorphism in a firn core from the Allan Hills, Antarctica, as an analogue for glacial conditions
European Geosciences Union General Assembly 2015, Vienna, Austria, 12-17 April, 2015.

A. Dal Farra
Effect of particulate matter on the albedo of Alpine glaciers
First Year Graduate Student Symposium of the Department of Chemistry and Biochemistry 2015, University of Bern, Switzerland, 8-9 September, 2015.

A. Dal Farra, M. Schwikowski
Effect of particulate matter on the albedo of Alpine glaciers
13th Swiss Geoscience Meeting, University of Basel, Switzerland, 20-21 November, 2015.

V. Goel, K. Matsuoka, J. Brown, A. Eichler, E. Isaksson, T. Martma, M. Schwikowski, C.P. Vega
Recent thickening of the Blåskimen Ice Rise in western Dronning Maud Land
XII International Symposium on Antarctic Earth Sciences, Goa, India, 13-17 July, 2015.

M.M. Grieman, E.S. Saltzman, J.R. McConnell, D. Fritzsche, T. Opel, E. Isaksson, M. Schwikowski
Arctic ice core records of vanillic acid from Siberia, Greenland, and Svalbard
AGU Fall Meeting, San Francisco, USA, 14-18 December, 2015.

T.M. Jenk, A. Ciric, L. Tobler, H.W. Gäggeler, U. Morgenstern, G. Casassa, M. Lüthi, J. Schmitt, M. Schwikowski
The Mercedario ice core - an excellent archive for ENSO reconstruction
European Geosciences Union General Assembly 2015, Vienna, Austria, 12-17 April, 2015.

T.M. Jenk, A. Graesslin-Ciric, L. Tobler, H.W. Gäggeler, U. Morgenstern, G. Casassa, M. Lüthi, J. Schmitt, A. Eichler, M. Schwikowski
Reconstruction of El Niño-Southern Oscillation from the Mercedario ice core
26th International Union of Geodesy and Geophysics (IUGG) General Assembly 2015, Prague, Czech Republic, 22 June-2 July, 2015.

D. Osmont, M. Sigl, L. Schmidely, I. Wendl, E. Isaksson, M. Schwikowski
A 250 year black carbon record from the Lomonosovfonna ice core, Svalbard
13th Swiss Geoscience Meeting, University of Basel, Switzerland, 20-21 November 2015.

J. Schmale, M. Flanner, M. Sprenger, S. Kang, J. Guo, Y. Li, Q. Zhang, M. Schwikowski
Dust, elemental carbon and other impurities on Central Asian glaciers: origin and radiative forcing
European Aerosol Conference, Milano, Italy, 6-11 September, 2015.

J. Schmale, M. Flanner, S. Kang, M. Sprenger, Q. Zhang, Y. Li, J. Guo, M. Schwikowski
Dust, elemental carbon and other impurities on Central Asian glaciers: origin and radiative forcing
AGU Fall Meeting, San Francisco, USA, 14-18 December, 2015.

M. Schwikowski, M. Sigl
The Tambora eruption as seen in high-alpine ice cores
Volcanoes, Climate and Society – Bicentenary of the great Tambora eruption. Bern, Switzerland, 7-10 April, 2015.

M. Schwikowski
European pollution history recorded in Colle Gnifetti ice cores
13th Swiss Geoscience Meeting, Basel, Switzerland, 20-21 November, 2015.

M. Sigl
Volcanic eruptions and global climate impact
Seminar of the Laboratory of Radiochemistry and Environmental Chemistry, Paul Scherrer Institut and University of Berne, Villigen, Switzerland, 6 March, 2015.

M. Sigl, J. R. McConnell, G. Plunkett, F. Ludlow
Volcanic Eruptions that Shook the World
16th Swiss Global Change Day, Bern, Switzerland, 1 April, 2015.

M. Sigl, M. Winstrup, J. R. McConnell, K. C. Welten, G. Plunkett, F. Ludlow, M. Toohey, U. Büntgen, M. Caffee, H. Fischer, S. Kipfstuhl, F. Mekhaldi, K. Krüger, R. Mulvaney, J. R. Pilcher, B. Vinther, T. E. Woffruff
A detailed history of stratospheric sulphate loading from Tambora-like eruptions during the Common Era from a new bipolar ice-core array
Volcanoes, Climate and Society – Bicentenary of the great Tambora eruption, Bern, Switzerland, 7-10 April, 2015.

M. Sigl, J. R. McConnell, M. Winstrup, T. J. Fudge, J. Cole-Dai, D. Ferris, K. Taylor, C. Buizert, R. Rhodes, K. McGwire, K. C. Welten, T. E. Woodruff, N. Dunbar, N. Iverson, O. J. Maselli, D. R. Pasteris, R. Muscheler
WD2014: A new reference chronology for ice cores from Antarctica?
European Geosciences Union General Assembly, Vienna, Austria, 12-17 April, 2015

M. Sigl, J. R. McConnell, M. Winstrup, K. C. Welten, G. Plunkett, F. Ludlow, M. Toohey, U. Büntgen, M. Caffee, S. Kipfstuhl, C. Kostick, K. Krüger, O. J. Maselli, R. Mulvaney, and T. E. Woodruff
Timing, global aerosol forcing, and climate impact of volcanic eruptions during the Common Era
European Geosciences Union General Assembly, Vienna, Austria, 12-17 April, 2015.

M. Sigl, M. Toohey
Towards new volcanic forcing for PMIP6
European Geosciences Union General Assembly, Splinter meeting: PMIP Past2K: Boundary Conditions for Late Holocene Simulations in CMIP6, Vienna, Austria, 12-17 April, 2015.

M. Sigl, J.R. McConnell, M. Winstrup, T.J. Fudge, J. Cole-Dai, D. Ferris, K. Taylor, K. McGwire, K.C. Welten, T.E. Woodruff, R. Muscheler
A precise ice-core chronology from Antarctica for the past 31,000 years
General Assembly of the International Union of Geodesy and Geophysics (IUGG), Prague, Czech Republic, 22 June -2 July, 2015.

M. Sigl, J.R. McConnell, M. Winstrup, M. Toohey, K. Welten, G. Plunkett, F. Ludlow, U. Büntgen, K. Krüger
Stratospheric sulfate aerosol loading, timing, and climate impact of volcanic eruptions during the Common Era
General Assembly of the International Union of Geodesy and Geophysics (IUGG), Prague, Czech Republic, 22 June -2 July, 2015.

M. Sigl, J.R. McConnell, M. Winstrup, G. Plunkett, F. Ludlow, C. Kostick, K. Welten, M. Toohey, K. Krüger, U. Büntgen, M. Baillie
Volcanic Eruptions and Global Climate Impact
Our Common Future Under Climate Change, International Scientific Conference, Paris, France, 7-10 July, 2015.

M. Sigl
An annually-dated ice-core chronology of ^{10}Be concentrations and volcanic activity from Antarctica for the past 15,000 years
International Zürich IntCal-Dendro Meeting, Birmensdorf, Switzerland, 4 August, 2015.

M. Sigl
A volcanic climate crisis in the Late Antiquity
Seminar Glaziologie: Alfred-Wegener-Institut Helmholtz-Zentrum für Polar- und Meeresforschung, Bremerhaven, Germany, 20 August, 2015.

M. Sigl
Volcanoes, ice-cores and tree-rings: one story or two?
Seminar School of Geography, Archaeology and Palaeoecology, Queen's University, Belfast, UK., 23 August, 2015.

M. Sigl
A common precise timescale for ice cores in Antarctica during the Common Era
PAGES 2k Meeting, Venice, Italy, 3-4 September, 2015.

M. Sigl
Ice-core dating versus dendrochronology
PIRE/ICEICS International Workshop, Grenoble, France, 9-11 September, 2015.

M. Sigl
Colle Gnifetti BC status report
Paleo fires from high-alpine ice cores, Annual Meeting, Zürich, Switzerland, 30 November, 2015.

C. Steinlin, C. Bogdal, P. Pavlova, M. Schwikowski, M. Lüthi, M. Scheringer, P. Schmid, K. Hungerbühler
Release of polychlorinated biphenyls from a temperate alpine glacier
35th Int. Symp. on Halogenated Persistent Organic Pollutants (Dioxin2015), São Paulo, Brazil, 23-28 August, 2015.

W. Tinner, M. Schwikowski, A. Eichler, U. Lohmann, S. Wunderle
Combining frozen fire, vegetation and climate records with satellite and modelling approaches
XIX INQUA Congress on Quaternary Perspectives on Climate Change, Natural Hazards and Civilization, Nagoya, Japan, 27 July-2 August, 2015.

C. Uglietti, A. Zapf, S. Szidat, G. Salazar, D. Hardy, M. Schwikowski
The controversial age of Kilimanjaro's plateau glaciers
European Geosciences Union General Assembly 2015, Vienna, Austria, 12-17 April 2015.

C. Uglietti, A. Zapf, T.M. Jenk, S. Szidat, G. Salazar, D. Hardy, M. Schwikowski
The controversial debate on the basal age of Kilimanjaro's plateau glaciers
26th International Union of Geodesy and Geophysics (IUGG) General Assembly 2015, Prague, Czech Republic, 22 June-2 July 2015.

C. Zuth, C. Müller-Tautges, A. Eichler, M. Schwikowski, T. Hoffmann
Non-Target Analyses of organic compounds in ice cores using HPLC-ESI-UHRMS
European Geosciences Union General Assembly 2015, Vienna, Austria, 12-17 April 2015.

RADWASTE ANALYTICS

M. Barbagallo, A. Musumarra, L. Cosentino, N. Colonna, P. Finocchiaro, A. Pappalardo, L. Damone, O. Aberle, B. Langhans, D. Schumann, E. Maugeri, S. Heinitz, R. Dressler, J. Andrzejewsky, J. Perkowski and the n_TOF Collaboration
Measurement of ^{7}Be(n,cp) at n_TOF: a big challenge for sample preparation and experimental setups
CHANDA Workshop on target preparation – the needs and the possibilities, Paul Scherrer Institut, Villigen, Switzerland, 23-25 November, 2015.

R. Dressler, D. Schumann,
53Mn – the aims, the needs and the problems
CHANDA Workshop on target preparation – the needs and the possibilities, Paul Scherrer Institut, Villigen, Switzerland, 23-25 November, 2015.

I. Duran, C. Paradela, L. Tassan-Got, D.Tarrio, E. Leal-Cidoncha, L-S. Leong, L. Audouin
On behalf of the n_TOF Collaboration
CERN-nTOF ^{235}U(n,f) cross-section in the Resolved Resonance Region
Wonder 2015: Fourth International Workshop on Nuclear Data Evaluation for Reactor Applications, Aix-en-Provence, France, 5-8 October, 2015.

C. Guerrero, C. Domingo-Pardo, S. Heinitz, U. Köster, J. Lerendegui-Marco, D. Schumann et al.,
Production (at ILL and PSI) and use (at n_TOF) of radioactive targets for nuclear astrophysics
CHANDA Workshop on target preparation – the needs and the possibilities, Paul Scherrer Institut, Villigen, Switzerland, 23-25 November, 2015.

St. Heinitz
Target manufacturing at PSI, CHANDA Workshop on target preparation – the needs and the possibilities,
CHANDA Workshop on target preparation – the needs and the possibilities, Paul Scherrer Institut, Villigen, Switzerland, 23-25 November, 2015.

E. E. Kading, M. Gai, M. Kahn, M. Lee, M. Tessler, M. Paul, A. Weiss, D. Berkovitz, S. Halfon, D. Kijel, A. Kreisler, A. Shor, I. Silverman, L. Weissman, M. Hass, I. Mukul, E. A. Maugeri, R. Dressler, D. Schumann, S. Heinitz, T. Stora, D. Ticehurst, C.R. Howell
Toward measurements of neutron interactions with 7Be and the primordial 7Li problem
CHANDA Workshop on target preparation – the needs and the possibilities, Paul Scherrer Institut, Villigen, Switzerland, 23-25 November, 2015.

E. Leal-Cidoncha, I. Duran, C. Paradela, D.Tarrio, L. Tassan-Got, L-S. Leong, L. Audouin and the n_TOF Collaboration
Fission Fragment Angular Distribution measurements of ^{235}U and ^{238}U at CERN-nTOF facility.
Fourth International Workshop on Nuclear Data Evaluation for Reactor Applications, Aix-en-Provence, France, 5-8 October, 2015.

E. Maugeri, S. Heinitz, R. Dressler, D. Schumann
Isotope production at PSI and 7Be target preparation
CHANDA Workshop on target preparation – the needs and the possibilities, Paul Scherrer Institut, Villigen Switzerland, 23-25 November, 2015.

J. Neuhausen
Chemistry of volatile radionuclides
MYRTE Kick-off Meeting, SCK·CEN, Mol, Belgium, 14 April, 2015.

J. Neuhausen
SEARCH WP6 - Release, Gas phase transport and Capture Studies of Volatiles & Task6.1
Joint SEARCH 6th and MAXSIMA 4th semi-annual review meeting, SCK·CEN, Mol, Belgium, 21 April, 2015.

J. Neuhausen
Status WP4 Chemistry of volatile radionuclides
MYRTE 1st TEC-Meeting, SCK·CEN, Brussels, Belgium, 29 October, 2015.

J. Neuhausen
Status WP4 Chemistry of volatile radionuclides
MYRTE 1st Governing Board Meeting, SCK·CEN, Brussels, Belgium, 29 October, 2015.

D. Schumann
Target preparation at PSI
n_TOF collaboration meeting, CERN, Geneva, Swiotzerland, 2-4 December, 2015.

D. Schumann
Exotic Radionuclides from Accelerator Waste for Science and Technology (ERAWAST)
NuPECC annual meeting, Basel, Switzerland, 12 June, 2015.

D. Schumann, J. Neuhausen, B. Hammer-Rotzer, M. Wohlmuther, D. Kiselev, V. Boutellier, H.-P. Linder, N. Sherbina
Radiochemical Analytics of the MEGAPIE target
ENSI seminar, Brugg, Switzerland, 21-22 May, 2015.

D. Schumann
Contribution of PSI to WP3
CHANDA collaboration meeting, Paris, France, 27-29 April, 2015.

D. Schumann
Contribution of PSI to WP11
CHANDA collaboration meeting, Paris, France, 27-29 April, 2015.

D. Schumann
Radiochemical Analysis of structure material
CHANDA meeting WP11, Dresden, Germany, 19 February, 2015.

D. Schumann
ERAWAST
CHANDA meeting WP3, Paul Scherrer Institut, Villigen, Switzerland, 15 April, 2015.

Tarifeño-Saldivia, C. Domingo-Pardo, J. L. Tain, J. Monserrate, F. Calviño, A. Casanovas, C. Guerrero, J. Lerendegui, S. Heinitz, N. Kivel, U. Koester, D. Schumann and The n_TOF Collaboration,
Characterization of the spatial distribution of high radioactive targets for capture cross section measurements of s-process branching nuclei at CERN n_TOF
CHANDA Workshop on target preparation – the needs and the possibilities, Paul Scherrer Institut, Villigen, Switzerland, 23-25 November, 2015.

B. Thomas, R. Dressler, U. Gießen, O. Hinrichs, M. Reich, R. Reifarth, S. Schmidt, D. Schumann, K. Sonnabend
The production of a ^{91}Nb –Target,
CHANDA Workshop on target preparation – the needs and the possibilities, Paul Scherrer Institut, Villigen, Switzerland, 23-25 November, 2015.

RADIONUCLIDE DEVELOPMENT

K. Domnanich
Studies towards matched pair theragnostics
Seminar of the Laboratory of Radiochemistry and Environmental Chemistry, Paul Scherrer Institut and University of Berne, Bern, Switzerland, 8 May, 2015.

K. Domnanich
^{43}Sc Production Development by Cyclotron Irradiation of ^{43}Ca and ^{46}Ti
GDCH-Wissenschaftsforum, Dresden, Germany, 31 August, 2015.

N. van der Meulen
Production and Application of ^{44}Sc Towards Clinical PET Imaging of Cancer
ICRT2015, Innsbruck, Austria, 6 May, 2015.

N. van der Meulen
Using the "matched pair" principle in radionuclide development for theragnostics
250th ACS Meeting, Boston, USA, 18 August, 2015.

N. van der Meulen
Tb radionuclides separated at ISOLDE; processed and used for radiolabelling and imaging experiments at PSI: an update"
External meeting with CHUV/MEDICIS, CERN, Geneva, Switzerland, 15 October, 2015.

N. van der Meulen,
^{44}Sc: from bench to bedside
The International Chemical Congress of Pacific Basin Societies (Pacifichem), Honolulu, Hawaii, USA, 15-20 December, 2015.

C. Vermeulen
Isotopes Tb-149 and Tb-152 in preclinical investigations: Report on the successes and challenges of the 2015 Medical Isotope Campaign for IS528",
ISOLDE Workshop and Users Meeting 2015, Geneva, Switzerland, 3 December, 2015.

ENVIRONMENTAL RADIONUCLIDES UNIVERSITÄT BERN

K. Agrios
Direct ^{14}C AMS measurements for carbonaceous aerosols source apportionment
Seminar of the Laboratory of Radiochemistry and Environmental Chemistry, Paul Scherrer Institute and University of Bern, Bern, Switzerland, 17 April, 2015.

K. Agrios, G. Salazar, S. Szidat
Online coupling of thermal-optical and radiocarbon analysis – deeper insight into sources of organic aerosols
European Aerosol Conference 2015, Milan, Italy, 6-11 September, 2015.

K. Agrios, G. Salazar, S. Szidat
Online coupling of thermal-optical and ^{14}C Accelerator Mass Spectrometry analysis in atmospheric aerosols source apportionment
22nd International Radiocarbon Conference, Dakar, Senegal, 16-20 November, 2015.

B.Z. Cvetković, E. Wieland, D. Kunz, G. Salazar, S. Szidat
Development of analytical techniques for the identification of organic species of carbon-14 released during anoxic corrosion of activated steel in a cementitious repository for radioactive waste
Migration 2015 Conference, Santa Fe, USA, 13-18 September, 2015.

S. Hammer, B. Kromer, R. Friedrich, T. Nakamura, V. Palonen, R. Reimer, S. Szidat, J. Turnbull, I. Levin
Compatibility of low level counting (LLC) and accelerator mass spectrometry (AMS) techniques for atmospheric radiocarbon measurements: a status report of the buildup of the ICOS Central Radiocarbon Laboratory (CRL)
18th WMO/IAEA Meeting on Carbon Dioxide, Other Greenhouse Gases and related Measurement Techniques (GGMT-2015), La Jolla (CA), USA, 13-17 September, 2015.

S. Hammer, B. Kromer, R. Friedrich, T. Nakamura, V. Palonen, R. Reimer, S. Szidat, J. Turnbull, I. Levin
Compatibility of low level counting (LLC) and accelerator mass spectrometry (AMS) techniques for atmospheric radiocarbon measurements: a status report of the buildup of the ICOS Central Radiocarbon Laboratory (CRL)
22nd International Radiocarbon Conference, Dakar, Senegal, 16-20 November, 2015.

P.L. Hayes, P.K. Ma, J.L. Jimenez, A.G. Carlton, K.R. Baker, R. Ahmadov, R.A. Washenfelder, S. Alvarez, B. Rappenglück, J.B. Gilman, W.C. Kuster, J.A. de Gouw, P. Zotter, A.S.H. Prévôt, S. Szidat, T.E. Kleindienst, J.H. Offenberg, Y. Zhao, A.L. Robinson
Modeling the formation and aging of secondary organic aerosols in the Los Angeles metropolitan region during the CalNex 2010 field campaign
AGU Fall Meeting 2015, San Francisco (CA), USA, 14-18 December, 2015.

M. Kistler, E.C. Cetintas, Y.L. Zhang, S. Szidat, I. Ježek, L. Drinovec, G. Močnik, H. Bauer, A. Kasper-Giebl
Source apportionment of winter carbonaceous matter in Central Europe – comparison of three methods
11th International Conference on Carbonaceous Particles in the Atmosphere, Berkeley (CA), USA, 10-13 August, 2015.

A. Madella, R. Delunel, S. Szidat, F. Schlunegger
On the uplift anomaly of the Arica Bend, Western Central Andes
European Geosciences Union, General Assembly 2015, Vienna, Austria, 12-17 April, 2015.

N. Marchand, J. Pey, H.L. DeWitt, B. Temime-Roussel, S. Hellebust, A. Même, B. Rmili, B. Charriere, R. Sempere, S. Mas, D. Parin, J.C. Cerro, N. Pérez, C. Rose, A. Schwier, M. Elser, S. Szidat, A.S.H. Prévôt, K. Sellegrini, B. D'Anna
Impact of air-sea exchanges on the Mediterranean marine boundary layer composition
249th ACS National Meeting, Denver (CO), USA, 22-26 March, 2015.

M. Morlock, J. Schilder, M. van Hardenbroek, S. Szidat, M. Wooller, O. Heiri
How does seasonality affect the δ13C values of cladoceran and bryozoan remains in lake sediments?
16th Swiss Global Change Day, Bern, Switzerland, 1 April, 2015.

P. Rinta, M. van Hardenbroek, R.I. Jones, P. Kankaala, F. Rey, S. Szidat, M. Wooller, O. Heiri
Multi-decadal variability in methane cycling in a small forest lake inferred from fossil zooplankton $\delta^{13}C$ analysis
9th Symposium for European Freshwater Sciences, Geneva, Switzerland, 5-10 July, 2015.

G.A. Salazar
^{14}C measurement from Liquid and Gas Samples
Project CAST (CArbon-14 Source Term), WP 2&3 Workshop, PSI, Villigen, Switzerland, 29 May, 2015.

S. Szidat, K. Agrios, G.A. Salazar
Offline and online ^{14}C measurements of carbonaceous aerosols
German Physical Society (DPG), Spring Meeting, Heidelberg, Germany, 23-27 March, 2015.

S. Szidat
Compound-specific radiocarbon analysis: Overview
Project CAST (CArbon-14 Source Term), WP 2&3 Workshop, PSI, Villigen, Switzerland, 29 May, 2015.

S. Szidat, I. El Haddad, A.S.H. Prevot
The benefit of the combination of ^{14}C and AMS analysis for source apportionment of carbonaceous aerosols
11th International Conference on Carbonaceous Particles in the Atmosphere, Berkeley (CA), USA, 10-13 August, 2015.

S. Szidat
Source apportionment of carbonaceous aerosols using ^{14}C: Results from Europe and China
2015 Goldschmidt Conference, Prague, Czech Republic, 16-21 August, 2015.

S. Szidat, E. Vogel, R. Gubler, S. Lösch
Radiocarbon dating of bones at the LARA laboratory at Bern
22nd International Radiocarbon Conference, Dakar, Senegal, 16-20 November, 2015.

V. Ulevicius, S. Bycenkiene, C. Bozzetti, A. Vlachou, K. Plauskaite, G. Mordas, V. Dudoitis, G. Abbaszade, J. Blees, R. Fröhlich, K.R. Dällenbach, F. Canonaco, J.G. Slowik, J. Dommen, R. Zimmermann, J. Schnelle-Kreis, G.A. Salazar, K. Agrios, S. Szidat, I. El Haddad, A.S.H. Prévôt
Fossil and non-fossil source contributions to atmospheric carbonaceous aerosols during grassland fires
European Aerosol Conference 2015, Milan, Italy, 6-11 September, 2015.

A. Vlachou, C. Bozzetti, Y. Sosedova, K.R. Dällenbach, G.A. Salazar, K. Agrios, S. Szidat, I. El Haddad, U. Baltensperger, A.S.H. Prévôt
AMS and Radiocarbon coupled source apportionment of carbonaceous aerosols during one year in Magadino
European Aerosol Conference 2015, Milan, Italy, 6-11 September, 2015.

M. Vonwiller, G.A. Salazar, S. Szidat
Isolation and ^{14}C analysis of humic-like substances (HULIS) from ambient aerosol samples
European Aerosol Conference 2015, Milan, Italy, 6-11 September, 2015.

M. Vonwiller
Isolation and ^{14}C analysis of atmospheric humic-like substances
Seminar of the Laboratory of Radiochemistry and Environmental Chemistry, Paul Scherrer Institute and University of Bern, Bern, Switzerland, 27 November, 2015.

R. Zech, T. Sprafke, S. Knoll, M. Haas, M. Zech, G. Salazar, S. Szidat
Compound-specific radiocarbon dating of leaf waxes in loess-paleosols
European Geosciences Union, General Assembly 2015, Vienna, Austria, 12-17 April, 2015.

PUBLIC RELATIONS AND OUTREACH ACTIVITIES

Radiochemistry

Fenster zur Forschung 2015
Ausgabe 1/2015 Paul Scherrer Institut, ISSN 1664-8854, Herausgeber: Paul Scherrer Institut
January 2015

Analytical Chemistry

ChemieExtra
Die Altlasten des Klimawandels
January/February 2015

Die Botschaft
Benzin schlägt Bergbau
4 March 2015

PSI Media Release
Gasoline beats mining
6 March 2015

SchweizerischeDepeschenagentur
Verbleites Benzin dominierte Bleiemissionen in Südamerika
6 March 2015

Neue Zürcher Zeitung, online
Luftverschmutzung in Südamerika. Verbleites Benzin schlimmer als Minen
7 March 2015

St. Galler Tagblatt AG
Verbleites Benzin dominierte
7 March 2015

NZZ am Sonntag
Dreckige alte Zeit
15 March 2015

NATURE CAREERS
Climatology on thin ice
16 April 2015

Neue Zürcher Zeitung, online
Ist der Kilimandscharo-Gletscher jünger als gedacht?
21 April 2015

Neue Zürcher Zeitung
Starke Klimazyklen in Afrika. Ist der Kilimandscharo-Gletscher jünger als gedacht?
22 April 2015

Kulturkreis.ch Mellingen, M. Schwikowski
Klimageschichte aus alpinen Eisbohrkernen
28 April 2015

Tages-Anzeiger SonntagsZeitung
Das Klima im Whiskyglas
22 November 2015

Environmental Radionuclides Universität Bern

Homepage Department of Chemistry and Biochemistry, Uni Bern
Molecule of the Month: Aerosol Pollution during Haze Events in China
http://mom.dcb.unibe.ch/mom_pages/mom_2015-01.html
January 2015

Radio SRF 4, HeuteMorgen
Holzheizungen sind die schlimmeren Luftverschmutzer (Radio interview)
http://www.srf.ch/news/schweiz/holzheizungen-sind-die-schlimmeren-luftverschmutzer
http://podcasts.srf.ch/world/audio/HeuteMorgen_14-02-2015-0630.mp3
14 February 2015

NZZ
Cheminées verursachen mehr Feinstaub als Autos (Newspaper article)
http://www.nzz.ch/panorama/feinstaubbelastung-durch-cheminees-erhoeht-1.18485302
18 February 2015

Chimia (Vol. 69, No. 6, p. 368), Highlights of Analytical Sciences in Switzerland
S. Szidat, A.S.H. Prévôt: What are the sources of aerosols during haze events in China?
http://dx.doi.org/10.2533/chimia.2015.368
June 2015

SDBB (Schweizerisches Dienstleistungszentrum Berufsbildung | Berufs-, Studien- und Laufbahnberatung)
Physiklaborant/Physiklaborantin EFZ (brochure)
December 2015

Chemical Laboratory Technician Apprenticeship

Lehrberufe a la carte (Berufsschau am PSI)
June 2015

Sommercamp (Experimente für Primarschüler)
July 2015

Lela Calancatal
Oktober 2015

Zukunftstag am PSI
November 2015

LECTURES AND COURSES

Prof. Dr. A. Türler
Universität Bern, FS2015
Bachelor
- Instrumentalanalytik II (with Dr. K. Krämer and Prof. M. Schwikowski) (3 ECTS)
- Allgemeine Chemie (Einführung Radioaktivität) (with Prof. R. Hähner and Prof. J. Hulliger) (4 ECTS)

Master
- Introduction to Radiopharmaceutical Chemistry (with Dr. M. Behe) (1.5 ECTS)

Universität Bern, HS2015
Bachelor
- Physikalische Chemie IV (with PD P. Broekmann) (3,75 ECTS)
- Praktikum Phys. Chemie II (with others) (4 ECTS)
- Biochemische Methoden I (with others) (3 ECTS)

Master
- Nuclear and Radiochemistry (with Dr. R. Eichler) (3 ECTS)
- Lab course: Nuclear and Radiochemistry at Bern, Basel, ETHZ and PSI (with others) (4 ECTS)
- Seminar Radio- und Umweltchemie in collaboration with Paul Scherrer Institut (organized by Dr. N. van der Meulen FS2015 / HS2015)

Prof. Dr. M. Schwikowski
Universität Bern, FS2015
Bachelor
- Instrumentalanalytik II (with Prof. A. Türler and Dr. K. Krämer) (3 ECTS)

Universität Bern, HS2015
Master
- Summer Course at Paul Scherrer Institut. 2months International Summer Student Programme (with Prof. A. Türler) (4 ECTS)
- Atmospheric and Aerosol Chemistry (3 ECTS)

Prof. Dr. M. Ammann
ETH Zürich, FS2015
Bachelor
- Systempraktikum Atmosphäre und Klima (with others) (7 ECTS)

ETH Zürich, HS2015
Bachelor
- Atmosphärenchemie (with Dr. D. Brunner) (3 ECTS)

Dr. R. Eichler
Universität Bern, HS2015
Master
- Nuclear and Radiochemistry (with Prof. A. Türler) (3 ECTS)

Universität Bern, HS2015
Bachelor
- Praktikum Phys. Chemie II (with Prof. A. Türler) (4 ECTS)

Master
- Lab course: Nuclear and Radiochemistry (with Prof. A. Türler and PD Dr. S. Szidat) (4 ECTS)

PD Dr. S. Szidat
Universität Bern, FS2015
Bachelor
- Ergänzungen zur analytischen Chemie für Pharmaziestudierende (2 ECTS)

Universität Bern, HS2015
Bachelor
- Chemie für Studierende der Veterinärmedizin (with C. Leumann) (4.5 ECTS)
- Praktikum Physikalische Chemie II (with others) (4 ECTS)

Master
- Environmental Radionuclides and Nuclear Dating (1.5 ECTS)
- Lab Course Nuclear and Radiochemistry (with A. Türler and R. Eichler) (4 ECTS)

N. Chiera
- Practice Course “Physical Chemistry I”, DCB University of Bern 2015
- Practice Course Physical Chemistry II “γ-Spectroscopy”, DCB University of Bern 2015

K. Domnanich
- Practice Course "Allgemeine Chemie für Biologen", DCB University of Bern 2015

EDUCATION OF APPRENTICIES AS CHEMISTRY LABORATORY TECHNICIANS

R. Bentz

The vocational training is very important at the Paul Scherrer Institute. 95 apprentices and 3 trainees are employed here. This corresponds to a proportion of about 5 percent of all employees (~ 2000). Already this percentage perfectly demonstrates the status belonging to the vocational training at our research centre.

Among the vocational trainings available at PSI also the apprenticeship as chemical laboratory technician is offered. Three apprentices are employed by PSI per year in this professional direction. Since the training lasts for three years, nine chemical laboratory technician trainees are permanently at PSI. The education and training follows a rotational principle. Thus the trainees work at 10 different research laboratories within PSI:

Atmospheric chemistry
Stable isotope analysis in conjunction with elemental analysis (EAII & Pyro-Cube, HPLC-IRMS, GC-IMRS);

Diffusion processes
Ion chromatography (anions, cations); carbon analysis (TOC, TIC); radiochemical analysis (beta and gamma measurements);

Molecular biology
Various tasks connected to gene expression; gene manipulation at plasmids; DNA preparation and DNA analyses;

Protein biochemistry
Purification of proteins applying various chromatographic methods (FPLC); Biophysical characterization of purified proteins; Help with cultivation of animal and human cells in appropriate nutrient medium;

Radiation protection / Radioanalytics
Various measurement methods including gamma spectrometry and alpha spectrometry using Ge- and Si-surface barrier detectors; alpha/beta liquid scintillation counting and proportional counting;

Bioenergy and catalysis
Exhaust analysis using FTIR, ion selective electrodes; production of catalyst modules with V_2O_5 or Pt/Pd as active components;

Nanotechnology
Binding of proteins to surfaces; characterization of surfaces by contact angle measurements, light microscopy and scanning force microscopy;

Radiopharmacy
Radionuclide labeling of bio molecules including quality control using HPLC; on vitro and ex vivo autoradiography including cryo-thin sectioning;

Organiic Synthesis
Synthesis of organic and inorganic chemicals; analysis of chemicals with UPLC, GC, GC-MS, NMR;

Sulfonation reactions with chlorosulfonic acid HSO_3Cl; *ex-situ* analysis (e.g.: titrations, FT-IR, SEM-EDX [with supervision]), permeation measurements, conduction measurements as function of relative humidity, temperature etc..

http://www.psi.ch/bab/
http://www.psi.ch/bab/laborantin-efz-fachrichtung-chemie

MEMBERS OF SCIENTIFIC COMMITTEES
EXTERNAL ACTIVITIES

Prof. Dr. Markus Ammann
- Atmospheric Chemistry and Physics, member of editorial board
- IUPAC Task Group on Atmospheric Chemical Kinetic Data Evaluation, member
- LabEx MiChem, Sorbonne Universités, Université Pierre et Marie Curie - Paris 06, member

Dr. Thorsten Bartels-Rausch
- Air-Ice Chemical Interactions (IGAC OASIS-AICI), Co-Chair
- Physics and Chemistry of Ice (PCI), member of the scientific committee
- European Geosciences Union General Assembly, Session: Boundary Layers in High Latitudes and Over Snow and Ice: Physics and Chemistry. Co-Convener
- Schweizerische Gesellschaft für Schnee, Eis und Permafrost (SEP), Financial Controller
- Atmospheric Chemistry and Physics, member of editorial board

Dr. Robert Eichler
- PSI internal research commission (FoKo), member
- Associate Editor of the International Journal of Modern Physics E (IJMPE)World Scientific Publishing

Dr. Dorothea Schumann
- PSI internal Neutron Source Development Group, member
- LIEBE, steering committee member

Prof. Dr. Margit Schwikowski
- Schweizerische Gesellschaft für Schnee, Eis und Permafrost (SEP), president
- Swiss Committee on Polar and High Altitude Research of the Swiss Academies of Arts and Sciences (SKPH), member
- Oeschger Centre for Climate Change Research (OCCR), member
- International Partnerships in Ice Core Sciences (IPICS) Steering Committee, member
- 26th General Assembly of the International Union of Geodesy and Geophysics (IUGG), Ice Cores and Climate session, co-convener

Dr. Theo M. Jenk
- European Geosciences Union General Assembly, The state-of-the-art in ice core sciences session, co-convener
- Dataset Papers in Science: Atmospheric Sciences, member of editorial board

Dr. Michael Sigl
- PAGES working group Antarctica2k, co-leader
- PAGES working group Volcanic Impact on Climate and Society, steering committee member

PD Dr. Sönke Szidat
- Bernese Chemical Society (Berner Chemische Gesellschaft, BCG), president
- Oeschger Centre for Climate Change Research (OCCR), member
- Swiss Accreditation Service (SAS), technical expert
- Department of Chemistry and Biochemistry of the University of Bern, head of the non-professorial lecturers (Oberer Mittelbau)

Prof. Dr. Andreas Türler
- Eidgenössische Kommission für Strahlenschutz und Überwachung der Radioaktivität (KSR), Vizepräsident
- Gesellschaft Deutscher Chemiker (GDCh), Fachgruppe Nuklearchemie, Vorstands-Beirat
- Radiochimica Acta, member of the advisory board
- Oeschger Centre for Climate Change Research (OCCR), Mitglied des Wissenschaftlichen Ausschusses
- Nuklearforum Schweiz, Mitglied des Vorstandes
- Member of the Albert Einstein Center for Fundamental Physics (AEC) Bern

Dr. Nicholas van der Meulen
- United States Department of Energy (DOE Isotope R&D FOA), Panel Reviewer
- Accelerator for Research in Radiochemistry and Oncology at Nantes Atlanti (ARRONAX) International Scientific Committee, member

Dr. Christiaan Vermeulen
- International Workshop on Targetry and Target Chemistry (WTTC) Scientific Committee, member

BACHELOR THESIS

Michael Liechti

Investigation of black carbon analysis in snow and ice core samples

Dr. T.M. Jenk / PSI
Prof. Dr. M. Schwikowski / PSI & Uni Bern
May 2015

Simon Schneider

Optimized ^{14}C dating of lake sediments

PD Dr. S. Szidat / Uni Bern
May 2015

Severin Flisch

Preparation of ^{7}Be targets using molecular plating

Dr. Dorothea Schumann / PSI
May 2015

MASTER THESIS

Loïc Schmidely

A 250-years black carbon record spanning the industrial era from the Lomo09 ice core, Svalbard

Prof. Dr. M. Schwikowski / PSI & Uni Bern
October 2015

DOCTORAL THESIS

Bernadette Hammer

Analysis of the nuclide inventory in MEGAPIE, a proton irradiated lead-bismuth eutectic spallation target

Dr. Dorothea Schumann / PSI
Prof. Dr. A. Türler / PSI & Uni Bern
May 2015

Lee Ming-Tao

The Role of organics in the chemical composition and reactivity at the surface of halide solutions relevant for marine aerosol or ocean surface water

Prof. Dr. Markus Ammann / PSI & ETHZ
Prof. Dr. A. Türler / PSI & Uni Bern
October 2015

AWARDS

Anna Dal Farra

Effect of particulate matter on the albedo of alpine glaciers

First Year Graduate Student Symposium of the Department of Chemistry and Biochemistry 2015, University of Bern
September 2015

Anna Dal Farra

Effect of particulate matter on the albedo of Alpine glaciers

The Swiss Snow, Ice and Permafrost Society (SEP) Prize for Young Researchers for the best communication of the Cryospheric Sciences Session, 13th Swiss Geoscience Meeting, Basel
November 2015

Dimitri Osmont

A 250 year black carbon record from the Lomonosovfonna ice core, Svalbard

The Swiss Snow, Ice and Permafrost Society (SEP) Prize for Young Researchers for the best communication of the Cryospheric Sciences Session, 13th Swiss Geoscience Meeting, Basel
November 2015

SUMMER STUDENTS

Anina Gilgen
Reaktion zwischen Ozon und Natriumbromid: Gibt es eine Oberflächenreaktion?
1 April - 7 August 2015

Simon Schneider
Characterization of orifice and capillary flows in the mbar range
29 June - 28 August 2015

Anna Barbara Lichti
Storage and transformation study of red selenium coating
1 July - 31 August 2015

Nadja Niggli
Removal of carbon dioxide and oxygen in a gas mixture
1 July - 31 August 2015

Pascal Nöti
Analysis of stables isotopes and major ions in the Colle Gnifetti ice core
1 July - 31 August 2015

Sarah Pfister
Separation of the long lived lanthanides from proton-irradiated lead targets
1 July - 31 August 2015

Philipp Steffen
Analysis of black carbon in snow and ice samples with the Single Particle Soot Photometer (SP2)
1 July - 31 August 2015

Stephanie Remke
Determination of accumulation rates from a shallow firn core of the Quelccaya Ice Cap
14 September - 18 December 2015

VISITING GUESTS AT PSI 2015

2 - 6 Februar
Marin Ayranov, European Commission, DG-Energy, Luxembourg
Separation of ^{7}Be

13 - 24 April
Eva Mezenen, Gymnasium Köniz-Lerbermatt, Switzerland
^{14}C-Messungen an Blattproben aus der Schweiz

15 - 17 April
Tomasz Goslar, Poznań Radiocarbon Laboratory, Poland
Dating lake and peat sediments in the Poznan ^{14}C lab - from ^{14}C measurements to chronologies

17 April
Karsten Kossert, Physikalisch-Technische Bundesanstalt, Braunschweig, Germany
Liquid scintillation counting with Ac-227, Ra-223 and progeny

8 May
Thomas Mindt, University of Basel, Switzerland
Development of Radiometal-Labelled Peptides for Tumor Targeting

17 - 24 August / 22 November - 4 December
Björn Dittmann, Uni Köln, Germany
Purification of ^{53}Mn samples

7 September - 4 December
Borja Gonzalez-Prieto, SCK·CEN, Mol, Belgium
Adsorption of Po evaporating from LBE on stainless steel and fused silica in various gas atmospheres

18 September
Prof. Dr. Ulrich Scherer, FH Aachen, Germany
From Cyclotron Targets to Waste Management: Nuclear Chemistry Research at FH Aachen

19 - 21 October 2015
Anil Mishra (INMAS, India), as part of the SNF India-Swiss grant:
a technical collaboration to launch ^{44}Sc in India

13 November
Domenico Paladeno, PSI/LTH, Villigen, Switzerland
PANDA: a Multi-Purpose Thermal-Hydraulics Facility devoted to Nuclear Safety Analysis

13 November
Christof Vockenhuber, ETHZ, Zurich, Switzerland
AMS nuclides with isobaric interferences

7 - 9 December
Klaus Kopka, Oliver Neels, Martin Schaefer, Viplav Gupta, DKFZ, Germany
as part of a technical collaboration (44Sc) between PSI and DKFZ

PAUL SCHERRER INSTITUT

LABOR FÜR RADIO- UND UMWELTCHEMIE
DES PAUL SCHERRER INSTITUTS UND DER UNIVERSITÄT BERN
31.12.2015

UNIVERSITÄT BERN

PSI — **Prof. Dr. Andreas Türler** — **Uni Bern**

Angela Blattmann (Secretary / 80 %)
Prof. Dr. Margit Schwikowski (Deputy)

Franziska Bornhauser (Secretary / 20 %)
Brigitte Oggier (Secretary / 20 %)

SURFACE CHEMISTRY
Prof. Dr. Markus Ammann

- Dr. Thorsten Bartels-Rausch
- Dr. Fabrizio Orlando
- Mario Birrer
- Ming-Tao Lee
- Astrid Waldner
- Pablo Corral Arroyo
- Jacinta Edebli

ANALYTICAL CHEMISTRY
Prof. Dr. Margit Schwikowski

- Dr. Theo Jenk (80%)
- Dr. Anja Eichler (70%)
- Dr. Chiara Uglietti
- Dr. Michael Sigl
- Sabina Brütsch
- Silvia Köchli
- Johannes Schindler
- Anna Dal Farra
- Sven Avak
- Dimitri Osmont
- Chaomin Wang
- Chetan Pandit
- Prof. Dr. Susan Kaspari

ENVIRONMENTAL RADIONUCLIDES
PD Dr. Sönke Szidat

- Dr. Gary Salazar
- Edith Vogel
- Michael Battaglia
- Konstantinos Agrios
- Matthias Vonwiller
- Christophe Espic
- Christian Steiner
- Prisca Lehmann
- Jan Strähl

RADIOPHARMACEUTICAL R&D
Dr. Josue Moreno

- Dr. Maruta Bunka
- Dr. Niurka Menese Moreno (60%)
- Oliver Leib
- Tais Basaco Bernabeu

HEAVY ELEMENTS
Dr. Robert Eichler

- Dr. Rugard Dressler
- Dr. Zeynep Talip
- Dave Piguet
- Alexander Vögele
- Nadine Chiera

RADWASTE ANALYTICS
Dr. Dorothea Schumann

- Dr. Jörg Neuhausen
- Dr. Emilio Maugeri
- Dr. Stephan Heinitz (80%)

RADIONUCLIDE DEVELOPMENT
Dr. Nicholas van der Meulen

- Katharina Domnanich
- Nadezda Gracheva
- Dr. Etienne Vermeulen

EDUCATION OF LAB TECHNICIANS / BCDP
Roman Bentz

- David Bölsterli
- Yves Erdin
- Celine Erismann
- Alexandra Kristen
- Dario Meier
- Naomi Peter
- Elio Strebel
- Ben Si Tran
- Xenia Wyss

- Graduate student
- Master student
- Position of CRS
- Apprentice
- Visiting scientist

AUTHOR INDEX

AFFILIATION INDEX

ABE	Abteilung Beschleuniger / Betrieb und Entwicklung (ABE), Paul Scherrer Institut, 5232 Villigen, Switzerland
ABK	Abteilung Beschleuniger Konzepte (ABK), Division Large Research Facilities (GFA), Paul Scherrer Institut, 5232 Villigen, Switzerland
AEC-LHEP	Albert Einstein Center for Fundamental Physics, Sidlerstrasse, 53012 Bern, Switzerland
AHL	Hot Laboratory Division of the Nuclear Energy and Safety Department (NES), Paul Scherrer Institut, 5232 Villigen, Switzerland
ASRC	Advanced Science research Center, Japan Atomic Energy Agency, Tokai, Ibaraki 319-1195, Japan
AtChS	Atmospheric Chemistry Services, Okehampton, Devon EX20 4QB, United Kingdom
BPCRC OSU	Byrd Polar and Climate Research Center, The Ohio State University, 108 Scott Hall, 1090 Carmack Road, Columbus, Ohio 43210-1002, United States
CAREERI CAS	Cold and Arid Regions Environmental and Engineering Research Institute, Chinese Academy of Sciences, Lanzhou, 730000, P.R. China
CAS-UOCHB	Institute of Organic Chemistry and Biochemistry, Academy of Sciences of the Czech Republic, Flemingovo nam. 2, CZ-16610 Prague 6,Czech Republic
CECS	Centro de Estudios Científicos, Valdivia, Chile
CERN-ISOLDE	European Organization for Nuclear Research, CERN CH-1211, Genève 23, Switzerland
CRS	Center for Radiopharmaceutical Sciences, Paul Scherrer Institut, 5232 Villigen, Switzerland
DCB	Departement für Chemie und Biochemie, Universität Bern, Freiestrasse 3, 3012 Bern, Switzerland
Desert Research Institute	2215 Raggio Parkway, 89512 Reno, NV, USA
EMPA	Swiss Federal Laboratories for Materials Science and Technology, Überlandstrasse 129, 8600 Dübendorf, Switzerland
ETHZ	Eidgen. Technische Hochschule Zürich, 8092 Zürich, Switzerland
EU	European Union
FLNR Dubna	Flerov Laboratory of Nuclear Reactions, Joliot-Curie, 6, Dubna, Moscow region 141980, Russia
Ford	Ford Motor Company, Research and Advanced Engineering, Mail Drop RIC-2122, Dearborn, Michigan 481212053
GIUB	Oeschger Centre for Climate Change Research & Institute of Geography, University of Bern, Erlachstrasse 9a T3, 3012 Bern, Switzerland
Goethe University	Goethe University Frankfurt, Theodor-W.-Adorno-Platz 1, 60323 Frankfurt am Main, Germany
ICARE	Institut de Combustion, Aérothermique, Réactivité et Environnement, OSUC, CNRS Centre National de la Recherche Scientifique), France
icedrill	icedrill.ch AG, Schuetzengasse 172, 2502 Biel, Switzerland
ILL	Institut Laue-Langevin, 71 avenue des Martyrs 38000 Grenoble, France
IRCELYON	UNIVERSITE DE LYON, Quartier Sergent Blandan, 37, rue du repos, 69365 LYON CEDEX 07, France
IRS	Institut für Radioökologie und Strahlenschutz, Leibniz Universität Hannover, Herrenhäuser Str. 2, 30419 Hannover, Germany

ITRP CAS	Institute of Tibetan Plateau Research, Chinese Academy of Sciences, Beijing 100101, P.R. China
JAEA	Japan Atomic Energy Agency, Tokai, Ibaraki 319-1195, Japan
JINR	International Intergovernmental Organization, Joint Institute for Nuclear Research Joliot-Curie, 6, Dubna, Moscow region 141980, Russia
KUP	Climate and Environmental Physics, Physics Institute, University of Bern, Sidlerstrasse 5, 3012 Bern, Switzerland
LAC	Laboratory of Atmospheric Chemistry, Paul Scherrer Institut, 5232 Villigen, Switzerland
LBK	Bioenergy and Catalysis Laboratory, Paul Scherrer Institut, 5232 Villigen, Switzerland
MPIC	Max-Planck-Institut für Chemie Division of Atmospheric Chemistry (Otto-Hahn-Institut), Joh.-Joachim-Becher-Weg 27, 55128 Mainz, Germany
NPI	Norwegian Polar Institute, N-9296 Tromsø, Norway
OCCR	Oeschger Centre for Climate Change Research, University of Bern, Falkenplatz 16, 3012 Bern, Switzerland
Province of Bolzano	Department of Environmental Sciences, University of Venice 'Ca' Foscari', Dorsoduro 2137, I-30123 Venice, Italy
PSI	Paul Scherrer Institut, 5232 Villigen, Switzerland
PTB	Physikalisch-Technische Bundesanstalt, Bundesallee 100, 38116 Braunschweig, Germany
SCK CEN	Belgian Nuclear Research Centre, Boeretang 200, B-2400 Mol, Belgium
SLF	Institut für Schnee- und Lawinenforschung, Flüelastrasse 11, 7260 Davos Dorf, Switzerland
SLS	Swiss Light Source, Paul Scherrer Institut, 5232 Villigen, Switzerland
SNF	Schweizerischer Nationalfonds SNF, Wildhainweg 3, 3001 Bern, Switzerland
SRI Center	Department of Environmental Research, SRI Center for Physical Sciences and Technology, Vilnius, 10222, Lithuania
TROPOS	Leibniz-Institut für Troposphärenforschung, 04318 Leipzig, Germany
UCam	Centre for Atmospheric Science, University of Cambridge, Lensfield Road Cambridge 1EP, United Kingdom
UGött	Institute of Physical Chemistry, University of Goettingen, Tammannstr. 6, 37077 Goettingen, Germany.
UManitoba	Department of Chemistry, University of Manitoba, Winnipeg, MB R3T 2N2, Canada
Univ. Albany	University at Albany, Department of Atmospheric and Environmental Sciences, Albany, NY, 12222, USA
Univ. Bergen	University of Bergen, Postboks 7800, 5020 Bergen, Norway
Univ. Bern	Departement für Chemie und Biochemie, Universität Bern, Freiestr. 3, 3012 Bern, Switzerland
Univ. Columbia	Department of Chemical Engineering, Columbia University, New York, NY 10027, USA
Univ. Gothenburg	University of Gothenburg, 405 30 Gothenburg, Sweden
Univ. Innsbruck	University of Innsbruck, Institute of Meteorology and Geophysics, A-6020 Innsbruck, Austria
Univ. Köln	Universität zu Köln, Albertus-Magnus-Plat, 50923 Köln, Germany
Univ. Mainz	Johannes Gutenberg-Universität Mainz, Saarstr. 21, 55122 Mainz, Germany
Univ. Massachusetts	University of Massachusetts Amherst, MA 01003, USA
Univ. Nanjing	Nanjing University, 22 Hankou Road, Gulou, Nanjing, Jiangsu, China
Univ. Napoli Federico	Universität Neapel Federico II, Corso Umberto I, 40, 80138 Napoli, Italy

Univ. Ohio	Byrd Polar and Climate Research Center, 108 Scott Hall, The Ohio State University, 1090 Carmack Road, Columbus, OH 43210, USA.
Univ. Toronto	University of Toronto, 27 King's College Circle, Toronto, Ontario M5S 1A1 Canada
Univ. Torino	University of Turin, Via Giuseppe Verdi, 8, Torino, Italy
Univ. Venice	Department of Environmental Sciences, University of Venice 'Ca' Foscari', Dorsoduro 2137, I-30123 Venice, Italy
WSL	Swiss Federal Research Institute WSL, 8903 Birmensdorf, Switzerland
Yale University	Yale Climate and Energy Institute, and Department of History, Yale University, 06520 New Haven, CT, USA

Paul Scherrer Institut :: 5232 Villigen PSI :: Switzerland :: Tel. +41 56 310 21 11 :: www.psi.ch